Institute of Physics

Interaction of the potential DNA-radiosensitizer 8-bromoadenine with free and plasmonically generated electrons

---

Doctoral thesis (cumulative)

in fulfillment of the requirements
for the degree of
" doctor rerum naturalium "
(Dr. rer. nat.)
in the scientific discipline " Chemical Physics "

submitted to the
Faculty of Science
of the University of Potsdam

by

Robin Mathis Schürmann

Potsdam, June 2017

Published online at the
Institutional Repository of the University of Potsdam:
URN urn:nbn:de:kobv:517-opus4-407017
http://nbn-resolving.de/urn:nbn:de:kobv:517-opus4-407017

Danksagung

Diese Arbeit ist im Zeitraum von Juni 2013 bis Juni 2017 (mit einer fünfmonatigen Unterbrechung bedingt durch Elternzeit) an der Universität Potsdam und der Bundesanstalt für Materialforschung und Prüfung (BAM) entstanden.
Das Zustandekommen dieser Doktorarbeit ist nur durch den Beitrag vieler Menschen möglich geworden bei denen ich mich in diesem Zuge bedanken möchte. Mein Dank gilt zuallererst meinem Betreuer JProf. Ilko Bald, der mir die Möglichkeit gegeben hat in seiner Arbeitsgruppe an diesem interessanten Thema zu arbeiten. Ich bin sehr dankbar für das in mich gesetzte Vertrauen und dafür dass er stets ansprechbar war. Die Gespräche waren stets inspirierend und Ansporn für neue Projekte. Ich hatte jederzeit die notwendigen Freiheiten um meine eigenen Ideen umzusetzen und erhielt dabei jede Unterstützung. Mir wurde die Möglichkeit für spannende Forschungsaufenthalte und Konferenzbesuche gegeben. Für all das bin ich sehr dankbar.
Des Weiteren möchte ich mich bei Prof. Hans-Gerd Löhmannsröben für die Übernahme der offiziellen Betreuung im Fach Physik und der Begutachtung dieser Arbeit bedanken. So konnte ich mir meine Chemiekenntnisse im Labor aneignen und mir blieb der Gang in den Vorlesungsaal erspart. Privatdozent Dr. Alexander Dorn möchte ich ebenfalls für die Erstellung des Zweitgutachtens danken.
Über dies hinaus gilt mein Dank meiner Arbeitsgruppe: Christian, Jenny, Julia, Kenny, Lisa, Lydia, Steffi, Till, Victoria und Youngeun. Ich habe die gute Arbeitsatmosphäre mit euch stets genossen, sei es beim gemeinsamen Mittagessen, im Seminar, im Labor oder in der Nachtschicht am Synchrotron. Die gute Zusammenarbeit, die inspirierenden Unterhaltungen und die vielfältige praktische Hilfe von euch allen hat sehr zum Erfolg dieser Arbeit beigetragen.
Ich möchte mich darüber hinaus bei S. V. Krishna Kumar und Thupten Tsering herzlich für die wundervolle Gastfreundschaft und die gute Zusammenarbeit bei meinem Forschungsaufenthalt am TIFR in Mumbai bedanken. Bei Stephan Denifl und Katrin Tanzer bedanke ich mich ebenfalls für den angenehmen und erfolgreichen Aufenthalt an der Universität Innsbruck.
Des Weiteren möchte mich bei meinen Bürokolleg*innen Axel, Stefanie, Arne, Aleksandra, Katrin und Zhiyang an der BAM für die nette Arbeitsatmosphäre und die gute Zusammenarbeit danken. Galina Jurchenko und Juliane Schäfer danke ich für ihre Unterstützung in allen administrativen Belangen. Eric Jablowski möchte ich für die aufwendige Synthese von Thiocyanatouracil und Jens Riedel für seine Hilfe bei meinen Laseraufbauten danken. Für die Unterstützung mit dem Raman Mikroskop bedanke ich mich bei Thomas Schmid, Stefan Seifert und Merwe Buurman. Darüber hinaus möchte ich mich bei allen Mitgliedern der Physikalischen Chemie an der Uni Potsdam sowie der (ehemaligen) Arbeitsgruppe 1. an der BAM für die schöne Zusammenarbeit bedanken.
Zu guter Letzt gilt mein Dank natürlich meinen Freunden und meiner Familie. Insbesondere bedanke ich mich bei Caro und Killian, die mit mir durch alle Höhen und Tiefen gegangen sind.

Abstract

In Germany more than 200.000 persons die of cancer every year, which makes it the second most common cause of death. Chemotherapy and radiation therapy are often combined to exploit a supra-additive effect, as some chemotherapeutic agents like halogenated nucleobases sensitize the cancerous tissue to radiation. The radiosensitizing action of certain therapeutic agents can be at least partly assigned to their interaction with secondary low energy electrons (LEEs) that are generated along the track of the ionizing radiation. In the therapy of cancer DNA is an important target, as severe DNA damage like double strand breaks induce the cell death. As there is only a limited number of radiosensitizing agents in clinical practice, which are often strongly cytotoxic, it would be beneficial to get a deeper understanding of the interaction of less toxic potential radiosensitizers with secondary reactive species like LEEs. Beyond that LEEs can be generated by laser illuminated nanoparticles that are applied in photothermal therapy (PTT) of cancer, which is an attempt to treat cancer by an increase of temperature in the cells. However, the application of halogenated nucleobases in PTT has not been taken into account so far.
In this thesis the interaction of the potential radiosensitizer 8-bromoadenine (^{8Br}A) with LEEs was studied. In a first step the dissociative electron attachment (DEA) in the gas phase was studied in a crossed electron-molecular beam setup. The main fragmentation pathway was revealed as the cleavage of the C-Br bond. The formation of a stable parent anion was observed for electron energies around 0 eV. Furthermore, DNA origami nanostructures were used as platformed to determine electron induced strand break cross sections of ^{8Br}A sensitized oligonucleotides and the corresponding non-sensitized sequence as a function of the electron energy. In this way the influence of the DEA resonances observed for the free molecules on the DNA strand breaks was examined. As the surrounding medium influences the DEA, pulsed laser illuminated gold nanoparticles (AuNPs) were used as a nanoscale electron source in an aqueous environment. The dissociation of brominated and native nucleobases was tracked with UV-Vis absorption spectroscopy and the generated fragments were identified with surface enhanced Raman scattering (SERS). Beside the electron induced damage, nucleobase analogues are decomposed in the vicinity of the laser illuminated

nanoparticles due to the high temperatures. In order to get a deeper understanding of the different dissociation mechanisms, the thermal decomposition of the nucleobases in these systems was studied and the influence of the adsorption kinetics of the molecules was elucidated. In addition to the pulsed laser experiments, a dissociative electron transfer from plasmonically generated "hot electrons" to ^{8Br}A was observed under low energy continuous wave laser illumination and tracked with SERS. The reaction was studied on AgNPs and AuNPs as a function of the laser intensity and wavelength. On dried samples the dissociation of the molecule was described by fractal like kinetics. In solution, the dissociative electron transfer was observed as well. It turned out that the timescale of the reaction rates were slightly below typical integration times of Raman spectra. In consequence such reactions need to be taken into account in the interpretation of SERS spectra of electrophilic molecules.

The findings in this thesis help to understand the interaction of brominated nucleobases with plasmonically generated electrons and free electrons. This might help to evaluate the potential radiosensitizing action of such molecules in cancer radiation therapy and PTT.

Zusammenfassung

Mit deutschlandweit über 200.000 Todesfällen pro Jahr ist Krebs die zweithäufigste Todesursache. In der Krebstherapie werden häufig Strahlen- und Chemotherapie kombiniert, da das Krebsgewebe durch die Gabe bestimmter Chemotherapeutika, z.B. halogenierte Nukleinbasen, gegenüber ionisierender Strahlung sensibilisiert wird. Die Wirkung dieser sogenannten Radiosensibilatoren lässt sich zumindest teilweise auf ihre Wechselwirkung mit niederenergetischen Elektronen zurückführen, welche in hoher Zahl entlang der Trajektorie hochenergetischer Teilchen oder Photonen erzeugt werden. In der Krebstherapie ist die DNA ein wichtiger Angriffspunkt, da schwere DNA-Schäden wie Doppelstrangbrüche zum Zelltod führen können. In der klinischen Praxis ist die Anzahl der eingesetzten meist zytotoxischen Radiosensibilisatoren relativ begrenzt. Zur Verbesserung der bestehenden Therapien durch den Einsatz von Medikamenten mit geringeren Nebenwirkungen, ist es notwendig die Wechselwirkungen zwischen potentiellen Radiosensibilisatoren und reaktiven Sekundärteilchen wie niederenergetischen Elektronen besser zu verstehen. Neben der Strahlentherapie werden niederenergetische Elektronen auch durch Laserbestrahlung von plasmonischen Nanopartikeln erzeugt, welche in der Photothermaltherapie (PTT) Anwendung finden. Die mögliche Anwendung von halogenierten Nukleinbasen zur Verbesserung der Photothermaltherapie ist jedoch bisher noch nicht in Erwägung gezogen worden.

Im Rahmen dieser kumulativen Dissertation wird die Wechselwirkung des potentiellen Radiosensibilisators 8-Bromoadenin (^{8Br}A) mit niederenergetischen Elektronen untersucht. Unter Verwendung eines gekreuzten Molekül-Elektronenstrahls wurde in einem ersten Schritt die dissoziative Elektronenanlagerung (DEA) an ^{8Br}A untersucht. Dabei zeigte sich, dass der Hauptzerfallskanal in dem Aufbrechen der C-Br Bindung besteht. Darüberhinausgehend wurde bei der Anlagerung von Elektronen mit einer Energie von 0 eV ein stabiles ^{8Br}A Anion beobachtet. Um den Einfluss der DEA-Resonanzen, die für freie Moleküle in der Gasphase beobachtet wurden, auf die elektroneninduzierten DNA-Strangbrüche zu untersuchen wurden DNA- Origami-Nanostrukturen mit Elektronen bestrahlt. Die DNA-Origami-Strukturen wurden sowohl mit ^{8Br}A modifizierten Oligonukleotiden und der nicht modifizierten Kontrollsequenz bestückt und die Strangbruch

Wirkungsquerschnitte in Abhängigkeit von der Elektronenenergie bestimmt. DEA-Prozesse hängen stark von dem umgebenden Medium ab. Aus diesem Grund wurden laserbestrahlte Gold-Nanopartikel (AuNPs) als Elektronenquellen auf der Nanoebene verwendet. Der Zerfall von bromierten und unmodifizierten Nukleinbasen wurde mit UV-Vis-Absorptions-Spektroskopie verfolgt, während die Identifizierung der entstandenen Fragmente über Oberflächenverstärkte Ramanstreuung (SERS) erfolgte. Neben dem elektroneninduzierten Schaden, werden die Nukleinbasen in der Umgebung der AuNPs durch die hohen Temperaturen auch thermisch zersetzt. Um diese verschiedenen Prozesse auseinander halten zu können, wurde die thermische Zersetzung auf den laserbestrahlten AuNPs detailliert untersucht und der Einfluss der Adsorptionskinetik herausgearbeitet. Elektroneninduzierte Reaktionen auf Nanopartikeln finden nicht nur bei Bestrahlung mit intensiven Laser-Pulsen statt. Ein dissoziativer Elektronentransfer auf ^{8Br}A, der zum Aufbrechen der C-Br Bindung führt, konnte ebenfalls während der Bestrahlung mit einem kontinuierlichen Laser geringer Intensität mit SERS beobachtet werden. Mit Hilfe von fraktaler Kinetik konnten dabei die Reaktionen auf getrockneten Proben beschrieben werden. Auf diese Art wurde die Reaktion sowohl auf AuNPs als auch auf AgNPs als Funktion der Laserintensität und -Wellenlänge untersucht. Ebenfalls in Lösung konnte das Auftrennen der C-Br Bindung beobachtet werden, wobei die Zeitskalen der Reaktion ein wenig kürzer als die typischen Integrationszeiten bei Ramanmessungen waren. Aus diesem Grund müssen Dissoziative-Elektronen-Transfer- Reaktionen bei der Interpretation von SERS Spektren mit in Betracht gezogen werden.

Die Ergebnisse dieser kumulativen Doktorarbeit fördern das Verständnis der Wechselwirkungen zwischen bromierten Nukleinbasen mit freien und plasmonisch erzeugten Elektronen. Dies könnte dabei helfen das Potential von ^{8Br}A als möglicher Radiosensibilisator besser beurteilen zu können.

Publications

- Molekulare Prozesse im DNA-Nanolabor - DNA-Nanostrukturen für die Analytik
  Christian Heck, Lydia Olejko, Julia Prinz, Robin Schürmann, Ilko Bald
  GIT Labor-Fachzeitschrift 11/2014, 25 - 27

- Using DNA Origami Nanostructures To Determine Absolute Cross Sections for UV Photon-Induced DNA Strand Breakage
  Stefanie Vogel, Jenny Rackwitz, Robin Schürmann, Julia Prinz, Aleksandar R. Milosavljević, Matthieu Réfrégiers, Alexandre Giuliani and Ilko Bald
  J. Phys. Chem. Lett., 2015, 6 (22), pp 4589 - 4593
  DOI: 10.1021/acs.jpclett.5b02238

- Decomposition of DNA Nucleobases by Laser Irradiation of Gold Nanoparticles Monitored by Surface-Enhanced Raman Scattering **(M3)**
  Robin Schürmann and Ilko Bald
  J. Phys. Chem. C, 2016, 120 (5), pp 3001 - 3009
  DOI: 10.1021/acs.jpcc.5b10564

- Ultra-Sonication of ZIF-67 Crystals Results in ZIF-67 Nano-Flakes
  Sebastian Beyer, Carsten Prinz, Robin Schürmann, Ines Feldmann, Annett Zimathies, Anna M. Blocki, Ilko Bald, Rudolf J. Schneider and Franziska Emmerling
  ChemistrySelect 2016, 1, 5905 - 5908
  DOI: 10.1002/slct.201601513

- Real-time monitoring of plasmon induced dissociative electron transfer to the potential DNA radiosensitizer 8-bromoadenine **(M5)**
  Robin Schürmann and Ilko Bald
  Nanoscale 2017, 9, 1951 - 1955
  DOI: 10.1039/C6NR08695K

- Effect of adsorption kinetics on dissociation of DNA-nucleobases on gold nanoparticles under pulsed laser illumination **(M4)**
  Robin Schürmann and Ilko Bald
  Phys. Chem. Chem. Phys. 2017, 19, 10796 - 10803
  DOI: 10.1039/C6NR08695K

- On the Stability of the Parent Anion of the Potential Radiosensitizer 8-Bromoadenine formed by Low Energy (<3 eV) Electron Attachment **(M1)**
  Robin Schürmann, Katrin Tanzer, Iwona Dabkowska, Stephan Denifl and Ilko Bald
  J. Phys. Chem. B, 2017
  DOI: 10.1021/acs.jpcb.7b02130

- Coating of Colloidal Zeolitic Imidazolate Framework (ZIF) Particles with a Nanometer thin Polyelectrolyte Membrane
  S. Beyer, R. Schürmann, I. Feldmann, A. Blocki, I. Bald, R. J. Schneider and F. Emmerling
  Submitted

- Resonant formation of strand breaks in sensitized oligonucleotides induced by low-energy electrons (0.5 - 9 eV) **(M2)**
  Robin Schürmann, Thupten Tsering, Katrin Tanzer, Stephan Denifl, S.V.K. Kumar, and Ilko Bald
  Submitted

Oral presentations

- "Dissociative electron attachment to the potential DNA radiosensitizer 8-Bromoadenine in condensed and gas phase"
  2nd International Workshop on Dissociative Electron Attachment (DEA)
  November 2015, Mumbai, India

- "Dissociative Electron Transfer from Noble Metal Nanoparticles to potential DNA-Radiosensitizer 8-Bromoadenine"
  DNA Mitteldeutschland Workshop
  16.09.2016, Potsdam, Germany

- "Plasmon induced reactions of DNA on metal nanoparticles"
  Nanobiophotonics workshop
  13.03.2017, Tel Aviv, Israel

- "Plasmon mediated decomposition of DNA radiosensitizers on metal nanoparticles"
  4th Annual Conference on Optical Nanospectroscopy
  30.03.2017, Lisbon, Portugal

- "Thermal and electron induced damage to DNA on laser illuminated plasmonic nanoparticles"
  Molecular Plasmonics 2017
  20.05.2017 Jena, Germany

Poster presentations

- Correlated SERS and AFM imaging to investigate DNA strand breaks at a single-molecule level",
  10th Symposium Confocal Raman Imaging,
  September 2013, Ulm, Germany

- "Radiosensitizing Effect of Gold Nanoparticles and Bromouracil studied by Surface enhanced Raman Spectroscopy and Atomic Force Microscopy" 113th General Assembly of the German Bunsen Society for Physical Chemistry,
  May 2014, Hamburg, Germany

- "Decomposition of DNA Components by Laser Irradiation of Noble Metal Nanoparticles monitored by Surface-Enhanced Raman Scattering"
  International Raman Fest 2016, 4 th Annual Conference on Applied Raman Spectroscopy
  May 2016, Berlin, Germany

Contents

List of Abbreviations

The list of abbreviations is sorted in alphabetic order and refers to the main text of this thesis. Abbreviations found in the manuscripts M1 - M5 are not necessarily found in this list but are explained in the manuscript itself.

^{2F}A	2-Fluoroadenine
^{5Br}C	5-Bromocytosin
^{5Br}U	5-Bromouracil
^{8Br}A	8-Bromoadenine
^{8Br}dADP	8-Bromo-2'-deoxyadenosine 3'5'-diphsophate
^{8Br}G	8-Bromoaguanine
A	Adenine
Abs	Absorbance
AFM	Atomic force microscopy
$AgNO_3$	Silver nitrate
AgNP	Silver nanoparticle
AuNP	Gold nanoparticle
$AuHCl_4$	Chloroauric acid
B	Parameter depending on details of the scattering process
Bt	Biotin
Br	Bromine
c	Concentration
c_{NB}	Concentration of nucleobases
c_{max}	Maximum concentration of adsorption sites
c_{Frag}	Concentration of fragmented nucleobases
c^0_{NB}	Initial concentration of nucleobases
C	Cytosine
cw	Continuous wave
d	Path length of light in medium
DEA	Dissociative electron attachment
DFT	Density functional theory
DNA	Deoxyribonucleic acid
DSB	Double strand break
e	Charge of an electron ($1.602 \cdot 10^{-19} C$)
e^-	Electron
e^-_{hyd}	Hydrated electron
em	Electromagnetic
E	Electrical field
E_{out}	Electrical field outside the particle
EA	Electron affinity
EDTA	Ethylenediaminetetraacetic acid
E_F	Fermi energy
EF_{SB}	Strand break enhancement factor
EF_{SERS}	SERS enhancement factor
EtOH	Ethanol
f	Filling factor
FWHM	Full width half at maximum
g	Enhancement factor of the E-Field
G	Guanine

h	Fractal dimension
$\hbar$	Planck constant ($1.034 \cdot 10^{-34} J \cdot s$)
HOMO	Highest occupied molecular orbital
HPLC	High-performance liquid chromatography
I	Intensity
I_{SERS}	Intensity of the SERS signal
$\mathcal{K}$	Wave vector
k	Rate constant
k_1	Rate constant at time = 1
k_{ad}	Adsorption rate constant
k_{obs}	Observed rate constant
KBr	Potassium bromide
K_L	Langmuir constant
l	Angular momentum of an electron
l_∞	Mean free path of electrons
L	Summation index of the partial waves
LEE	Low energy electron
LUMO	Lowest unoccupied molecular orbital
m	Ratio of complex refractive indexes of metal and medium
M13mp18	Genome of bacteriophage M13mp18
$MgCl_2$	Magnesium chloride
MO	Molecular Orbital
mRNA	Messenger ribonucleic acid
n	Complex refractive index of metal
n_m	Complex refractive index of surrounding medium
N	Free electron density
N_{Puls}	Number of laser pulses
NaOH	Sodium hydroxide
NB	Nucleobase
Nd:YAG	Neodymium-doped yttrium aluminum garnet
NIR	Near infrared
m_e	Effective mass
PTT	Photothermal therapy
q	Displacement of nuclei from equilibrium position
q_0	Maximal elongation of molecular bond
Q	Heat
r	Radial distance
$\mathbf{r}$	Radial vector
R	Radius of nanoparticle
RNA	Ribonucleic acid
SAv	Streptavidin
SERS	Surface enhanced Raman scattering
Si	Silicon
SI	Supporting Information
SP	Surface plasmon
SPR	Surface plasmon resonance
SSB	Single strand break
ssDNA	Single stranded DNA
t	Time
T	Thymine

TAE	TRIS Acetate EDTA
TNI	Transient negative ion
TRIS	Tris(hydroxymethyl)aminomethane
U	Uracil
UHV	Ultra high vacuum
UV	Ultra violett
v_F	Fermi velocity
V_{eff}	Effective potential
V_l	Centrifugal potential
V_α	Charge induced dipole potential
VAE	Vertical attachment energy
VDE	Vertical detachment energy
Vis	Visible
x, y, z	Cartesian coordinates
Z	atomic number
α	Polarizability of the molecule
α_0	Polarizability of the molecule in equilibrium position
γ	Damping constant
γ_0	Size independent damping constant
Γ	Plasmon absorption band width
ϵ	Extinction coefficient
ε	Complex dieletric function of the metal
ε_1	Real part of dielectric function
ε_2	Imaginary part of dielectric function
ε_D	Drude term of dielectric function
ε_{IB}	Interband term of dielectric function
ε_m	Dielectric function of the surrounding medium
θ	Angle between the electrical field and the vector $\mathbf{r}$
κ	Thermal conductivity
κ_α	Heat capacity
λ	Wavelength
μ	Induced dipole moment
ν_0	Frequency of incident light
ν_{vib}	Vibrational frequency of harmonic oscillator
σ_{abs}	Absorption cross section
σ_{ext}	Extinction cross section
σ_{sca}	Scattering cross section
σ_{SB}	Strand break cross section
τ	Collision time of all electron scattering events
τ_{e-e}	Collision time of electron-electron scattering
τ_{e-ph}	Collision time of electron-phonon scattering
τ_{ph-ph}	Collision time of phonon-phonon scattering
ψ	Illuminated ratio of the solution
Ψ, η	Cylindrical Bessl-Ricatti functions
ω	Frequency
ω_P	Plasma frequency

1 Introduction

Cancer is a lethal disease, where body cells abnormally grow and tend to spread over the body. Cancer therapy generally requires harsh methods like surgery, chemotherapy and radiation therapy, which can have severe side effects and bear risks for the patient [1]. In radiation therapy cancer cells are killed by irradiating the tumorous tissue with energetic particles or photons. It is assumed that the cell death is caused by damage of the deoxyribonucleic acid (DNA) located in the nucleus that contains the heretic information required to build new cells [2]. A single double strand break (DSB) is assumed to be sufficient to induce the cell death [3]. The majority of the DNA damage is mediated by reactive secondary species like hydroxyl radicals and low energy electrons that are generated in the hydrolysis of water [4]. The latter ones are the most abundant secondary species, however it is assumed that their reactivity towards the DNA is limited to a femtosecond (fs) timescale [5]. As soon as water molecules solvate the electrons, they are assumed to be relatively unreactive, hence their relevance in the DNA damage was assumed to be negligible [4]. Consequently, it is beneficial for radiation therapy if the reactivity of DNA in cancer cells can be enhanced towards hydrated and prehydrated electrons. To increase the radiation damage to cancerous tissue, radiosensitizing agents are administered, which accumulate in cancer cells due to their enhanced metabolism [6]. One example of radiosensitizers are modified nucleobases (NBs), which are incorporated into the DNA doublestrand to enhance the damage to the DNA or inhibit its repair[7]. Incorporated electrophlic molecules can capture an electron and decay rapidly via dissociative electron attachment (DEA). In DEA a short lived anion is formed, which subsequently relaxes by forming an anionic and one or more neutral fragments [8]. In this way, radicals in the DNA strand can be formed, which might act as a precursor for a strand break [9]. Additionally such radiosensitizing molecules act as a kind of antenna that captures the electrons [10] and subsequently transfers them towards the DNA backbone. In consequence the DNA backbone can break due to the attachment of the excess electron [11].
The importance of the NB adenine in the electron induced DNA damage was underestimated for a long time as a weak interaction with electrons was assumed [12]. However, recent studies show that the low energy electron (LEE) induced damage to DNA oligonucleotides depends on their sequence with the highest strand break cross section for adenine rich sequences [13].

Moreover, the incorporation of bromine containing NBs like 5-bromouracil (^{5Br}U) significantly enhances the single strand break (SSB) cross section [13]. Hence, the focus of this thesis is to evaluate the potential of the brominated adenine analougue 8-bromoadenine (^{8Br}A) as radiosensitizer. The interaction of LEEs with ^{8Br}A is studied with different approaches. For example, their decomposition around laser illuminated gold nanoparticles (AuNPs) is investigated. AuNPs are used e.g. in cancer photothermal therapy (PTT). In PTT the extraordinary absorption of AuNPs of visible and near infrared (NIR) photons is exploited to convert the light of a NIR laser into heat and kill the cells due to the elevated temperatures [14]. The heating of the AuNPs is mediated by the non-radiative decay of collective oscillations of the conduction electrons, the so called surface plasmons (SP), which are excited by the electrical field of the incoming light. There are different attempts using continuous wave (cw) and pulsed lasers in PTT. In the former the cells are killed by hypothermia and in the latter especially the DNA is damaged by a short ranged high temperature and pressure region close to the AuNPs [15]. Moreover, from plasmonic catalysis it is known that so called "hot electrons", which are an intermediate in the plasmon induced AuNPs heating can be transfered to adsorbed molecules and trigger chemical reactions [16]. This effect might be exploited in the combination of electrophilic DNA-radiosensitizers together with laser illuminated AuNPs to enhance the DNA damage in PTT and on the long term help to improve this therapy.

In order to study the interaction of ^{8Br}A with LEEs and evaluate its potential as radiosensitizer, DEA experiments in the gas phase have been performed with a crossed electron-molecular beam setup. The results for electron energies below 3 eV are published in manuscript 1 (M1) [17] and show the generation of a stable parent anion by the attachment of electrons with an energy close to 0 eV by forming a complex of an almost closed shell Br^- and an adenyl radical. As observed for all native NBs the subtraction of a hydrogen atom is also an important relaxation channel for $^{8Br}A^-$. However, the main fragmentation channel is the cleavage of the C-Br bond and the formation of Br^- as well as its anionic counterpart with a lower intensity. The abstraction of the bromine and the formation of the adenyl radical was assumed to act as a precursor for a subsequent SSB [9].

Consequently, in the present work ^{8Br}A modified oligonucleotides have been placed on DNA origami nanostructures together with their native analogues and irradiated in ultra high vacuum (UHV) conditions with LEEs to examine the influence of the bromination on the formation of SSBs. The results are presented in the manuscript 2 (M2) [18]. The SSB yield was determined as a function of the energy of the incident electrons ranging from 0.5 eV to 9 eV showing a maximum at around 7 eV for the modified and unmodified sequence. Based on this data the enhancement factor of the ^{8Br}A modified strands was determined revealing an increased damage over the whole energy spectrum by a factor of 1.9 ± 0.6. However, as the damage induced by electrons with an energy below 2 eV was comparably low, the cleavage of the C-Br bond might not be solely responsible for the enhancement. Moreover, ^{8Br}A might serve as an antenna that captures the electrons, which subsequently can induce a variety of DEA reactions in the DNA causing a SSB. Additionally, DEA measurements of ^{8Br}A in the gas phase at higher electron energies (> 5) eV reveal a rich fragmentation of the

molecule including multiple bond cleavage rupturing the ring structure.

The previous experiments were performed under UHV condition, however the DEA towards DNA is influenced by an aqueous environment [19]. In manuscript 3 (M3) [20] the interaction of the NBs analogues thymine (T), uracil (U) and ^{5Br}U with AuNPs has been examined. AuNPs emit electrons due to thermionic emission when they are illuminated with intense nanosecond (ns) laser pulses [21]. Furthermore, the high temperatures in close proximity to the AuNPs surface also may decompose the NBs under these conditions. The fragmentation of the NBs was observed with UV-Vis spectroscopy and surface enhanced Raman scattering (SERS) in order to identify single fragments. For U and T a decomposition of the ring was observed forming CN and NCO by multiple bond cleavages, whereas for ^{5Br}U a rupture of the C-Br bond was observed leaving the uracil residue intact.

In a further study published in manuscript 4 (M4) [22] the decomposition of all four NBs and their brominated analogues on pulsed laser illuminated AuNPs was investigated under conditions where thermal effects are predominating. The kinetics of the photo induced dissociation was carefully determined and a great influence of the adsorption of the molecules on the AuNP surface was pointed out. The experimental data was compared with theoretical calculations based on the Langmuir adsorption assumptions.

Finally, in manuscript 5 (M5) [23] the electron transfer from plasmonically excited noble metal nanoparticles to ^{8Br}A was studied with SERS. A rapid transformation form ^{8Br}A to A was observed by changes in the wavenumber of the ring breathing mode. The reaction was induced by a continuous wave laser at low energies in a typical SERS setup. The reaction was described by fractal like kinetics revealing a dependence of the reaction rate on the wavelength of the incident light as well as on the material of the nanoparticles. On silver nanoparticles (AgNPs) the processes are significantly faster than on gold probably due to the stronger plasmonic enhancement. However, at comparably low photons energies (1,6 eV) the reaction rates do not correlate with the plasmonic properties of the nanoparticles indicating a resonant electron transfer into the lowest unoccupied molecular orbital (LUMO) of the adsorbed ^{8Br}A. The dissociative electron transfer takes place in dried samples as well as in aqueous environment and the timescales of the reaction were comparable to typical accumulation times in SERS measurements. Hence, such reactions have to be taken into account in the interpretation of SERS spectra of electrophilic molecules. Beyond that, a dissociative electron transfer from AuNPs towards molecules incorporated in the DNA of cancer cells might find potential applications in PTT.

2 Theory

2.1 DNA

DNA consists of two complementary polynucleotide chains. Each nucleotide is composed of one out of four NBs (shown in figure 2.1 a)) connected to a desoxyribose moiety with an attached phosphate group [24]. In order to form the doublestrand, the four canonical NBs adenine (A), cytosine (C), guanine (G) and T are interlinked with each other by the Watson-Crick base pairing, where the two complementary base pairs A-T and G-C are connected via hydrogen bonds[25] as shown in figure 2.1 b).

Due to the stacking interaction between neighboring base pairs the DNA-structure is stabilized [26] (see figure 2.1 c)). The resulting double strand forms a double helix shown in figure 2.1 d) with a diameter of 2 nm and a distance between the base pairs along the helical axis of 0.34 nm [27]. The strong UV absorption of DNA at 260 nm arises from the $\pi - \pi^*$-transition of the NBs [28] as shown in figure 2.1 e). The excited $\pi - \pi^*$ state relaxes to a "dark" $n - \pi^*$ state that subsequently depopulates within 1 - 2 ps [29]. Due to the base stacking the decay of the excited state of single stranded DNA (ssDNA) is 1 - 2 orders of magnitude slower [28]. The relaxation ends in the electronic ground state, whereas deleterious reactions are prevented by the highly efficient non-radiative pathways [28].
Long chains of DNA form 23 pairs of chromosomes that contain the genetic code [30] of a human and are found in every cell, where they are stored in the nucleus. The DNA determines the cell growth, its lifetime and how often it divides. A DNA sequence of a certain length is called a gene and contains the information required to produce a protein [24]. In a two step process the information of a gene is transferred to a protein. At first the DNA-sequence is transcribed via messenger ribonucleic acid (mRNA) and subsequently the information of the mRNA is translated inside the cytoplasm with the help of a ribosome to a sequence of amino acids. A sequence of three nucleotides is translated to one amino acid using transfer RNA [24]. If the nucleobases in a DNA strand are chemically modified for example by methylation [31] or by formation of 8-hydroxyguanosine due to reactions with radical oxygen species [32], cancer can occur. There are several modifications of nucleobases in certain sequences like the DNA mismatch repair gene known to be relevant in the pathogenesis of cancer [33]. Especially the G rich telomeric sequence that is responsible for the aging of cells plays an important role in

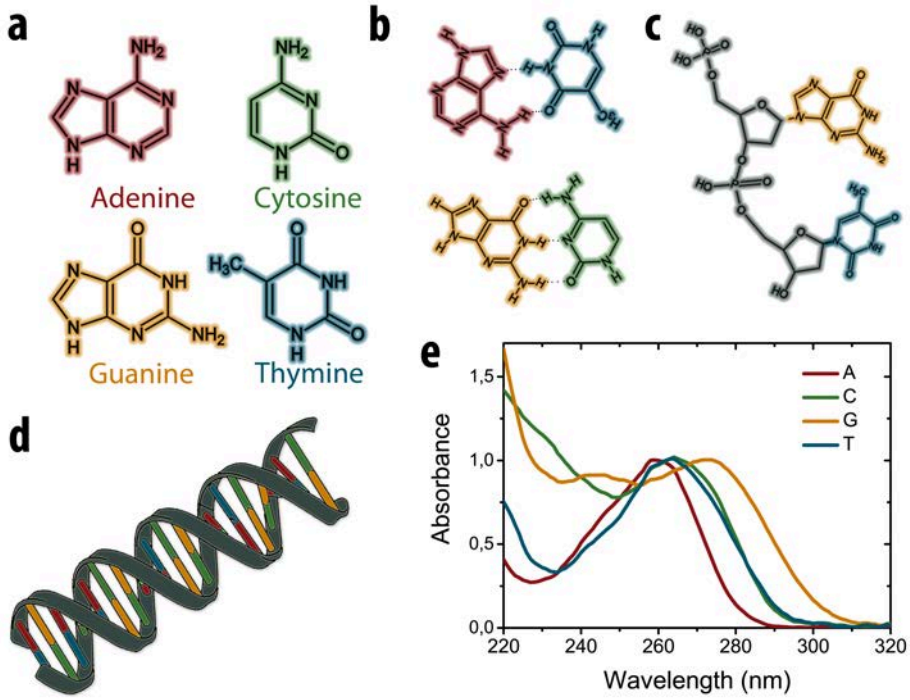

Figure 2.1: a) Chemical structure of the four canonical NBs A (red), C (green), G (yellow) and T (blue). d) Watson-Crick base pairing of A-T and G-C connected by hydrogen bonds. c) Base stack of G and T. d) Scheme of a DNA double strand. e) Normalized UV-Vis spectra of DNA nucleobases recorded with a Nanodrop 2000 from Fisher Scientific.

carcinogenic cells and serves therefore on the other hand as a target for cancer therapy [34, 35]. There are various therapeutic agents applied in cancer therapy aiming at the DNA in order to kill the carcinogenic tissue [36]. In the framework of this thesis the focus is on modified nucleobases that are incorporated into the doublestrand and sensitize the DNA towards ionizing radiation [6].

2.1.1 DNA damage induced by low energy electrons

The DNA can be directly harmed by ionizing radiation. However, around two third of the DNA radiation damage is caused by secondary species generated through the hydrolysis of water molecules in the cells [37]. A particle or photon with high energy ionizes a water molecule and generates a free electron and a H_2O^+ cation that subsequently further decays (see equation (2.1)). Together with an additional water molecule the cation forms a H_3O^+ ion and an $OH\bullet$ radical (see equation (2.2)). In the past decades $OH\bullet$ radical was made responsible for almost all secondary DNA damage [4]. LEEs are the most abundant intermediates in DNA damage as around 40 000 secondary electrons are generated along the track of a 1 MeV photon [38]. The highest yield is found for electrons with energy between 9 - 10 eV [39]. The secondary electrons were assumed to be relatively harmless to the

DNA as water molecules form a stabilizing complex around the electrons [40] (see equation (2.3)).

$$h\nu + H_2O \rightarrow H_2O^+ + e^- \tag{2.1}$$

$$H_2O^+ + H_2O \rightarrow H_3O^+ + OH\bullet \tag{2.2}$$

$$e^- \rightarrow e^-_{hyd} \tag{2.3}$$

The energy of these hydrated electrons lies below the energy of the LUMO of the DNA and therefore an electron transfer is unlikely [41]. Nevertheless, on a subpicosecond lifetime ($10^{-13}s$) the electrons are in a prehydrated state and can be transfered to the DNA and subsequently cause molecular bond breaks via DEA [5]. DEA will be described in detail in the subsequent subsection. Beside DEA, there are versatile interactions between LEEs and biomolecules like ionization [42] and electronic excitation [43] leading to severe DNA damage. DNA damage generally comprises SSBs, DSBs, damages of a NB or sugar moiety, clustered damage, interstrand crosslinks and intrastrand crosslinks [36]. In order to study the interaction between LEEs and DNA, several experiments with electron irradiated plasmid DNA with a subsequent agarose gel electrophoresis analysis were performed, revealing certain DNA damage as a function of the incident electron energy under UHV conditions [44]. All experiments exhibit a resonant dependence of SSBs and DSBs induced by LEEs [45], nevertheless the energies of the resonances differ in the experiments performed by L. Sanche et al. [46], S.V.K. Kumar et al. [47] and T.M. Orlando et al. [48] that all used different plasmids. The incorporation of the chemotherapeutic agent cisplatin exhibit a radiosensitizing effect when the DNA is irradiated with electrons between 2 eV and 20 eV, which means that the LEE induced DNA damage is increased when the agent is bound to the DNA [49]. However, a precise positioning of modifications in the plasmid DNA is not possible and the influence of the DNA sequence on the strand break cross sections remains unknown. Using high-performance liquid chromatography (HPLC) short oligonucleotide trimers with a well defined sequence [50] irradiated with electrons were investigated. Beside SSBs also damage like base losses and base modifications were revealed [51, 52]. Although even the effect of incorporated halogenated nucleotides can be studied [53, 54], the scope of this technique is limited to short trimeric oligonucleotides. This disadvantage can be tackled using so called DNA origami structures that allow the determination of DNA SSBs in well defined oligonucleotides [55, 56].

DNA origami structures are self-assembled nanostructures, which were invented by P.W.K. Rothemund in 2006 [57] and serve as a molecular pegboard that allows the precise positioning of analyte molecules or further nanostructures and macromolecules. The binding of streptavidin (SAv) to biotin (Bt) modified staple strands on the DNA origami can be monitored by atomic force microscopy (AFM) [58, 59] and allows the observation of chemical reactions on the template [60]. In figure 2.2 the principle of the SSB detection is sketched. Briefly, DNA origami structures wearing two target sequences equipped with a Bt group at the end are located at the side or center position of the template. Irradiation with LEEs causes SSBs leading to a loss of the Bt containing fragment. A subsequent binding of SAv is only possible at the intact target strands and visualized by AFM for

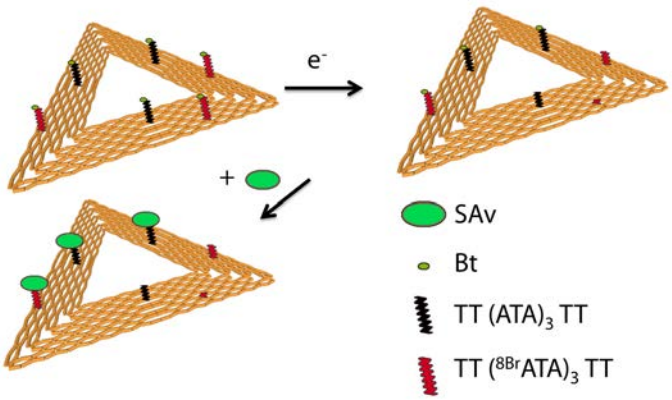

Figure 2.2: Principle of DNA SSB detection by DNA origami templates, where after the irradiation with LEEs the intact biotinilated target strands are marked with SAv (figure adapted from M2).

further analysis. In this manner the absolute SSB cross sections of specific sequences can be determined. At 18 eV electron energy, a strong dependence of the SSB cross section on the DNA sequence was found with a strong sensitivity of A rich sequences [13], whose impact was underestimated so far [12]. Furthermore, potentially radiosensitizing molecules like ${}^{5Br}U$ and [13] 2-fluoradenine ${}^{2F}A$ [61] inside the target sequence significantly enhance the SSB yield. The cross sections for the molecule-electron interactions, which reflect the DNA damage (electronic exitation, ionization, DEA), depend on the electron energies. For subionization electrons DEA is the most relevant process as even DNA strand breaks (SBs) can be induced by prehydrated electrons, which attach to the DNA in an ultrafast transfer process [62]. Thereby electrons with an energy down to a few hundred meV are captured by the π^* orbitals of the NBs, which serve as "antenna". This is followed by an electron transfer to the sugar phosphate backbone by orbital overlap and finally cleavage of the sugar-phosphate σ bond [11, 5, 63]. The electron induced reactions in DNA are very sensitive to the surrounding medium [19], as NB anions, which tend to fragment in the gas phase, get stabilized in an aqueous environment [64, 65]. Experimental studies of LEE induced damage to DNA in solution are quite limited due to the short free path length of electrons in water. Therefore free electrons with an energy in the keV regime are required [66] or the experiments are limited to a few hydration layers [67]. Hence, new electron sources in an aqueous environment are desirable providing electrons with an energy of only a few eV.

2.1.2 Dissociative Electron attachment

For LEEs with an energy below 20 eV DEA is an important DNA damaging pathway [68]. An incoming electron can be captured by a molecule and form a typically unstable anion with a short lifetime, a so called transient negative ion (TNI) [69]. Thereby the electron is trapped for a certain time in an unoccupied molecular orbital (MO). In this process the molecule is excited via a Frank-Cordon-transition into an excited state as shown in figure 2.3 a),

whereas the energy difference in this transition is called vertical attachment energy (VAE) [70].

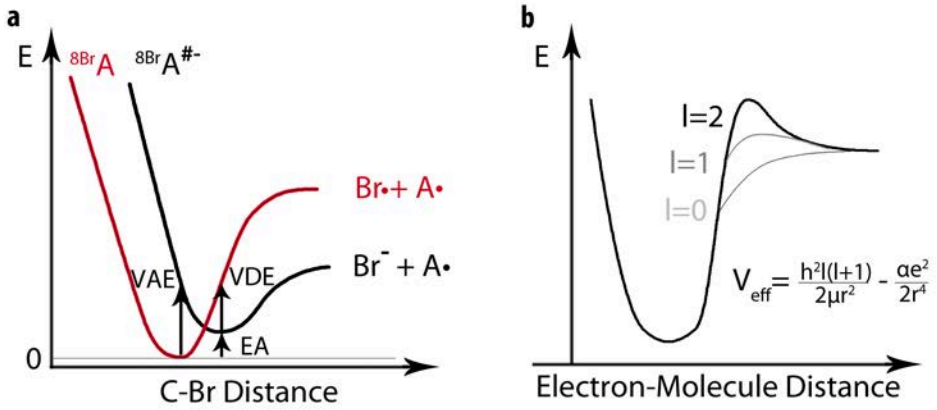

Figure 2.3: a) Schematic energy diagram of a neutral ^{8Br}A molecule with a σ^* shape resonances. b) Effective interaction potential of an electron approaching a molecule showing the formation of a centrifugal barrier for $l > 0$. Figures are adapted from source [8].

Furthermore, the Frank Condon transition from the ground state of the anion to the unoccupied MO of the neutral parent is denoted as vertical detachment energy (VDE) and the difference between the ground state of the neutral MO and the ground state of the TNI is called electron affinity (EA) [70]. In this picture the Born-Oppenheimer approximation is assumed, where the position of the cores remain unchanged during electronic processes. When an electron approaches a molecule, it experiences the long range attractive charge induced dipole potential V_α [8]. On the contrary at short distances the repulsive centrifugal potential V_l emerging from the electrons angular momentum is dominating as shown in figure 2.3 b). If $l > 0$, the effective potential $V_{eff} = V_\alpha + V_l$ forms a potential barrier that can trap the electron for certain time [8]. The effective potential is given by:

$$V_{eff} = \frac{\hbar^2 \cdot l \cdot (l+1)}{2\mu r^2} - \frac{\alpha e^2}{2r^4} \tag{2.4}$$

where α is the polarizability of the molecule, r is the distance between the electron and the molecule, e is the charge and l the angular momentum of an electron [70]. As the electron occupies a previously empty σ^* MO, the electron configuration of the molecule remains unchanged. Such resonances are called shape resonances and generally occur at energies below 4 eV with a lifetime from 10^{-14} s to 10^{-10} s [8]. If the electron energy is high enough to excite the neutral molecule, the resonances are referred to as core excited resonances. It is differentiated between core excited shape resonances and core excited Feshbach resonances, depending on whether the energy of the excited state of the anion is higher or lower than the neutral excited state. In the latter case the lifetime of the resonance is increased, as a relaxation into the lower lying neutral state by autodetachment of an electron is in-

hibited. Alternatively, vibrationally excited Feshbach resonances with an energy typically close to 0 eV are formed if the vibrational levels of the TNI are lower than the neutral ones. Molecular resonances mainly decay via autodetachment of the electron but likewise a relaxation via DEA is possible. In this case the TNI stabilizes by dissociating into an anionic and one or more neutral fragments:

$$AB + e^- \rightarrow AB^{\#-} \rightarrow A^- + B \tag{2.5}$$

# denotes a metastable state. DEA is a selective process, where the cleavage of a certain bond depends in a resonant way on the energy of the incident electrons [71].

DEA to DNA components

Due to its relevance in the secondary damage of DNA, the DEA to DNA subunits was already studied in detail [37]. Crossed electron-molecular beam experiments of the five nitrogenous bases A [72], T [73], C [74], U [75] and G [76] reveal that at low electron energies the most abundant fragmentation channel is the decay into a neutral hydrogen atom and a closed shell $(\mathrm{NB} - \mathrm{H})^-$ anion:

$$NB + e^- \rightarrow NB^{\#-} \rightarrow (NB - H)^- + H \tag{2.6}$$

The hydrogen loss is caused by a vibrationally excited Feshbach resonance coupled to the temporary anion state formed by occupation of the σ^* MO that is located around 1 eV [77]. At higher electron energies starting at 6 eV, beside the exocyclic bond clevages, also multiple bond cleavages occur that rupture the ring structure. For the pyrimidine molecules the most common anion is NCO^-, whereas for the purines CN^- is strongly generated [37]. In the sugar phosphate backbone a strand break is represented by the cleavage of the P-O or the C-O bond, respectively. Such bond breaks occur due to the attachment of electrons with an energy around 8 eV in RNA [78] and DNA backbones [79]. Furthermore potential radiosensitizing molecules like 5-halouracils show a high reactivity to LEEs, as the C-halogen bond is already cleaved by electrons with an energy down to 0 eV [80, 81]. The interplay of the σ^*, π^* and dipole bound state is made responsible for the low lying resonances in ^{5Br}U and 5-iodouracil [82]. Comparable observations were made for halogenated A analogues like 2-chloroadenine [83]. The attachment of a single LEE with a kinetic energy of 0 eV to the radiosensitizer cisplatin even causes the simultaneous loss of both chloride atoms [84].

2.1.3 Radiosensitization

In cancer treatment radiation- and chemotherapy is often combined due to a superadditive effect called radiosensitization [6]. There are different explanations for the radiosensitizing action depending on the agent, since some of them inhibit DNA repair process and others increase the radiation damage. The focus of this work lies on the physicochemical background of the latter one. Generally, radiosensitizers do not require a cytotoxic activity as in the case of the non-toxic ^{5Br}U. However, toxic chemotherapeutic agents are typically applied as radiosensitizers in clinical practice [85]. Two

important groups of radiosensitizers are platinum containing compounds like cisplatin and carboplatin and halogenated nucleobases like gemcitabime [86], 5-fluoruracil and fludarabine, which are incorporated in the DNA double helix [6]. The radiosensitizing action of electrophilic nucleosides is assumed to originate at least partly from their interaction with LEEs, as they make the DNA sensitive towards solvated electrons and consequently enhance the secondary damage [7]. Studies by Q. B. Lu et al. reveal an ultrafast electron transfer of prehydrated electrons to ^{5Br}U that induces the cleavage of the C-Br bond generating a uracil radical, which serves as a precursor for severe DNA damage [87]. For potential radiosensitizing NB analogues it is required that they are good electron acceptors and likewise the substitute is bound relatively weakly to the NB residue to act as a predetermined breaking point [88]. Also cisplatin exhibits a high reactivity with hydrated electrons [89], whereby a double strand break in cisplatin containing DNA can be triggered by a single subexcitation electron [90].

In a different approach AuNPs are suggested as potential radiosensitizer due to their high photon absorption cross section and the resulting emission of reactive secondary species like LEEs and photons [91]. Biological tissue mainly interacts with high energy photons via the Compton effect, where a photon is scattered at an outer shell electron and partly transfers its energy. On the contrary, for AuNPs the photoelectric effect, which is scaling with the fourth power on the atomic number Z^4, strongly contributes to the photoabsorption [92]. In the photoelectric effect mainly inner shell electrons are ejected, as the effect is resonant if the photon energy is close to the binding energy of the electrons [92]. Beside the ejected core shell electrons further fluorescence photons and auger electrons are emitted at the recombination of the electronic structure. Nevertheless, the dose deposition is limited to the close vicinity of the AuNPs on a sub cellular level [93].

It might be beneficial to combine the two presented approaches and use AuNPs as a nanoscale source of LEEs together with electrophilic molecules incorporated in the DNA strand to enhance the DNA damage at a certain dose. Beyond that, the high photoabsorption cross section of AuNPs is also exploited in the cancer PTT, where the AuNPs serve first of all as a source of heat [15]. However, laser illuminated AuNPs further release LEEs due to thermionic emission or transfer plasmonically generated electrons to molecules in their surrounding. Hence, it might be promising to apply electrophilic nucleobase analogues in PTT to increase the effect of the hyperthermia by additionally triggering precise DNA damage [94].

2.1.4 8-Bromoadenine

In the manuscripts M1, M2, M4 and M5 the interaction of ^{8Br}A with LEEs and and AuNPs was studied to examine the potential of ^{8Br}A as a potential radiosensitizer in PTT and radiation therapy. ^{8Br}A is an adenine analogue containing a bromine atom at C8 (see Fig. 2.4 a)) that is supposed to act as a predetermined breaking point. Density functional theory (DFT) calculations of L. Chomicz et al. reveal that due to the substitution of the bromine group ^{8Br}A is a better electron acceptor than unmodified A [95]. Furthermore, the attachment of an additional electron leads to the cleavage of the C-Br bond and the formation of a bromine ion and an adenyl radical.

The intermediate state in the dissociative decay is not stable, as the C-Br bond elongates to 2.56 Å.

$$e^- + {}^{8Br}A \rightarrow {}^{8Br}A^{\#-} \rightarrow Br^- + A\bullet \tag{2.7}$$

Also when an aqueous medium is taken into account ^{8Br}A decomposes via a barrierless decay, since the main fraction of the anions spin density is located at the C8 atom and the Br atom occupying the σ^* orbital [96].

In terms of cancer therapy one of the relevant questions is if the cleavage of the C-Br bond enhances the probability for a DNA strand break or other severe DNA damage resulting in cell death. L. Chomicz et al. reveal two degradation pathways (see Fig. 2.4 b)) following the attachment of an additional electron to 8-bromo-2'-deoxyadenosine 3'5'-diphsophate (^{8Br}dADP), which mimic ^{8Br}A connected to the DNA-backbone [97]. In a first step the ^{8Br}dADP anion decays via abstraction of the bromine atom. Subsequently the molecule either stabilizes via the formation of 5',8-cycloadenosine or transfers a hydrogen atom from the C3' or C5' sites of the deoxyribose moiety to the C8 of the adenine. This leads to the cleavage of the P-O bond at the 3' site or the 5' site what is equivalent with a DNA SSB.

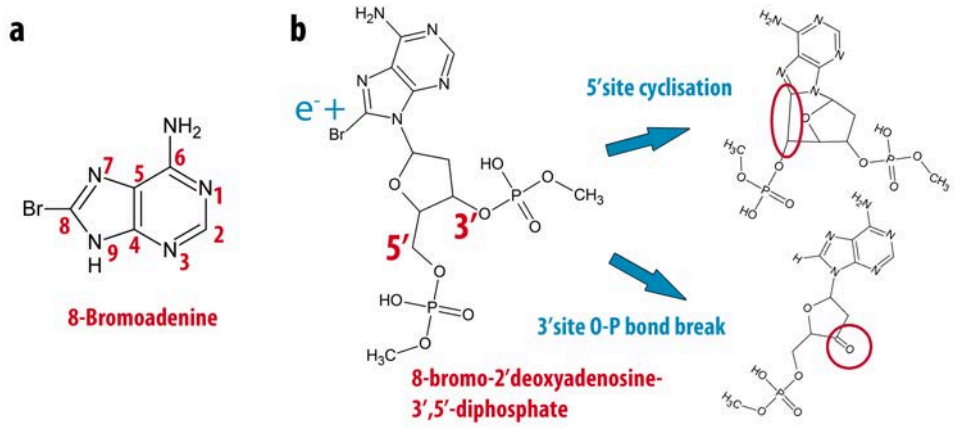

Figure 2.4: a)Structure of the ^{8Br}A molecule. b) Suggested pathways for the electron induced decomposition of ^{8Br}dADP leading on the one hand to a DNA SSB and on the other hand to the formation of 5',8-cycloadenosine. (Figure adapted from source [97])

Experimental studies with ^{8Br}A containing oligonucleotide trimers in solution reveal an enhanced damage of the ^{8Br}A containing sequence compared to its native analogue that was relatively unaffected by hydrated electrons generated during the irradiation with high energy photons from a ^{60}Co source [98]. Furthermore, T^{8Br}AT oligonucleotide trimers showed the highest SSB rate compared to trimers that carry a different brominated or native nucleotide in its center position under irradiation with 10 eV electrons under UHV conditions [53] and are highly reactive towards organic radicals [99]. However, beside the SSBs that are triggered by the cleavage of the C-Br bond further mechanisms have to be taken into account to understand the interaction between ^{8Br}A and LEEs. The capture of an hydrated electron leads to the formation of 5',8-cycloadenosine [100, 101, 102] and moreover

^{8Br}A acts as a strong electron acceptor that significantly influences the electron transport through the DNA [10].

2.2 Noble metal nanoparticles

Noble metal nanoparticles are particles consisting of Ag, Au or Cu with a size ranging from 1 nm to 100 nm that exhibit properties which differ from those found in the bulk samples [103]. Especially the interaction of light with the free electron gas of the nanoparticles is the foundation of versatile applications ranging from sensing to catalysis [104].

AuNPs in cancer therapy

As gold is chemically more inert than silver it is generally favored in medical applications due to its higher biocompatibility [92]. The outstanding optical and thermal properties of AuNPs, especially their high photon absorption cross section, allow versatile potential applications in cancer therapy [14, 105]. The utilization of AuNPs as radiosensitizer and contrast agents are generally based on their high absorptivity of x-ray photons that is attributed to their high atomic number [106]. Furthermore, AuNP are stabilized by capping agents in order to prevent aggregation by electrostatic repulsion or steric hindrance [107]. By choosing the right capping agents, AuNPs can target certain carcinogenic cells and therefore they are utilized in the cancer-diagnosis and drug delivery [108]. Beyond that tailored noble metal nanoparticles absorb light efficiently in the visible and NIR spectrum and convert its energy to heat. In PTT laser illuminated AuNPs elevate the temperature in cancer cells and cause the cells death via hypothermia [109]. In order to pass the biological spectral window gold nanorods [110] and gold nanoshells [111] are used, as they exhibit an absorption maximum in the NIR regime. The irradiation with intense laser pulses increases the damage in the nucleus, where the DNA is located, in contrast to continuous wave lasers [112]. Furthermore, the strong enhancement of electrical fields in the close proximity of AuNPs mediated by SPs is exploited in surface enhanced Raman scattering (SERS) that allows the in vivo detection of cancer cells [113].

2.2.1 Surface Plasmons

SPs are light waves coupled to the electron plasma at a metal/dielectric interface that allow the confinement of light to very small dimensions below its own wavelength [114]. Due to the electrical field of the incoming light the conduction band electrons of the nanoparticles are accelerated along the direction of the electrical field and accumulate at the particles surface where an electrical dipole is formed as shown in figure 2.5.

The direction of the induced electrical field opposes the generating field of the light forcing the electrons to return to their equilibrium position. If the external electrical field is removed, the restoring force leads to an oscillation of the electron gas with their resonance frequency, which is called plasmon frequency and can be described with a damped harmonic oscillator [115]. These collective oscillation of the electron gas induced by the action

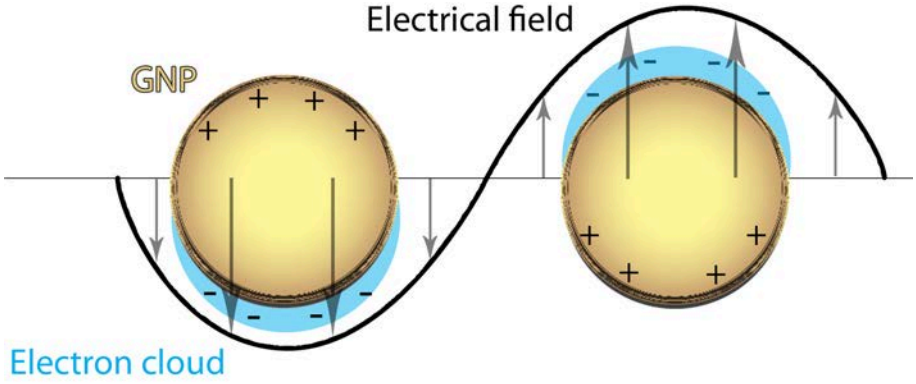

Figure 2.5: Schematic of a surface plasmon resonance of a AuNP excited by the oscillating electrical field of incident light.

of an electromagnetic (em)-field can lead to the reemission of a photon in a scattering process [116]. Alternatively, the surface plasmon can relax in a non-radiative way and transform the energy of the incoming photon into thermal energy [117]. The quantity that is accessible in a typical experimental setup is called extinction and is given by the sum of the absorption and the scattering events.

$$\sigma_{ext} = \sigma_{abs} + \sigma_{sca} \tag{2.8}$$

The cross section of the AuNPs extinction exceeds the extinction of typical organic dyes by 4-5 orders of magnitude [118]. The extinction cross section can be up to ten times larger than the particle size as the NPs also adsorbs and scatter photons away from its physical position due to its extended electrical field [115]. In general the particles are smaller than the wavelength of the light but large enough that classical theory can be applied and quantum effects can be neglected. In 1908 G. Mie calculated for the first time the extinction of a noble metal nanoparticle by solving Maxwell's equation for the interaction of light with a small metallic sphere having the same dielectric properties like the bulk metal [119]. These calculations were leading to a series of multipole oscillations:

$$\sigma_{ext} = \frac{2\pi}{|\mathcal{K}^2|} \sum_{L=1}^{\infty} (2L+1) \cdot Re[a_L + b_L] \tag{2.9}$$

where $\mathcal{K}$ is the wave vector, $x = |\mathcal{K}| \cdot R$, R is the radius of the nanoparticle $m = n/n_m$ is the ratio between the complex refractive index of the metal n and the surrounding medium n_m. L is the summation index of the partial wave [120].

$$a_L = \frac{m\Psi_L(mx) \cdot \Psi'_L(x) - \Psi'_L(mx) \cdot \Psi_L(x)}{m\Psi_L(mx) \cdot \eta'_L(x) - \Psi'_L(mx) \cdot \eta_L(x)} \tag{2.10}$$

and

$$b_L = \frac{\Psi_L(mx) \cdot \Psi'_L(x) - m\Psi'_L(mx) \cdot \Psi_L(x)}{\Psi_L(mx) \cdot \eta'_L(x) - m\Psi'_L(mx) \cdot \eta_L(x)} \tag{2.11}$$

where $\eta_L(x)$ and $\psi_L(x)$ are the cylindrical Bessel-Riccati functions. If the dimensions of the particle are small compared to the wavelength of the light ($2R \ll \lambda$), only the dipole term with L=1 contributes significantly to the extinction cross-section and equation (2.9) reduces to [121]:

$$\sigma_{ext} = \frac{24\pi^2 R^3 \varepsilon_m^{3/2}}{\lambda} \frac{\varepsilon_2}{(\varepsilon_1 + 2\varepsilon_m)^2 + \varepsilon_2^2} \tag{2.12}$$

where λ is the wavelength of the incoming light, ε_m is the real dielectric function of the surrounding medium and ε_1 and ε_2 are the real and imaginary part of the complex dielectric function ε_D of the metal.

$$\varepsilon_D = \varepsilon_1 + i\varepsilon_2 \tag{2.13}$$

Thus, the extinction cross section is proportional to the volume of the particle and depends on the dielectric function of the metal and the surrounding medium. The cross section maximizes whenever the imaginary part ε_2 gets small and the real part equals $-2\varepsilon_m$. This is the case for a free electron metal at long wavelength, as the real part of its dielectric function is negative and large [122]. The real part defines the wavelength position of the SP resonance (SPR), whereas the imaginary part is only weakly dependent on the wavelength and determines the bandwidth [123]. Experimentally determined dielectric functions ε_{exp} generally show two contributions: the Drude term ε_D and the interband term ε_{IB}, as beside the intraband transition of the SP also electronic excitations between separated bands are possible.

$$\varepsilon_{exp} = \varepsilon_{IB} + \varepsilon_D \tag{2.14}$$

Even though in a metal valence and conduction band typically form a continuous spectrum of available states, some inner levels due not split enough to overlap with these bands and allow electronic excitations [115] that are usually located in the UV region [116]. Figure 2.6 shows the absorption spectra of AgNPs and AuNPs revealing that the interband and intraband contributions are well seperated for AgNPs while they significantly overlap for AuNPs.

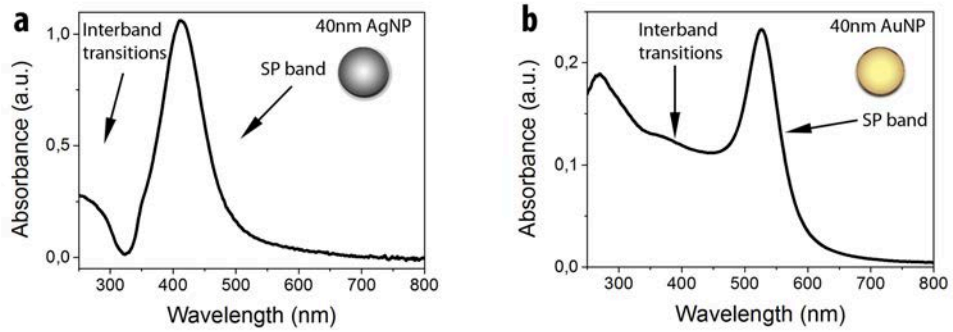

Figure 2.6: Absorption spectra of 40 nm AgNPs (a) and AuNPs (b) showing the contribution of the interband transitions and the SP band.

Intraband transitions occur close to the Fermi energy in a partly filled or overlapping band and can be described with the classical Drude model of a free electron gas [116]:

$$\varepsilon_D(\omega) = 1 - \frac{\omega_P^2}{\omega^2 + i\gamma\omega} \tag{2.15}$$

where γ is the damping constant and ω_P is the plasma frequency of the electrons:

$$\omega_P = \sqrt{\frac{\pi N e^2}{m_e}} \tag{2.16}$$

ω_P depends on the free electron density N and the effective mass m_e. The phenomenological damping constant γ equals the plasmon absorption bandwidth Γ in the limit $\gamma \ll \omega$. γ is related to the collision time τ of all electron scattering events in the bulk metal that are basically electron-electron, electron-phonon and phonon-phonon scattering [120]:

$$\gamma_0 = \sum_i \tau^{-1} = \tau_{e-e}^{-1} + \tau_{e-ph}^{-1} + \tau_{ph-ph}^{-1} \tag{2.17}$$

where γ_0 is the size independent damping term for the scattering of conduction electrons at the ionic cores of the gold lattice that only depends on the mean free path of the electrons in the metal l_∞ and the speed of the electrons at the Fermi energy, the so called Fermi velocity $\gamma_0 = l_\infty \nu_F$. As the mean free path of an electron is longer than the particle diameter, also surface scattering has to be taken into account by addition of a size dependent term.

$$\gamma = \gamma_0 + B \cdot \frac{\nu_F}{R} \tag{2.18}$$

where B is a parameter that depends on details of the scattering process. Equation (2.18) shows an anti-proportional dependence of the size depended damping term on the particle radius. Hence, the plasmon absorption bandwidth broadens with decreasing particle size.

Even though Mie theory describes the plasmonic properties of single nanoparticle very well, it is only valid for a dilute nanoparticle solution, where the electrical field of a nanoparticle is not felt by the neighboring particles. If the nanoparticles form aggregates or the interparticle distance gets so small that the SPs of neighboring particles interact with each other, the SPR is red shifted, broadened and secondary maxima might occur [124, 125]. Such systems can be calculated using the Maxwell-Garnett effective medium theory, where the heterogeneous medium of nanoparticles in the dielectric is replaced by an homogeneous medium with the same dielectric polarization under illumination with light [115]. Therefore a statistical average over a large number of clusters and the averaged volume fraction f is considered to describe the topology of the sample [121]. Hence, the effective complex dielectric function ε_{eff} is given by:

$$\frac{\varepsilon_{eff} - \varepsilon_m}{\varepsilon_{eff} + 2\varepsilon_m} = f \cdot \frac{\varepsilon - \varepsilon_m}{\varepsilon - 2\varepsilon_m} \tag{2.19}$$

where the filling factor f is given by the ratio of the volume of the particles to the volume of the sample. Interacting nanoparticle systems like aggregates strongly enhance the plasmonic response of a system.

2.2.2 Nanoparticle heating

For small AuNPs with a size under 40 nm the scattering processes are not contributing significantly to the extinction cross section [126]. Therefore the SPR mainly decays non-radiatively via electron-hole pair formation whereby its energy is transferred to a conduction band electron [16]. These non equilibrium electrons are called "hot electron" and dissipate their energy via electron-electron scattering until the electron distribution is described by Fermi-Dirac statistics. The thermalization of an electron takes around 500 fs, as several electron-electron scattering events with a typical interaction time of 10 fs are required [120]. Electron-phonon collisions transfer the heat of the hot electron gas to the lattice of the AuNP within approximately 3.4 ps [120]. Subsequently the energy is dissipated to the surrounding medium via phonon-phonon scattering thereby cooling the particle down in 100 ps [120]. Due to the short time scales compared to the laser illumination time a one temperature model is used to describe the heating of the AuNP and its vicinity assuming a homogeneous temperature of the AuNP [127]. In general the heat generation depends in a complex way on the morphology of the particle [128]. For a spherical AuNP the following heat diffusion equations can be applied [127]:

$$\nabla \cdot [\kappa(r)\nabla\mathcal{T}(r)] = q(r), \qquad r < R \tag{2.20}$$

$$\nabla \cdot [\kappa(r)\nabla\mathcal{T}(r)] = 0, \qquad r > R \tag{2.21}$$

where $\kappa(r)$ is the thermal conductivity, $\mathcal{T}(r)$ is the steady state temperature distribution and $q(r)$ is heat power density. According to G. Baffou et al. the temperature increase $\delta\mathcal{T}$ inside and outside a spherical AuNP is given by[129]:

$$\delta\mathcal{T}(r) = \delta\mathcal{T}_{NP}\frac{R}{r}, \qquad r > R \tag{2.22}$$

$$\delta\mathcal{T}(r) \approx \delta\mathcal{T}_{NP}, \qquad r < R \tag{2.23}$$

with

$$\delta\mathcal{T}_{NP} = \frac{Q}{4\pi\kappa_s R} \tag{2.24}$$

where κ_s is the heat capacity of the surrounding medium and Q is the absorbed heat that is determined by the absorption cross section σ_{abs} and the laser intensity I:

$$Q = \sigma_{abs} I \tag{2.25}$$

The linear dependency of the temperature increase on the laser intensity is only valid for single particles, as for high concentrations of AuNPs collective photoheating needs to be taken into account [130].

Regarding to theoretical studies performed by A. O. Govorov et al., which are presented in reference [131, 132] in detail, the maximum increase of the temperature occurring at the AuNP surface is given by :

$$\delta\mathcal{T}_{max}(I_0) = \frac{R^2}{3\kappa_s}\frac{\omega}{8\pi}|\frac{3\epsilon_m}{2\epsilon_m+\epsilon}|^2 \cdot \varepsilon_2 \cdot \frac{8\pi I_0}{c\sqrt{\epsilon_m}} \tag{2.26}$$

The temperature increase scales quadratically with the radius of the particle, since the absorbed heat depends on the AuNP volume. The statements in this chapter are also valid for the illumination with ns laser pulses due to the nearly uniform temperature distribution of the nanoparticle during the duration of a pulse, as the typical lattice heating time is much smaller than the pulse duration time. Hence a homogeneous heating of the particle and a quasi steady state heat exchange with the surrounding medium can be assumed [133].

2.3 Pulsed irradiation of AuNP

Irradiation of AuNPs with an intense laser pulse with a pulse width of a few nanoseconds generally leads to reshaping and fragmentation of the AuNP [134]. The relevant processes that occur under pulsed irradiation are sketched in figure 2.7. During the pulse the AuNPs are exposed to high power densities of around 10^{10} to $10^{14}\frac{W}{m^2}$, so the temperature of the AuNPs rises up to several thousand K [135, 136]. A temperature increase above 1337 K leads to a melting of the AuNP and to an evaporation of the top layers of the surface resulting in a bimodal size distribution of the AuNPs [137]. Even at temperatures of around 673K, well below the melting temperature of the bulk gold, surface melting occurs and causes a reshaping of the AuNPs [138]. In order to induce a change in the morphology and decompose the AuNPs a single laser pulse is sufficient [139]. The cooling down of the AuNPs to room temperature proceeds orders of magnitude faster than the delay time between two pulses, so an accumulation of heat can be neglected [139].

The produced AuNP fragments rapidly coagulate [140] and form snake-like structures depending on the properties of the laser pulse [141]. Furthermore, the heat transfer to the surrounding medium leads to an explosive evaporation of the solute in close proximity to the surface. Nanoscale vapor bubbles with an expansion of a few hundred nanometers and a lifetime of approximately 10 ns are formed [142]. The threshold for the bubble formation is around $10^{10}\frac{W}{m^2}$ for 40 nm AuNPs illuminated with ns laser pulses and drastically increases for smaller particles [143]. Beside the photothermal effects based on the gold lattice temperature also the high temperature of the electron gas has to be taken into account. The energy of a small fraction of the Fermi-Dirac distributed electrons exceeds the work function of the metal and thus electron emission from the AuNPs is caused. This thermionic emission generates highly charged AuNPs that undergo spontaneous fission in a so called coulomb explosion due to the repulsion of the positive charges that remain in the particle [144]. In solution, solvated electrons can be detected at high laser fluences [21], whereas at intensities below $10^{12}\frac{W}{m^2}$ it is assumed that the photothermal effects are dominating [145]. In the high temperature and pressure region in the vicinity of a laser illuminated AuNP DNA molecules are severely damaged. If the DNA is adsorbed

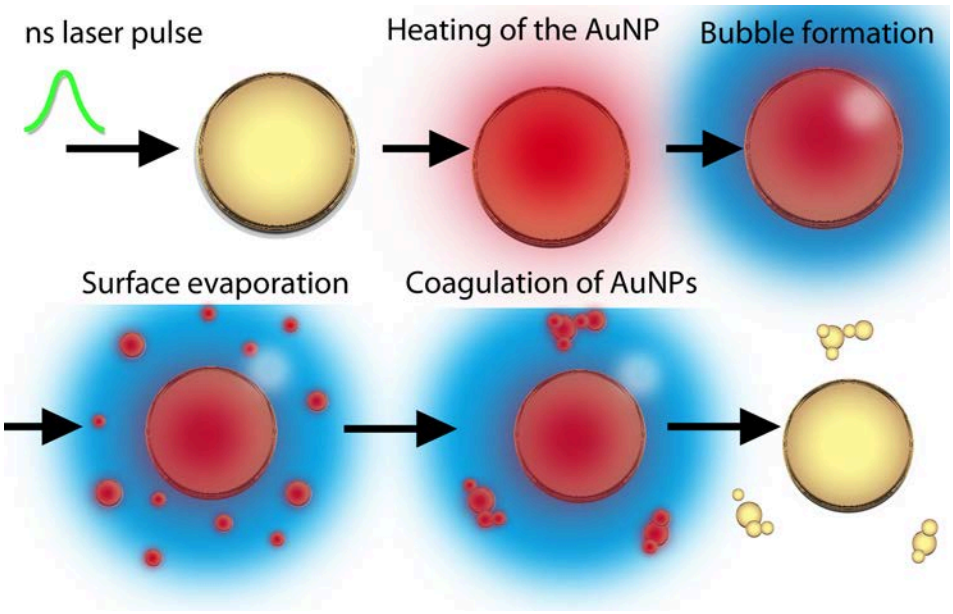

Figure 2.7: Steps of the thermal decomposition of a laser illuminated AuNPs. Figure adapted from source [138].

on the AuNP, the decomposition rate is highly increased [146]. Therefore pulsed laser illumination of AuNPs accumulated in cancer cells might lead to future applications in cancer therapy [15].

2.4 Plasmonic catalysis

Based on their strong optical response plasmonic nanoparticles act as catalysts in photo reactions [147]. Generally, in catalysis the rate of a chemical reaction is increased by lowering the activation barrier [148]. In the framework of this thesis the catalytic properties of noble metal nanoparticles are of great interest as they describe a method to enhance photo reactions causing damage to DNA strands. The photocatalytic properties of nanoparticles originate from the fact that they act as a source of light, heat and electrons under illumination with light [16]. The decay of SPs provides electrons with an energy between 1 and 3 eV on a fs timescale before they get thermalized [149]. In figure 2.8 it is shown that these "hot electrons" can be transfered into an unoccupied molecular orbital of an adsorbed molecule and form a TNI, which subsequently decomposes in a DEA reaction [150].

In this mechanism the required photon energy is significantly lowered compared to an electronic excitation from the highest occupied MO (HOMO), since the electron transfer originates from electrons of the nanoparticle around the Fermi level. Therefore bond selective reactions can be triggered that cannot be activated with conventional thermal or photocatalytic processes [151]. It is still under discussion whether the plasmonically generated electrons firstly dissipate their energy to the conduction electrons until a Fermi-Dirac distribution is reached and subsequently one of these electrons tunnels into the unoccupied orbital of the adsorbate [152], or if resonant electron transfer into the MO occurs [153] as it was predicted by

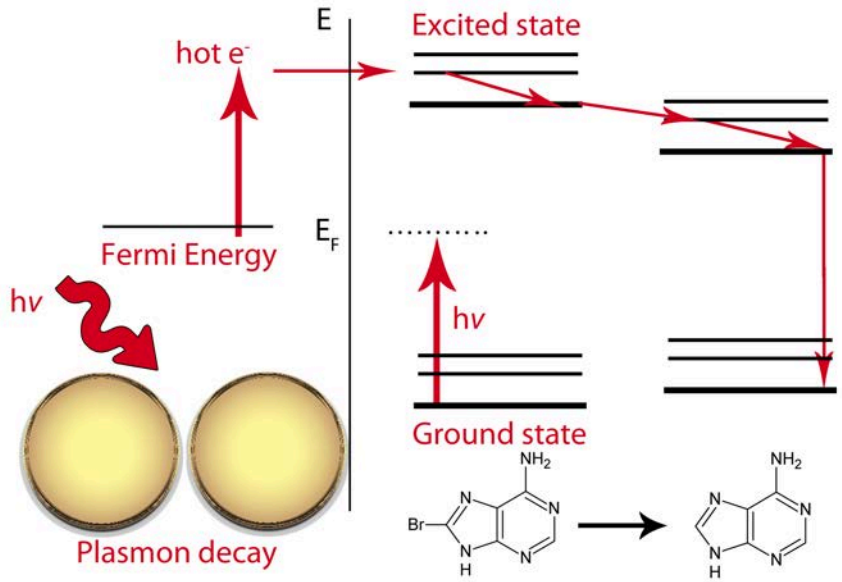

Figure 2.8: Scheme of electron transfer from AuNPs to an adsorbed molecule with the subsequent decay.

B.N.J Persson in 1993 [154]. Plasmon induced reactions can be sensitively controlled by tuning the plasmonic properties of the nanoparticles [155] and the wavelength of the incoming laser light [117]. In combination with electrophilic molecules like halogenated nucleobases that are incorporated in a DNA strand AuNP might be used to trigger electron induced reactions leading to DNA strand breaks or other relevant damage in cancerous tissue. In order to study such processes the focused laser light of a confocal Raman microscope can be used to induce precisely plasmon mediated reactions on certain micro- or nanostructures and simultaneously monitor them with SERS [156].

2.5 Surface enhanced Raman Scattering

The enhanced near field that molecules experience in close proximity to a nanoparticle and the charge transfer from the nanoparticle to an adsorbed molecule are exploited in SERS [157, 158]. SERS is an analytical technique that combines the molecular fingerprint of the Raman scattering and high sensitivity due to the field enhancement [159]. Therefore it is a sensitive method that allows molecular detection down to a single molecule level [160, 161].

Raman effect

The Raman effect describes inelastic scattering between a photon and a molecule and is named after Chandrasekhara Venkata Raman, who received the Nobel price in 1930 for the observation. During the interaction of a photon with a molecule, the electrical field of incoming light displaces the electrons inside a molecule relative to its nuclei and thus induces an electric

dipole moment [162]:

$$\mu = \alpha \cdot E \tag{2.27}$$

where μ is the induced dipole moment under action of an electrical field E and α the polarizability of the molecule. The frequency of the light is ν_0 and its alternating electrical field is given by:

$$E(t) = E_0 \cos(2\pi\nu_0 t) \tag{2.28}$$

A molecular bond can be described as a quantum mechanical harmonic oscillator with a vibrational frequency ν_{vib}. Therefore the displacement of the nuclei from their equilibrium position is given by:

$$q(t) = q_0 \cos(2\pi\nu_{vib} t) \tag{2.29}$$

where q_0 is the maximal elongation of the bond. For small changes in the atomic positions the change in the polarizability can be approximated by a first order Taylor series:

$$\alpha = \alpha_0 + \frac{\partial\alpha}{\partial q} dq \tag{2.30}$$

where α_0 is the polarizability of the molecule in the equilibrium position. If the equations (2.28), (2.29) and (2.30) are inserted in equation (2.27) and the equation is rearranged by using a trigonometrical identity the following expression for the polarization of a molecule is derived:

$$\mu = \alpha_0 E_0 \cos(2\pi\nu_0 t) + (\frac{\partial\alpha}{\partial q}\frac{q_0 E_0}{2})[\cos(2\pi(\nu_0 - \nu_{vib})t) + \cos(2\pi(\nu_0 + \nu_{vib})t)] \tag{2.31}$$

The polarization has contributions of three induced dipole moments with a vibrational frequency of ν_0, $(\nu_0 - \nu_{vib})$ and $(\nu_0 + \nu_{vib})$. Each of these dipoles emits light with its vibrational frequency. The first term referring to elastic scattering is called Rayleigh scattering, whereas the inelastic scattering terms are called Stokes- and Anti-Stokes Raman scattering, respectively. A necessary condition for Raman scattering is that the $\frac{\partial\alpha}{\partial q}$ term is non-zero, which means that during a molecular vibration the polarization of the molecule changes.

In a quantum mechanical picture the photon excites the molecule from its ground state into a virtual state as shown in figure 2.9 [163]. The subsequent relaxation into the ground state is the Rayleigh scattering and if the decay ends in a vibrationally excited state, it is denoted as Stokes scattering. In the case that the excitation is induced from a vibrationally excited state and ends in the ground state, the process is referred to Anti-Stokes scattering. However, this effect is not in the scope of this thesis. The cross section for Raman scattering is very sensitive to the excitation wavelength, as it varies with the fourth power on the frequency of the incoming light [163]:

$$\sigma \propto (\nu_0 - \nu_{vib})^4 \tag{2.32}$$

Typically these cross sections are very low in the range of $10^{-30} cm^2/sr$ up to $10^{-24} cm^2/sr$ for dyes when they are excited into a real electronic state instead of a virtual one [164].

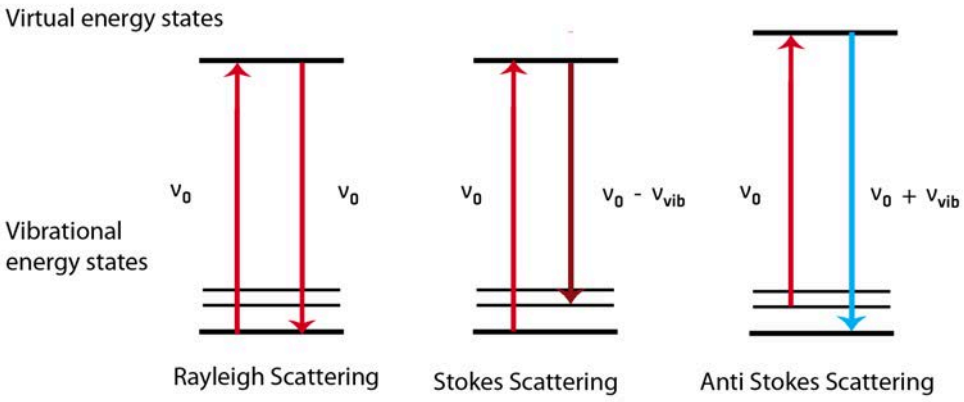

Figure 2.9: Schematic representation of Rayleigh, Stokes and Anti-Stokes Raman scattering

Electromagnetic enhancement

The electromagnetic enhancement is an effect that acts independently of the analyte molecules and only depends on the plasmonic interaction of the noble metal nanostructures with the probe light and the resulting electrical fields. Due to the coupling of the polarizability of a molecule with the polarizability of a nanoparticle the Raman scattering cross section is highly increased [165]. If the wavelength of the light is small compared to the dimensions of the nanoparticle, the electrical field outside the particle can be denoted as [122]:

$$\mathbf{E}_{out} = E_0\mathbf{z} - \alpha E_0[\frac{\mathbf{z}}{r^3} - \frac{3z}{r^5}(z\mathbf{z} + x\mathbf{x} + y\mathbf{y})] \tag{2.33}$$

where x,y,z are the Cartesian coordinates, r is the radial distance and $\mathbf{x}, \mathbf{y}, \mathbf{z}$ are the Cartesian unit vectors. According to the model of a free electron gas described in section 2.2.1, the polarizability of a spherical noble metal particle is given by:

$$\alpha = 4\pi^2\varepsilon_0 R^3 \frac{\varepsilon - \varepsilon_m}{\varepsilon + 2\varepsilon_m} \tag{2.34}$$

For simplicity reasons the factor g is defined as $g = \frac{\varepsilon - \varepsilon_m}{\varepsilon + 2\varepsilon_m}$. Thus the Raman intensity at the surface of the particle, which is given by the absolute square of the outgoing electrical field, can be written with formula (2.33) as:

$$E_{out}^2 = E_{out}^2[|1 - g|^2 + 3\cos^2\theta(2Re(g) + |g|^2)] \tag{2.35}$$

where θ is the angle between the applied electrical field and the vector $\mathbf{r}$ that is pointing at the particular position of the sphere surface. As the absolute value of g is large for noble metals the equation (2.36) reduces to:

$$E_{out}^2 = E_{out}^2|g|^2(1 + 3\cos^2\theta) \tag{2.36}$$

This equation reveals that the largest fields occur for angles θ equal to 0° or 180°. The ratio of the smallest to largest field enhancement is 4. An important magnitude to describe the effect of the substrate on the Raman scattering is the enhancement factor EF_{SERS} that is defined as the ratio of the enhanced Raman signal per molecule to the normal Raman signal per molecule [166]. Theoretically the enhancement factor for molecules located on the position with the highest electrical fields is given by the following formula, where it has to be taken into account that the Stokes scattered light is emitted at a different wavelength than the incoming light:

$$EF_{SERS} = \frac{E_{out}^2 E_{out}'^2}{E_0^4} = 16|g|^2|g'|^2 \tag{2.37}$$

The primed symbols refer to the fields evaluated at the scattered frequency. For materials like Ag with a high value for $|g|$ the enhancement on a single particle can exceed 10^5. Furthermore, the enhancement is very surface sensitive, since the electrical field strength of dipolar radiation scales with $E \propto r^{-3}$ and consequently the SERS intensity $I_{SERS} \propto r^{-12}$ [159]. According to G.C. Schatz et al. the scattering cross section can be rewritten as [122]:

$$\sigma_{sca} = \frac{128 \cdot \pi^4 \cdot R^4 \cdot \varepsilon^2}{3 \cdot \lambda^4}|g|^2 \tag{2.38}$$

showing that the forth power dependence on λ^{-4} is still preserved. Due to the coupling of the molecular and nanoparticle polarization the em-enhancement depends on the orientation of the molecule to the induced electrical field of the nanoparticle [167]. In this section the em-enhancement is deduced for a single nanoparticle, however like described in section 2.2.1 the plasmonic response and therefore the enhanced scattering cross section is generally larger for coupled particles [168] and aggregates [169].

Chemical enhancement

In contrast to the non-selective em-enhancement the chemical enhancement is an effect that affects only adsorbed molecules on the plasmonic surface and strongly depends on the molecule and the excitation wavelength [157]. As well as in resonant Raman scattering the molecule is not excited into a virtual state but into its LUMO. Due to the adsorption on the metal surface the HOMO and LUMO are broadened and shifted towards the Fermi energy. Furthermore, new electronic states may arise. Commonly UV light is required to bridge the HOMO-LUMO gap of the analyte molecules. However, due to a charge transfer from the Fermi level of the nanoparticle towards adsorbed molecules or vice versa, the adsorbate can be excited with photons in the visible or even NIR region of the spectrum [170].

SERS of Nucleobases

The SERS spectrum of a molecule depends strongly on its orientation on the nanoparticle, as the alignment of the polarization of the molecular vibration to the electrical field of the nanoparticle is crucial for the em-enhancement. Therefore the normal Raman spectrum of a powder with an arbitrary orientation of the molecules to the incoming light generally differs significantly in

the relative intensities of the peaks compared to the SERS spectrum [171]. The orientation of the adsorbed NBs depends on the shape of the surface, whether it is flat or curved [172]. In figure 2.10 the adsorption of the four canonical NBs on AuNPs are shown, demonstrating that the binding is mediated by the amino- and keto-groups of the nucleobases [173], whereas the binding strength follows the order $G > A > C > T > U$ [174].

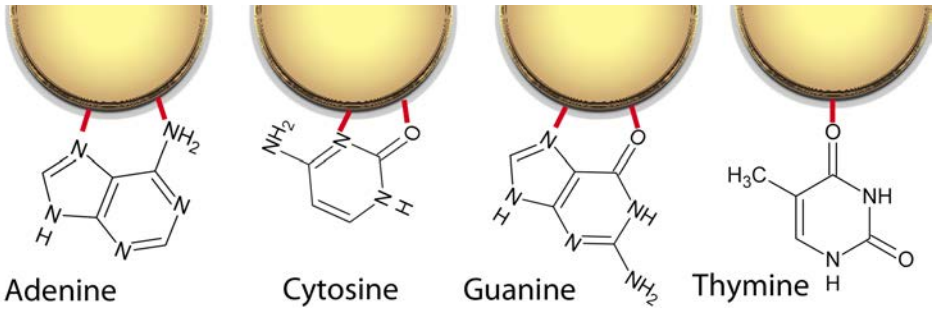

Figure 2.10: Adsorption of A, C , G and T on the surface of AuNPs based on reference [173]

The SERS spectra of NBs are furthermore influenced by the environmental conditions like solvation, pH value and analyte concentration, since protonation and deprotonation as well as multiple layer adsorption significantly influence the orientation of the adsorbed NBs on the surface [175]. One of the strongest Raman bands in SERS of DNA bases is generally the ring breathing mode [176], as it is relatively independent of the orientation and therefore more molecules are contributing to the signal. Beside the effect of the orientation, the enhancement of certain vibrational modes is also determined by the chemical interaction of the substrate with the NB due to resonant charge transfer processes [177]. Hence, the optimal SERS signal of nucleobases can be obtained by matching the em- and chemical resonances [178] so even very low NB concentrations can be detected down to a single molecule [179]. Interactions of the NBs with radiosensitizing agents like cisplatin give rise to changes in the spectral fingerprints revealing the formation of chemical bonds [180]. Also the Raman spectra of brominated nucleobases are distinguishable from the native ones by the occurrence of the C-Br stretching and deformation vibrations as well as in a shift of the ring breathing mode for $^{8\mathrm{Br}}\mathrm{A}$ [181] or the C5=C6 stretching vibration in ^{5Br}U [182]. These makes chemical reactions like the cleavage of the C-Br bond easily traceable by SERS.

3 Materials and methods

3.1 Chemicals

All chemicals used in the experiments are listed in table 3.1 and were used without further purifications. Unless otherwise stated the chemicals were diluted in Millipore filtered water.

Table 3.1: List of chemicals

	Purchased from	Purity
40 nm AuNPs	BBI solutions [1]	-
^{5Br}C	Sigma Aldrich [2]	$\geq 99\%$
^{5Br}U	Sigma Aldrich [2]	$\geq 98\%$
^{8Br}A	Carbosynth [3]	$\geq 95\%$
^{8Br}G	Sigma Aldrich [2]	-
A	Sigma Aldrich [2]	$\geq 99\%$
$AgNO_3$	Sigma Aldrich [2]	$\geq 99\%$
C	Sigma Aldrich [2]	$\geq 99\%$
Ethanol (EtOH)	Sigma Aldrich [2]	$\geq 99\%$
G	Sigma Aldrich [2]	$\geq 98\%$
$HAuCl_4$	Sigma Aldrich [2]	$\geq 99.9\%$
KBr	Sigma Aldrich [2]	$\geq 99.0\%$
$MgCl_2$ hexahydrate	Sigma Aldrich [2]	$\geq 98\%$
NaOH (0.1 M in water)	Sigma Aldrich [2]	-
Sodium citrate	Sigma Aldrich [2]	$\geq 98\%$
T	Sigma Aldrich [2]	$\geq 99\%$
Tris-acetate EDTA (TAE) buffer 10x	Sigma Aldrich [2]	-
U	Sigma Aldrich [2]	$\geq 99.0\%$

[1] BBI Solutions, Cardiff, UK
[2] Sigma-Aldrich Chemie GmbH, Munich, Germany
[3] Carbosynth Ltd, Berkshire, UK

The list of unmodified DNA staple strands used for the synthesis of the DNA origami are given in source [57] and the modified staple strands are listed in table 3.2. All unmodified staple strands were desalted whereas the modified strands were purified by HPLC.

Table 3.2: List of DNA strands

Sequence (5'-3')	Purchased from
M13mp18 (scaffold strand)	New England Biolabs [1]
Non modified staple strands (see reference [57])	IDT [2]
[Bt]TT[8BrdA]TA)$_3$ TT t-5s8g *	Sigma Aldrich [3]
[Bt]TT([8BrdA]TA)$_3$ TT t-5s18g *	Sigma Aldrich [3]
[Bt] TT ([8BrdA]TA)$_3$ TT t5s28g *	Sigma Aldrich [3]
[Bt] TT (ATA)$_3$ TT t1s-4i *	Metabion [4]
[Bt] TT (ATA)$_3$ TT t1s-14i *	Metabion [4]
[Bt] TT (ATA)$_3$ TT t1s-24i *	Metabion [4]

[1] New England Biolabs GmbH, Frankfurt am Main, Germany
[2] Integrated DNA Technologies BVBA, Leuven, Belgium
[3] Sigma-Aldrich Chemie GmbH, Munich, Germany
[4] Metabion international AG, Planegg/Steinkirchen, Germany
* The nomenclature of the staple strands is adopted from reference [57]

3.2 Nanoparticle synthesis

Citrate reduced AgNPs were synthesized by the well-known method from Lee and Meisel [183]. Briefly, 250 ml of 1 mM $AgNO_3$ solution were heated up to a rolling boil and 10 ml 1% sodium citrate was added dropwise under rigorous stirring. Thereby the color of the solution turns to yellow and subsequently to grey. For an additional hour the solution was kept boiling and afterwards cooled down slowly to room temperature. The AgNP were stable for several weeks under storage at 4°C.
AuNPs were produced by reduction of $HAuCl_4$ with sodium citrate. For this 20 ml of 1 mM $HAuCl_4$ solution was heated under rigorous stirring to a rolling boil and 2 ml 1% sodium citrate solution were added leading to a color change from pale yellow to deep red. After 15 min of further boiling the solution was cooled down and stored at 4°C.

3.3 Raman spectroscopy

Raman spectra were recorded using two different confocal Raman microscopes: a Witec alpha 300 with laser wavelengths of 532 nm and 785 nm and a Horiba Labram with laser wavelength of 633 nm. The spectrometer of the Witec alpha 300 that is shown in figure 3.1 a) contains a 600 mm^{-1} and a 1800 mm^{-1} grating and the Labram a 300 mm^{-1} as well as a 1800 mm^{-1}. As the concentrations of NB samples were relatively low compared to its Raman cross section, citrate reduced AgNPs are used as a SERS substrate to enhance the signal. In order to minimize the contribution of the citrate capping to the Raman signal, the AgNPs were washed three times with Millipore water to reduce the citrate concentration. Measurements in solution were performed using a 4-6 μl droplet of a highly concentrated AgNP solution mixed with the same volume of the analyte solution. The droplet was placed on a clean Si wafer that was surrounded by a bath of Millipore water (see figure 3.1 b)). The laser was focused with a 50x objective from

Olympus with a long focal length inside the droplet. High concentrations of AgNP were required to obtain strongly enhanced and stable signal without the addition of aggregating agents [184, 185] .

For the preparation of dried samples the analyte molecules were incubated

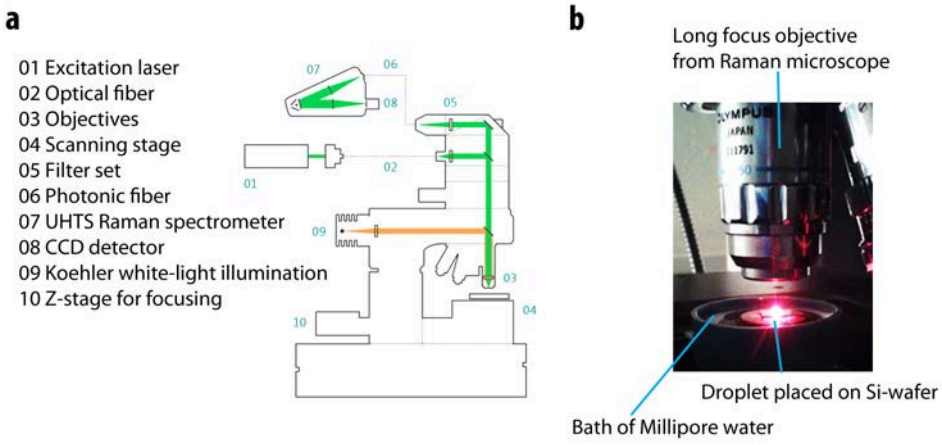

Figure 3.1: a) Schematic setup of the Witec alpha 300 confocal Raman microscope (figure adapted from source [186]). b) Picture of the experimental setup of a liquid droplet measurement with the Horiba Labram microscope.

on the AgNPs for 2 hours before the solution was centrifuged two times at 3000g for 5 minutes to get rid of the excess analyte molecules and reduce the citrate concentration. Each time the supernatant was discarded and the AgNP solution was dissolved again in Millipore water. After a final centrifugation step 1 μl of the solution was dried on an airplasma cleaned Si wafer. Raman spectra on visible AgNP aggregates were taken using a 10x Olympus Objective with a 10 μm spot size to get an averaged signal from several hot spots.

3.3.1 Dark field spectroscopy

Dark field spectra were recorded with the Witec alpha 300 confocal microscope equipped with a 50x/0.75 HD objective from Zeiss for dark field spectroscopy. All spectra were normalized by the spectra of the lamp that was recorded in absence of a sample and dark count corrected according to the subsequent formula:

$$I_{norm} = \frac{I_{measured} - I_{dark}}{I_{lamp} - I_{dark}} \tag{3.1}$$

3.4 UV-Vis Absorption spectroscopy

UV-Vis Absorption spectroscopy of aqueous solutions of NB and AuNPs samples was processed with a Jasco 650 Photospectrometer in a spectral range of 200 nm to 800 nm and a scan speed of 200 nm/min. The spectra were normalized by subtracting a so called blank sample containing the solute. Typically 2 ml of the analyte was placed in a quarz macrocuvette

from Hellma Analytics. Small amounts of sample were measured with a Nanodrop 2000 from Thermo scientific, where only 1 - 2 μl are required. The concentration c of the samples can be determined from the UV-Vis spectra using the Lambert-Beer law:

$$Abs = \epsilon \cdot c \cdot d \tag{3.2}$$

where Abs is the absorbance, ϵ is the molar extinction coefficient and d is the path length of the light in the medium. The extinction coefficients of the nucleobases are given in table 3.3.

Table 3.3: Extinction coefficients of NBs analogues

	π-π^* (nm)	Extinction (cm^{-1}/M)
A [187]	261	13400
C [187]	266	6100
G [187]	243	10700
T [187]	263	7900
U [187]	258	8200
^{8Br}A [188]	271	17000
^{5Br}C	282	6200
^{8Br}G	281	8100
^{5Br}U [189]	275	7010

Apart from ^{5Br}C and ^{8Br}G, the extinction coefficients were taken from the literature cited above. For ^{5Br}C and ^{8Br}G the coefficients were determined within this work from the initial weight of the dry samples.

3.5 Laser irradiation

Aqueous samples of AuNPs with NB analogues were irradiated with ns pulses of a Minilite I Nd:YAG laser from Continuum using the second harmonic with a wavelength of 532 nm, a pulse length of 3 to 5 ns and an energy of 16 mJ per pulse. The diameter of unfocused laser beam was 3 mm and the repetition rate was chosen between 5 and 15 Hz.
Typically 2 ml of a 30 pM AuNPs and 20 μM NBs mixture were placed in a quartz cuvette on a stirring plate. When the sample was irradiated with the unfocused laser the beam passed the cuvette from the side. Since the optical density of AuNPs at the SPR was well below 1 and consequently the influence of scattering is small, the laser intensity can be assumed to be constant along the optical path.
In experiments that require higher laser fluences, the beam was focused with a 30 mm objective on the surface of the sample. In order to prevent damage of the cuvette the sample was irradiated from above and concentration of the AuNPs was high to reduce the laser intensity at the bottom of the cuvette through absorption and scattering of light on the AuNPs. For the subsequent analysis only 5 to 10 μl of the sample were removed to minimize the changes in the laser fluence on the surface during the illumination. 5 μl of the extracted sample was further diluted in 195 μl Millipore water for the subsequent UV-Vis analysis.

3.6 Dissociative electron attachment in the gas phase

DEA measurements in the gas phase were performed at the University of Innsbruck at the Institute of Ion Physics in the group of Assoc. Prof. Stephan Denifl.

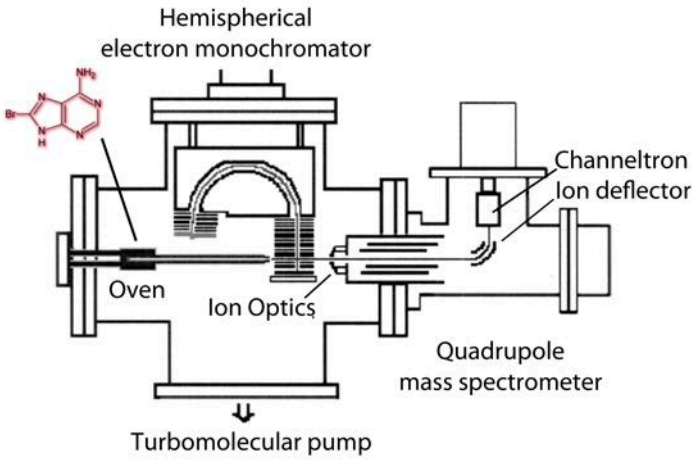

Figure 3.2: Sketch of the crossed electron molecular beam setup. Figure adapted from source [75]

In the crossed electron-molecular beam setup that is shown in figure 3.2, a molecular beam was generated through a thin capillary that was connected to a copper oven, where solid ^{8Br}A was heated up to a temperature of 410 K, which is still well below its melting point ($T_m > 250°C$). Electrons were emitted from a filament and pass a set of electrostatic lenses in a hemispherical electron monochromator that allows only electrons with a certain energy to pass. The electron beam crosses the molecular beam to produce anions that were filtered by mass with a quadrupole and subsequently detected with a channeltron detector. The energy resolution was 120 meV and determined by the full width at half maximum (FWHM) of the 0 eV resonance of the following reaction of tetrachloromethane with LEEs:

$$CCl_4 + e^- \rightarrow CCl_4^{\#-} \rightarrow CCl_3 + Cl^- \tag{3.3}$$

In order to tune the temperature of the oven to maximize molecular emission and prevent thermal decomposition of ^{8Br}A , 70 eV electrons were used to collide with the molecules and positive ion mass spectra were recorded to detect the fragments generated via electron impact ionization. Furthermore, for electron energies between 0 eV and 11 eV negative ion mass spectra were taken and for all observed anions energy spectra were recorded. Thereby the ion yield was measured for a fixed mass as a function of the electron energy.

3.7 DNA origami technique

DNA origami structures were used to determine SSBs of certain target sequences. Therefore, triangular DNA origami templates were synthesized

based on the design of P.W.K. Rothemund [57]. The basic principle of the self assembly is shown in figure 3.3.

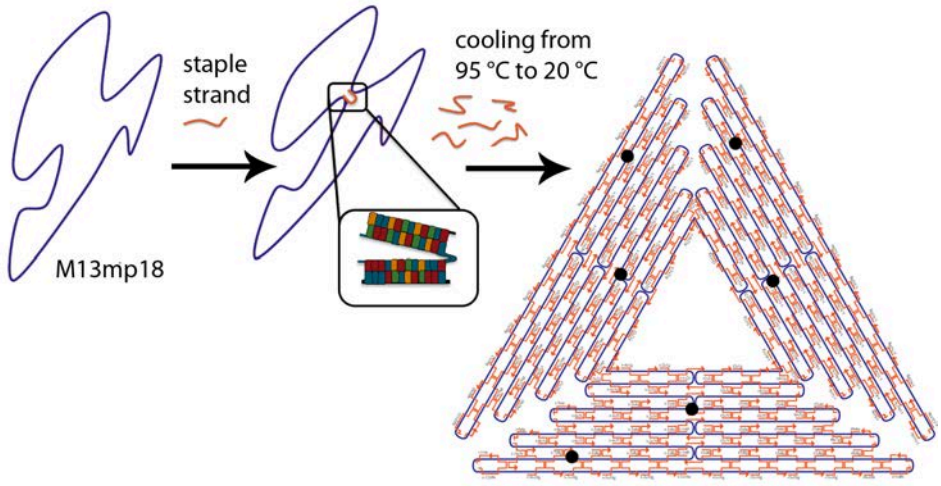

Figure 3.3: Schematic formation of triangular DNA origami via hybridization of a M13mp18 scaffold strand with 208 staple strands. The black dots on the DNA origami structure mark the position of the protruding target sequences.

To prepare triangular DNA origami structures a 7249 NBs long M13mp18 virus DNA single strand was used as a scaffold in a concentration of 5 nM and 208 short oligonucleotides with a typical length of 32 NBs were added in 30 fold excess. The short oligos have a complementary sequence to two or more sections on the scaffold strand and staple it together when a double strand is formed via hybridization. Each of the staple strands can be modified internally or with an additional sequence at the $3'$ or $5'$ end that protrudes from the DNA origami template. Here two target sequences were used:
Sequence 1: Bt TT $(ATA)_3$ TT
Sequence 2: Bt TT $(^{8Br}ATA)_3$ TT
At the $5'$ end of the t1s-4i, t1s-14i and t1s-24i strand (Sequence 1) in the DNA origami that are located in the center of the sides of the triangle and at the t-5s8g, t-5s18g, and t5s28g strand (Sequence 2) that are located close to the edges. The DNA was diluted in 1x TAE Buffer to mimic a biological environment and heated up to 95 °C to unfold the scaffold strand. Subsequent cooling down to room temperature overnight leads to the formation of a double strand via hybridization. 20 mM $MgCl_2$ were added to overcome the Coulomb repulsion of the negatively charged backbone of the DNA strands, since they need to be approached down to 2 nm. The shape of the resulting DNA origami is predetermined by the selection of tailored staple strands and thus, beyond the triangle used in this work, every conceivable shape might be generated. To purify the DNA origami templates the excess staple strands were removed by two rounds of spin filtering through a 100 kDa Millipore filter for 10 minutes at 4000 g.

In order to immobilize the DNA origami templates on a Si substrate, a cleaning procedure of the surface is required. Therefore the Si wafer was cleaned by rinsing with 4 ml of H_2O:EtOH (1:1) and dried with a flow of compressed nitrogen gas. After the wet cleaning, the substrates were illuminated for 10 minutes with 254 nm UV light and exposed for additional 5 minutes to an oxygen plasma to make the surface more hydrophilic. Especially the final steps of the cleaning are crucial to keep the DNA origami structures well adsorbed on the surface during the subsequent irradiation procedure. To bind the DNA origami electrostatically on the surface, a 0.8 μl droplet of the DNA origami solution was placed on the cleaned Si wafer together with 20 μl of 10 x TAE buffer with 200 mM $MgCl_2$. After an incubation time of 60 minutes the wafer was rinsed with 0.5 ml of H_2O:EtOH (1:1) and placed in a bath of absolute Ethanol for one more hour to reduce the amount of H_2O bound inside the DNA origami structures before it was dried with nitrogen. The samples were irradiated with LEEs under UHV conditions as described in the following subsection in detail. In order to mark the intact strands, the irradiated samples were incubated with 50 nM SAv diluted in 1 x TAE with 20 mM $MgCl_2$ for 2 minutes in order to bind at the Bt group of the intact target strands. Subsequently the sample was washed with 0.5 ml H_2O:EtOH (1:1) and dried with nitrogen to avoid further unspecific binding of SAv on the sample. For the subsequent analysis every sample was imaged with AFM.

3.7.1 Electron irradiator

The irradiation of DNA origami samples with LEEs was performed in the group of S.V.K. Kumar at the Tata institute of fundamental research (TIFR) in Mumbai, India using a custom built irradiator equipped with a pierce type electron gun [190]. In figure 3.4 a detailed sketch of the electron gun located in a UHV chamber is shown.

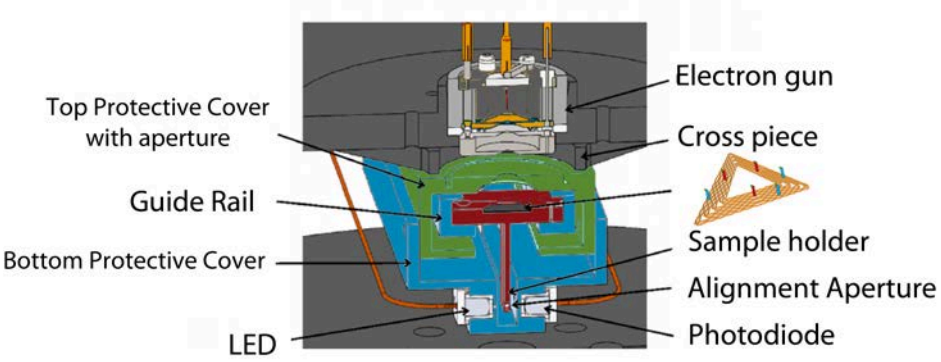

Figure 3.4: Schematic experimental setup of the electron irradiator in the UHV chamber adapted from source [190]

Usually the irradiator was operated at pressures of 10^{-8} Torr that were produced using oil free pumps. Eight samples can be placed in the sample holder whereby only seven samples were irradiated in each run and one sample served as control in order to determine potential influences of the evacuation and venting procedure to the DNA origami structures. Further-

more one additional sample that passed as well through the same procedure apart from the transfer into vacuum is used as a reference. Careful venting and pumping of the chamber over a period of at least one hour was required to prevent influences on the nanostructures. The Si chips had a size of 12 mm x 12 mm and were marked in the center with a thin cross that was scratched into the surface. In this way the center of the electron beam can be precisely determined in the subsequent analysis, as the samples were accurately placed under the electron beam with a positioning system shown in figure 3.4 b). A protective cover with an aperture of 3 mm in the center allowed for the irradiation of a well defined area. Furthermore, the samples were protected against stray electrons as they were biased at -20 V during the entire period when they were stored in the chamber. All samples were irradiated with an electron current of 1 nA at a fixed electron energy between 0.5 eV and 9 eV. The energy resolution of the electron beam was approximately 1 eV. The dose was precisely controlled by a software and was chosen between 60 nC and 240 nC. In order to determine the exact dose at a certain distance from the center of the sample a current profile of the irradiator was evaluated.

3.8 Atomic force microscopy

AFM [191] is a form of scanning probe microscopy where a small tip is mounted on a flexible cantilever that bends due to the molecular forces between the tip and a sample. The sample is scanned to receive a topographical image of the surface, while the deflection of the cantilever is detected by the reflection of a laser beam focused on the cantilever [192]. In this work NPs and DNA origami nanostructures were imaged in the tapping mode, where the cantilever is excited with a vibration close to its resonance frequency that is influenced by external forces that change the phase and amplitude of the oscillating cantilever. All measurements with the DNA origami and most of nanoparticle measurements were performed with an AFM 5500 from Agilent using a Tap 150 Al-G cantilever from Budgetsensors with a nominal spring constant of 5 N/m and a nominal frequency of 150 kHz. In all remaining cases a Flex AFM from Nanosurf was used with the same cantilevers. Subsequent data processing described below was performed with Gwyddion 2.34 software.
In order to determine the size distribution of the nanoparticles the underlying Si substrate was carefully flattened by several steps of polynomic background subtraction and base line correction under exclusion of the NPs. The NPs were identified with a mask, marking all structures with a height slightly above the surface roughness of the substrate and the NPs diameter was determined by its maximum height.
SAv molecules on top of the DNA origami need to be identified for the analysis of several thousand structures in an adequate time frame. Therefore a background subtraction and low pass filtering of the image and the choice of a color code highlighting height differences of around 1nm on top of the nanostructures were required.

4 Manuscripts

4.1 M1: "On the Stability of the Parent Anion of the Potential Radiosensitizer 8-Bromoadenine formed by Low Energy (< 3 eV) Electron Attachment"

Robin Schürmann, Katrin Tanzer, Iwona Dabkowska, Stephan Denifl and Ilko Bald

J. Phys. Chem. B, 2017
DOI: 10.1021/acs.jpcb.7b02130

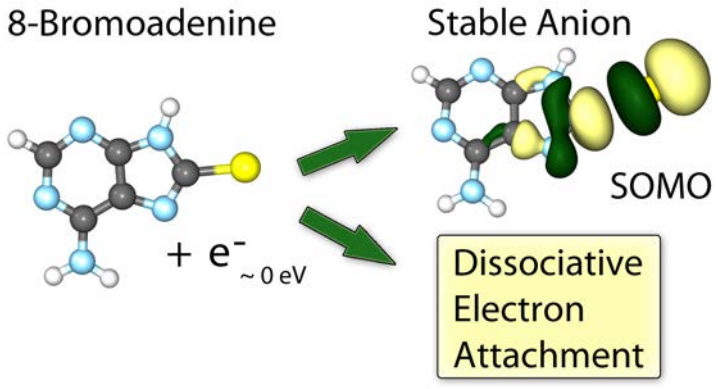

Author contributions to the manuscript:
I performed the DEA measurements at the University Innsbruck together with Dr. Katrin Tanzer. I analyzed the mass spectrometry data and prepared the published spectra. I prepared the manuscript in cooperation with Iwona Dabkowska, Stephan Denifl and Ilko Bald.

THE JOURNAL OF PHYSICAL CHEMISTRY B

Article

pubs.acs.org/JPCB

Stability of the Parent Anion of the Potential Radiosensitizer 8-Bromoadenine Formed by Low-Energy (<3 eV) Electron Attachment

Robin Schürmann,[†,‡] Katrin Tanzer,[§] Iwona Dąbkowska,[∥] Stephan Denifl,[§] and Ilko Bald*[,†,‡]

[†]Institute of Chemistry – Physical Chemistry, University of Potsdam, Karl-Liebknecht-Str. 24-25, 14476 Potsdam, Germany

[‡]BAM Federal Institute for Materials Research and Testing, Richard-Willstätter Str. 11, 12489 Berlin, Germany

[§]Institute of Ion Physics and Applied Physics and Center for Molecular Biosciences, University of Innsbruck, Technikerstrasse 25, A-6020 Innsbruck, Austria

[∥]Department of Chemistry, University of Gdansk, Sobieskiego 18, Gdansk, 80-952, Poland

ABSTRACT: 8-Bromoadenine (^{8Br}A) is a potential DNA radiosensitizer for cancer radiation therapy due to its efficient interaction with low-energy electrons (LEEs). LEEs are a short-living species generated during the radiation damage of DNA by high-energy radiation as it is applied in cancer radiation therapy. Electron attachment to ^{8Br}A in the gas phase results in a stable parent anion below 3 eV electron energy in addition to fragmentation products formed by resonant exocyclic bond cleavages. Density functional theory (DFT) calculations of the ^{8Br}A$^-$ anion reveal an exotic bond between the bromine and the C8 atom with a bond length of 2.6 Å, where the majority of the charge is located on bromine and the spin is mainly located on the C8 atom. The detailed understanding of such long-lived anionic states of nucleobase analogues supports the rational development of new therapeutic agents, in which the enhancement of dissociative electron transfer to the DNA backbone is critical to induce DNA strand breaks in cancerous tissue.

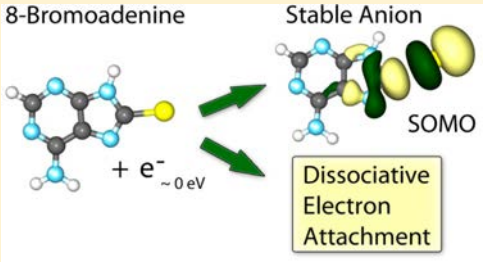

INTRODUCTION

In radiotherapy high-energy radiation, such as photons, electrons, and ions, is used to kill cancer tissue. Upon the initial interaction of the primary radiation with biological tissue, a large number of secondary particles like OH radicals and low-energy electrons (LEEs) are generated, which induce most of the cellular damage.[1,2] LEEs have been demonstrated to induce DNA damage in the form of single strand breaks (SSBs), double strand breaks (DSBs), and cross-links by dissociative electron attachment (DEA).[3−6] In DEA an electron is resonantly captured at a specific electron energy to form a transient negative ion (TNI). The TNI is typically unstable with respect to electron detachment or dissociation. Dissociation results in bond breaking on the time scale of the vibrational motion of the molecule (≈10^{-14} s). Some chemotherapeutic drugs, which are clinically administered for decades such as 5-fluorouracil (^{5F}U), cisplatin, and gemcitabine have an additional radiosensitizing effect that is exploited in concomitant radiochemotherapy.[7,8] These compounds exhibit a particular reactivity toward LEEs.[9−11] In the case of ^{5F}U and cisplatin it has been demonstrated that their association to DNA also leads to enhanced DNA strand breakage induced by LEEs.[11−15] Cisplatin binds to two guanine bases in the DNA, which can be facilitated by LEE attachment.[9] Once bound to DNA, attachment of a single electron to the cisplatin−DNA complex and formation of a Pt-centered TNI have been demonstrated to be able to induce a DNA double strand break.[13] Radiosensitization to LEEs acts on a femtosecond time scale, in contrast to biological sensitization, which is operative on a time scale of hours to days. In this context it was very recently demonstrated that this knowledge can be used to optimize the treatment protocols in radiochemotherapy such that irradiation is performed when the maximum amount of Pt is bound to DNA.[16,17] In this way it was shown that the formation of TNIs by electron attachment is a relevant process in DNA radiation damage and radiosensitization, which can be exploited to improve cancer radiation therapy.

Recently, it was proposed that apart from established radiosensitizers also electrophilic molecules in general could act on a physicochemical level as radiosensitizers due to an enhanced DEA cross section, which could create specific reaction products leading presumably to more severe DNA damage.[18−20]

As an example also the incorporation of brominated nucleobases and fluorinated adenine into DNA oligonucleotides generally leads to enhanced DNA strand breakage induced

Received: March 6, 2017
Revised: May 17, 2017
Published: May 19, 2017

DOI: 10.1021/acs.jpcb.7b02130
J. Phys. Chem. B XXXX, XXX, XXX−XXX

by LEEs.[21−23] In this context 8-bromo-2′-deoxyadenosine has been proposed as a novel radiosensitizer.[24] Density functional theory (DFT) calculations and radiolytic experiments indicate that electron attachment can result in barrier-free Br^- abstraction followed by hydrogen atom transfer within the remaining neutral radical nucleotide.[24−26] This finally leads on the one hand to formation of cyclic adenosine and on the other hand to P−O bond cleavage within the DNA backbone, which is equivalent to a DNA strand break. Nevertheless, DFT calculations on electron attachment to brominated nucleobases dissolved in water exhibit a shallow minimum in the free energy profile along the C−Br coordinate around 2.7 Å, indicating that this anion may be stable in an aqueous environment.[27]

Here, we demonstrate that electron attachment to 8-bromoadenine (^{8Br}A) below 1 eV indeed leads to a parent anion in the gas phase, which is stable enough to be detectable in a mass spectrometry setup. In the present work we elucidate the mechanism of parent anion stabilization using DFT calculations. Additionally, low-energy (i.e., <3 eV) electron attachment to ^{8Br}A results in several fragmentation reactions that are further characterized and shed some light on the potential of ^{8Br}A to act as a radiosensitizer.

RESULTS AND DISCUSSION

The formation of parent and fragment anions formed by electron attachment to ^{8Br}A is probed in a crossed molecular-electron beam setup. A hemispherical electron monochromator is used to provide a low-energy electron beam with an energy resolution of about 120 meV. Negative ions are detected by a quadrupole mass spectrometer (see the Methods section for more details). The intensity of a mass-selected anion is recorded as a function of the electron energy, resulting in ion yield curves as shown in Figures 1 and 3, and the molecular structure of ^{8Br}A is shown in Figure 2a.

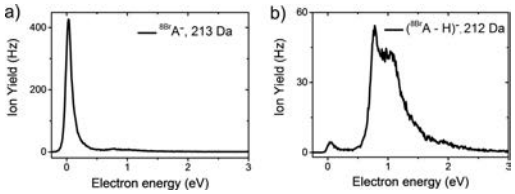

Figure 1. Ion yield curves of the parent anion $^{8Br}A^-$ observed at 213 Da (a) and the parent ion after loss of hydrogen $[^{8Br}A - H]^-$ observed at 212 Da (b).

As Br has two stable isotopes with an atomic mass of 79 and 81 Da at a ratio of 51% and 49%, the Br-containing fragments are easy to identify as they show two peaks in the mass spectrum.

The parent anion $^{8Br}A^-$ is observed at 213 and 215 Da, and the ion yield curve for 213 Da is shown on the left of Figure 1. It is mostly formed within a single resonance close to 0 eV. In previous electron attachment experiments neither for adenine (A) nor any other nonmodified nucleobase a stable parent anion was observed.[28,29] Only for 5-bromouracil (^{5Br}U) and 5-bromouridine (^{5Br}dU) stable molecular anions were observed previously.[30,31]

In this low-energy regime TNIs are typically formed by electron attachment to a formerly empty molecular orbital (MO) without excitation of the other electrons. The extra

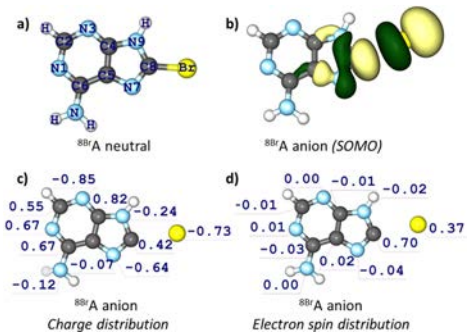

Figure 2. Results of DFT calculations: (a) molecular structure of 8-bromoadenine (^{8Br}A), (b) SOMO of the ground state ^{8Br}A anion, (c) charge distribution within the ^{8Br}A anion determined using the Merz−Singh−Kollman scheme,[33] and (d) electron spin distribution within the ^{8Br}A anion.

electron can then be temporarily trapped within a centrifugal barrier in the interaction potential representing a shape resonance.[32] In addition to the peak at 0 eV a weak feature around 0.8 eV is observed. This peak is not assigned to a further resonance resulting in the formation of the parent anion, but it originates from the dehydrogenated parent anion with a molecular mass of 213 Da due to the natural ratio of the $^{12}C/^{13}C$ and $^{14}N/^{15}N$ isotopes.

We have performed DFT calculations, which confirm that a stable $^{8Br}A^-$ can be formed with an adiabatic electron affinity of 0.89 eV (in terms of thermal free energy for 298.15 K). This is in contrast to other halogenated A derivatives, namely ^{2Br}A, ^{2F}A, and ^{8F}A, which are not able to adiabatically bind an extra electron.[23] The DFT calculations reveal a unique binding mechanism of the electron by ^{8Br}A. The additional electron approaches the ^{8Br}A molecule and occupies the lowest unoccupied MO (LUMO) of the neutral, thereby forming a transient negative ion. The vertical electron affinity is negative and is equal to −0.373 eV. It corresponds to the vertical transition energy from the neutral ground state to the TNI. It is likely that a transition close to 0 eV is possible within the Franck−Condon region, as it is observed in the experiments. The transition into a stable anionic state is associated with significant geometrical reorganization. The SOMO (singly occupied MO) of the newly formed anion has a nodal plane in the A−Br bond and thus is strongly antibonding (Figure 2b). Hence, the A−Br bond weakens and extends from 1.87 to 2.62 Å. Because of the strongly elongated A−Br bond, the minimum-energy structure of $^{8Br}A^-$ can be considered as a complex of [A − H] with Br, with a particular distribution of charge (Figure 2c) and spin (Figure 2d). The charge distribution has been determined using the Merz−Singh−Kollman scheme[33] (see Methods section for details). Accordingly, the majority of the excess charge (−0.73*e*) resides on Br, whereas the partial charge allocated on A is only −0.27*e*. The energy of the asymptote ($[A - H]^\bullet$) + Br^- is 1.24 eV lower than that of $[A - H]^-$ + $Br^\bullet$ (0.8 eV versus 2.04 eV). From this perspective, we interpret the minimum-energy structure of the ^{8Br}A anion as a complex Br^---$[A - H]^\bullet$, even though the effective charge on Br is only −0.73*e*. This picture is supported by the spin density distribution, which is the largest on the imidazole ring. This is in accordance with the earlier

DOI: 10.1021/acs.jpcb.7b02130
J. Phys. Chem. B XXXX, XXX, XXX−XXX

findings,[34] where the barrierless formation of such a complex was first postulated. The experiment demonstrates that such a complex survives long enough to be extracted by the ion optics of the mass spectrometer (i.e., several microseconds); therefore, this can be considered as an anionic state of the parent molecule. The energy to separate the Br^- ion and the $[A - H]^\bullet$ radical is calculated to be 1.20 eV (in terms of electron energy), while the Gibbs energy for this reaction is 0.80 eV. In $^{8Br}A^-$ the unpaired electron is partially localized on the imidazole ring of A, which is more stable than an A radical with the unpaired electron on the pyrimidine ring. Consequently, the situation is different when Br is bound to A at a different position. Our DFT calculations show that the anion of the ^{2Br}A molecule is not stable, the latter having a negative electron affinity of −0.02 eV. Also, the fluorinated A derivatives ^{8F}A and ^{2F}A do not form a stable molecular anion since the A−F bond (135 kcal/mol) is much stronger than the A−Br bond (85 kcal/mol).

In addition to the parent ion also anions with a mass of 212 Da (Figure 1b) and 214 Da are observed, which are due to the dehydrogenation of $^{8Br}A^-$:

$$^{8Br}A + e^- \rightarrow {}^{8Br}A^- \rightarrow [{}^{8Br}A - H]^- + H$$

For nonmodified nucleobases, this is the most abundant fragment.[29,35] Besides a weak signal at 0 eV there are two further signals at 0.78 and 1.02 eV. The most intense signal is found to be at 0.78 eV, which is at slightly lower energy than the strongest signal for dehydrogenated A located at 1.14 eV.[36] The sharp onset at low energies indicates that this fragment ion is produced right at its thermodynamic threshold. The H abstraction can either proceed from C2 or N9 of the ^{8Br}A molecule (see Figure 2a for the atom labeling). Our DFT calculations reveal the thermodynamic threshold ($\Delta_R G$) of the H abstraction from different sites of the molecule: $\Delta_R G = \Delta_F G([{}^{8Br}A - H]^-) + \Delta_F G(H) - \Delta_F G({}^{8Br}A)$. The thermodynamic threshold for the abstraction of H from C2 is found to be −3.15 eV, whereas for the cleavage of the N9−H bond it is −0.26 eV. This indicates that both fragmentation pathways are thermodynamically possible within the resonances observed here.

All fragment anions observed in DEA to ^{8Br}A at electron energies below 3 eV are summarized in Table 1. The most abundant fragment anions generated in DEA to ^{8Br}A are the isotopes of Br^- with a mass of 79 and 81 Da (see Figure 3). The corresponding ion yield curve (Figure 3a) shows a strong resonance close to 0 eV with two shoulders at 0.35 and 1.05 eV. The complementary negative ion $[{}^{8Br}A - Br]^-$ with molecular mass of 134 Da is also generated through resonances at 0, 0.35, and 1.1 eV, but with less intensity (Figure 3b). The slightly more pronounced shoulder at 1.1 eV can be explained by ^{13}C- and ^{15}N-containing isotopologues of the $[{}^{8Br}A - Br - H]^-$ fragment anion observed at 133 Da (Figure 3c). This fragment anion is assigned to the loss of Br and a hydrogen atom resulting in $[{}^{8Br}A - Br - H]^-$. For this fragment anion the two resonances at 0.35 and 1.15 eV are more pronounced compared to the ion yield curves of Br^- and the negative ion with a mass of 134 Da. It is also interesting to note that DEA to A at low energies results in several fragment anions, which could not be detected in DEA to ^{8Br}A, e.g., fragment anions with mass-to-charge ratios of 117 and 119 Da.[36] This indicates that DEA to ^{8Br}A leads to fewer fragmentation channels compared to A, but higher signal intensities for fragmentation reactions involving the cleavage of the C−Br bond.

Table 1. Fragment Anions Observed in DEA to ^{8Br}A at Electron Energies below 3 eV

ion	mass (Da)	peak energy (eV)		
Br^-	79/81	0	0.35	1.05
$(^{8Br}A-Br-H)^-$	133	0	0.35	1.15
$(^{8Br}A-Br)^-$	134	0	0.35	1.1
$(^{8Br}A-H)^-$	212/214	0.05	0.78	1.02
$^{8Br}A^-$	213/215	0		

CONCLUSIONS

In summary, electron attachment to ^{8Br}A close to 0 eV results in a remarkably stable molecular anion, which is assigned by means of DFT calculations to a Br^---$[A - H]^\bullet$ complex, in which the C−Br bond is elongated to 2.62 Å. At the same time intense fragmentation of the transient negative ion is observed, which is associated with the cleavage of the C−Br bond within at least three different resonances below 2 eV. Compared to DEA to A, electron attachment to ^{8Br}A results in fewer fragmentation reactions, but with higher signal intensities. A subject of further studies is the effect of the characteristic electron attachment to ^{8Br}A on DNA strand breakage when ^{8Br}A is incorporated into DNA. It needs to be elucidated whether the long lifetime of the $^{8Br}A^-$ parent anion is preserved when ^{8Br}A is incorporated in a DNA strand and whether it has an effect on the DNA strand breakage. In general, ^{8Br}A might serve as an "antenna" in the capture of electrons. On the other hand, the formation of stable parent anions might compete with dissociative pathways and thus decrease the probability for a strand break to take place. One potential precursor for strand breaks in DNA would be the radical site on A formed by abstraction of Br^- through DEA.

METHODS

Crossed Electron Molecular Beam Experiment. In the present experiment a crossed molecular electron beam setup with high electron energy resolution was used that was previously described elsewhere in detail.[36] The molecular beam was produced from a capillary connected to a copper oven, where ^{8Br}A powder was heated up to 147 °C, well below its boiling temperature that is above 250 °C. The working pressure was around 8×10^{-7} mbar, and internal lamps kept the chamber at 350 K to avoid condensation of molecules on the lenses of the monochromator. In the collision region, the neutral molecular beam crossed at right angle an electron beam that was generated by a hemispherical electron monochromator (HEM). A weak electrostatic field guides the negative ions toward a quadrupole mass spectrometer. Electron energy calibration was performed using the DEA reaction of CCl_4. The 0 eV resonance in the ion efficiency curve of Cl^- was used to calibrate the energy scale, and the energy resolution of 120 meV was determined from the fwhm. ^{8Br}A was purchased from Carbosynth Ltd. (UK) and used without further purifications.

Computational Details. The structures of the neutral and anionic ^{8Br}A were fully optimized with the DFT method with Becke's three-parameter hybrid functional (B3LYP)[37−39] and the 6-31++G** basis set.[40] All the energy differences here are given in terms of Gibbs free energies (ΔG's), where electronic energies are corrected for zero-point vibration terms, thermal contributions to energy, the pV term, and the entropy term. These terms were calculated in the rigid rotor−harmonic

DOI: 10.1021/acs.jpcb.7b02130
J. Phys. Chem. B XXXX, XXX, XXX−XXX

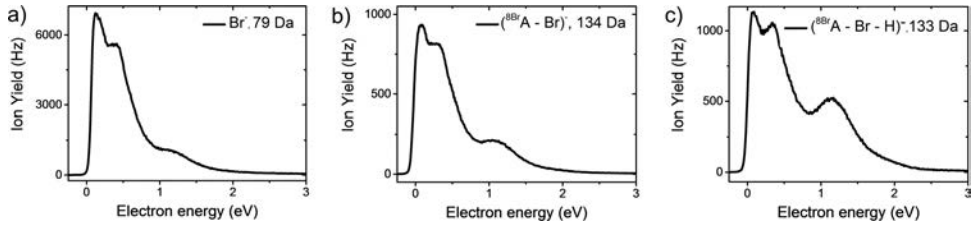

Figure 3. Ion yield curves of the anionic fragments with a mass of (a) 79, (b) 134, and (c) 133 Da.

oscillator approximation for T = 298 K and p = 1 atm. The adiabatic electron affinity is calculated as the difference of energy between the fully optimized neutral and the corresponding fully optimized anion. The charge distribution is determined using the Merz−Singh−Kollman (MK) scheme.[33] Accordingly, atomic charges are fitted to reproduce the molecular electrostatic potential (MEP) at a number of points around the molecule. We have used 1192 grid points located on five layers around the molecule. The layers are constructed as an overlay of van der Waals spheres around each atom. The first layer is the van der Waals envelope, and the following ones are added with the scaling factors of 1.4, 1.6, 1.8, and 2.0. All quantum chemical calculations were carried out with the GAUSSIAN09 rev.E suite of programs using the computational resources provided by Wroclaw Centre for Networking and Supercomputing (WCSS), grant No. 352. The visualizations of molecules were performed with the ChemCraft program.[38]

AUTHOR INFORMATION

Corresponding Author

*(I.B.) E-mail ilko.bald@uni-potsdam.de.

ORCID

Stephan Denifl: 0000-0001-6072-2070

Ilko Bald: 0000-0002-6683-5065

Notes

The authors declare no competing financial interest.

ACKNOWLEDGMENTS

This research was supported by the Federal Institute for Materials Research (BAM), a Marie Curie FP7 Integration Grant within the seventh European Union Framework Programme, by the Deutsche Forschungsgemeinschaft (DFG) and the University of Potsdam. R.S. acknowledges a travel grant for a visit to Innsbruck by the European Union via the COST Action MP1002 (Nano-IBCT). I.D. was supported by the Foundation for Polish Science (POMOST/2012-6/3 cofunded from POIG 2007-2013). S.D. acknowledges support from the Austrian Science Fund (FWF): P30332.

REFERENCES

(1) Alizadeh, E.; Sanz, A. G.; García, G.; Sanche, L. Radiation Damage to DNA: The Indirect Effect of Low-Energy Electrons. *J. Phys. Chem. Lett.* **2013**, *4* (5), 820−825.

(2) Nguyen, J.; Ma, Y.; Luo, T.; Bristow, R. G.; Jaffray, D. A.; Lu, Q.-B. Direct Observation of Ultrafast-Electron-Transfer Reactions Unravels High Effectiveness of Reductive DNA Damage. *Proc. Natl. Acad. Sci. U. S. A.* **2011**, *108* (29), 11778−11783.

(3) Baccarelli, I.; Bald, I.; Gianturco, F. A.; Illenberger, E.; Kopyra, J. Electron-Induced Damage of DNA and Its Components: Experiments and Theoretical Models. *Phys. Rep.* **2011**, *508* (1−2), 1−44.

(4) Boudaïffa, B.; Cloutier, P.; Hunting, D.; Huels, M. A.; Sanche, L. Resonant Formation of DNA Strand Breaks by Low-Energy (3 o 20 eV) Electrons. *Science* **2000**, *287* (5458), 1658−1660.

(5) Huels, M. A.; Boudaïffa, B.; Cloutier, P.; Hunting, D.; Sanche, L. Single, Double, and Multiple Double Strand Breaks Induced in DNA by 3−100 eV Electrons. *J. Am. Chem. Soc.* **2003**, *125* (15), 4467−4477.

(6) Luo, X.; Zheng, Y.; Sanche, L. DNA Strand Breaks and Crosslinks Induced by Transient Anions in the Range 2−20 eV. *J. Chem. Phys.* **2014**, *140* (15), 155101.

(7) Seiwert, T. Y.; Salama, J. K.; Vokes, E. E. The Concurrent Chemoradiation Paradigm—general Principles. *Nat. Clin. Pract. Oncol.* **2007**, *4* (2), 86−100.

(8) Sanche, L. Interaction of Low Energy Electrons with DNA: Applications to Cancer Radiation Therapy. *Radiat. Phys. Chem.* **2016**, *128*, 36−43.

(9) Kopyra, J.; Koenig-Lehmann, C.; Bald, I.; Illenberger, E. A Single Slow Electron Triggers the Loss of Both Chlorine Atoms from the Anticancer Drug Cisplatin: Implications for Chemoradiation Therapy. *Angew. Chem., Int. Ed.* **2009**, *48* (42), 7904−7907.

(10) Kopyra, J.; Keller, A.; Bald, I. On the Role of Fluoro-Substituted Nucleosides in DNA Radiosensitization for Tumor Radiation Therapy. *RSC Adv.* **2014**, *4* (13), 6825.

(11) Rackwitz, J.; Ranković, M. L.; Milosavljević, A. R.; Bald, I. A Novel Setup for the Determination of Absolute Cross Sections for Low-Energy Electron Induced Strand Breaks in Oligonucleotides − The Effect of the Radiosensitizer 5-Fluorouracil. *Eur. Phys. J. D* **2017**, *71* (2), e2016-70608-4.

(12) Rezaee, M.; Hunting, D. J.; Sanche, L. New Insights into the Mechanism Underlying the Synergistic Action of Ionizing Radiation With Platinum Chemotherapeutic Drugs: The Role of Low-Energy Electrons. *Int. J. Radiat. Oncol., Biol., Phys.* **2013**, *87* (4), 847−853.

(13) Rezaee, M.; Alizadeh, E.; Cloutier, P.; Hunting, D. J.; Sanche, L. A Single Subexcitation-Energy Electron Can Induce a Double-Strand Break in DNA Modified by Platinum Chemotherapeutic Drugs. *ChemMedChem.* **2014**, *9* (6), 1145−1149.

(14) Zheng, Y.; Hunting, D. J.; Ayotte, P.; Sanche, L. Role of Secondary Low-Energy Electrons in the Concomitant Chemoradiation Therapy of Cancer. *Phys. Rev. Lett.* **2008**, *100* (19), 198101.

(15) Bao, Q.; Chen, Y.; Zheng, Y.; Sanche, L. Cisplatin Radiosensitization of DNA Irradiated with 2−20 eV Electrons: Role of Transient Anions. *J. Phys. Chem. C* **2014**, *118* (28), 15516−15524.

(16) Tippayamontri, T.; Kotb, R.; Paquette, B.; Sanche, L. Efficacy of Cisplatin and Lipoplatin in Combined Treatment with Radiation of a Colorectal Tumor in Nude Mouse. *Anticancer Res.* **2013**, *33* (8), 3005−3014.

(17) Tippayamontri, T.; Kotb, R.; Sanche, L.; Paquette, B. New Therapeutic Possibilities of Combined Treatment of Radiotherapy with Oxaliplatin and Its Liposomal Formulation, Lipoxal, in Rectal Cancer Using Xenograft in Nude Mice. *Anticancer Res.* **2014**, *34* (10), 5303−5312.

(18) Lu, Q.-B.; Zhang, Q.-R.; Ou, N.; Wang, C.-R.; Warrington, J. In Vitro and In Vivo Studies of Non-Platinum-Based Halogenated Compounds as Potent Antitumor Agents for Natural Targeted Chemotherapy of Cancers. *EBioMedicine* **2015**, *2* (6), 544−553.

(19) Rak, J.; Chomicz, L.; Wiczk, J.; Westphal, K.; Zdrowowicz, M.; Wityk, P.; Żyndul, M.; Makurat, S.; Golon, Ł. Mechanisms of Damage

DOI: 10.1021/acs.jpcb.7b02130
J. Phys. Chem. B XXXX, XXX, XXX−XXX

to DNA Labeled with Electrophilic Nucleobases Induced by Ionizing or UV Radiation. *J. Phys. Chem. B* **2015**, *119* (26), 8227−8238.
(20) Chomicz, L.; Zdrowowicz, M.; Kasprzykowski, F.; Rak, J.; Buonaugurio, A.; Wang, Y.; Bowen, K. H. How to Find Out Whether a 5-Substituted Uracil Could Be a Potential DNA Radiosensitizer. *J. Phys. Chem. Lett.* **2013**, *4* (17), 2853−2857.
(21) Park, Y.; Polska, K.; Rak, J.; Wagner, J. R.; Sanche, L. Fundamental Mechanisms of DNA Radiosensitization: Damage Induced by Low-Energy Electrons in Brominated Oligonucleotide Trimers. *J. Phys. Chem. B* **2012**, *116* (32), 9676−9682.
(22) Keller, A.; Rackwitz, J.; Cauët, E.; Liévin, J.; Körzdörfer, T.; Rotaru, A.; Gothelf, K. V.; Besenbacher, F.; Bald, I. Sequence Dependence of Electron-Induced DNA Strand Breakage Revealed by DNA Nanoarrays. *Sci. Rep.* **2015**, *4*, 7391.
(23) Rackwitz, J.; Kopyra, J.; Dąbkowska, I.; Ebel, K.; Ranković, M. L.; Milosavljević, A. R.; Bald, I. Sensitizing DNA Towards Low-Energy Electrons with 2-Fluoroadenine. *Angew. Chem., Int. Ed.* **2016**, *55* (35), 10248−10252.
(24) Chomicz, L.; Leszczynski, J.; Rak, J. Electron-Induced Degradation of 8-Bromo-2′-Deoxyadenosine 3′,5′-Diphosphate, a DNA Radiosensitizing Nucleotide. *J. Phys. Chem. B* **2013**, *117* (29), 8681−8688.
(25) Chatgilialoglu, C.; Guerra, M.; Mulazzani, Q. G. Model Studies of DNA C5′ Radicals. Selective Generation and Reactivity of 2′-Deoxyadenosin-5′-Yl Radical. *J. Am. Chem. Soc.* **2003**, *125* (13), 3839−3848.
(26) Schürmann, R.; Bald, I. Real-Time Monitoring of Plasmon Induced Dissociative Electron Transfer to the Potential DNA Radiosensitizer 8-Bromoadenine. *Nanoscale* **2017**, *9* (5), 1951−1955.
(27) Wieczór, M.; Wityk, P.; Czub, J.; Chomicz, L.; Rak, J. A First-Principles Study of Electron Attachment to the Fully Hydrated Bromonucleobases. *Chem. Phys. Lett.* **2014**, *595*−*596*, 133−137.
(28) Denifl, S.; Sulzer, P.; Huber, D.; Zappa, F.; Probst, M.; Märk, T. D.; Scheier, P.; Injan, N.; Limtrakul, J.; Abouaf, R.; et al. Influence of Functional Groups on the Site-Selective Dissociation of Adenine upon Low-Energy Electron Attachment. *Angew. Chem., Int. Ed.* **2007**, *46* (27), 5238−5241.
(29) Abdoul-Carime, H.; Gohlke, S.; Illenberger, E. Site-Specific Dissociation of DNA Bases by Slow Electrons at Early Stages of Irradiation. *Phys. Rev. Lett.* **2004**, *92* (16), 168103.
(30) Abdoul-Carime, H.; Huels, M. A.; Brüning, F.; Illenberger, E.; Sanche, L. Dissociative Electron Attachment to Gas-Phase 5-Bromouracil. *J. Chem. Phys.* **2000**, *113* (7), 2517.
(31) Denifl, S.; Candori, P.; Ptasińska, S.; Limão-Vieira, P.; Grill, V.; Märk, T. D.; Scheier, P. Positive and Negative Ion Formation via Slow Electron Collisions with 5-Bromouridine. *Eur. Phys. J. D* **2005**, *35* (2), 391−398.
(32) Bald, I.; Langer, J.; Tegeder, P.; Ingólfsson, O. From Isolated Molecules through Clusters and Condensates to the Building Blocks of Life. *Int. J. Mass Spectrom.* **2008**, *277* (1−3), 4−25.
(33) Singh, U. C.; Kollman, P. A. An Approach to Computing Electrostatic Charges for Molecules. *J. Comput. Chem.* **1984**, *5* (2), 129−145.
(34) Chomicz, L.; Rak, J.; Storoniak, P. Electron-Induced Elimination of the Bromide Anion from Brominated Nucleobases. A Computational Study. *J. Phys. Chem. B* **2012**, *116* (19), 5612−5619.
(35) Ptasinska, S.; Denifl, S.; Scheier, P.; Illenberger, E.; Märk, T. D. Bond- and Site-Selective Loss of H Atoms from Nucleobases by Very-Low-Energy Electrons (<3 eV). *Angew. Chem., Int. Ed.* **2005**, *44* (42), 6941−6943.
(36) Huber, D.; Beikircher, M.; Denifl, S.; Zappa, F.; Matejcik, S.; Bacher, A.; Grill, V.; Märk, T. D.; Scheier, P. High Resolution Dissociative Electron Attachment to Gas Phase Adenine. *J. Chem. Phys.* **2006**, *125* (8), 084304.
(37) Becke, A. D. Density-Functional Exchange-Energy Approximation with Correct Asymptotic Behavior. *Phys. Rev. A: At., Mol., Opt. Phys.* **1988**, *38* (6), 3098−3100.
(38) Becke, A. D. Density-functional Thermochemistry. III. The Role of Exact Exchange. *J. Chem. Phys.* **1993**, *98* (7), 5648−5652.
(39) Lee, C.; Yang, W.; Parr, R. G. Development of the Colle-Salvetti Correlation-Energy Formula into a Functional of the Electron Density. *Phys. Rev. B: Condens. Matter Mater. Phys.* **1988**, *37* (2), 785−789.
(40) Hehre, W. J.; Ditchfield, R.; Pople, J. A. Self—Consistent Molecular Orbital Methods. XII. Further Extensions of Gaussian—Type Basis Sets for Use in Molecular Orbital Studies of Organic Molecules. *J. Chem. Phys.* **1972**, *56* (5), 2257−2261.

DOI: 10.1021/acs.jpcb.7b02130
J. Phys. Chem. B XXXX, XXX, XXX−XXX

4.2 M2: "Resonant formation of strand breaks in sensitized oligonucleotides induced by low-energy electrons (0.5 - 9 eV)"

Robin Schürmann, Thupten Tsering, Katrin Tanzer, Stephan Denifl, S.V.K. Kumar and Ilko Bald
Submitted

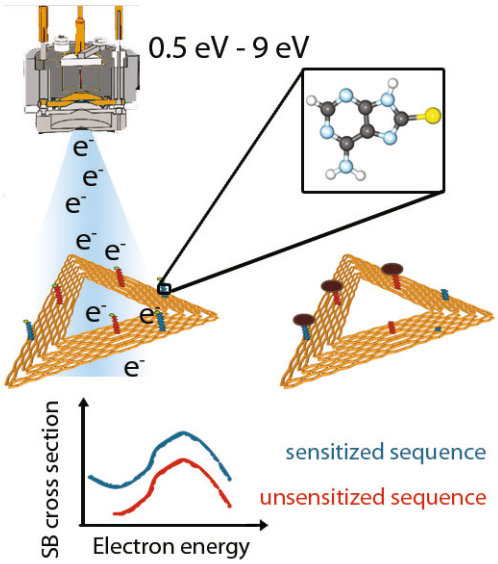

Author contributions to the manuscript:
I performed the DEA measurements together with Dr. Katrin Tanzer at the University Innsbruck. I analyzed the mass spectrometry data. Furthermore, I did all sample preparations of the DNA origami structures by myself. I performed the LEE irradiation of the DNA origami structures together with Thupten Tsering at the TIFR in Mumbai. I did all AFM measurements of the irradiated samples and the subsequent analysis of the images. I prepared all figures for the manuscript and the supporting info. I prepared the manuscript in cooperation with S.V.K. Kumar, Stephan Denifl and Ilko Bald.

Resonant formation of strand breaks in sensitized oligonucleotides induced by low-energy electrons (0.5 – 9 eV)

Robin Schürmann [a,b], Thupten Tsering [c], Katrin Tanzer [d], Stephan Denifl [d], S.V.K. Kumar [c], and Ilko Bald*[a,b]

Abstract: Halogenated nucleobases act as radiosensitizers in cancer radiation therapy, enhancing the reactivity of DNA to secondary low-energy electrons (LEEs). LEEs induce DNA strand breaks at specific energies (resonances) *via* dissociative electron attachment (DEA). Although halogenated nucleobases show intense DEA resonances at various electron energies in the gas phase, it is inherently difficult to investigate the influence of halogenated nucleobases on the actual DNA strand breakage over a broad range of electron energies in which DEA can take place (< 12 eV). Using DNA origami nanostructures, we determine the energy dependence of the strand break cross section for oligonucleotides modified with 8-Bromoadenine (^{8Br}A). These results are evaluated against measurements of DEA to isolated ^{8Br}A in the gas phase. Contrary to expectations, the major contribution to strand breaks is from resonances around 7 eV, while resonances at very low energy (< 2 eV) have little influence on strand breaks.

Low energy electrons (LEEs) are an important short-living species, which are formed in radiation damage to DNA,[1] e.g. during cancer radiation therapy. DNA strand breaks are induced by LEEs even below the ionization threshold *via* dissociative electron attachment (DEA).[2] DEA takes place at specific energies resulting in resonant structures in the cross sections of single strand breaks (SSBs) and double strand breaks (DSBs) upon irradiation, as reported for model plasmid DNA systems with LEEs.[1a,3] Furthermore, it has been demonstrated also for chemotherapeutic agents like cisplatin,[4] gemcitabine [5] and 2-Fluoroadenine (^{2F}A) [6] that LEEs cause enhanced damage, which accounts at least partly for their radiosensitizing action.[7] Nevertheless, the use of plasmid DNA for irradiation experiments is limited as the influence of the DNA sequence, DNA conformation or specific preparation conditions on the strand break cross section remains unknown. Short oligonucleotides (shorter than tetramers) with a distinct sequence and also with incorporated radiosensitizers have been studied using HPLC for post irradiation damage analysis.[8] However, there are strict limitations concerning the length of the oligonucleotides that can be used in such experiments. By using DNA origami structures these limitations can be overcome and it allows the determination of absolute strand break cross sections of tailored target sequences.[6,9] Electron energy dependent measurements aimed at revealing the resonant character of the LEE induced strand breakage with oligonucleotides has not been performed up to now using the DNA origami technique, although it remains a critical task to support previous studies using plasmid DNA and to study the influence of sequence modifications on the DEA resonances.

The commonly used chemotherapeutic halogen containing compound cisplatin[4] and brominated nucleobases[10] show strong DEA resonances close to 0 eV in the gas phase causing the release of a halide anion and leaving behind a neutral radical. These radicals are expected to be an important precursor in the formation of SSBs, as they can abstract a hydrogen atom from the adjacent deoxyribose unit, which leads to a SSB after several intermediate steps.[11] A strong energy dependence of the SSB cross section is expected especially at very low electron energies, if the formation of the Br^- ion is the relevant reaction channel in the formation of SSBs in DNA strands containing brominated radiosensitizers. On the other hand, the initial electron attachment could be the decisive step for DNA strand breakage. It is generally assumed that for non-modified DNA strands, depending on the environmental conditions,[12] the LEEs are captured by the electrophilic nucleobases and transferred via molecular orbital overlap to the DNA-backbone where the cleavage of the C-O σ-bond causes a SSB.[13]

Here we present the energy dependence of DNA strand breaks in single stranded oligonucleotides using the established DNA origami technique[6,9] and elucidate the influence of the potential radiosensitizer 8-Bromoadenine (^{8Br}A)[8b,11a,14] on the absolute strand break (SB) cross section. The data is supported by DEA measurements performed with the isolated molecule ^{8Br}A in the gas phase. DEA to all the DNA building blocks was previously studied in detail in the gas phase,[15] but the influence of distinct fragmentation channels on the SB cross section is still not fully understood. Thus we correlate energy dependent SB cross sections of well-defined oligonucleotides in the condensed phase with DEA data from the gas phase in the relevant energy regime to get a deeper understanding of the underlying mechanisms.

The general principle of the SB detection is illustrated in Figure 1a showing triangular DNA origami templates that are modified with two different protruding target oligonucleotides carrying a Biotin (Bt) group at the 5' end. At the central position of the DNA origami template the sequence $TT(ATA)_3TT$ is positioned and studied to compare and check the reproducibility of the results from earlier measurements done using different irradiation setups at specific electron energies.[6,9b] In the previous experiments using 18 eV electrons this Adenine (A) rich sequence showed an enhanced SB cross section under electron irradiation compared to other non-modified oligonucleotides.[6,9b] In the second target sequence $TT(^{8Br}ATA)_3TT$, which is positioned close to the edges of the DNA origami triangles, three A bases are exchanged by the potential DNA radiosensitizer ^{8Br}A. In this way,

[a] Prof. Dr. Ilko.Bald, Robin Schürmann
Department of Chemistry—Physical Chemistry
University of Potsdam
Karl-Liebknecht-Strasse 24-25, D-14476 Potsdam-Golm, Germany
E-mail: bald@uni-potsdam.de
[b] Prof. Dr. Ilko.Bald, Robin Schürmann
Department 1—Analytical Chemistry and Reference Materials
BAM Federal Institute for Materials Research and Testing
Richard-Willstätter Str.11, 12489 Berlin, Germany
[c] Thupten Tsering, Prof. Dr. S.V.K. Kumar
Tata Institute of Fundamental Research
Homi Bhabha Road, Colaba Mumbai 400 005, India
[d] Dr. Katrin Tanzer, Prof. Dr. Stephan Denifl
Institute of Ion Physics and Applied Physics
University of Innsbruck
Technikerstrasse 25, A-6020 Innsbruck, Austria

Supporting information for this article is given via a link at the end of the document.

both oligonucleotides can be compared within the same irradiation procedures.

The DNA origami nanostructures have been immobilized on plasma cleaned Si substrates and have been exposed to an electron beam from a pierce type electron gun in a UHV chamber with a well-defined dose D between 60 and 240 nC at an incident electron energy between 0.5 eV and 9 eV.[16] Remaining intact target strands have been marked with Streptavidin (SAv) and imaged by atomic force microscopy (AFM; see Figure 1a). The relative number of SBs (N_{SB}) of each sample has been determined from the number of intact strands on an irradiated sample compared to the number of intact strands on a non-irradiated control sample. As the electron doses were chosen well below the saturation of N_{SB},[9a] the absolute SB cross section σ_{SB} of the target strands can be determined by a linear fit of the SB yield against the electron dose (see Figure 1 d).

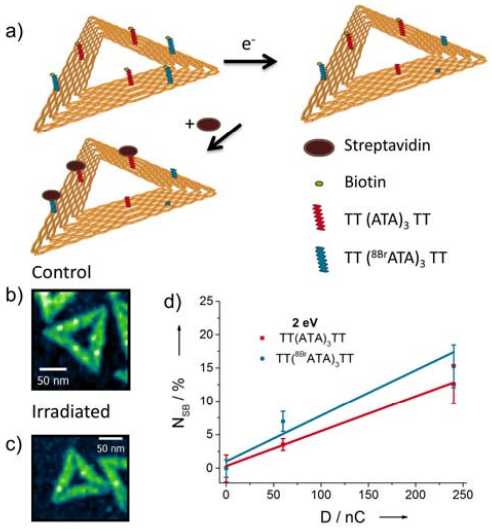

Figure 1. a) Principle of DNA strand break detection with DNA origami substrates; b) Example of an AFM image of a non-irradiated control sample; c) Example of an AFM image of a DNA origami sample irradiated with 7 eV electrons at a fluence of 0.53 x 10^{13} cm^{-2}; d) Relative number of SBs (N_{SB}) plotted against electron dose D at 2 eV. The SB cross section σ_{SB} is determined from the slope of the linear fit.

In Figure 2a σ_{SB} is plotted as a function of the electron energy for the two target strands $TT(ATA)_3TT$ and $TT(^{8Br}ATA)_3TT$. The strand break cross sections for both sequences exhibit a broad resonant structure centred around 7 eV. For all energies, σ_{SB} for the $TT(^{8Br}ATA)_3TT$ strand is higher than σ_{SB} for the unmodified sequence.

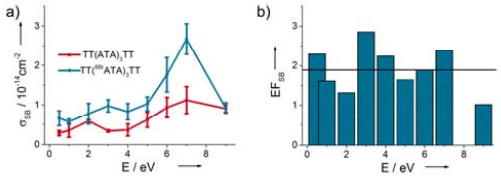

Figure 2. (a) SB cross sections as a function of the electron energy for the two target sequences. Solid lines connect the data points to guide the eye, (b) Strand break enhancement factors calculated from the data shown in a).

Strand break enhancement factors (EF_{SB}) are calculated as the ratio of the SB cross sections for modified and non-modified strands: $EF_{SB} = \sigma_{SB}(TT(^{8Br}ATA)_3TT) / \sigma_{SB}(TT(ATA)_3TT)$. The obtained values are plotted in Figure 2b against the electron energy, revealing an average EF_{SB} of 1.9 ± 0.6, which is one of the highest strand break enhancement factors reported for halogenated oligonucleotides so far.[6,9b,c] With oligonucleotides containing ^{2F}A ($TT(^{2F}AT^{2F}A)_3TT$) an EF_{SB} of 1.7 at 10 eV was found,[6] while 5-Bromouracil (^{5Br}U) gave rise to EF_{SB} = 1.2 (for $TT(A^{5Br}UA)_3TT$ at 18 eV) and EF_{SB} = 1.65 (for $TT(G^{5Br}UG)_3TT$ at 18 eV);[9b] and the highest EF_{SB} found for 5-Fluorouracil (^{5F}U) containing sequences was EF_{SB} = 1.65 ($TT(^{5F}UT^{5F}U)_3TT$ at 10 eV).[9c] Since ^{8Br}A is a good electron acceptor,[17] it acts as an antenna for the capture of electrons in DNA that subsequently can trigger a variety of fragmentation reactions in the DNA.

The fragmentation of all DNA subunits through DEA has been carefully studied in the gas phase.[15] In the energy regime around 7 eV all DNA subunits give rise to various resonant fragmentation pathways including multiple bond cleavages like in the formation of NCO^- in DEA to Thymine (T).[18] A remarkable electron induced reaction in this energy regime is the resonant C-O cleavage at the sugar moiety that corresponds to a SB, even though its overall intensity is relatively low.[19] These reactions are mediated by core excited resonances, in which the electron attachment is accompanied by an electronic excitation.

In order to understand the basic interactions of LEEs with ^{8Br}A and the potential initial steps of strand breakage, we have studied DEA to isolated ^{8Br}A in the gas phase. Figure 3 shows negative ion mass spectra of gaseous ^{8Br}A crossed with an electron beam of energy 0 eV and 6 eV, respectively. At 0 eV the main dissociation pathway is the cleavage of the C-Br bond, as the most abundant fragment anion is the bromide anion (79 and 81 Da). The corresponding anionic counterpart at 134 Da is relatively weakly formed.

The features in the energy-dependent σ_{SB} in Figure 2a at low energies are mainly within the error bars and might be also influenced by DEA to the Bt group.[20] Notably, the values of σ_{SB} of the modified strand are the lowest at energies ≤ 2 eV. At these electron energies an effective cleavage of the C-Br bond has been observed in DEA to isolated ^{8Br}A (see Fig. 3 and a more detailed discussion below).[21] The C-Br breakage is induced via shape resonances, where the electron temporally occupies a formerly empty molecular orbital.[2] In this way an adeninyl radical is

generated that is assumed to be a relevant precursor of the SB process.[11a] Nevertheless, a possible explanation for the minor σ_{SB} at such low energies is a competitive reaction channel initiated by an 8-adeninyl radical resulting in the formation of 5'desoxy 8,5' cyclo-adenosine that does not lead to a SB.[11a,22] Furthermore, the lifetimes of the shape resonances could be lower in the condensed phase than in the gas phase. This can suppress the DEA at low energies, similar to previous experiments, which showed only minor electron induced DNA damage below 4 eV.[1b,7b,23]

At 6 eV the bromide ion is still the most intense fragment even though the intensity drops by more than two orders of magnitude. Besides this exocyclic bond cleavage of the bromine and/or one hydrogen atom,[21] multiple bond cleavages are observed leading to the formation of fragments with 26, 65, 90, 92, 105 and 106 Da with an intensity comparable to DEA to A.[24] For all these anions, we have recorded ion yield curves, which are shown in Figure 4 and in Figure SI2 of the supporting information (SI). Here, we focus on the fragments formed in the energy region 5 eV to 9 eV, where also the strand breakage (Fig. 2a) follows a clear resonant process.

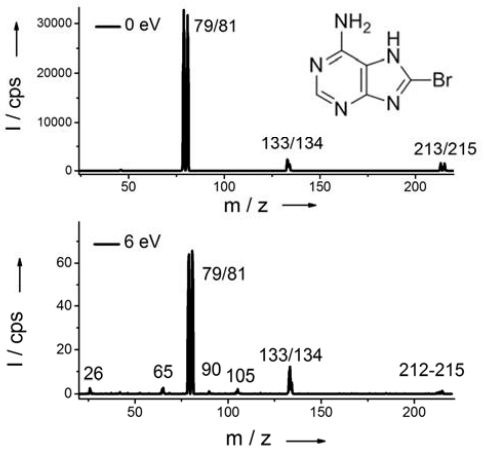

Figure 3. Negative ion mass spectra of gaseous ^{8Br}A crossed with 0 and 6 eV electrons.

The anion with a mass-to-charge ratio of 26 Da is assigned to CN^-, which is formed within at least three different resonances located at 2.0 eV, 5.8 eV and 7.1 eV (Figure 4a). It can be formed by excision from the aromatic purine ring of ^{8Br}A. Even though CN^- was also detected in DEA to A with a comparable yield, the particular resonant structures generating the anion by DEA to ^{8Br}A are more pronounced at electron energies below 5 eV.[24] In previous studies it was already demonstrated that CN^- is a central fragmentation product in DEA to organic molecules, which can be formed with high energy selectivity[25] and also within aqueous solutions by electrons released from gold nanoparticles.[26] The 65 Da fragment corresponds to $HC(CN)_2^-$ and is formed by the subtraction of the debrominated imidazole ring. It is created by a core excited resonance peaking at 5.0 eV that is shifted by 0.8 eV towards lower energies compared to A.[24] In a similar manner the 105 Da anion is generated within a resonance at 5.7 eV that is not observed for A.[24] The anion with a molecular mass of 90 Da exhibits two peaks at 2.3 eV and a broader at 5.2 eV, respectively, and is most probably due to $C_4N_3^-$.

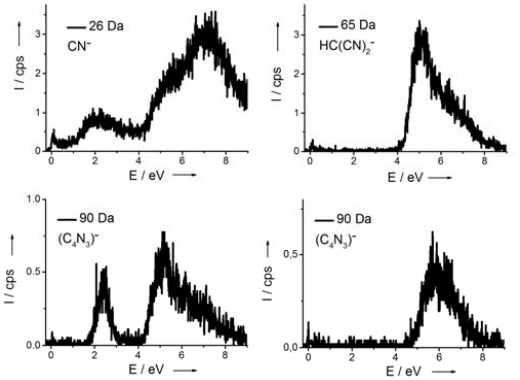

Figure 4. Ion yield of the 26, 65, 90 and 105 Da anionic fragments plotted as a function of the incident electron energy.

The similarity of the resonant profiles of the gas phase DEA products (Fig. 4) and the strand break cross sections in the condensed phase (Fig. 2a) indicate that the corresponding anion states located on ^{8Br}A can be precursors for SBs. The general enhancement of the SBs in the sensitized oligonucleotide over the whole electron energy range from 0.5 eV to 9 eV can be caused by a higher electron capture cross section of the ^{8Br}A bases. This allows for an increased electron transfer towards the sugar phosphate backbone leading to a SB in a secondary step and resulting in the observed average SB enhancement by a factor of 1.9 ± 0.6 for the sensitized sequence compared to the non-sensitized sequence over the whole energy range studied here. The lack of clear resonant features at low energies points to a minor role of the C-Br bond as a predetermined breaking point for the formation of SBs, as the cleavage of this bond is mainly observed within resonances below 2 eV in DEA to ^{8Br}A. On the other hand, it cannot be excluded that the electron partly loses its energy to the environment in a two-center process before it attaches to the DNA, which consequently leads to a shift of the low-energy resonance towards higher energies.[27]

In summary, the current study indicates that ^{8Br}A serves as an efficient radiosensitizer as the SB cross section is approximately doubled for oligonucleotides containing ^{8Br}A compared to non-modified ones over the whole energy range from 0.5 eV to 9 eV. A clear resonant structure of strand breakage is found with a maximum around 7 eV. Unexpectedly, no new resonances are observed in the sensitized oligonucleotides that are exclusive to ^{8Br}A. These observations shed new light on the relevant

processes leading to DNA strand breaks by LEEs and will have a clear impact on the search for potential DNA radiosensitizers for cancer radiation therapy.

Experimental Section

A detailed description of the experimental setup is given in the SI. Briefly, triangular DNA origami nanostructures were synthesized with an established protocol[6] based on the synthesis of P.W.K. Rothemund[28] and irradiated with an electron irradiator at Tata Institute of Fundamental Research, Mumbai, India which is described elsewhere in detail.[16] The negative ion mass spectrometry was performed with a crossed molecular electron beam setup equipped with a hemispherical electron monochromator with an energy resolution of around 120 meV.[24]

Acknowledgements

This research was supported by the Federal Institute for Materials Research and Testing (BAM), by a Marie Curie FP7 Integration Grant within the 7th European Union Framework Programme and by the Deutsche Forschungsgemeinschaft (DFG). R.S. acknowledges a travel grant to Innsbruck University by the European Union via the COST Action MP1002 (Nano-IBCT), and the Potsdam Graduate School for support for a travel to the Tata Institute for Fundamental Research (Mumbai). We thank Dr. Jenny Rackwitz for advice in preparation of DNA origami structures and analysis of AFM images and Ajit P. Ravishankar for quality checks of the irradiated samples via AFM imaging at the TIFR.

Keywords: DNA radiation damage • DNA origami • Cancer radiation therapy • Dissociative electron attachment • Radiosensitizer

[1] a) B. Boudaiffa, *Science* **2000**, *287*, 1658–1660, b) S.Kouass Sahbani, P. Cloutier, A. D. Bass, D. J. Hunting, L. Sanche, *J. Phys. Chem. Lett.* **2015**, *6*, 3911–3914.

[2] I. Bald, J. Langer, P. Tegeder, O. Ingólfsson, *Int. J. Mass Spectrom.* **2008**, *277*, 4–25.

[3] a) E. Alizadeh, T. M. Orlando, L. Sanche, *Annu. Rev. Phys. Chem.* **2015**, *66*, 379–398, b) S. V. K. Kumar, T. Pota, D. Peri, A. D. Dongre, B. J. Rao, *J. Chem. Phys.* **2012**, *137*, 045101.

[4] J. Kopyra, C. Koenig-Lehmann, I. Bald, E. Illenberger, *Angew. Chem. Int. Ed.* **2009**, *48*, 7904–7907.

[5] J. Kopyra, A. Keller, I. Bald, *RSC Adv.* **2014**, *4*, 6825.

[6] J. Rackwitz, J. Kopyra, I. Dąbkowska, K. Ebel, M. L. Ranković, A. R. Milosavljević, I. Bald, *Angew. Chem. Int. Ed.* **2016**, *55*, 10248–10252.

[7] a) Y. Zheng, D. J. Hunting, P. Ayotte, L. Sanche, *Phys. Rev. Lett.* **2008**, *100*, 198101. b) Q. Bao, Y. Chen, Y. Zheng, L. Sanche, *J. Phys. Chem. C* **2014**, *118*, 15516–15524.

[8] a) K. Westphal, K. Skotnicki, K. Bobrowski, J. Rak, *Org Biomol Chem* **2016**, *14*, 9331–9337, b) Y. Park, K. Polska, J. Rak, J. R. Wagner, L. Sanche, *J. Phys. Chem. B* **2012**, *116*, 9676–9682, c) Z. Li, P. Cloutier, L. Sanche, J. R. Wagner, *J. Phys. Chem. B* **2011**, *115*, 13668–13673.

[9] a) A. Keller, I. Bald, A. Rotaru, E. Cauët, K. V. Gothelf, F. Besenbacher, *ACS Nano* **2012**, *6*, 4392–4399, b) A. Keller, J. Rackwitz, E. Cauët, J. Liévin, T. Körzdörfer, A. Rotaru, K. V. Gothelf, F. Besenbacher, I. Bald, *Sci. Rep.* **2014**, *4*, 7391. c) J. Rackwitz, M. L. Ranković, A. R. Milosavljević, I. Bald, *Eur. Phys. J. D* 2017, *71*, 70608.

[10] H. Abdoul-Carime, M. A. Huels, F. Brüning, E. Illenberger, L. Sanche, *J. Chem. Phys.* **2000**, *113*, 2517.

[11] a) L. Chomicz, J. Leszczynski, J. Rak, *J. Phys. Chem. B* **2013**, *117*, 8681–8688, b) Ł. Golon, L. Chomicz, J. Rak, *Chem. Phys. Lett.* **2014**, *612*, 289–294, c) S. Makurat, L. Chomicz-Mańka, J. Rak, *ChemPhysChem* **2016**, *17*, 2572–2578.

[12] a) J. Kočišek, A. Pysanenko, M. Fárník, J. Fedor, *J. Phys. Chem. Lett.* **2016**, *7*, 3401–3405, b) M. McAllister, M. Smyth, B. Gu, G. A. Tribello, J. Kohanoff, *J. Phys. Chem. Lett.* **2015**, *6*, 3091–3097.

[13] a) J. Simons, *Acc. Chem. Res.* **2006**, *39*, 772–779, b) C.-R. Wang, J. Nguyen, Q.-B. Lu, *J. Am. Chem. Soc.* **2009**, *131*, 11320–11322, c) Y. Zheng, P. Cloutier, D. J. Hunting, L. Sanche, J. R. Wagner, *J. Am. Chem. Soc.* **2005**, *127*, 16592–16598.

[14] M. Wieczór, P. Wityk, J. Czub, L. Chomicz, J. Rak, *Chem. Phys. Lett.* **2014**, *595–596*, 133–137.

[15] I. Baccarelli, I. Bald, F. A. Gianturco, E. Illenberger, J. Kopyra, *Phys. Rep.* **2011**, *508*, 1–44.

[16] S. V. K. Kumar, S. T. Tare, Y. V. Upalekar, T. Tsering, *Rev. Sci. Instrum.* **2016**, *87*, 034302.

[17] A. Manetto, S. Breeger, C. Chatgilialoglu, T. Carell, *Angew. Chem. Int. Ed.* **2006**, *45*, 318–321.

[18] F. F. da Silva, C. Matias, D. Almeida, G. García, O. Ingólfsson, H. D. Flosadóttir, B. Ómarsson, S. Ptasinska, B. Puschnigg, P. Scheier, et al., *J. Am. Soc. Mass Spectrom.* **2013**, *24*, 1787–1797.

[19] a) C. König, J. Kopyra, I. Bald, E. Illenberger, *Phys. Rev. Lett.* **2006**, *97*, 018105, b) I. Baccarelli, F. A. Gianturco, A. Grandi, N. Sanna, R. R. Lucchese, I. Bald, J. Kopyra, E. Illenberger, *J. Am. Chem. Soc.* **2007**, *129*, 6269–6277.

[20] A. Keller, J. Kopyra, K. V. Gothelf, I. Bald, *New J. Phys.* **2013**, *15*, 083045.

[21] a) R. Schürmann, K. Tanzer, I. Dabkowska, S. P. Denifl, I. Bald, *J. Phys. Chem. B* **2017**, DOI 10.1021/acs.jpcb.7b02130., b) R. Schürmann, I. Bald, *Nanoscale* **2017**, *9*, 1951–1955.

[22] a) L. B. Jimenez, S. Encinas, M. A. Miranda, M. L. Navacchia, C. Chatgilialoglu, *Photochem Photobiol Sci* **2004**, *3*, 1042–1046, b) C. Chatgilialoglu, M. Guerra, Q. G. Mulazzani, *J. Am. Chem. Soc.* **2003**, *125*, 3839–3848.

[23] X. Luo, Y. Zheng, L. Sanche, *J. Chem. Phys.* **2014**, *140*, 155101.

[24] D. Huber, M. Beikircher, S. Denifl, F. Zappa, S. Matejcik, A. Bacher, V. Grill, T. D. Märk, P. Scheier, *J. Chem. Phys.* **2006**, *125*, 084304.

[25] I. Bald, I. Dąbkowska, E. Illenberger, O. Ingólfsson, *Phys Chem Chem Phys* **2007**, *9*, 2983–2990.

[26] R. Schürmann, I. Bald, *J. Phys. Chem. C* **2016**, *120*, 3001–3009

[27] J. Lengyel, J. Kočišek, M. Fárník, J. Fedor, *J. Phys. Chem. C* **2016**, *120*, 7397–7402.

[28] P. W. K. Rothemund, *Nature* **2006**, *440*, 297–302.

Resonant formation of strand breaks in sensitized oligonucleotides induced by low-energy electrons (0.5 – 9 eV)

Robin Schürmann [a,b], Thupten Tsering [c], Katrin Tanzer [d], Stephan Denifl [d], S.V.K. Kumar [c], and Ilko Bald*[a,b]

[a] Department of Chemistry—Physical Chemistry, University of Potsdam, Karl-Liebknecht-Strasse 24-25, D-14476 Potsdam-Golm, Germany
[b] Department 1—Analytical Chemistry and Reference Materials, BAM Federal Institute for Materials Research and Testing, Richard-Willstätter Str.11, 12489 Berlin, Germany
[c] Tata Institute of Fundamental Research, Homi Bhabha Road, Colaba Mumbai 400 005, India
[d] Institute of Ion Physics and Applied Physics, University of Innsbruck, Technikerstrasse 25, A-6020 Innsbruck, Austria

*Corresponding Author: ilko.bald@uni-potsdam.de

Supporting Information

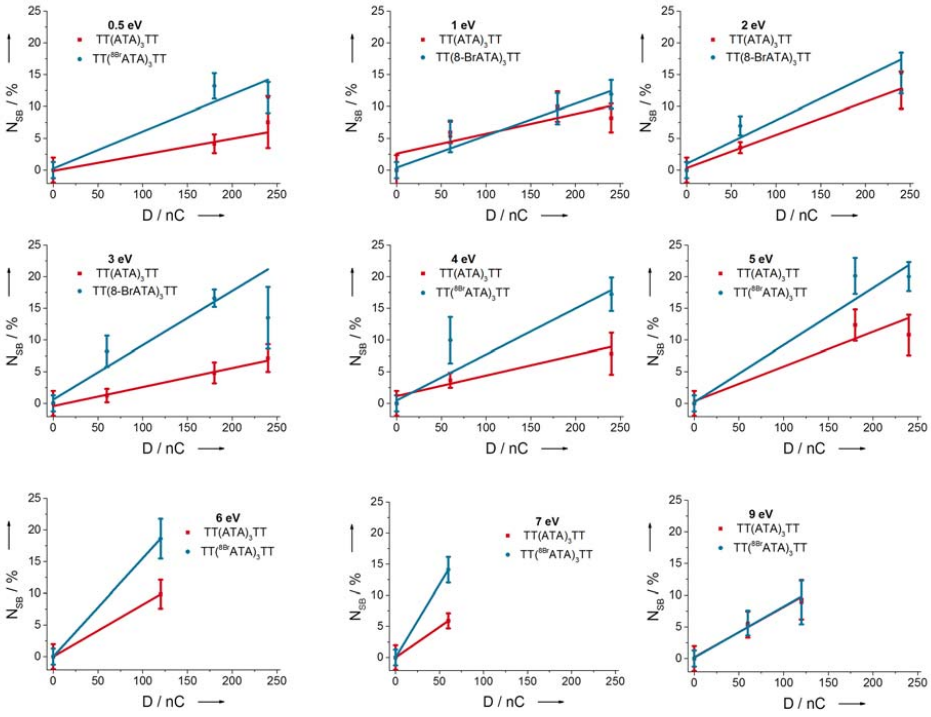

Figure S1: Exposure-damage curves for energies between 0.5 and 9 eV. SB cross section was determined from the linear fit of the data.

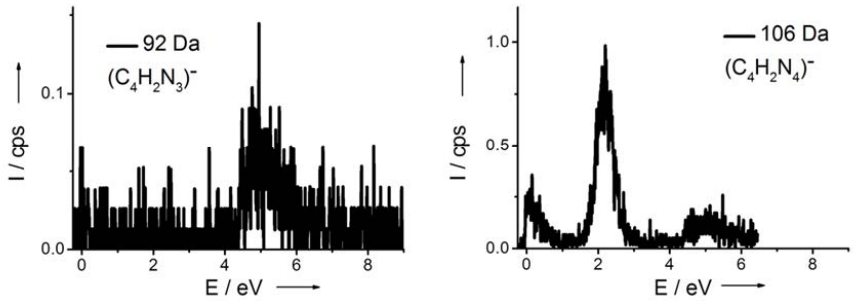

Figure S2: Ion yield of the fragments with a mass of 92 Da and 106 Da plotted as a function of the electron energy.

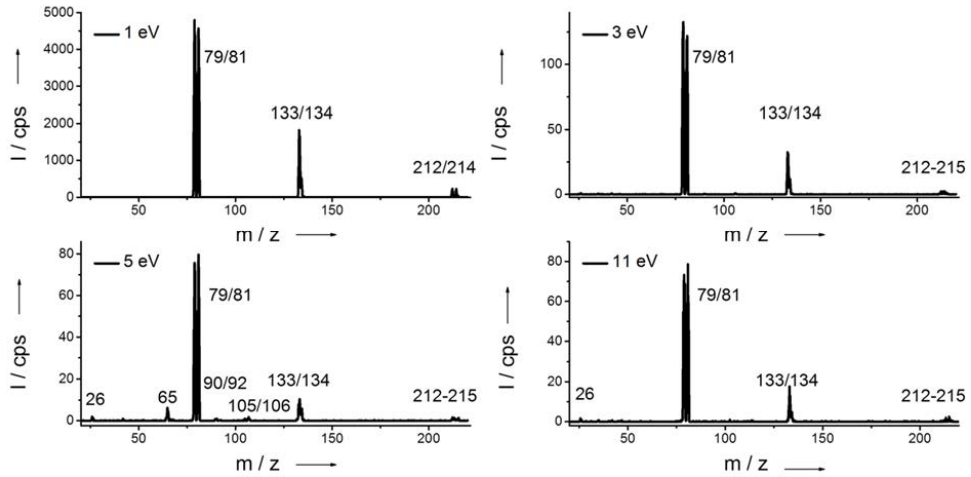

Figure S3: Negative Ion mass spectra of ^{8Br}A taken at electron energies between 1 eV and 11 eV.

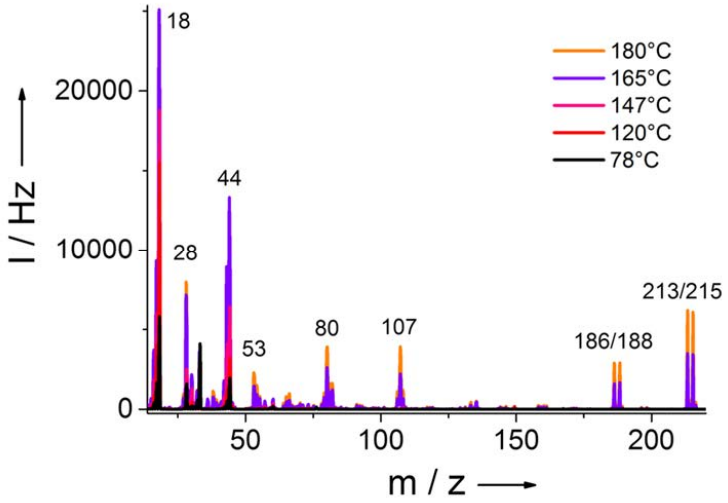

Figure S4: Positive Ion mass spectra of ^{8Br}A taken at electron energies of 70 eV at different temperatures.

Experimental

DNA origami structures:

The synthesis of the DNA origami structures was based on the protocol of P.W.K Rothemund for triangular nanostructures[1]. Therefore circular single stranded M13mp18 virus DNA (5 nM) with a known sequence of 7249 nucleobases was used as a scaffold. Furthermore, 208 short oligonucleotides were added in a 30 fold excess to staple the scaffold into the desired shape. At the positions t1s-4i, t1s-14i and t1s-24i on the origami, the staple strand was prolonged at the 5' end by the sequence $TT(ATA)_3TT$ with a biotin (Bt) group at the end, whereas at the positions T-5s8g, T-5s18g and T5s28g a Bt labeled $TT(^{8Br}ATA)_3TT$ sequence is attached. The mixture was in 1x TAE buffer containing 20mM $MgCl_2$. In order to form the nanostructures by self-assembly, the solution was heated in a water bath to 95°C and cooled down to room temperature overnight. For purification of the origami the excess staple strands were removed by two rounds of spin filtering using a 100 kDa Millipore filter.

The DNA origami structures were immobilized on Si substrates that were cleaned previously in an O_2-plasma and rinsed with ethanol:H_2O (1:1). 0.8 µl of the origami solution and 20 µl 10x TAE + 200 mM $MgCl_2$ were incubated for 60 min on the wafer, subsequently rinsed with 1 ml EtOH:H_2O and placed for another 60 minutes in absolute ethanol. Afterwards the sample was dried with nitrogen gas and irradiated in the UHV chamber. In order to bind streptavidin (SAv) to the intact target strands, the irradiated samples were incubated with 15 µl SAv (50 nM) diluted in 1x TAE buffer with 20 mM $MgCl_2$ for 2 minutes and subsequently rinsed with 0.5 ml EtOH:H_2O (1:1) and dried with nitrogen .

Electron irradiation:

The irradiation of the DNA origami structures was performed in a custom build electron irradiator that is described elsewhere in detail [2]. In the sample holder eight samples were placed, whereas seven

were irradiated and one serves as a reference for each set. Additionally one more sample was prepared under the same condition but it was not transferred into the vacuum chamber and used as external control. The irradiator is a pierce type electron gun inside a UHV-chamber operated at a pressure of 10^{-8} Torr. Before the irradiation was started, the current was set to approximately 1 nA and stabilized manually. The dose was precisely controlled by a software and chosen between 60 and 240 nC. A protective cover with an aperture of 3 mm defined the irradiated area.

AFM:

The atomic force microscopy (AFM) imaging of the DNA origami structures was performed with an Agilent 5500 AFM in the tapping mode using Tap 150 Al-G soft tapping cantilevers. For each sample at 4 positions images were taken that located around 400 µm away from the irradiation center. The intact strands of 500 – 1000 origamis were counted to determine the SB yield. The SB yield of each irradiated sample were subtracted by the SB yield of the unirradiated control sample and the error bars are given by the standard deviation of the 4 positions. For the subsequent analysis of the AFM images the software Gwyddion 2.34 was used.

Negative Ion Mass Spectrometry

The dissociative electron attachment (DEA) experiments were performed in a crossed molecular-electron beam setup that was described previously in detail[3]. The electron beam was generated in a hemispherical electron monochromator with an energy resolution of around 120 meV that was determined by the full width half maximum of the 0 eV resonance in the Cl- generation by DEA to tetrachloromethane:

$CCl_4 + e^- \rightarrow CCl_4^{\#-} \rightarrow CCl_3 + Cl^-$

In order to generate the molecular beam, solid ^{8Br}A was heated to 450 K in a copper oven that is connected to a capillary. The anions formed by the collision of the two beams are mass filtered by a quadrupole and detected with a channeltron.

[1] P. W. K. Rothemund, *Nature* **2006**, *440*, 297–302.
[2] S. V. K. Kumar, S. T. Tare, Y. V. Upalekar, T. Tsering, *Rev. Sci. Instrum.* **2016**, *87*, 034302.
[3] S. Denifl, S. Ptasińska, G. Hanel, B. Gstir, M. Probst, P. Scheier, T. D. Märk, *J. Chem. Phys.* **2004**, *120*, 6557–6565.

4.3 M3: "Decomposition of DNA Nucleobases by Laser Irradiation of Gold Nanoparticles Monitored by Surface-Enhanced Raman Scattering"

Robin Schürmann and Ilko Bald
J. Phys. Chem. C, 2016, 120 (5), pp 3001 - 3009
DOI: 10.1021/acs.jpcc.5b10564

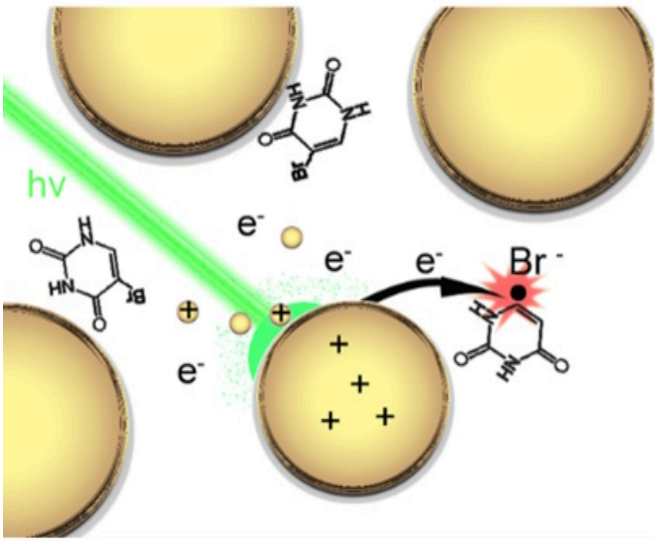

Author contributions to the manuscript:
I synthesized the AuNPs and AgNPs and did all further experimental preparations. I conducted all irradiations of the AuNPs/NBs mixtures. I performed all UV-Vis spectroscopy and SERS measurement and analyzed the spectra. I prepared all figures for the manuscript and the supporting info. I prepared the manuscript in cooperation with Ilko Bald.

THE JOURNAL OF PHYSICAL CHEMISTRY C

Article

pubs.acs.org/JPCC

Decomposition of DNA Nucleobases by Laser Irradiation of Gold Nanoparticles Monitored by Surface-Enhanced Raman Scattering

Robin Schürmann[†,‡] and Ilko Bald*[,†,‡]

[†]Institute of Chemistry − Physical Chemistry, University of Potsdam, Potsdam, Germany

[‡]BAM Federal Institute for Materials Research and Testing, Berlin, Germany

Supporting Information

ABSTRACT: Different approaches have been proposed to treat cancer cells using gold nanoparticles (AuNPs) in combination with radiation ranging from infrared lasers to high-energy ion beams. Here we study the decomposition of the DNA/RNA nucleobases thymine (T) and uracil (U) and the well-known radiosensitizer 5-bromouracil (BrU) in close vicinity to AuNPs, which are irradiated with a nanosecond pulsed laser (532 nm) matching the surface plasmon resonance of the AuNPs. The induced damage of nucleobases is analyzed by UV−vis absorption spectroscopy and surface-enhanced Raman scattering (SERS). A clear DNA damage is observed upon laser irradiation. SERS spectra indicate the fragmentation of the aromatic ring system of T and U as the dominant form of damage, whereas with BrU mainly the cleavage of the Br−C bond and formation of Br^- ions is observed. This is accompanied by a partial transformation of BrU into U. The observed damage is at least partly ascribed to the intermediate formation of low-energy electrons from the laser-excited AuNPs and subsequent dissociative electron attachment to T, U, and BrU. These reactions represent basic DNA damage pathways occurring on the one hand in plasmon-assisted cancer therapy and on the other hand in conventional cancer radiation therapy using AuNPs as sensitizing agents.

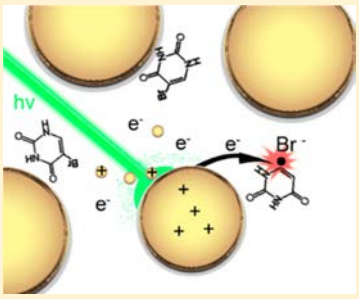

INTRODUCTION

The excitation of the surface plasmon resonance (SPR) of Au and Ag nanostructures leads to collective oscillations of free electrons in the metal resulting in high electromagnetic fields close to the metal surface. Depending on the irradiation conditions, the SPR excitation can be accompanied by an elevated temperature at the nanoparticle (NP) surface[1] and the release or transfer of electrons from the nanoparticle to the surrounding medium.[2−4] In this way the material in close vicinity of the NP is modified, which is for instance exploited in the targeted decomposition of biological materials[5,6] and the optical processing of organic materials with high local precision (depending only on the dimensions of the nanostructures).[7−9] A prominent example of plasmon supported cell damage is the irradiation of gold shell nanoparticles with continuous wave near-infrared lasers as a novel type of cancer therapy.[10,11]

The decomposition of biological material in the vicinity of irradiated NPs can be ascribed to the generation of reactive photoelectrons upon irradiation with nanosecond (ns) pulsed lasers and/or to a thermal effect.[2,12] When ns laser pulses are used, photoelectrons are ejected by thermionic emission due to the rapid relaxation of photoexcited AuNPs to the electronic ground state.[2] In this way vibrational energy is accumulated before it is lost to the environment, resulting in a temperature rise of the AuNP and a thermal ejection of electrons. Previously, it was demonstrated that the NP heating and thus the yield of solvated electrons correlates with the interband transition in absorption spectra and not with the surface plasmon resonance (SPR).[2,12] Taking the lower work function of AuNPs compared to bulk Au into account (3.6 eV for 10 nm AuNPs),[13] two photons of a 532 nm laser (2.33 eV) are sufficient to ionize the AuNP. However, direct multiphoton ionization is only possible with laser pulses that are shorter than the radiationless decay of excited states, which is in the femtosecond (fs) regime.

In aqueous solutions the thermionic electron emission readily produces solvated electrons, which can be detected by transient absorption spectroscopy.[12] However, prior to complete solvation, the electrons in aqueous solution are in a prehydrated state within the first 0.5 ns after generation.[14] The prehydrated electrons are considerably more reactive than solvated electrons due to their lower binding energy.[14] Nevertheless, both prehydrated and hydrated electrons can directly react with biomolecules such as DNA nucleobases by formation of transient negative ions, which can quickly dissociate.[15] This bond breaking mechanism is referred to as dissociative electron attachment (DEA)[16] and represents a highly efficient way for the decomposition of molecules that is relevant for various processes such as nanolithography[17] and DNA radiation damage.[18] Low-energy electrons (LEEs) belong

Received: October 28, 2015
Revised: January 20, 2016
Published: January 20, 2016

DOI: 10.1021/acs.jpcc.5b10564
J. Phys. Chem. C 2016, 120, 3001−3009

The Journal of Physical Chemistry C Article

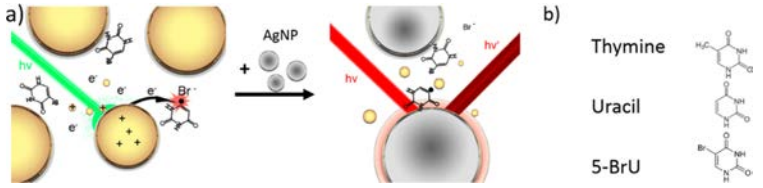

Figure 1. (a) Illustration of the experimental strategy to study the decomposition of DNA model compounds by laser irradiation of AuNPs. In a first step a green laser (532 nm) is used to excite the SPR of the AuNPs and to release photoelectrons. The damaged DNA bases are detected after addition of AgNPs by SERS using a red continuous laser (633 nm). (b) Molecular structures of the investigated compounds.

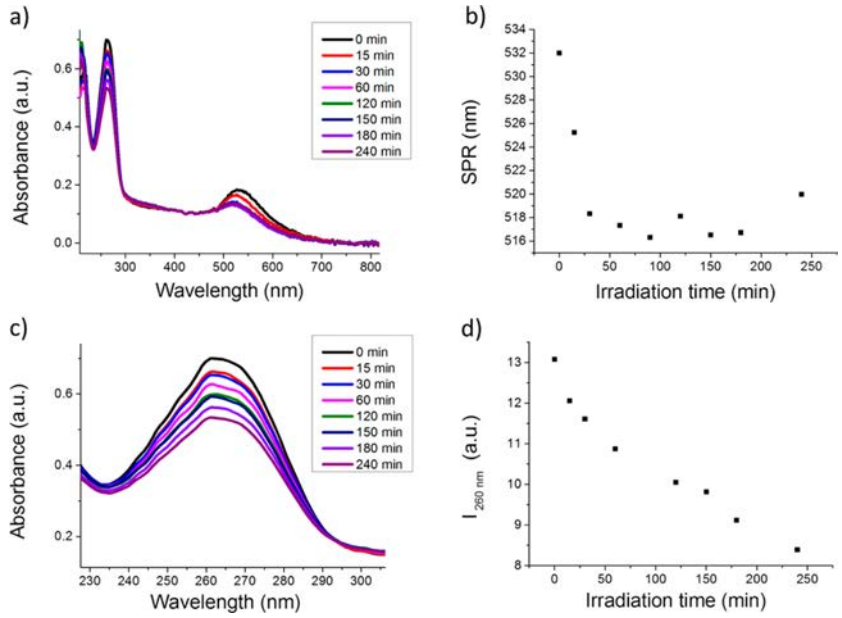

Figure 2. UV−vis absorption spectra of thymine. The absorption spectra are dominated by the absorption of thymine at 260 nm and the SPR of AuNPs around 520 nm. The intensity of the SPR band decreases upon laser irradiation and shows a slight shift toward lower wavelengths. This indicates that the AuNPs decrease in size due to Coulomb explosion. The absorption band of thymine also decreases with irradiation time indicating a decomposition of the ring structure.

to the most important intermediates in radiation damage to DNA.[18,19] Since free LEEs are produced by irradiation of gold nanoparticles (AuNPs) with X-rays or γ-rays,[20,21] AuNPs are proposed as a novel therapeutic in radiation cancer therapy to increase the local LEE dose in tumor tissue.[22,23]

To unravel the fundamental mechanisms of DNA radiation damage, the interaction of LEEs with simple model compounds (such as nucleobases and nucleosides) has been studied in great detail during the past years.[18] It was found that LEEs effectively decompose all DNA compounds at specific (resonant) electron energies due to the formation of characteristic anion resonances. But as a central challenge, the question remains whether the mechanisms developed on the basis of such model compounds under extreme conditions such as gas or condensed phase in ultrahigh vacuum can reflect a situation in a real biological environment. Especially the role of more complex DNA structures[24−26] and the role of an aqueous solution in electron induced DNA damage are currently studied in detail.[27,28]

In the present work the decomposition of the DNA nucleobase thymine (T), the RNA base uracil (U), and the well-known radiosensitizer 5-bromouracil (BrU) in aqueous solution in the presence of AuNPs upon irradiation with pulsed laser light at 532 nm is studied. The decomposition of the DNA model compounds is followed by UV−vis absorption spectroscopy, and the fragmentation products are detected by surface-enhanced Raman scattering (SERS). SERS represents a highly sensitive analytical technique, which yields a characteristic vibrational fingerprint of the compounds present in close vicinity to noble metal nanoparticles (NPs).[29] The Raman scattering is enhanced by several orders of magnitude through excitation of the SPR of the NPs, and thus also small amounts of sample can be detected and reactions be observed.[30]

The purpose of the present work is to develop a better understanding of DNA damage close to plasmon excited AuNPs and to compare the observed damage with LEE induced DNA damage typically studied in dry conditions.

DOI: 10.1021/acs.jpcc.5b10564
J. Phys. Chem. C 2016, 120, 3001−3009

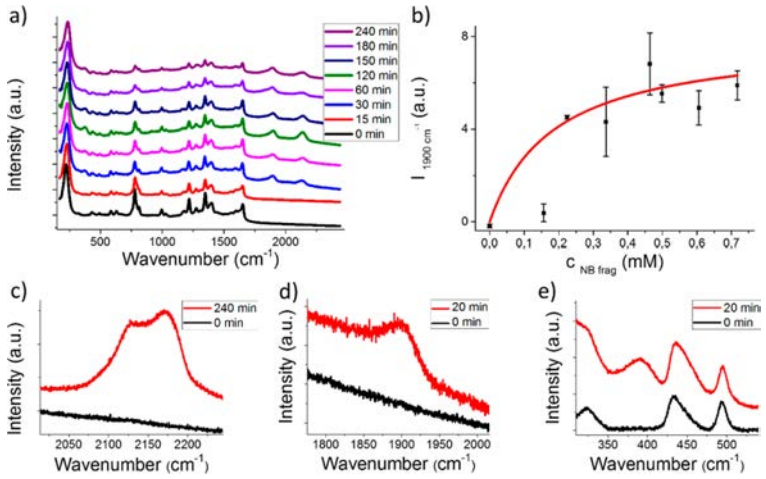

Figure 3. SERS spectra of thymine. The most prominent feature upon laser irradiation is the appearance of new bands at 380, 1900, and 2140 cm^{-1}.

Table 1. Assignment of SERS Bands Observed in the Present Experiment and Comparison to Values Reported Previously

thymine	description[46]	uracil	description[44]	BrU	description[37]
1648	ν(C═O) + δ(N−H, C−H)	1629	ν(C2═O) + ν(C4═O), δ(N1−H)	1637	ν(C2═O)
1602				1625	ν(C4═O)
1560		1393	δ(C6−H, N1−H, C5−H)	1562	ν(C5═C6)
1394	δ(N−H)	1370	δ(N3−H, C5−H, C6−H) + ν(C2−N3)	1396	ν(ring) + δ(N1−H)
1348	δ(N−H, C−H)	1276	ν(N3−C4(−C4C5− C6N1), δ(N1−H, C5−H, C6−H)	1326	δ(C6−H) + ν(ring)
1276		1209	δ(N1−H, C6−H, C5−H) + ν(C6−N1)	1276	δ(N1−H, C6−H) + ν(ring)
1217	ν(C−N)	1101	δ(C5−H, C6−H) + ν(C5═C6, C6−N1)	1180	δ(N1−H, C6−H) + ν(ring)
1178		1047	ν(ring)	1071	ν(ring)
1029				1024	δ(N3−H, C6−H) + ν(C−N)
996	ring breathing + $\nu(CH_3)$	800	ring breathing	798	ring breathing
808		598	δ(ring)	683	
779	δ(C6−H) + ν(C5═C6)	562	δ(ring)	653	δ(ring) + v(C−Br)
630				621	
586		441	δ(C2═O, C4═O)	577	δ(ring) + δ(CO)
491				434	δ(CO) + δ(ring)
434				346	γ(C−H) + γ(ring)
				291	δ(C−Br) + δ(ring)

RESULTS AND DISCUSSION

The nucleobases T, U, and BrU have been used as DNA model compounds and have been mixed with Au colloids and irradiated with a pulsed Nd:YAG laser at 532 nm for up to 240 min while stirring the solution (see Experimental Section for details). After a specific irradiation time some sample is removed and subjected to further analysis by either UV−vis absorption or SERS spectroscopy. For the SERS analysis, AgNPs are added to the separated part of the solution to obtain a sufficient SERS enhancement. The AgNPs are required since the irradiated AuNPs are too small to provide sufficient SERS signal. The experimental approach is illustrated in Figure 1.

Thymine and Uracil. UV−vis absorption spectra of irradiated T + AuNP solutions are shown in Figure 2a and are dominated by two absorption bands located at 520 and 260 nm, respectively. The signal at 520 nm is due to the SPR of Au, and its intensity decreases rapidly when the laser irradiation is started and remains rather constant after around 25 min. The intensity drop is accompanied by a slight blue-shift of the SPR band, which is plotted in Figure 2b as a function of irradiation time. The blue-shift is due to the coulomb explosion of the AuNPs upon irradiation with the 532 nm laser pulses as a consequence of the accumulation of positive charge upon multiple ionization. This leads to a decrease of the AuNP diameter, which is accompanied by a decrease of the extinction coefficient.[31]

The absorption band at 260 nm is due to the lowest π−π^* transition in T. The intensity of the band decreases almost linearly with irradiation time indicating the decomposition of the T bases (see Figure 2c for a zoom-in of the absorption band and Figure 2d for a plot of the intensity vs irradiation time) and a constant rate of product formation.

The nucleobases in solution can be decomposed (i) by released photoelectrons through the DEA mechanism and (ii) thermally due to a short-term temperature rise in close proximity to the nucleobases. The linear intensity drop of the absorption band of T does not correspond to the time evolution of the SPR band. Nevertheless, it must be noted that

DOI: 10.1021/acs.jpcc.5b10564
J. Phys. Chem. C 2016, 120, 3001−3009

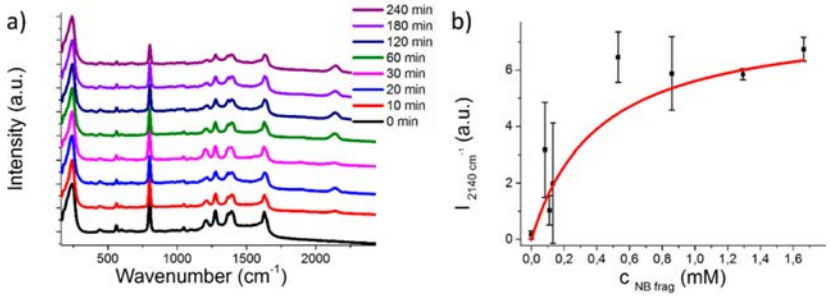

Figure 4. SERS spectra of uracil. The intensity is normalized to the Ag vibration at around 240 cm^{-1}. Upon laser irradiation the SERS spectra of uracil change in a similar manner as for thymine; i.e., new bands arise at 2140, 1900, and 380 cm^{-1}. The signal at 2140 cm^{-1} is assigned to the CN stretch vibration, and the intensity of the band at 2140 cm^{-1} increases according to a Langmuir isotherm with irradiation time. The band at 380 cm^{-1} is assigned to CO/CN or other C binding to Ag.

the formation of solvated electrons does not correspond to the SPR excitation but to the interband excitation of gold,[2] which can still occur in smaller AuNPs with less pronounced SPR band.

The UV−vis spectra of the U + AuNP system are very similar to the ones obtained from T (Figure 2) and are shown in the Supporting Information (Figure S1).

More specific chemical information about fragmentation products can be obtained from SERS spectra, which are shown in Figure 3 for laser-irradiated solutions containing AuNPs and T. The black spectrum was obtained from a nonirradiated sample, and the other spectra were obtained from samples irradiated for 15−240 min with a pulsed laser at 532 nm. The appearance of new Raman bands at 2100−2200, 1900, and 379 cm^{-1} can be clearly observed (see high-resolution scans in Figure 3c−e and Table 1 for a summary of observed SERS bands and their assignment), indicating the formation of decomposition products. A new band appears with low intensity, but clearly recognizable at 1295 cm^{-1}. A zoom-in is shown in the Supporting Information (Figure S2). The signal at 2100−2200 cm^{-1} consists of two contributions located at 2140 and 2172 cm^{-1}, which are assigned to C≡N stretch vibrations arising most likely from CN^- ions or CN containing fragments formed by decomposition of the ring structure. The band at 2170 cm^{-1} might also be assigned to the OCN^- ion that is typically accompanied by signals at 1207 and 1300 cm^{-1}, the former being overlapped by the thymine signal at 1217 cm^{-1}. From gas phase DEA studies of T[32] and U[33] it is well-known that electron attachment to T and U results in a decomposition of the aromatic ring structure, and CN^- is an important decomposition product:[34]

$$T/U + e^- \rightarrow T^{\#-}/U^{\#-} \rightarrow CN^- + \text{other fragments} \quad (1)$$

In the DEA process the electron occupies a formerly empty molecular orbital (MO) to form a transient negative anion (denoted as $T^{\#-}/U^{\#-}$). Because of the antibonding nature of the MO, the anionic state is typically repulsive and the transient anion is unstable toward dissociation. In this way even complex dissociation reactions with multiple bond breakings is possible at rather low electron energies below 2 eV,[34,35] which is reasonable to assume for the electrons created under the present conditions.

The thermodynamics of low-energy electron induced reactions especially in complex systems (including the environment in the present case) is not straightforward and different aspects play a role. The formation of CN containing fragments from gas phase T subsequent to electron attachment was extensively studied by Ferreira da Silva et al.[36] Accordingly, the thermodynamic threshold of e.g. metastable NCO^- formation was found to be below 2 eV. The thermodynamic threshold depends strongly on the specific other products formed during the process. In several studies it was demonstrated that the thermodynamic threshold of e.g. CN^- can be significantly reduced (even down to almost 0 eV) through the formation of stable neutral products.[37,38] Furthermore, the comparison with gas phase data is not sufficient, and it must be taken into account that the present experiments are performed in condensed phase, in which additional reaction channels can be operative. Since we are working in an aqueous solution, hydration of ions and other reaction products might be the most important contribution. For the CN^- ion a stabilization of 2.0 eV upon solvation was determined by photoelectron spectroscopy and *ab initio* calculations.[39] Thus, the formation of CN containing fragments by electron attachment in aqueous solution can be rendered thermoneutral or even exothermal.

The energy distribution of thermionic electrons released from gold nanoparticles upon laser irradiation was previously determined to be on average 1 eV for 355 nm irradiation (0.5 ns pulse width and 7.2 J cm^{-2} peak energy).[40] Thus, the ring cleavage observed in the present experiment can basically be explained by an electron-induced reaction. According to the above-mentioned considerations, this is thermodynamically easily possible before the photoelectrons are partly solvated. From the presolvated state the reaction requires the formation of stable (and hydrated) byproducts.

The appearance of multiple signals at 2100−2200 and at 1900 cm^{-1} suggests that a variety of fragments containing CN bonds or cumulated dienes, respectively, is formed.

Furthermore, a new band is observed in the low-wavenumber region at 379 cm^{-1}. This band is assigned to a Ag−CN vibration due to the reaction of CN containing fragments binding to the Ag colloid.[41]

The signal intensity (I) of the band at 1900 cm^{-1} is plotted vs the concentration of fragmented nucleobase in Figure 3d. The concentration was calculated from the peak intensity of the 260 nm absorption band in the UV−vis spectra. As we expect that only the first layer of the adsorbed molecules on the AgNPs contributes to the SERS signal, the data are fitted with a Langmuir isotherm using the equation

DOI: 10.1021/acs.jpcc.5b10564
J. Phys. Chem. C 2016, 120, 3001−3009

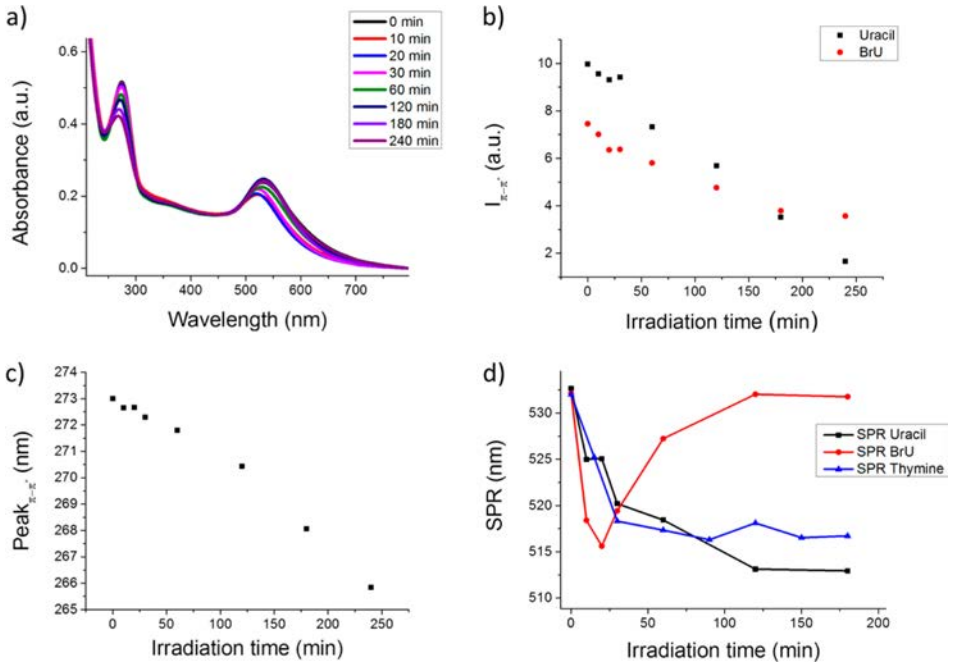

Figure 5. Absorption spectra of BrU before and after laser irradiation. The absorption at 260 nm decreases after irradiation. The SPR band is first (after starting the irradiation) shifted to lower wavelength due to Coulomb explosion. However, after longer exposure times the SPR band is again shifted to longer wavelength, which is attributed to the generation of aggregates due to the increasing concentration of Br^- ions.

$$I = \frac{K_L I_{max} c_{NBfrag}}{1 + K_L c_{NBfrag}} \quad (2)$$

with K_L being the Langmuir sorption coefficient.

Figure 4 shows the SERS spectra of U + AuNP upon irradiation with laser pulses of green light, which show similar characteristics as the SERS spectra of T (see Table 1). The appearance of an intense band at 2140 cm^{-1} is clearly visible in Figure 4a. This signal is due to the generation of C≡N containing fragments, which can be generated by the reaction of photoelectrons with U.[33] The signal intensity increases with irradiation time according to a Langmuir isotherm, and saturation is reached at irradiation times longer than 100 min (Figure 4b).

The fragmentation pathway appears to be slightly different in U compared to T since in the SERS measurements with U the signal at 2140 cm^{-1} clearly dominates the spectral region of 1800−2300 cm^{-1}, and in contrast to T only a weak contribution appears at 1900 cm^{-1} (see Supporting Information). Furthermore, the signal at 1295 cm^{-1} could not be observed.

5-Bromouracil. BrU is a well-known radiosensitizer inducing enhanced DNA strand breakage[26] due to its high reactivity with LEEs especially at very low energies close to 0 eV.[42]

UV−vis spectra of irradiated solutions of BrU and AuNPs are shown in Figure 5. The absorption band of BrU has a maximum at 273 nm, and upon laser irradiation the intensity drops and at the same time the absorption maximum shifts to shorter wavelengths. As is illustrated in Figure 5b, the intensity drop of the BrU absorption band is less pronounced than in the case of U, indicating a stronger decomposition of the aromatic ring structure of U compared to BrU. The shift of the absorption maximum (Figure 5c) suggests a chemical transformation of BrU while maintaining the aromatic structure. Since the absorption maximum of U is at lower wavelength (λ_{abs} = 260 nm) than the absorption maximum of BrU (λ_{abs} = 273 nm), a partial transformation of BrU into U can be assumed (which is further discussed below using SERS spectra).

The peak maximum of the SPR band at 520 nm also initially shifts to shorter wavelengths accompanied by an intensity drop due to Coulomb explosion after starting the laser irradiation (Figure 5d). However, after 20 min the peak maximum of the SPR band shifts again to longer wavelengths and the intensity increases again, indicating the formation AuNP aggregates (Figure 5d). The formation of AuNP aggregates can be induced by halogen anions, and it is likely that the observed shift and intensity change of the SPR band are due to the formation of Br^- ions upon laser irradiation. The Br^- ions can be formed by electron attachment to BrU according to the following equations:

$$h\nu + \text{AuNP} \rightarrow \text{AuNP}^{n+} + ne^- \quad (3)$$

$$e^- + \text{BrU} \rightarrow \text{BrU}^{\#-} \rightarrow Br^- + \text{U} \quad (4)$$

$BrU^{\#-}$ indicates again the transient negative ion, which can be formed with very high efficiency by attachment of electrons close to 0 eV.[42] The molecular anion relaxes by dissociation and a stable Br^- anion is formed along with a reactive neutral radical $U^{\bullet}$.

DOI: 10.1021/acs.jpcc.5b10564
J. Phys. Chem. C 2016, 120, 3001−3009

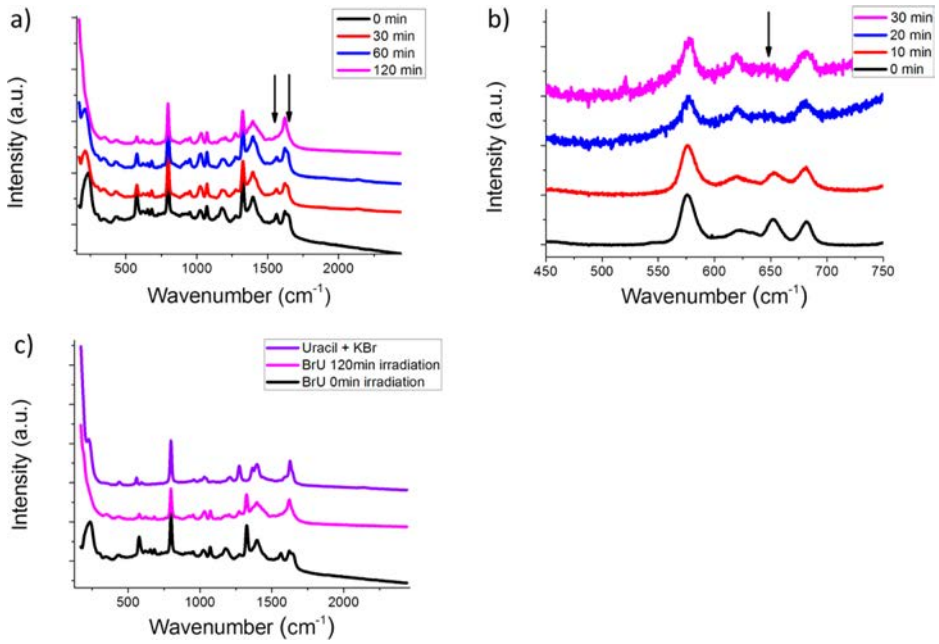

Figure 6. SERS spectra of bromouracil. The SERS signals change in a different way upon irradiation compared to thymine and uracil. Most remarkably, the signal at 2140 cm^{-1} is recognizable, but with only very low intensities. Instead, a clear new band arises below 180 cm^{-1} due to AgBr, and the bands at 550−750 cm^{-1} change significantly, indicating the cleavage of the C−Br bond.

The SERS spectra of BrU upon laser irradiation in the presence of AuNPs are displayed in Figure 6, and band assignments are collected in Table 1. The change of SERS signals upon laser irradiation are remarkably different compared to T and U. In contrast to U and T, irradiation of BrU results only in a very weak signal at 2140 cm^{-1}, indicating a considerably smaller amount of ring fragmentation reactions involving products with CN groups.

Instead, the cleavage of the Br−C bond is directly visible in the SERS spectra. The band at 1561 cm^{-1} can be assigned to the stretching vibration of the C═C double bond (C5═C6),[43] which only appears with high intensity when Br is present at C5. In U only a weak shoulder is present at this spectral position.[44] The intensity of the band at 1561 cm^{-1} drops and is completely vanished after about 2 h of irradiation. The same applies to a band that appears as a shoulder around 1650 cm^{-1} (see arrows in Figure 6a) and to a series of vibrational bands at 550−700 cm^{-1}, the intensity of which drops clearly upon irradiation (Figure 6b). Especially the peak at 653 cm^{-1} vanishes completely after 2 h of irradiation. It is assigned to the ν(C−Br) + δ(ring) combinational mode, which was predicted by DFT calculations to be around 620 cm^{-1} and found at 615 cm^{-1} in solid BrU.[43] The deformation mode of the C−Br group is observable in BrU as a band at 290 cm^{-1}. Similar to the cases described above, this band vanishes after 120 min of irradiation indicating the cleavage of the C−Br bond.

Thus, in accordance with UV−vis spectra, the SERS spectra indicate an effective cleavage of the C−Br bond while the BrU ring fragmentation is much less pronounced than for U and T. This agrees well with previous observations of LEE-induced decomposition of BrU measured in the gas phase. In DEA measurements strong resonances were observed at energies down to almost 0 eV associated with cleavage of the Br−C bond, but the intensity of ring fragmentation products such as CN^- was much lower than for the nonbrominated T and U.[42] The SERS spectra confirm the predominant cleavage of the C−Br bond according to eq 4, whereas the decomposition of the ring structure of BrU is only a minor fragmentation channel in the electron-induced decomposition. As a consequence, a U radical is formed (eq 4), which most likely relaxes quickly in the surrounding solvent, resulting in stable U molecules. In a complete DNA strand the formation of a radical on the nucleobase can lead to strand breakage, which explains the previous observation that incorporation of BrU into DNA leads to higher strand breakage upon LEE irradiation.[26]

To check whether BrU is indeed converted to U, the SERS spectra of irradiated and nonirradiated BrU are compared to the SERS spectrum of U + KBr in Figure 6d. The spectrum of irradiated BrU is indeed very similar to the one obtained from U + KBr, especially because the bands at 1650, 1561, and 653 cm^{-1} are missing and 1180 cm^{-1} is decreased. A transformation of BrU into U also explains the shift of the π−π^* absorption band in Figure 5c. However, a complete transformation of BrU into U does not occur since some bands (e.g., at 1524, 1349, and 1075 cm^{-1}) only appear in the BrU spectra and do not vanish completely.

Another feature in the SERS spectra of BrU is the appearance of a strong signal peaking below 200 cm^{-1} upon irradiation, which is mainly observable as a strong background signal. It is assigned to the Ag−Br bond,[45] which is formed by intermediate formation of Br^- and subsequent reaction with the AgNPs. This

DOI: 10.1021/acs.jpcc.5b10564
J. Phys. Chem. C 2016, 120, 3001−3009

signal is a clear indicator for the presence of Br^-, which is also observable in the upper (violet) spectrum of Figure 6c.

CONCLUSIONS

We have studied the decomposition of the nucleobases T, U, and BrU in aqueous solution by plasmon excitation of AuNPs using a nanosecond pulsed laser. The decomposition reactions are observed by UV−vis absorption spectroscopy and SERS. The SERS spectra reveal the formation of different CN containing fragmentation products from T and U upon AuNP laser irradiation indicating pronounced ring fragmentation. The decomposition pathways of BrU are remarkably different compared to T and U. A predominant C−Br cleavage has been observed while decomposition of the aromatic ring structure was found to be only a minor decomposition channel. The cleavage of the C−Br bond is observable through the intensity drop of characteristic SERS bands. At the same time the generation of Br^- ions can be deduced from a shift of the SPR band in UV−vis absorption spectra. Furthermore, the SERS spectra indicate a partial transformation of BrU into U. The different behavior of T and U compared to BrU has already been observed previously in dissociative electron attachment to the respective compounds. Thus, the decomposition of biomolecules upon plasmon excitation of AuNPs is at least partly ascribed to the laser-induced formation of low-energy electrons, which are then attached to the nucleobase molecules to form negative ion resonances. These anionic states can quickly dissociate to form the observed fragmentation products. The effective cleavage of the C−Br bond in BrU creates a U radical as an intermediate, which in the present experiment results in stable U. In a DNA strand such a U radical represents a precursor for DNA strand breakage. For the first time we demonstrate that dissociative electron attachment occurs also in aqueous solution in a similar way as predicted by gas phase experiments.

EXPERIMENTAL SECTION

Chemicals. Silver nitrate ($AgNO_3$), $HAuCl_4$, sodium citrate, uracil, thymine, and 5-bromouracil were purchased from Sigma-Aldrich and dissolved in Millipore filtered water.

Preparation of Gold and Silver Nanoparticles. Citrate reduced gold nanoparticles were produced by bringing 20 mL of a 1 mM $HAuCl_4$ to boil and adding 2 mL of 1% sodium citrate. After the color changed from pale yellow to deep red the solution was boiled for 15 min more.

Silver nanoparticles were synthesized using the well-established protocol of Lee and Meisel.[47] Briefly 250 mL of a 1 mM $AgNO_3$ solution was heated up to rolling boil; subsequently, 10 mL of 1% sodium citrate solution was added and kept boiling for 1 h under rigorous stirring while Millipore water was added to keep the volume constant.

When the concentration of the nanoparticles is given, it refers to the concentration of silver or gold atoms as defined by the concentration of the respective precursor. To increase the concentration of the gold nanoparticles, 3.2 mL of the 1 mM AuNP solution was centrifuged in multiple steps through a 100 kDa centrifugal filter at 4000*g* for 2 min. In order to reduce Raman signals from the citrate capping and to avoid secondary reactions during the laser irradiation, the AuNP solution was washed several times with Millipore water. The concentration of the nanoparticle solution after the washing procedure was approximately 10 mM and was determined by the relative absorbance of the plasmon band from the UV−vis spectra compared to the initial nanoparticle solution.

Laser Irradiation. 625 μL of the solution containing 2 mM of the analyte and 2 mM of AuNP was placed in a glass cuvette on a magnetic stir plate. The irradiation was performed using the second harmonic of a Nd:YAG laser (wavelength 532 nm; pulse width 3−5 ns, intensity 67 mW (120 mW); repetition rate 10 Hz; Minilite I, Continuum). The beam was focused with a 30 mm lens on a 0.16 mm^2 spot on the surface to achieve a laser fluence of 4 J/cm^2. For the UV−vis and SERS analysis 10 μL of the sample was extracted at each time interval.

UV−Vis Measurements. The UV−vis spectra concerning the preparation of the nanoparticles and during the laser irradiation were performed with a Nanodrop 2000 (Thermo scientific) and Jasco v650 photospectrometer. For the latter 5 μL of the sample was diluted in 195 μL of Millipore water and filled in a quartz cuvette with an optical path length of 1 cm.

Surface-Enhanced Raman Spectroscopy (SERS). All Raman measurements were conducted with a Labram confocal Raman microscope from Horiba (wavelength 633 nm; laser power 9.4 mW) using a 50× objective (Olympus) with a focal length of 18 mm. A spectral range of 170−2440 cm^{-1} was chosen with typical integration times between 1 and 2 s averaged over 10 accumulations.

As the plasmonic enhancement of metal nanoparticles crucially depends on the particle size, the intensity and stability of the Raman signal are drastically lowered with ongoing irradiation of the AuNP solution. Therefore, 2 μL of the analyte was mixed with 2 μL of AgNP solution to obtain strong and reproducible SERS signals. The droplet was placed on a silicon wafer that was surrounded by a bath of Millipore water to reduce evaporation. The fluctuations of signal intensity with irradiation time are ascribed to the dependence of SERS signal intensity on many parameters such as the distance of analyte molecules from the nanoparticles and their localization and conformation within the hot spots of nanoparticle aggregates.

ASSOCIATED CONTENT

Supporting Information

The Supporting Information is available free of charge on the ACS Publications website at DOI: 10.1021/acs.jpcc.5b10564.

Figure S1: UV−vis absorption spectra of laser-irradiated AuNP−uracil solutions; Figure S2: high-resolution SERS spectra of U before and after laser irradiation; Figure S3: zoom-in into the absorption band of BrU around 270 nm and the SPR band around 520 nm for the BrU−AuNP system irradiated at 532 nm (PDF)

AUTHOR INFORMATION

Corresponding Author

*E-mail ilko.bald@uni-potsdam.de (I.B.).

Notes

The authors declare no competing financial interest.

ACKNOWLEDGMENTS

This research was supported by the Federal Institute for Materials Research (BAM), a Marie Curie FP7 Integration Grant within the seventh European Union Framework Programme, by the Deutsche Forschungsgemeinschaft (DFG) and the University of Potsdam.

DOI: 10.1021/acs.jpcc.5b10564
J. Phys. Chem. C 2016, 120, 3001−3009

REFERENCES

(1) Garwe, F.; Bauerschäfer, U.; Csáki, A.; Steinbrück, A.; Ritter, K.; Bochmann, A.; Bergmann, J.; Weise, A.; Akimov, D.; Maubach, G.; et al. Optically Controlled Thermal Management on the Nanometer Length Scale. *Nanotechnology* **2008**, *19* (5), 55207.

(2) Yamada, K.; Miyajima, K.; Mafune, F. Thermionic Emission of Electrons from Gold Nanoparticles by Nanosecond Pulse-Laser Excitation of Interband. *J. Phys. Chem. C* **2007**, *111* (30), 11246−11251.

(3) Mukherjee, S.; Libisch, F.; Large, N.; Neumann, O.; Brown, L. V.; Cheng, J.; Lassiter, J. B.; Carter, E. A.; Nordlander, P.; Halas, N. J. Hot Electrons Do the Impossible: Plasmon-Induced Dissociation of H 2 on Au. *Nano Lett.* **2013**, *13* (1), 240−247.

(4) Xie, W.; Schlücker, S. Hot Electron-Induced Reduction of Small Molecules on Photorecycling Metal Surfaces. *Nat. Commun.* **2015**, *6*, 7570.

(5) Takeda, Y.; Kondow, T.; Mafuné, F. Selective Decomposition of Nucleic Acids by Laser Irradiation on Probe-Tethered Gold Nanoparticles in Solution. *Phys. Chem. Chem. Phys.* **2011**, *13* (2), 586−592.

(6) Takeda, Y.; Mafuné, F.; Kondow, T. Selective Degradation of Proteins by Laser Irradiation onto Gold Nanoparticles in Solution. *J. Phys. Chem. C* **2009**, *113* (13), 5027−5030.

(7) Csaki, A.; Garwe, F.; Steinbrück, A.; Maubach, G.; Festag, G.; Weise, A.; Riemann, I.; König, K.; Fritzsche, W. A Parallel Approach for Subwavelength Molecular Surgery Using Gene-Specific Positioned Metal Nanoparticles as Laser Light Antennas. *Nano Lett.* **2007**, *7* (2), 247−253.

(8) Wirth, J.; Garwe, F.; Hähnel, G.; Csáki, A.; Jahr, N.; Stranik, O.; Paa, W.; Fritzsche, W. Plasmonic Nanofabrication by Long-Range Excitation Transfer via DNA Nanowire. *Nano Lett.* **2011**, *11* (4), 1505−1511.

(9) Hashimoto, S.; Werner, D.; Uwada, T. Studies on the Interaction of Pulsed Lasers with Plasmonic Gold Nanoparticles Toward Light Manipulation, Heat Management, and Nanofabrication. *J. Photochem. Photobiol., C* **2012**, *13* (1), 28−54.

(10) Lal, S.; Clare, S. E.; Halas, N. J. Nanoshell-Enabled Photothermal Cancer Therapy: Impending Clinical Impact. *Acc. Chem. Res.* **2008**, *41* (12), 1842−1851.

(11) Huang, X.; Jain, P.; El-Sayed, I.; El-Sayed, M. Plasmonic Photothermal Therapy (PPTT) Using Gold Nanoparticles. *Lasers Med. Sci.* **2008**, *23* (3), 217−228.

(12) Shoji, M.; Miyajima, K.; Mafune, F. Ionization of Gold Nanoparticles in Solution by Pulse Laser Excitation as Studied by Mass Spectrometric Detection of Gold Cluster Ions. *J. Phys. Chem. C* **2008**, *112* (6), 1929−1932.

(13) Zhang, Y.; Pluchery, O.; Caillard, L.; Lamic-Humblot, A.-F.; Casale, S.; Chabal, Y. J.; Salmeron, M. Sensing the Charge State of Single Gold Nanoparticles via Work Function Measurements. *Nano Lett.* **2015**, *15* (1), 51−55.

(14) Lu, Q.-B. Effects and Applications of Ultrashort-Lived Prehydrated Electrons in Radiation Biology and Radiotherapy of Cancer. *Mutat. Res., Rev. Mutat. Res.* **2010**, *704* (1−3), 190−199.

(15) Siefermann, K. R.; Abel, B. The Hydrated Electron: A Seemingly Familiar Chemical and Biological Transient. *Angew. Chem., Int. Ed.* **2011**, *50* (23), 5264−5272.

(16) Bald, I.; Langer, J.; Tegeder, P.; Ingólfsson, O. From Isolated Molecules Through Clusters and Condensates to the Building Blocks of Life. *Int. J. Mass Spectrom.* **2008**, *277* (1−3), 4−25.

(17) Thorman, R. M.; Kumar, T. P.; Ragesh; Fairbrother, D. H.; Ingólfsson, O. The Role of Low-Energy Electrons in Focused Electron Beam Induced Deposition: Four Case Studies of Representative Precursors. *Beilstein J. Nanotechnol.* **2015**, *6*, 1904−1926.

(18) Baccarelli, I.; Bald, I.; Gianturco, F. A.; Illenberger, E.; Kopyra, J. Electron-Induced Damage of DNA and its Components: Experiments and theoretical models. *Phys. Rep.* **2011**, *508* (1−2), 1−44.

(19) Bald, I.; Dabkowska, I.; Illenberger, E. Probing Biomolecules by Laser-Induced Acoustic Desorption: Electrons at Near Zero Electron Volts Trigger Sugar-Phosphate Cleavage. *Angew. Chem., Int. Ed.* **2008**, *47* (44), 8518−8520.

(20) McMahon, S. J.; Hyland, W. B.; Muir, M. F.; Coulter, J. A.; Jain, S.; Butterworth, K. T.; Schettino, G.; Dickson, G. R.; Hounsell, A. R.; O'Sullivan, J. M. Biological Consequences of Nanoscale Energy Deposition Near Irradiated Heavy Atom Nanoparticles. *Sci. Rep.* **2011**, *1*, 18.

(21) Verkhovtsev, A. V.; Korol, A. V.; Solov'yov, A. V. Revealing the Mechanism of the Low-Energy Electron Yield Enhancement from Sensitizing Nanoparticles. *Phys. Rev. Lett.* **2015**, *114* (6), 063401.

(22) Jain, S.; Hirst, D. G.; O'Sullivan, J. M. Gold Nanoparticles as Novel Agents for Cancer Therapy. *Br. J. Radiol.* **2012**, *85* (1010), 101−113.

(23) Jeremic, B.; Aguerri, A. R.; Filipovic, N. Radiosensitization by Gold Nanoparticles. *Clin. Transl. Oncol.* **2013**, *15* (8), 593−601.

(24) Keller, A.; Bald, I.; Rotaru, A.; Cauet, E.; Gothelf, K. V.; Besenbacher, F. Probing Electron-Induced Bond Cleavage at the Single-Molecule Level Using DNA Origami Templates. *ACS Nano* **2012**, *6* (5), 4392−4399.

(25) Keller, A.; Kopyra, J.; Gothelf, K. V.; Bald, I. Electron-Induced Damage of Biotin Studied in the Gas Phase and in the Condensed Phase at a Single-Molecule Level. *New J. Phys.* **2013**, *15*, 083045.

(26) Keller, A.; Rackwitz, J.; Cauet, E.; Lievin, J.; Körzdörfer, T.; Rotaru, A.; Gothelf, K. V.; Besenbacher, F.; Bald, I. Sequence Dependence of Electron-Induced DNA Strand Breakage Revealed by DNA Nanoarrays. *Sci. Rep.* **2014**, *4*, 7391.

(27) Alizadeh, E.; Sanz, A. G.; García, G.; Sanche, L. Radiation Damage to DNA: The Indirect Effect of Low-Energy Electrons. *J. Phys. Chem. Lett.* **2013**, *4* (5), 820−825.

(28) McAllister, M.; Smyth, M.; Gu, B.; Tribello, G. A.; Kohanoff, J. Understanding the Interaction between Low-Energy Electrons and DNA Nucleotides in Aqueous Solution. *J. Phys. Chem. Lett.* **2015**, *6* (15), 3091−3097.

(29) Kneipp, J.; Kneipp, H.; Kneipp, K. SERS—a Single-Molecule and Nanoscale Tool for Bioanalytics. *Chem. Soc. Rev.* **2008**, *37* (5), 1052.

(30) Prinz, J.; Schreiber, B.; Olejko, L.; Oertel, J.; Rackwitz, J.; Keller, A.; Bald, I. DNA Origami Substrates for Highly Sensitive Surface-Enhanced Raman Scattering. *J. Phys. Chem. Lett.* **2013**, *4* (23), 4140−4145.

(31) Liu, X.; Atwater, M.; Wang, J.; Huo, Q. Extinction Coefficient of Gold Nanoparticles with Different Sizes and Different Capping Ligands. *Colloids Surf., B* **2007**, *58* (1), 3−7.

(32) Huels, M. A.; Hahndorf, I.; Illenberger, E.; Sanche, L. Resonant Dissociation of DNA Bases by Subionization Electrons. *J. Chem. Phys.* **1998**, *108* (4), 1309.

(33) Hanel, G.; Gstir, B.; Denifl, S.; Scheier, P.; Probst, M.; Farizon, B.; Farizon, M.; Illenberger, E.; Märk, T. D. Electron Attachment to Uracil: Effective Destruction at Subexcitation Energies. *Phys. Rev. Lett.* **2003**, *90* (18), 188104.

(34) Ptasińska, S.; Denifl, S.; Mróz, B.; Probst, M.; Grill, V.; Illenberger, E.; Scheier, P.; Märk, T. D. Bond Selective Dissociative Electron Attachment to Thymine. *J. Chem. Phys.* **2005**, *123* (12), 124302.

(35) Kopyra, J.; Koenig-Lehmann, C.; Bald, I.; Illenberger, E. A Single Slow Electron Triggers the Loss of Both Chlorine Atoms from the Anticancer Drug Cisplatin: Implications for Chemoradiation Therapy. *Angew. Chem., Int. Ed.* **2009**, *48* (42), 7904−7907.

(36) da Silva, F. F.; Matias, C.; Almeida, D.; García, G.; Ingólfsson, O.; Flosadóttir, H. D.; Ómarsson, B.; Ptasinska, S.; Puschnigg, B.; Scheier, P.; et al. NCO−, a Key Fragment Upon Dissociative Electron Attachment and Electron Transfer to Pyrimidine Bases: Site Selectivity for a Slow Decay Process. *J. Am. Soc. Mass Spectrom.* **2013**, *24* (11), 1787−1797.

(37) Bald, I.; Dabkowska, I.; Illenberger, E.; Ingolfsson, O. Energy Selective Excision of CN- Following Electron Attachment to Hexafluoroacetone Azine ($(CF_3)_2CNNC(CF_3)_2$). *Phys. Chem. Chem. Phys.* **2007**, *9* (23), 2983.

DOI: 10.1021/acs.jpcc.5b10564
J. Phys. Chem. C 2016, 120, 3001−3009

(38) Papp, P.; Urban, J.; Matejčík, Š.; Stano, M.; Ingolfsson, O. Dissociative Electron Attachment to Gas Phase Valine: A Combined Experimental and Theoretical Study. *J. Chem. Phys.* **2006**, *125* (20), 204301.
(39) Wang, X.-B.; Kowalski, K.; Wang, L.-S.; Xantheas, S. S. Stepwise Hydration of the Cyanide Anion: A Temperature-Controlled Photoelectron Spectroscopy and Ab Initio Computational Study of CN[sup −](H[sub 2]O)[sub n], n = 2−5. *J. Chem. Phys.* **2010**, *132* (12), 124306.
(40) Grua, P.; Morreeuw, J.; Bercegol, H. Kinetic Study of Laser Damage Initiation by Creation of an Electron Plasma from Absorbing Nano-Inclusions. *Proc. SPIE* **2002**, No. No. 4679, 293−302.
(41) Bowmaker, G. A.; Kennedy, B. J.; Reid, J. C. Crystal Structures of AuCN and AgCN and Vibrational Spectroscopic Studies of AuCN, AgCN, and CuCN †. *Inorg. Chem.* **1998**, *37* (16), 3968−3974.
(42) Abdoul-Carime, H.; Huels, M. A.; Brüning, F.; Illenberger, E.; Sanche, L. Dissociative Electron Attachment to Gas-Phase 5-Bromouracil. *J. Chem. Phys.* **2000**, *113* (7), 2517.
(43) Rastogi, V. K.; Palafox, M. A.; Mittal, L.; Peica, N.; Kiefer, W.; Lang, K.; Ojha, S. P. FTIR and FT-Raman Spectra and Density Functional Computations of the Vibrational Spectra, Molecular Geometry and Atomic Charges of the Biomolecule: 5-Bromouracil. *J. Raman Spectrosc.* **2007**, *38* (10), 1227−1241.
(44) Giese, B.; McNaughton, D. Surface-Enhanced Raman Spectroscopic Study of Uracil. The Influence of the Surface Substrate, Surface Potential, and pH. *J. Phys. Chem. B* **2002**, *106* (6), 1461−1470.
(45) Garrell, R. L.; Shaw, K. D.; Krimm, S. Surface Enhanced Raman Spectroscopy of Halide Ions on Colloidal Silver: Morphology and Coverage Dependence. *Surf. Sci.* **1983**, *124* (2−3), 613−624.
(46) Zhang, L.; Li, Q.; Tao, W.; Yu, B.; Du, Y. Quantitative Analysis of Thymine with Surface-Enhanced Raman Spectroscopy and Partial Least Squares (PLS) Regression. *Anal. Bioanal. Chem.* **2010**, *398* (4), 1827−1832.
(47) Lee, P. C.; Meisel, D. Adsorption and Surface-Enhanced Raman of Dyes on Silver and Gold Sols. *J. Phys. Chem.* **1982**, *86* (17), 3391−3395.

DOI: 10.1021/acs.jpcc.5b10564
J. Phys. Chem. C 2016, 120, 3001−3009

Supporting Information

Decomposition of DNA nucleobases by laser irradiation of gold nanoparticles monitored by surface-enhanced Raman scattering (SERS)

Robin Schürmann[a,b], *Ilko Bald*[a,b]*

[a]Institute of Chemistry – Physical Chemistry, University of Potsdam, Potsdam, Germany

[b]BAM Federal Institute for Materials Research and Testing, Berlin, Germany

Keywords: Gold nanoparticles, electrons, DNA damage

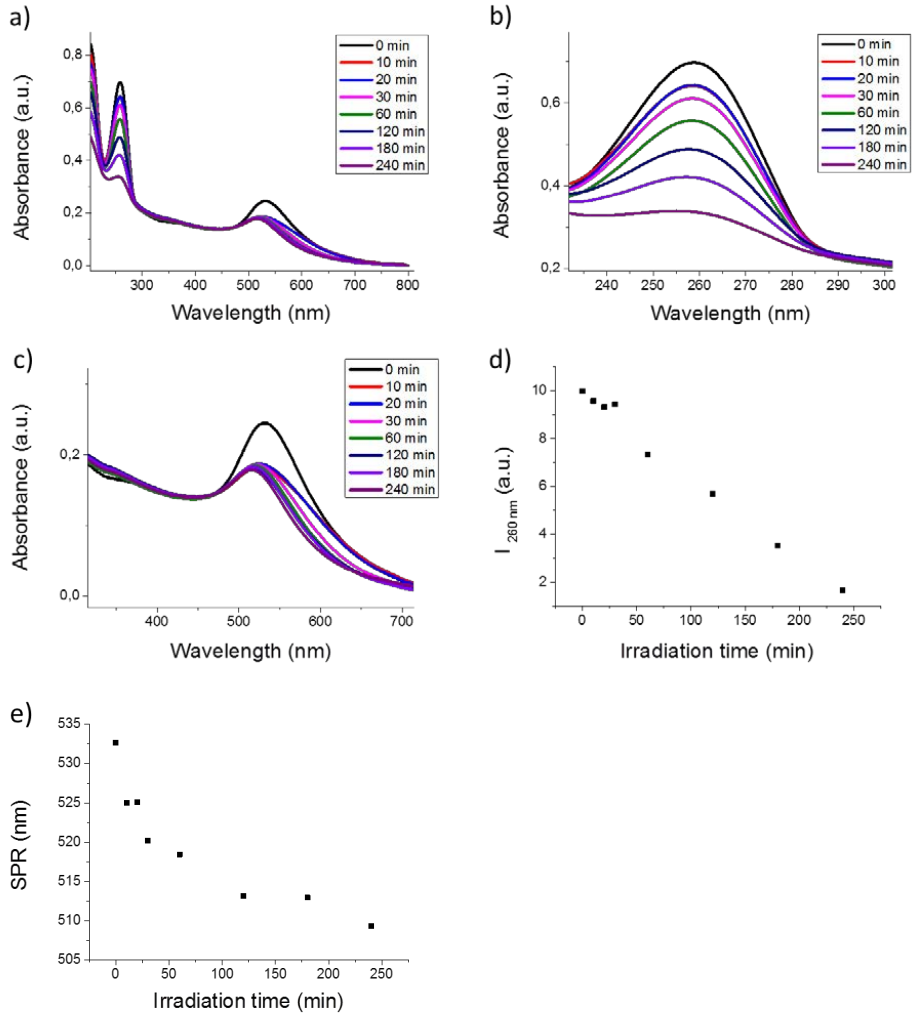

Figure S1: UV-Vis absorption spectra of laser irradiated AuNP-Uracil solutions.

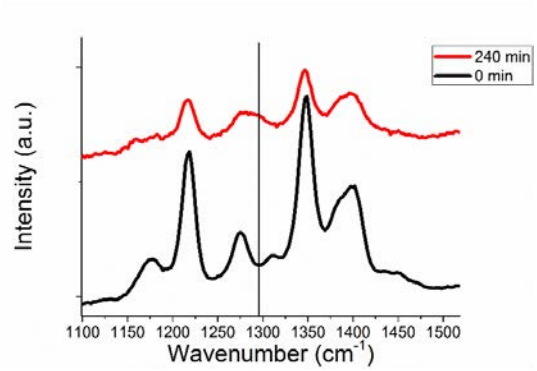

Figure S2: Zoom-in into the spectral region 1100 cm^{-1} – 1525 cm^{-1} of the SERS spectra of T + AuNPs. A weak, but clear new band arises at 1295 cm^{-1} upon laser irradiation and is indicated by the vertical line.

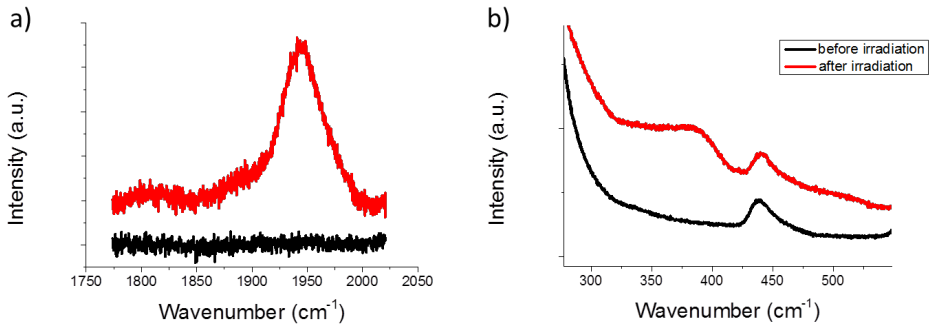

Figure S3: High-resolution SERS spectra of U before and after laser irradiation.

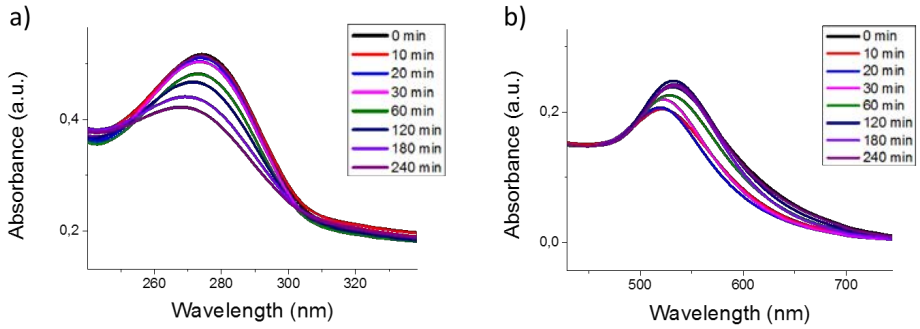

Figure S4: Zoom-in into the absorption band of BrU around 270 nm and the SPR band around 520 nm for the BrU-AuNP system irradiated at 532 nm.

4.4 M4: "Effect of adsorption kinetics on dissociation of DNA-nucleobases on gold nanoparticles under pulsed laser illumination"

Robin Schürmann and Ilko Bald
Phys. Chem. Chem. Phys. 2017, 19, 10796 - 10803
DOI: 10.1039/C6NR08695K

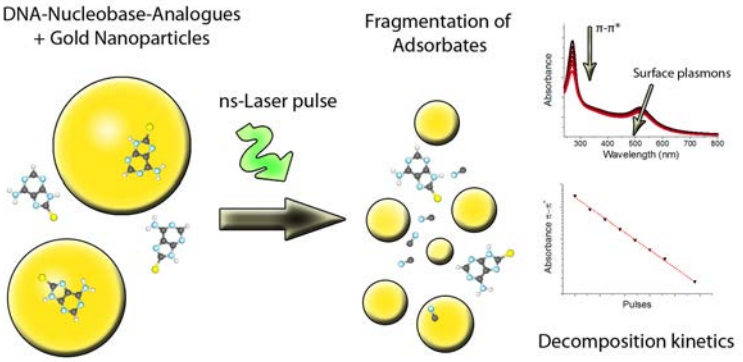

Author contributions to the manuscript:
I prepared all samples and performed all irradiations of the AuNPs/NBs mixtures. I performed all AFM, UV-Vis spectroscopy and SERS measurement and analyzed the data. Beyond that, I derived all kinetics equations. I prepared all figures for the manuscript and the supporting info. I prepared the manuscript in cooperation with Ilko Bald.

PCCP

PAPER

View Article Online
View Journal | View Issue

Cite this: *Phys. Chem. Chem. Phys.*, 2017, **19**, 10796

Effect of adsorption kinetics on dissociation of DNA-nucleobases on gold nanoparticles under pulsed laser illumination†

Robin Schürmann[ab] and Ilko Bald*[ab]

Received 9th December 2016,
Accepted 7th February 2017

DOI: 10.1039/c6cp08433h

rsc.li/pccp

Photothermal therapy is a novel approach to destroy cancer cells by an increase of temperature due to laser illumination of gold nanoparticles (GNPs) that are incorporated into the cells. Here, we study the decomposition of DNA nucleobases *via* irradiation of gold nanoparticles with ns-laser pulses. The kinetics of the adsorption and decomposition process is described by a theoretical model based on the Langmuir assumptions and correlated with experimentally determined reaction rates revealing a strong influence of the nucleobase specific adsorption. Beside the four nucleobases, their brominated analogs, which are potential radiosensitizers in cancer therapy, are also investigated and show a significant modification of the decomposition rates. The fastest decomposition rates are observed for adenine, 8-bromoadenine, 8-bromoguanine and 5-bromocytosine. These results are in good agreement with the relative adsorption rates that are determined from the aggregation kinetics of the GNPs taking the effect of an inhomogeneous surface into account. For adenine and its brominated analog, the decomposition products are further analyzed by surface enhanced Raman scattering (SERS) indicating a strong fragmentation of the molecules into their smallest subunits.

Introduction

Gold nanoparticles (GNPs) have found versatile applications in cancer therapy[1] such as drug delivery,[2] cancer diagnostics,[3] radiosensitization in cancer radiation therapy[4,5] and photothermal therapy[6–8] (PTT). In PTT, GNPs are transferred into the cancer cells and illuminated with a near infrared (NIR) laser to pass the therapeutic window.[9] It has been shown previously that the efficiency of PTT can be increased by using pulsed lasers especially if the GNPs are located in the nucleus,[10] where the DNA is located. In various cancer therapies, the DNA is targeted in order to cause the cell death by irreparable damage.[11,12] Generally, to severely damage the DNA higher energetic photons close to or beyond the ionization threshold of DNA are required,[13] as DNA and its components are transparent in the visible and near infrared spectrum of light and after excitation of the lowest π–π^* transition of the nucleobases in the UV region the electronic ground state is rapidly restored.[14] However, tailored GNPs[15] absorb efficiently visible or NIR light due to excitation of their surface plasmon resonance (SPR) that elevates the temperature of the GNPs and their surrounding through non-radiative relaxation channels.[16] Hence, pulsed laser irradiation of GNPs can destroy the DNA[17,18] and other important biomolecules like peptides[19] in their vicinity by local heating effects.

During the illumination of the GNPs their surface temperature rises up to several thousand K[20] and around the particles a supercritical layer[21] and high pressure nanobubbles[22] are formed above certain laser intensities.[23] Additionally, secondary reactive species such as low energy electrons (LEEs) are generated[24] that cleave bonds in nearby molecules *via* dissociative attachment[25] very efficiently and selectively,[26] but the range of the damage is limited to the nanometer scale.

Some therapies aim at specific DNA sequences such as the guanine (G) rich telomeres[27,28] that play an important role in the emergence and therapy[29] of cancer. For the purpose of targeting such sequences, the specific interaction between the individual DNA components and the nanoparticles in terms of binding strength[30,31] and adsorption kinetics[32] needs to be studied. Furthermore, in order to increase the DNA damage in cancerous tissue, radiosensitizing agents like halogenated nucleobases can be incorporated into the double helix,[33] as they enhance the strand-break formation.[34,35] In the present study, besides the four nucleobases, their brominated analogs[36] are also examined with a special focus on adenine (A)[34,37] and the modified 8-bromoadenine[38,39] (^{8Br}A). We hope that understanding the mechanisms underlying the interaction between GNPs and DNA components and potential radiosensitizing agents might

[a] *Institute of Chemistry – Physical Chemistry, University of Potsdam, Potsdam, Germany. E-mail: ilko.bald@uni-potsdam.de*
[b] *BAM Federal Institute for Materials Research and Testing, Berlin, Germany*
† Electronic supplementary information (ESI) available. See DOI: 10.1039/c6cp08433h

View Article Online

Paper PCCP

help to further improve PTT. Therefore, we analyze the decomposition of nucleobase analogs on irradiated GNPs and compare it with the nucleobase specific adsorption on the GNPs to elucidate the underlying damage mechanisms.

Results and discussion

To study the decomposition of the GNPs, 2 ml of a 30 pM citrate reduced GNP dispersion with a mean diameter of 40 nm was irradiated in a quartz cuvette with the second harmonic of a pulsed Nd:YAG laser (532 nm). Each laser pulse had an energy of 16 mJ with a 5 ns pulse width and the laser spot diameter was 3 mm. Hence, the GNPs in the illuminated area (3.5% of the sample) are exposed to a laser fluence of approximately 230 mJ cm^{-2}. After a certain number of pulses, the UV-Vis absorption spectra of the GNPs were recorded and 2 μl of the sample were dried on a plasma cleaned Si wafer to determine the size distribution of the GNPs *via* atomic force microscopy (AFM). In Fig. 1a, the UV-Vis absorption spectra are shown and reveal a decrease and a blue shift of the SPR from 526 nm to 511 nm indicating a rapid decrease of the nanoparticle size. The histograms of diameters of the nanoparticles determined by AFM are shown in Fig. 1b–e and Fig. S1 (ESI†) demonstrating the decrease in the size of the GNPs and the formation of a bimodal distribution after exposure of the GNPs to the first laser pulses. At the fluences used here, electron ejection from the particles can be neglected,[40] nevertheless heating, melting and surface evaporation lead to a change in the size distribution and morphology of the GNPs even at single pulses.[41,42] Up to an exposure to 100 pulses, which correlates with an average exposure of 3 pulses per GNP according to Poisson statistics, the absorbance above 600 nm significantly increases most likely due to the formation of complex nanoparticle aggregates (Fig. 1).[42–45] With a higher number of pulses, the absorbance of the sample in the red and near infrared wavelength regime declines again and the SPR as well as the particle size distribution barely changes above 500 pulses, whereby hardly any GNPs with a diameter above 10 nm are observed. Therefore, we assume that the particle size distribution is constant on the relevant timescales (*i.e.* 3–80 min) for the subsequent experiment.

The addition of 20 μM ^{8Br}A to the GNP dispersion results in a new band in the absorbance spectrum with a maximum located at 271 nm caused by the π–π* transition of the nucleobase analogue. As the absorption of ^{8Br}A is superposed with the interband transition of the GNPs in the UV region, the UV-Vis-spectra are corrected by subtracting a spectrum of the pure GNPs irradiated under the same experimental conditions for the subsequent analysis as shown in Fig. S2 (ESI†). In Fig. 2a, the UV-Vis absorption spectra of an ^{8Br}A/GNP solution irradiated with a certain number of pulses with a 10 Hz repetition rate are shown and reveal, beside the changes in the SPR, a decrease of the 271 nm absorption band clearly indicating a decomposition of the ^{8Br}A ring structure into smaller fragments. Single exocyclic bond cleavages like the cleavage of the C–Br bond are unlikely since the position of the maximum was not shifted. Fig. 2c shows an exponential decay of the normalized absorbance that corresponds to a (pseudo-) first order reaction.

In Fig. 3a the normalized absorbance at 271 nm is plotted against the number of pulses at different initial GNP concentrations ranging from 7.5 pM to 60 pM (corresponding to $\varepsilon_{520\,nm}$ = 0.05–0.4), while all other experimental parameters were kept constant. The reaction rate of the decomposition of ^{8Br}A clearly increases with a higher concentration of the GNPs. However, when keeping the GNP concentration constant but varying the initial ^{8Br}A concentration from 8 μM to 32 μM, as shown in Fig. 3b, the rate constant decreases with higher ^{8Br}A concentration. This anti-proportional dependence of the reaction rate is generally reported for heterogeneous reactions following Langmuir–Hinshelwood kinetics,[46] where the adsorption of the reactant (here ^{8Br}A) on the catalyst (in this case the GNP surface[47]) is in equilibrium and the (photo-) reaction on the surface is the rate determining step. However, Langmuir–Hinshelwood kinetics cannot be applied in this case as the rate constant depends on the repetition rate of the laser (as shown in Fig. 3c), and therefore on the incubation time of the nucleobases on the gold surface between two pulses.

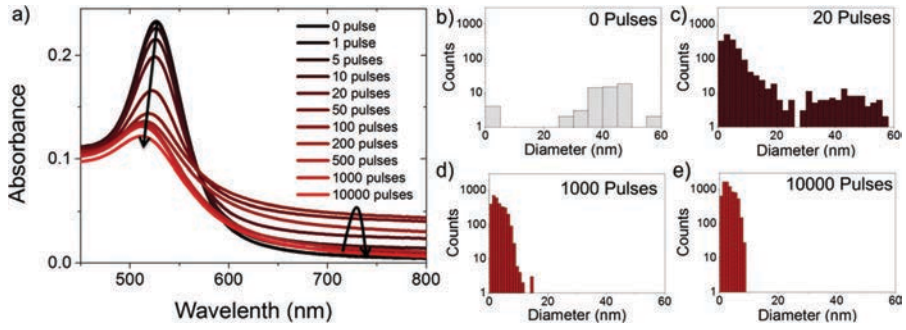

Fig. 1 (a) UV-Vis spectra of 40 nm GNPs irradiated with 0 to 10 000 laser pulses. (b–e) Size distribution of irradiated GNPs after illumination with 0, 20, 1000 and 10 000 pulses, respectively.

View Article Online

PCCP Paper

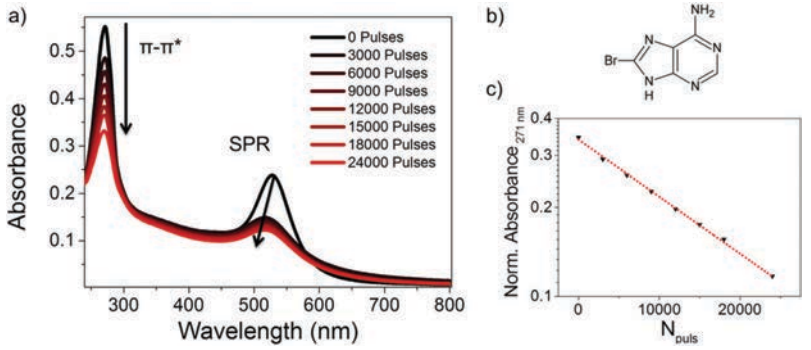

Fig. 2 (a) UV-Vis absorption spectra of 40 nm gold nanoparticles with 20 μM ^{8Br}A irradiated with different number of laser pulses. (b) Molecular structure of ^{8Br}A. (c) Normalized adsorption of the ^{8Br}A π–π* transition at 271 nm determined for the spectra shown in (a) plotted as a function of the laser pulses. The red dotted line shows an exponential fit of the data.

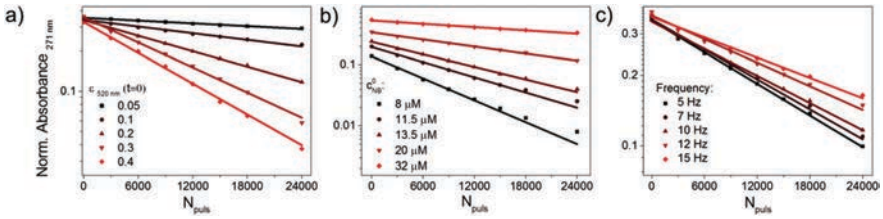

Fig. 3 Normalized absorbance at 271 nm of an irradiated GNP ^{8Br}A solution plotted against the number of pulses at various initial concentrations of GNPs (a), ^{8Br}A (b) and different laser repetition rates (c). Data are fitted with an exponential function (solid line).

The reciprocal dependence of the reaction rate on the initial ^{8Br}A concentration and the comparably weak dependence on the incubation time indicate that the equilibrium of the adsorption of the reactant on the catalyst is not reached under these conditions.

We assume that the reaction is divided into 3 reaction steps ("*" denotes an adsorption site or the adsorbed state):

1. adsorption of the NBs on the GNPs: $^{8Br}A + * \rightleftharpoons {}^{8Br}A*$
2. decomposition of the NBs due to the laser pulse $^{8Br}A* + h\nu \rightarrow$ Prod
3. adsorption of decomposition products Prod + * $\rightleftharpoons$ Prod*

Due to the extreme conditions on the GNP surface under laser illumination, it is expected that all adsorbed molecules decompose, hence the decomposition of a nucleobase (NB) is given by:

$$\frac{dc_{nb}}{dN_{puls}} = -\varphi \cdot c_{ad}, \quad (1)$$

with c_{nb} being the concentration of the nucleobases in the dispersion, c_{ad} the concentration equivalent of the adsorbed molecules, N_{puls} is the number of laser pulses and $\varphi = \frac{\text{irradiated volume}}{\text{total volume}}$.

The coverage of nucleobases on the GNP surface follows Langmuir adsorption kinetics,[48,49] as it is assumed that the total number of adsorption sites does not change due to the irradiation of the GNPs and the surface is free of adsorbate molecules directly after exposure to a laser pulse, because a catalyst poisoning was not observed in the experiment. For the rate of photoinduced decomposition of adsorbed molecules we can write:

$$\frac{dc_{ad}}{dN_{puls}} = k_{ad} \cdot (c_{eq} - c_{ad}) - \varphi \cdot c_{ad}, \quad (2)$$

where c_{eq} is the concentration equivalent representing the equilibrium adsorption and k_{ad} is the adsorption constant with respect to the number of pulses. It has to be mentioned that in this case, the adsorption constant k_{ad} depends on the repetition rate of the laser f,

$$k_{ad} = k_{ad}' \cdot \tau = \frac{k_{ad}'}{f}, \quad (3)$$

since the adsorption between two laser pulses is described by $\frac{dc_{ad}}{dN_{puls}} = \frac{dc_{ad}}{dt} \cdot \tau$, k_{ad}' is the adsorption constant with respect to time and τ is the time between two pulses.

Eqn (2) can be rearranged as:

$$\frac{dc_{ad}}{\left(c_{eq} - \left(1 + \frac{\varphi}{k_{ad}}\right) \cdot c_{ad}\right)} = k_{ad} \cdot dN_{puls} \quad (4)$$

and *via* integration we obtain

$$-\frac{1}{\left(1+\frac{\varphi}{k_{ad}}\right)}\cdot\ln\frac{\left(c_{eq}-\left(1+\frac{\varphi}{k_{ad}}\right)\cdot c_{ad}\right)}{c_{eq}}=k_{ad}\cdot N_{puls} \quad (5)$$

Rearranging eqn (5) as c_{ad} yields:

$$c_{ad}=\frac{1}{\left(1+\frac{\varphi}{k_{ad}}\right)}\cdot c_{eq}\cdot\left(1-e^{-(k_{ad}+\varphi)\cdot N_{puls}}\right) \quad (6)$$

Already after 100 pulses the exponential term can be neglected, as $\varphi \approx 0.035$ and $(k_{ad}+\varphi) > \varphi$, so:

$$1-e^{-(k_{ad}+\varphi)\cdot N_{puls}}\rightarrow 1 \text{ for } \frac{1}{\varphi}\ll N_{puls} \quad (7)$$

Hence eqn (6) simplifies to

$$c_{ad}=\frac{1}{\left(1+\frac{\varphi}{k_{ad}}\right)}\cdot c_{eq} \quad (8)$$

Inserting eqn (8) into eqn (1) leads to:

$$\frac{dc_{nb}}{dN_{puls}}=-\varphi\frac{1}{\left(1+\frac{\varphi}{k_{ad}}\right)}\cdot c_{eq}, \quad (9)$$

whereby the equilibrium concentration c_{eq} is given by the Langmuir isotherm, in which K_L is the Langmuir coefficient and c_{max} is the total number of adsorption sites. Taking into account that the reaction products in the solution can also adsorb competitively on the GNP surface, c_{eq} can be written as:

$$c_{eq}=\frac{c_{max}\cdot K_L\cdot c_{nb}}{\left(1+K_L\cdot c_{nb}+K_L\cdot c_{prod}\right)}=\frac{c_{max}\cdot K_L\cdot c_{nb}}{\left(1+K_L\cdot c_{nb}^0\right)}, \quad (10)$$

since the concentration of reaction products is given by

$$c_{prod}=c_{nb}^0-c_{nb} \quad (11)$$

and c_{nb}^0 is the initial nucleobase concentration. When eqn (10) is inserted into eqn (9), a pseudo-first order reaction equation is obtained:

$$\frac{dc_{nb}}{dN_{puls}}=-\varphi\cdot\frac{k_{ad}}{(k_{ad}+\varphi)}\cdot\frac{c_{max}\cdot K_L}{\left(1+K_L\cdot c_{nb}^0\right)}\cdot c_{nb}, \quad (12)$$

where the rate constant k

$$\frac{dc_{nb}}{dN_{puls}}=-k\cdot c_{NB} \quad (13)$$

is given by

$$k=\varphi\cdot\frac{k_{ad}}{(k_{ad}+\varphi)}\cdot\frac{c_{max}\cdot K_L}{\left(1+K_L\cdot c_{nb}^0\right)}. \quad (14)$$

The derived rate constant explains the major observations in the decomposition of ^{8Br}A with laser irradiated GNPs namely the exponential decay of the nucleobase concentration, the linear dependence of the reaction rate on the GNPs that is associated with the maximum number of adsorption sites c_{max} and the proportional correlation on the reciprocal initial concentration of the nucleobases. Beyond that, the reaction rate decreases with the frequency like it was determined in the experiment.

Calculations based on the theoretical model derived above have been performed to establish the rate constants. As even for thiolated DNA[50,51] the adsorption time is typically in the range of hours due to the ligand exchange with the citrate capping,[52] the observed reaction rates cannot be explained using these adsorption rates. Recent studies reveal a fast and a slow adsorption process on GNPs attributed to adsorption on low- and high-coordinated Au surface sites.[53] Here, only the fast adsorption process is taken into account, as on the one hand, the adsorption time between two pulses is too short to observe a relevant contribution of the slow process and on the other hand, the diameter of the irradiated GNPs is smaller than 10 nm so the contribution from high-coordinated surface sites can be neglected. Therefore, k_{ad}' was set to 0.45 s^{-1} to fit the experimental data and a Langmuir constant K_L of 10 μM^{-1} was chosen as a lower boundary, since the rate constant does not change at higher values. Furthermore, a capacity for adsorption of 800 pmol cm^{-2} is used, which is slightly higher but still in good agreement with experimentally determined values,[54] together with a surface area of 55 cm^2, which is calculated from the known concentration of gold atoms in the solution and the size distribution of the nanoparticles after irradiation specified by AFM. In Fig. 4a, the rate constants k determined from the slopes in Fig. 3 are plotted together with the theoretical values obtained from eqn (14). The theoretical and experimental data are in fairly good agreement; nevertheless at low

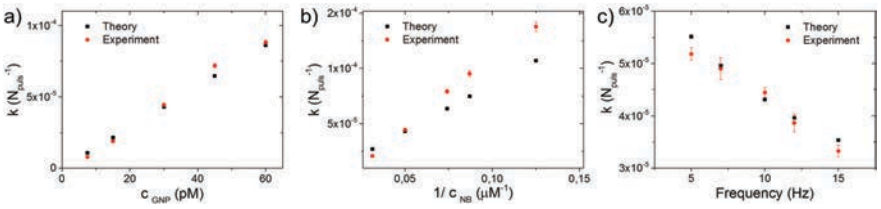

Fig. 4 Rate coefficients for the dissociation of ^{8Br}A on 40 nm GNPs determined *via* an exponential fit of the data in Fig. 3 and calculated theoretically using formula (14) plotted as a function of the initial GNP concentration (a), the inverse initial concentration of ^{8Br}A (b) and laser repetition rate (c).

View Article Online

PCCP Paper

^{8Br}A concentrations the experimental values are lower than the predicted ones.

In order to obtain more information about the dissociation products surface enhanced Raman scattering (SERS) measurements of A and ^{8Br}A have been performed. The SERS spectrum of the A/GNP solution shown in Fig. 5 reveals the characteristic SERS peaks of A with the intense ring-breathing mode located at 735 cm^{-1}. After irradiation with 3000 laser pulses the signal intensity is significantly decreased mainly due to the lower enhancement of the smaller GNPs. The ring breathing mode is still clearly observable, but at 2140 cm^{-1} a broad new band arises that is assigned to the CN stretching vibration. CN^- is a common dissociation fragment in the interaction of A with low energy electrons.[55] The detection of fragments using SERS is limited by the adsorption of the molecules on the nanoparticles and the related signal enhancement,[18] so the determination of a full set of decomposition fragments is still part of ongoing research. As ^{8Br}A is highly reactive towards plasmonically generated electrons,[56] the laser power of the Raman microscope has to be reduced in the Raman measurements to minimize this effect. Before irradiation, the ring breathing mode of ^{8Br}A is located at 767 cm^{-1} and no transformation to A is observed. Due to the pulsed laser illumination, a new band arises at 2140 cm^{-1} and the ring breathing mode is still observable. A transformation from ^{8Br}A to A does not take place indicating that LEEs play a minor role in the dissociation of ^{8Br}A under laser irradiation at these intensities (230 mJ cm^{-2}) and the fragmentation is due to thermal decomposition on the nanoparticle surface.

Besides A and its analogs, the other canonical DNA nucleobases, namely thymine (T), cytosine (C) and G, and their brominated forms 5-bromouracil (^{5Br}U), 5-bromocytosine (^{5Br}C) and 8-bromoguanine (^{8Br}G) have also been measured to study the nucleobase specificity of the decomposition rate (Fig. 6a). Fig. 6b shows the rate constants determined for the four nucleobases and their brominated analogs at various laser repetition rates. For all studied molecules, the reaction rate decreases with increasing laser frequency indicating an influence of the adsorption on the decomposition in all cases. In Fig. 6c, the reaction rates at 10 Hz are plotted for all molecules revealing the highest rates for A and the brominated compounds ^{8Br}A, ^{8Br}G and ^{5Br}C. It is remarkable that the decomposition rate of A decreases upon bromination, whereas k is higher for all other brominated nucleobases compared with their non-modified form.

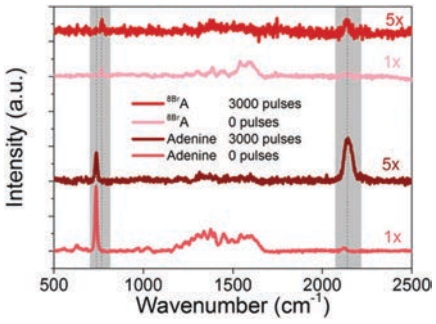

Fig. 5 Raman spectra of ^{8Br}A (red) and A (blue) before and after irradiation with 3000 laser pulses. Peaks in the region between 1000 cm^{-1} and 1600 cm^{-1} of the non-irradiated samples are partly assigned to the citrate capping of the GNPs.

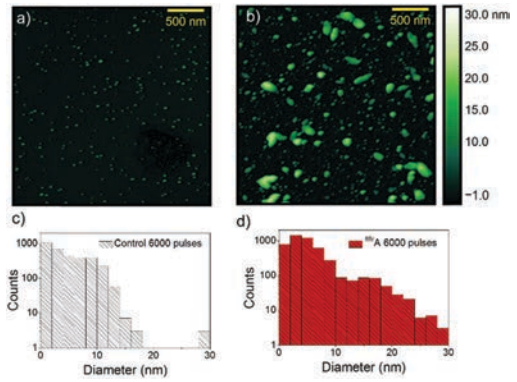

Fig. 7 GNPs on Si imaged by AFM before (a) and after addition of 20 μM ^{8Br}A (b) after illumination with 6000 laser pulses. (c–d) Size distribution of the GNP samples imaged in (a and b).

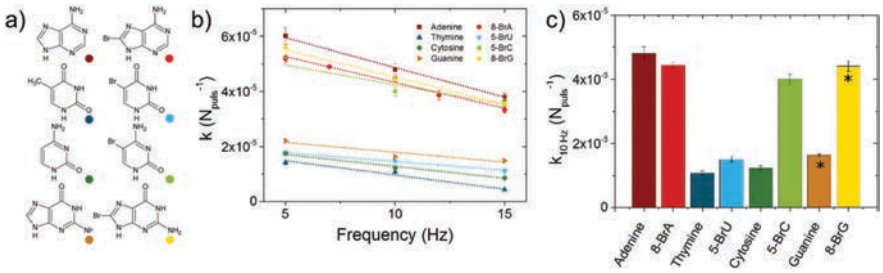

Fig. 6 (a) Molecular structures of A (dark red), ^{8Br}A (light red), T (dark blue), ^{5Br}U (light blue), C (dark green), ^{5Br}C (light green), G (dark yellow) and ^{8Br}G (light yellow). (b) Decomposition rate of nucleobase analogs plotted as a function of the laser repetition rate. (c) Reaction rate of the nucleobases at 10 Hz (same data like (b)). G and ^{8Br}G are marked with a star as the measurements were performed in a different environment.

View Article Online

Paper PCCP

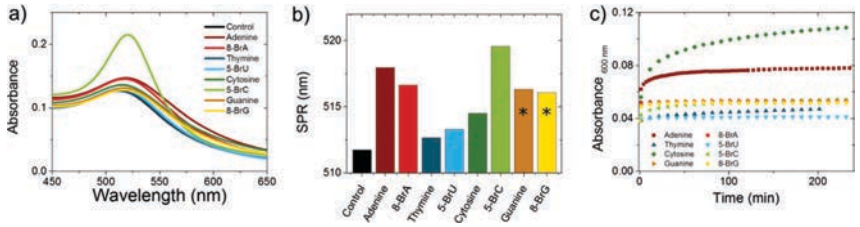

Fig. 8 (a) Absorption spectra of GNPs illuminated with 6000 laser pulses recorded directly after the addition of the analyte molecules. (b) Maximum of the SPR determined from the spectra shown in (a). The guanine analogs are marked with a star as the measurements were performed in a different environment. (c) Absorbance at 600 nm of irradiated GNPs after the addition of the nucleobases as a function of time.

In order to decide whether there indeed is a nucleobase specific decomposition cross section or whether the different decomposition rates are caused by the nucleobase specific binding affinity to the GNPs, the formation of GNP aggregates has been examined. This has been done because recent studies showed that the aggregation kinetics of the GNPs is associated with the binding strength of the NBs on the GNPs.[57,58] Here, we investigate whether the decomposition rates can be correlated with the binding strength of the NBs on the GNPs[30] to work out the contribution of adsorption to the apparent DNA damage.

20 μM ^{8Br}A were added to an irradiated GNP solution to form aggregates and subsequently the nanoparticle sizes were determined using AFM, as shown in Fig. 7. Before the addition of ^{8Br}A, mainly particles with a diameter below 15 nm are observed, whereas the presence of ^{8Br}A leads to an aggregation of the GNPs that causes the formation of GNP clusters with sizes up to 30 nm.

The aggregation of the GNPs is caused by the adsorption of ^{8Br}A on their surface and the subsequent formation of hydrogen bonds with ^{8Br}A molecules on neighboring GNPs.[59,60] This process was also followed by using UV-Vis absorption spectroscopy as the aggregation of GNPs leads to an increase and red shift of the SPR.[61] In Fig. 8a the SPRs of irradiated GNPs are plotted before and directly after the addition of the different nucleobases showing a distinct red-shift for all analyte molecules. Even though the width of the SPR also varies, indicating the generation of differently shaped nanoclusters depending on the nucleobase, the shift of the SPR maximum is used as a measure of aggregation. The maxima of the SPR are plotted in Fig. 8b revealing a red shift for all eight molecules with the strongest shifts for ^{5Br}C, A and ^{8Br}A. The results for G and ^{8Br}G cannot be compared directly with those obtained for the other nucleobases, as the measurements had to be performed in dilute sodium hydroxide solution due to the poor water solubility of both molecules. This influences the aggregation by virtue of a higher ion concentration and the adsorption due to the deprotonation of the nucleobases. However, for T, C and A the SPR shifts correlate with the expected order of the binding energies of the nucleobases on the GNPs: G > A > C > T.[62] The deviation in adsorption for non-modified and brominated nucleobases is probably due to different Hammett parameters.[63] If the decomposition rates of A, C and T are compared with the SPR shifts of the GNPs, the main features correlate with each other like high reaction rates and strongly red shifted SPR for A, ^{8Br}A and ^{5Br}C and low SPR shifts and reaction rates for C, T, ^{5Br}U. Also, the difference between brominated and non-modified nucleobases is reflected. Nevertheless the values of the SPR shift for C and ^{5Br}C are slightly higher than expected, since the determined SPR of the GNPs does not exactly reflect the aggregation state during the irradiation induced decomposition. The absorption spectra are completed 2 minutes after the addition of the nucleobases to the GNPs, while the relevant timescale for the decomposition under laser illumination is around 2 seconds.

In Fig. 8c, the absorbance at 600 nm of the GNP solutions is plotted as a measure of the aggregation against the incubation time, revealing a differing aggregation kinetics of the GNPs depending on the added nucleobases with the strongest time dependency for C. All these functions cannot be fitted by an exponential decay function, but very well with a biexponential decay function indicating a two-step adsorption process (see Fig. S3 of the ESI†). Hence, it is important to differentiate between the thermodynamic parameters determined from the equilibrium state and the adsorption kinetics on a certain timescale in order to estimate the amount of adsorbed molecules on the nanoparticle surface.

Conclusion

We have probed the dissociation of non-modified and brominated DNA nucleobases upon laser illumination of GNPs by using UV-Vis absorption spectroscopy, revealing a (pseudo-) first order reaction. It was demonstrated that the reaction rate depends on the initial concentrations of the nucleobases and the GNPs as well as on the laser repetition rate, which determines the incubation time of the analyte molecules on the surface. These results are in good agreement with the theoretically expected rate constants that are calculated under the assumption that adsorbed molecules on the nanoparticles decompose under irradiation and taking into account that there is a faster adsorption at certain sites on the nanoparticle surface. Among all tested molecules, A, ^{8Br}A, ^{8Br}G and ^{5Br}C show the highest decomposition rate constants. The adsorption of the nucleobases on the nanoparticles is investigated by monitoring the SPR of the nanoparticles that reflects the degree of aggregation, which is linked to the amount of adsorbed molecules. It is shown that the aggregation of the

View Article Online

PCCP Paper

GNPs due to the nucleobase adsorption is related to the decomposition rate constants under laser irradiation and again a strong impact of the inhomogeneity of the GNP surface on the adsorption is determined. Furthermore, a strong influence of bromination on the decomposition rate and adsorption behavior of certain nucleobases is observed, which might help to target and destroy distinct sequences in the DNA more effectively to improve cancer therapy.

Experimental section

Chemicals

^{8Br}A was purchased from Carbosynth Ltd. ^{5Br}U, T, C, ^{5Br}C, G, ^{8Br}G and A were purchased from Sigma Aldrich. ^{8Br}G and G were dissolved in 10 mM NaOH aqueous solution and all other components were dissolved in Millipore filtered water. Citrate capped gold nanoparticles with nominal sizes of 40 nm and 60 nm were purchased from BBI and used as delivered.

Irradiation

A quartz cuvette containing 2 ml 20 μM NB solution and citrate reduced 30 pM GNPs with an optical density of 0.2 at 520 nm was illuminated with a Minilite I laser from Continuum (532 nm, 16 mJ, 3–5 ns pulse length, 10 Hz) under rigorous stirring. The diameter of the laser beam was determined to be 3 mm, hence, the energy density was approximately 230 mJ cm^{-2}.

Spectroscopy and imaging

At certain time intervals, UV-Vis spectra were recorded using a Jasco 650 photospectrometer. Furthermore, 2 μl of the sample were removed and dried on an air plasma cleaned Si-chip. The dried GNPs were imaged on an Agilent 5500 atomic force microscope (AFM) using a Tap 150 cantilever in the tapping mode and analyzed using the software Gwyddion 2.39.

In order to perform surface enhanced Raman scattering (SERS) measurements, higher GNP concentrations are required to obtain a sufficiently high signal enhancement and the citrate capping has to be reduced to minimize its contribution to the signal. Therefore, 60 nm GNPs were centrifuged for 10 min at 1000*g* and the supernatant was discarded. The residuum was redissolved in Millipore water and the centrifugation was repeated two more times. The Raman spectra of a 20 μl droplet of the analyte solution positioned on a clean glass slide were recorded using a Horiba Labram Raman microscope equipped with a 9.1 mW 633 nm laser that was focused by a 60× Olympus immersion objective. Data were processed using Origin 9.1 and the background of all Raman spectra was subtracted using a cubic spline fit.

Acknowledgements

This research was supported by the Federal Institute of Materials Research (BAM), a Marie Curie FP7 Integration Grant within the 7th European Union Framework Programme, the Deutsche Forschungsgemeinschaft (DFG) and the University of Potsdam.

References

1 J. A. Webb and R. Bardhan, *Nanoscale*, 2014, **6**, 2502.
2 A. Latorre, C. Posch, Y. Garcimartín, A. Celli, M. Sanlorenzo, I. Vujic, J. Ma, M. Zekhtser, K. Rappersberger, S. Ortiz-Urda and Á. Somoza, *Nanoscale*, 2014, **6**, 7436.
3 T. Zheng, N. Pierre-Pierre, X. Yan, Q. Huo, A. J. O. Almodovar, F. Valerio, I. Rivera-Ramirez, E. Griffith, D. D. Decker, S. Chen and N. Zhu, *ACS Appl. Mater. Interfaces*, 2015, **7**, 6819–6827.
4 K. T. Butterworth, S. J. McMahon, F. J. Currell and K. M. Prise, *Nanoscale*, 2012, **4**, 4830.
5 K. Haume, S. Rosa, S. Grellet, M. A. Śmiałek, K. T. Butterworth, A. V. Solov'yov, K. M. Prise, J. Golding and N. J. Mason, *Cancer Nanotechnol.*, 2016, **7**, DOI: 10.1186/s12645-016-0021-x.
6 X. Huang, P. K. Jain, I. H. El-Sayed and M. A. El-Sayed, *Lasers Med. Sci.*, 2008, **23**, 217–228.
7 A. M. Gobin, M. H. Lee, N. J. Halas, W. D. James, R. A. Drezek and J. L. West, *Nano Lett.*, 2007, **7**, 1929–1934.
8 D. Jaque, L. Martínez Maestro, B. del Rosal, P. Haro-Gonzalez, A. Benayas, J. L. Plaza, E. Martín Rodríguez and J. García Solé, *Nanoscale*, 2014, **6**, 9494.
9 N. S. Abadeer and C. J. Murphy, *J. Phys. Chem. C*, 2016, **120**, 4691–4716.
10 X. Huang, B. Kang, W. Qian, M. A. Mackey, P. C. Chen, A. K. Oyelere, I. H. El-Sayed and M. A. El-Sayed, *J. Biomed. Opt.*, 2010, **15**, 058002.
11 T. Helleday, E. Petermann, C. Lundin, B. Hodgson and R. A. Sharma, *Nat. Rev. Cancer*, 2008, **8**, 193–204.
12 C. J. Lord and A. Ashworth, *Nature*, 2012, **481**, 287–294.
13 S. Vogel, J. Rackwitz, R. Schürman, J. Prinz, A. R. Milosavljević, M. Réfrégiers, A. Giuliani and I. Bald, *J. Phys. Chem. Lett.*, 2015, **6**, 4589–4593.
14 C. T. Middleton, K. de La Harpe, C. Su, Y. K. Law, C. E. Crespo-Hernández and B. Kohler, *Annu. Rev. Phys. Chem.*, 2009, **60**, 217–239.
15 A. Carattino, S. Khatua and M. Orrit, *Phys. Chem. Chem. Phys.*, 2016, **18**, 15619–15624.
16 V. K. Pustovalov, *RSC Adv.*, 2016, **6**, 81266–81289.
17 Y. Takeda, T. Kondow and F. Mafuné, *Phys. Chem. Chem. Phys.*, 2011, **13**, 586–592.
18 R. Schürmann and I. Bald, *J. Phys. Chem. C*, 2016, **120**, 3001–3009.
19 D. Lin, R. He, S. Li, Y. Xu, J. Wang, G. Wei, M. Ji and X. Yang, *ACS Chem. Neurosci.*, 2016, **7**, 1728–1736.
20 M. Strasser, K. Setoura, U. Langbein and S. Hashimoto, *J. Phys. Chem. C*, 2014, **118**, 25748–25755.
21 S. Hashimoto, T. Katayama, K. Setoura, M. Strasser, T. Uwada and H. Miyasaka, *Phys. Chem. Chem. Phys.*, 2016, **18**, 4994–5004.
22 T. Katayama, K. Setoura, D. Werner, H. Miyasaka and S. Hashimoto, *Langmuir*, 2014, **30**, 9504–9513.
23 K. Metwally, S. Mensah and G. Baffou, *J. Phys. Chem. C*, 2015, **119**, 28586–28596.
24 K. Yamada, K. Miyajima and F. Mafuné, *J. Phys. Chem. C*, 2007, **111**, 11246–11251.
25 I. Baccarelli, I. Bald, F. A. Gianturco, E. Illenberger and J. Kopyra, *Phys. Rep.*, 2011, **508**, 1–44.

26 I. Bald, I. Dąbkowska, E. Illenberger and O. Ingólfsson, *Phys. Chem. Chem. Phys.*, 2007, **9**, 2983–2990.
27 J. W. Shay and W. E. Wright, *Semin. Cancer Biol.*, 2011, **21**, 349–353.
28 N. Kim, M. Piatyszek, K. Prowse, C. Harley, M. West, P. Ho, G. Coviello, W. Wright, S. Weinrich and J. Shay, *Science*, 1994, **266**, 2011–2015.
29 H. Han and L. H. Hurley, *Trends Pharmacol. Sci.*, 2000, **21**, 136–142.
30 J. Liu, *Phys. Chem. Chem. Phys.*, 2012, **14**, 10485.
31 J. M. Carnerero, A. Jimenez-Ruiz, P. M. Castillo and R. Prado-Gotor, *ChemPhysChem*, 2017, **18**, 17–33.
32 S. Azizian, *J. Colloid Interface Sci.*, 2004, **276**, 47–52.
33 C. Van Bree, N. A. P. Franken, P. J. M. Bakker, L. J. Klomp-Tukker, G. W. Barendsen and J. B. A. Kipp, *Int. J. Radiat. Oncol., Biol., Phys.*, 1997, **39**, 489–496.
34 A. Keller, J. Rackwitz, E. Cauët, J. Liévin, T. Körzdörfer, A. Rotaru, K. V. Gothelf, F. Besenbacher and I. Bald, *Sci. Rep.*, 2014, **4**, 7391.
35 J. Rackwitz, J. Kopyra, I. Dąbkowska, K. Ebel, M. L. Ranković, A. R. Milosavljević and I. Bald, *Angew. Chem., Int. Ed.*, 2016, **55**, 10248–10252.
36 M. Wieczór, P. Wityk, J. Czub, L. Chomicz and J. Rak, *Chem. Phys. Lett.*, 2014, **595–596**, 133–137.
37 S. Wang, P. Zhao, C. Zhang and Y. Bu, *ChemPhysChem*, 2016, **17**, 1669–1677.
38 L. Chomicz, J. Leszczynski and J. Rak, *J. Phys. Chem. B*, 2013, **117**, 8681–8688.
39 Y. Park, K. Polska, J. Rak, J. R. Wagner and L. Sanche, *J. Phys. Chem. B*, 2012, **116**, 9676–9682.
40 A. Pyatenko, M. Yamaguchi and M. Suzuki, *J. Phys. Chem. C*, 2009, **113**, 9078–9085.
41 R. E. Cavicchi, D. C. Meier, C. Presser, V. M. Prabhu and S. Guha, *J. Phys. Chem. C*, 2013, **117**, 10866–10875.
42 N. Matsuo, H. Muto, K. Miyajima and F. Mafuné, *Phys. Chem. Chem. Phys.*, 2007, **9**, 6027.
43 A. Poletti, G. Fracasso, G. Conti, R. Pilot and V. Amendola, *Nanoscale*, 2015, **7**, 13702–13714.
44 D. Werner, S. Hashimoto and T. Uwada, *Langmuir*, 2010, **26**, 9956–9963.
45 G. González-Rubio, A. Guerrero-Martínez and L. M. Liz-Marzán, *Acc. Chem. Res.*, 2016, **49**, 678–686.
46 A. R. Khataee, M. Fathinia and S. Aber, *Ind. Eng. Chem. Res.*, 2010, **49**, 12358–12364.
47 G. Baffou and R. Quidant, *Chem. Soc. Rev.*, 2014, **43**, 3898.
48 X. Zhang, M. R. Servos and J. Liu, *Langmuir*, 2012, **28**, 3896–3902.
49 Y. Liu and L. Shen, *Langmuir*, 2008, **24**, 11625–11630.
50 X. Zhang, M. R. Servos and J. Liu, *J. Am. Chem. Soc.*, 2012, **134**, 7266–7269.
51 Y. Zu and Z. Gao, *Anal. Chem.*, 2009, **81**, 8523–8528.
52 J.-W. Park and J. S. Shumaker-Parry, *ACS Nano*, 2015, **9**, 1665–1682.
53 R. Dinkel, B. Braunschweig and W. Peukert, *J. Phys. Chem. C*, 2016, **120**, 1673–1682.
54 K. Siriwardana, M. Gadogbe, S. M. Ansar, E. S. Vasquez, W. E. Collier, S. Zou, K. B. Walters and D. Zhang, *J. Phys. Chem. C*, 2014, **118**, 11111–11119.
55 D. Huber, M. Beikircher, S. Denifl, F. Zappa, S. Matejcik, A. Bacher, V. Grill, T. D. Märk and P. Scheier, *J. Chem. Phys.*, 2006, **125**, 084304.
56 R. Schürmann and I. Bald, *Nanoscale*, 2017, **9**, 1951–1955.
57 L. Yu and N. Li, *Langmuir*, 2016, **32**, 5510–5518.
58 S. Basu, S. Jana, S. Pande and T. Pal, *J. Colloid Interface Sci.*, 2008, **321**, 288–293.
59 J. P. Vanegas, E. Zaballos-García and J. Pérez-Prieto, *Chem. Commun.*, 2014, **50**, 11335.
60 J. P. Vanegas, L. E. Peisino, S. Pocoví-Martínez, R. J. Zaragozá, E. Zaballos-García and J. Pérez-Prieto, *Chem. – Eur. J.*, 2013, **19**, 16248–16255.
61 W. Haiss, N. T. K. Thanh, J. Aveyard and D. G. Fernig, *Anal. Chem.*, 2007, **79**, 4215–4221.
62 A. Sarmah and R. K. Roy, *J. Phys. Chem. C*, 2015, **119**, 17940–17953.
63 J. Abelard, A. R. Wilmsmeyer, A. C. Edwards, W. O. Gordon, E. M. Durke, C. J. Karwacki, D. Troya and J. R. Morris, *J. Phys. Chem. C*, 2016, **120**, 13024–13031.

Electronic Supplementary Material (ESI) for Physical Chemistry Chemical Physics.

Electronic Supplementary Information

Effect of Adsorption Kinetics on Dissociation of DNA-Nucleobases on Gold Nanoparticles under Pulsed Laser Illumination

R. Schürmann[a,b] and I. Bald[a,b]*

[a]*Institute of Chemistry, Physical Chemistry, University of Potsdam, Karl-Liebknecht-Str. 24-25, 14776 Potsdam, Germany*

**Email: bald@uni-potsdam.de*

[b]*BAM Federal Institute for Materials Research and Testing, Richard-Willstätter-Str. 11, 12489 Berlin, Germany*

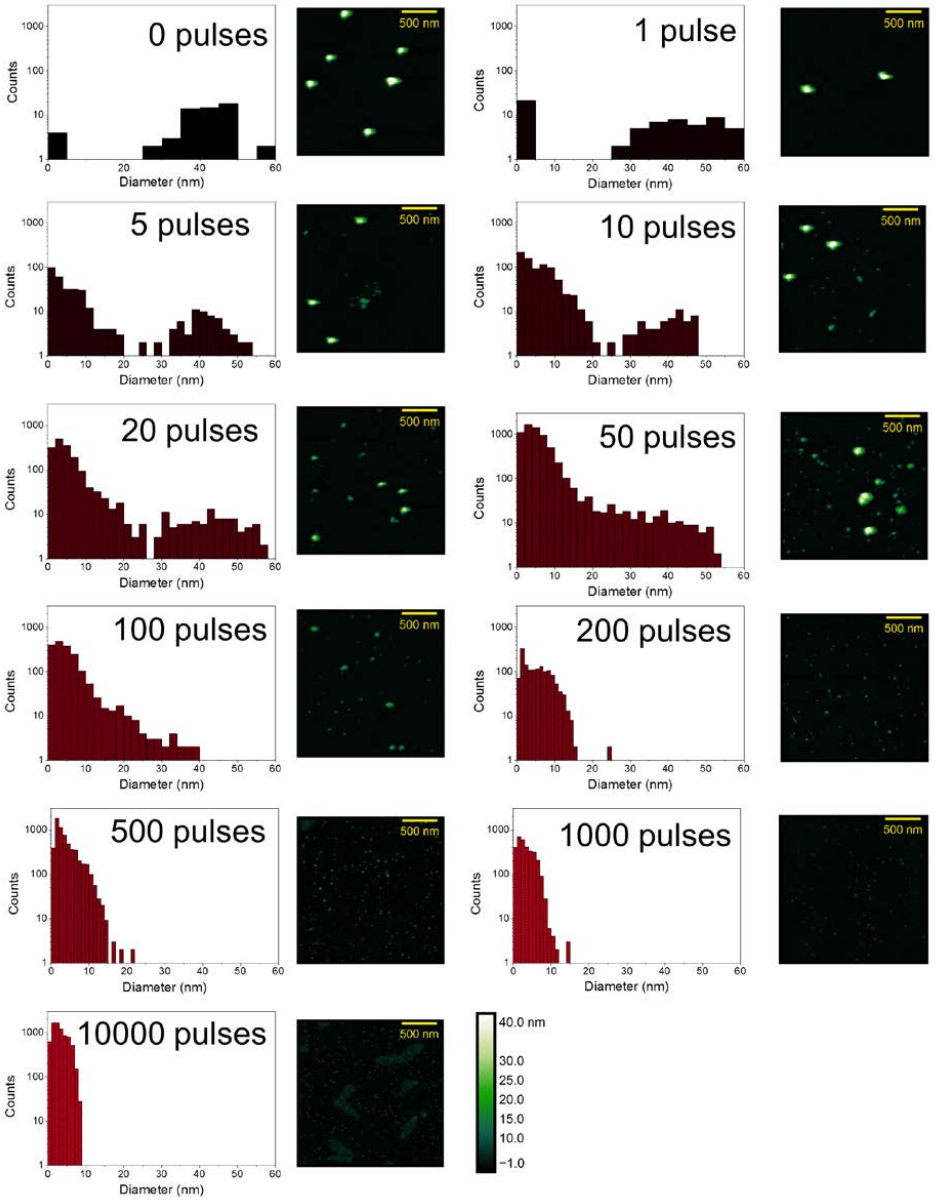

Figure S1: AFM images and size distribution of GNP with a nominal size of 40 nm dried on a Si-substrate after irradiation with a certain number of laser pulses.

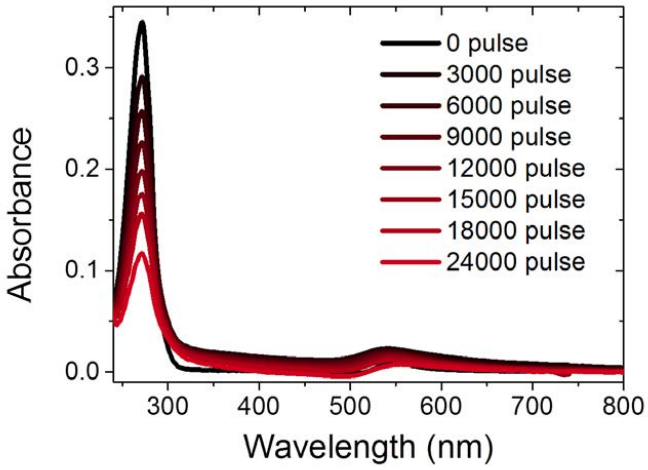

Figure S2: Absorbance spectra of irradiated ^{8Br}A and GNP corrected by subtracting a spectrum of the pure GNPs irradiated under the same experimental conditions. The features for wavelengths above 300 nm are caused by the aggregation of the nanoparticles.

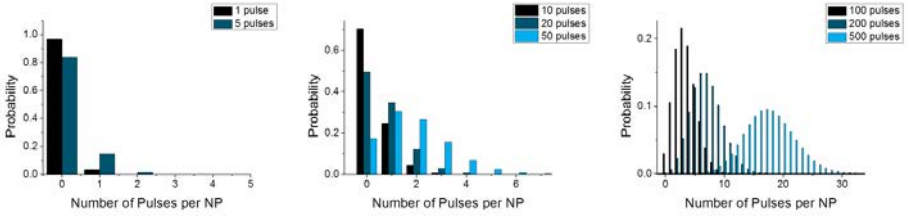

Figure S3: Poisson probability distribution of laser pulses that hit a GNP in the illuminated area.

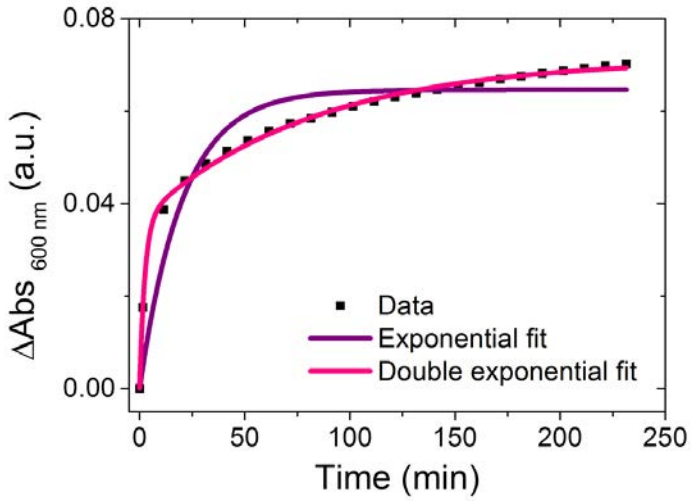

Figure S4: Increase of the Absorbance at 600 nm of irradiated GNP after the addition of 20 µM Cytosine.

4.5 M5: "Real-time monitoring of plasmon induced dissociative electron transfer to the potential DNA radiosensitizer 8-bromoadenine"

Robin Schürmann and Ilko Bald
Nanoscale 2017, 9, 1951 - 1955
DOI: 10.1039/C6NR08695K

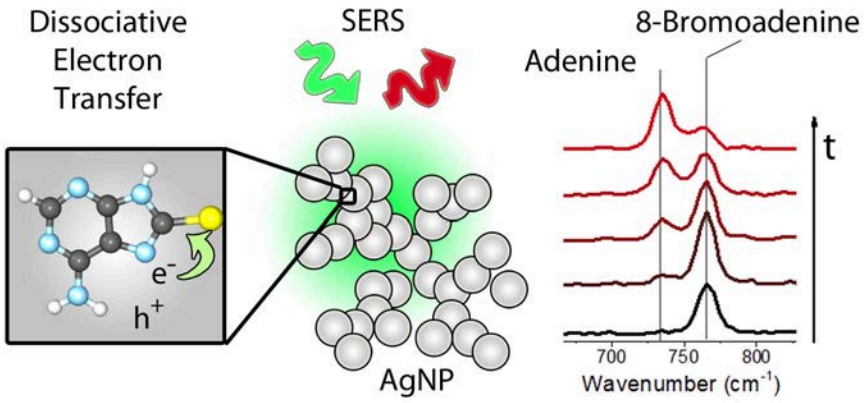

Author contributions to the manuscript:
I synthesized the AgNP solution and did all further sample preparations. I performed all AFM, UV-Vis spectroscopy and SERS measurement and analyzed the spectra and images. Furthermore, I interpreted the data and derived all kinetics equations. I prepared all figures for the manuscript and the supporting info. I prepared the manuscript in cooperation with Ilko Bald.

Nanoscale

PAPER

View Article Online
View Journal | View Issue

Cite this: *Nanoscale*, 2017, **9**, 1951

Real-time monitoring of plasmon induced dissociative electron transfer to the potential DNA radiosensitizer 8-bromoadenine†

R. Schürmann[a,b] and I. Bald*[a,b]

Received 7th November 2016,
Accepted 22nd December 2016

DOI: 10.1039/c6nr08695k

rsc.li/nanoscale

The excitation of localized surface plasmons in noble metal nanoparticles (NPs) results in different nanoscale effects such as electric field enhancement, the generation of hot electrons and a temperature increase close to the NP surface. These effects are typically exploited in diverse fields such as surface-enhanced Raman scattering (SERS), NP catalysis and photothermal therapy (PTT). Halogenated nucleobases are applied as radiosensitizers in conventional radiation cancer therapy due to their high reactivity towards secondary electrons. Here, we use SERS to study the transformation of 8-bromoadenine (^{8Br}A) into adenine on the surface of Au and AgNPs upon irradiation with a low-power continuous wave laser at 532, 633 and 785 nm, respectively. The dissociation of ^{8Br}A is ascribed to a hot-electron transfer reaction and the underlying kinetics are carefully explored. The reaction proceeds within seconds or even milliseconds. Similar dissociation reactions might also occur with other electrophilic molecules, which must be considered in the interpretation of respective SERS spectra. Furthermore, we suggest that hot-electron transfer induced dissociation of radiosensitizers such as ^{8Br}A can be applied in the future in PTT to enhance the damage of tumor tissue upon irradiation.

Introduction

Illumination of noble metal nanoparticles (NPs) with visible light leads to resonant oscillations of the electron gas, which are referred to as localized surface plasmons (LSP). In close proximity to the metal surface the electric field of the incoming and scattered light is highly enhanced by the LSP, which is exploited in surface enhanced Raman scattering (SERS), as the Raman scattering cross sections increase by several orders of magnitude.[1,2] LSP can relax inelastically *via* reemitting a photon or through a non-radiative channel *via* electron hole pair production.[3,4] These so called "hot electrons" can tunnel into unoccupied molecular orbitals of chemisorbed or physisorbed molecules and induce chemical reactions[5–9] that can be monitored in real time using SERS.[10,11]

Besides the direct electron transfer that is exploited in plasmonic catalysis "hot electrons" lose their energy very quickly *via* electron–electron scattering and subsequently *via* electron phonon scattering, which increases the temperature of the nanoparticles and their surroundings.[12] In photothermal therapy (PTT) the increased temperature around hollow AuNPs[13] or nanorods[14] is used to kill cancer cells under illumination with NIR-lasers.[15,16] Based on the work presented here we suggest that the combination of NPs with molecules incorporated in the DNA that strongly react with plasmon induced electrons might improve the efficiency of this therapy. Such potential radiosensitizers are halogenated nucleobases like 8-bromoadenie (^{8Br}A) that strongly interact with low energy electrons[17–20] *via* dissociative electron attachment (DEA)[21] whereby a transient negative ion decays into anionic and neutral fragments. This mechanism allows the damage of DNA below the ionization threshold.[22] Brominated nucleobases that can be easily incorporated into the DNA possess a high electron affinity and the C–Br-bond is easily cleaved by attachment of electrons close to 0 eV.[23,24] The formation of a radical inside the DNA leads to a strand break in a second step[25] and thus increases the single strand break cross section.[26]

Here we demonstrate the dissociative hot electron transfer from plasmonically excited Au and AgNPs to ^{8Br}A in a dry and aqueous environment monitored in real time using SERS. The reaction follows a fractal like kinetics and shows a fast reaction rate, as under typical SERS settings the majority of the analyte molecules are decomposed in a few hundred milliseconds.

[a]*Institute of Chemistry, Physical Chemistry, University of Potsdam, Karl-Liebknecht-Str. 24-25, 14776 Potsdam, Germany. E-mail: bald@uni-potsdam.de*
[b]*BAM Federal Institute for Materials Research and Testing, Richard-Willstätter-Str. 11, 12489 Berlin, Germany*

†Electronic supplementary information (ESI) available. See DOI: 10.1039/c6nr08695k

View Article Online
Paper Nanoscale

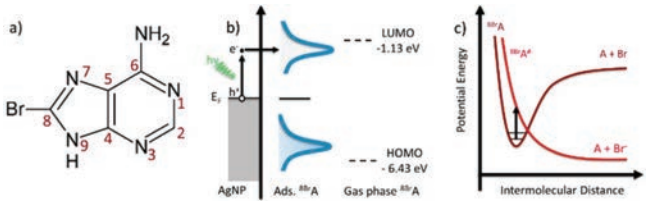

Fig. 1 (a) Molecular structure of ^{8Br}A; (b) schematic "hot electron" excitation in the silver nanoparticle with subsequent tunnelling into the LUMO of the adsorbed ^{8Br}A; (c) schematic potential energy diagram illustrating DEA to ^{8Br}A.

Results and discussion

LSP that are created *via* laser illumination of AgNPs can decay non-radiatively by the formation of an electron hole pair, whereby the electron is excited from the sp-conduction band and has an energy between E_f and $E_f + h\nu$ (Fig. 1):

$$h\nu + \mathrm{AgNP} \rightarrow e^- + h^+ \quad (1)$$

On a time scale below 10 fs the excited electron loses its energy *via* electron–electron scattering until the electron gas approaches a Fermi–Dirac distribution.[3] These so called "hot electrons" can tunnel into the lowest unoccupied molecular orbital (LUMO) of adsorbed ^{8Br}A molecules and form a transient negative ion (TNI).[21] Beyond that the electron can be directly injected into the LUMO *via* a coherent tunneling process before the electron interacts with the electron gas.[27,28] In both cases a relatively unstable ^{8Br}A anion is formed that can relax through the cleavage of the C8–Br bond.[17,18]

$$^{8Br}A + e^- \rightarrow {}^{8Br}A^{\#-} \rightarrow A^{\bullet} + Br^- \quad (2)$$

In the present experiment a AgNP solution with adsorbed ^{8Br}A was dried on a Si wafer and SERS spectra were recorded as a function of the illumination time using a 532 nm laser with 250 μW focused on a 10 μm diameter spot. For a relatively short time of around 1 s Raman spectra were recorded with a band structure that is clearly assigned to ^{8Br}A (Fig. 2a). The most remarkable bands are the ring breathing mode at 767 cm^{-1} and the C–Br bending- and stretching-mode at 299 cm^{-1} and 575 cm^{-1}, respectively. With ongoing illumination, these bands are significantly decreasing in their intensity while simultaneously new bands arise at 336 cm^{-1}, 629 cm^{-1}, 735 cm^{-1}, 967 cm^{-1}, 1267 cm^{-1}, 1329 cm^{-1}, 1409 cm^{-1}, 1465 cm^{-1} and 1575 cm^{-1} (indicated by a grey background in Fig. 2) that can be assigned to the SERS-spectrum of adenine (A).[29] This indicates that the C–Br bond of the adsorbed ^{8Br}A ruptures during laser irradiation most likely due to the dissociative attachment of an additional electron according to eqn (2). By capture of an H radical from the environment A is formed on the nanoparticle surface. A similar reaction has previously been demonstrated already with uracil.[24] The transformation from ^{8Br}A to A can be tracked by the intensity of the ring breathing mode at 735 cm^{-1} and 767 cm^{-1} (Fig. 2c).

The rate of the reaction depends on the concentration of ^{8Br}A and the concentration of "hot electrons" in the illuminated area:

$$\mathrm{Rate} = -k\,[^{8Br}A]\,[e^-] \quad (3)$$

However, it is difficult to monitor both concentrations simultaneously, in particular the number of hot electrons remains unknown. During continuous laser irradiation, a constant equilibrium concentration of "hot electrons" can be assumed as they are frequently reproduced and their timescales for excitation and relaxation are several orders of magnitude shorter than the timescales of the DEA reaction. Hence pseudo first-order kinetics is assumed to determine the observed rate coefficient k_{obs} of the dissociation of ^{8Br}A:

$$k_{obs} = \frac{1}{t} \cdot \ln \frac{[^{8Br}A]_0}{[^{8Br}A]_t} \quad (4)$$

In Fig. 3a k_{obs} is plotted against time t, which demonstrates that the rate coefficient is not constant as expected for a (pseudo-) first order reaction, but decreases in time. This is

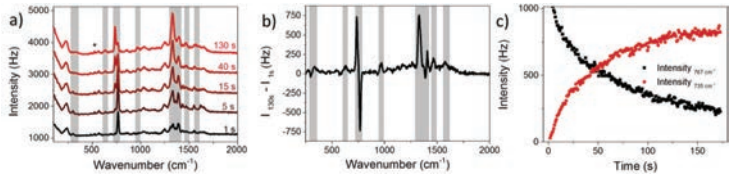

Fig. 2 (a) SERS spectra of ^{8Br}A on AgNPs dried on a Si-substrate for different illumination times. The Si band from the substrate at 521 cm^{-1} is marked with a *. (b) Difference spectra of t = 1 s and t = 130 s (same data set like in a). (c) Intensity of ring-breathing mode of ^{8Br}A at 767 cm^{-1} *vs.* ring breathing mode of A at 735 cm^{-1}.

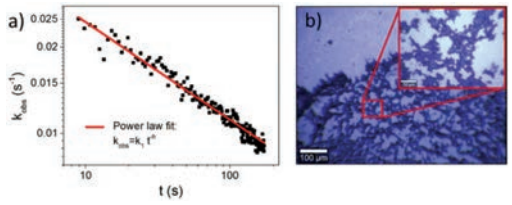

Fig. 3 (a) Observed rate coefficient plotted against illumination time shows a power law dependence with h = 0.34 ± 0.01. (b) Light microscopy image of a dried AgNP sample on Si reveals a fractal structure of aggregated AgNPs.

attributed to the inhomogeneous distribution of reaction sites on the surface giving rise to a broad range of signal intensities and thus rate constants. In close proximity to the noble metal surface the electric field of the incoming and scattered light is strongly increased due to its interaction with the LSP, which strongly depends on the arrangement and structure of the nanoparticles. This electromagnetic enhancement increases the intensity of the Raman signal (I_j) by some orders of magnitude:[1]

$$I_j = \alpha^2 \cdot g_j^4 \cdot I_0 \quad (5)$$

where α is the Raman scattering cross section, g_j is the electromagnetic enhancement factor of a specific reaction site and I_0 is the incoming laser power. The detected Raman signal is the sum of all signals from all molecules in the focused area:

$$I_{\mathrm{SERS}} = \sum_j I_j(x,y) \quad (6)$$

When assuming that the concentration of hot electrons at a certain position is in coherence with the magnitude of LSP, the local reaction rate correlates with the electromagnetic enhancement in the "hotspot". Hence the $^{8\mathrm{Br}}$A molecules that experience the strongest signal enhancement have the highest decomposition probability. Thus, the reaction centers with the highest rates only contribute in the beginning to the overall reaction, and consequently the observed reaction rate decreases with time.

This time dependence can be characterized by fractal-like kinetics,[30] which describes heterogeneous reactions with geometrical constraints like hot electron catalyzed reactions,[31] with a time dependent rate coefficient:

$$k_{\mathrm{obs}} = k_1 \cdot t^{-h}, 0 \leq h \leq 1, t \geq 1, \quad (7)$$

where h is the fractal dimension of the system, t is the time/1 s and k_1 is the rate coefficient at t = 1.

According to eqn (4) k_{obs} strongly depends on the starting intensity of the $^{8\mathrm{Br}}$A signal that rapidly decreases during the first integration time. Assuming that the Raman enhancement factors of $^{8\mathrm{Br}}$A and A are equivalent the sum of the intensities at 735 cm^{-1} and 767 cm^{-1} was used to determine the starting intensity of the 767 cm^{-1} peak.

20 measurements on the same sample at different positions have been performed and h was determined to be h = 0.36 ± 0.09, which indicates a 2-dimensional fractal lattice, for which h = 0.33.[30] Fig. 3a shows one of these measurements. The determined fractal dimension is in accordance with the fractal shape of the nanoparticle aggregates, which were observed in the bright field images (Fig. 3b) and described previously.[32,33] It has to be mentioned that the standard deviation of h is larger than the error of h determined from the power law fit, as the composition of aggregates may vary on different positions of the sample.

Since k_1 and h are not independent fitting parameters, h was set to 0.33 to avoid artifacts in the subsequent analysis. The rate constant k_1 was determined as a function of the incident laser power P and fitted with a power function (see Fig. 4a):

$$k_1 = a \cdot P^b \quad (8)$$

The linear correlation between k_1 and P with b = 0.92 ± 0.09 indicates a one photon process that is characteristic for hot electron induced reactions. For (partly) thermally induced reactions a super-linear power law dependence[5] would be expected due to the exponential dependence of the reaction rate on temperature according to the Arrhenius equation. This conclusion is valid as long as the temperature on the AgNPs rises linearly with the incident laser power.[12] Beyond that a direct photoexcitation is also unlikely for low photon fluences (10^2–10^4 W cm^{-2}), because the HOMO–LUMO gap is about 5.3 eV according to *ab initio* calculations performed at the MP2/aug-cc-pVDZ level of theory.[34] Therefore at least 3 photons with 2.33 eV (532 nm) are required to overcome the HOMO–LUMO gap.

We have also studied the transformation from $^{8\mathrm{Br}}$A to A on a nanoparticle surface for 633 nm and 785 nm laser wavelength as well as on gold nanoparticles (AuNPs). In all cases a linear dependence on the laser power was observed (Fig. S3 in the ESI† and Fig. 4a). This is remarkable as the work functions of AgNPs (4.3 eV) and AuNPs (5.1 eV) are well above the photon energy of 1.61 eV (785 nm). This supports the model of dissociative electron transfer into the low lying LUMO of $^{8\mathrm{Br}}$A. Normalizing k_1 by the laser power reveals that the reaction rate increases with photon energy and is lower on AuNPs compared

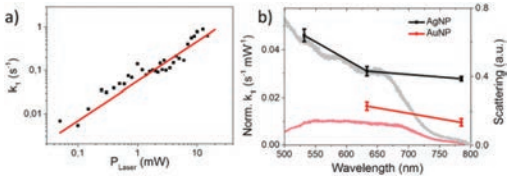

Fig. 4 (a) Rate constant k_1 as a function of the incident laser power fitted by a power law function ($k_1 = a \cdot P_{\mathrm{Laser}}{}^b$ with b = 0.92 ± 0.09). (b) Rate constant normalized by laser intensity for $^{8\mathrm{Br}}$A dissociation on AgNPs (black) and AuNPs (red) for different laser wavelength and typical dark field spectra of aggregated NPs (grey and light red).

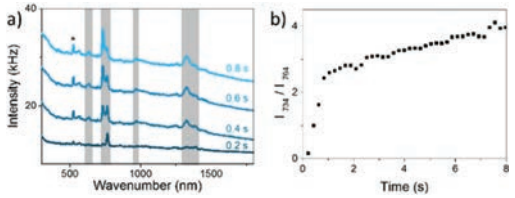

Fig. 5 (a) SERS spectra of ^{8Br}A on AgNPs in aqueous solution taken after different illumination times, irradiated with 785 nm with a power of 5.1 mW. The Si-band is marked with a *. (b) Ratio between ^{8Br}A ring breathing mode at 764 cm^{-1} and A ring breathing mode at 734 cm^{-1} as a function of the illumination time (same data as in a).

to AgNPs (see Fig. 4b) most probably due to the increased plasmonic enhancement on the AgNPs. We have recorded dark field scattering spectra on several spots of the sample, which show a broad surface plasmon resonance (SPR) ranging from around 400 nm for AgNPs and 500 nm for AuNPs to 700 nm. In particular for the near infrared photons with 785 nm wavelength, where the plasmonic enhancement is relatively weak, the SPR does not directly correspond to the normalized k_1, even though the major trends are reflected. This might be explained by a resonant direct electron transfer into the adsorbed ^{8Br}A. Nevertheless, on the basis of the present data it is not possible to say whether the reaction is dominated by a coherent tunnelling process or by Fermi–Dirac distributed electrons scattering into the molecular orbitals of the ^{8Br}A molecule. In order to study the influence of the environment additional measurements have been performed in water using a 785 nm laser with 5.1 mW. Already after less than 400 ms more than half of the ^{8Br}A in the relevant hotspots are dissociated (see Fig. 5). In solution it is difficult to determine accurate rate constants as the photoproduct is diffusing out of the focused area, hence the observed reaction rates represent only an infimum of the real reaction rate. In an aqueous environment the electron tunneling is much more favorable as the tunneling barrier is lowered by 0.8 eV.[35] Therefore, an increased speed of reaction is expected as compared to dry samples.

Conclusions

We demonstrate a dissociative electron transfer from laser illuminated noble metal nanoparticles to the potential DNA radiosensitizer ^{8Br}A dried on a Si substrate as well as in solution. The reaction is described with fractal like kinetics. The observed interaction between the nanoparticles and ^{8Br}A might help to improve photothermal cancer therapy. As the utilized substrate as well as the applied laser settings in this experiment were typical of SERS measurements, the plasmonically catalysed reaction can cause problems in the analysis of the Raman spectra, because the probe laser for the spectral analysis is the same that induces the decomposition of the analyte. As the time scale of the reaction is equivalent or faster than the typical accumulation time, one has to distinguish carefully between the SERS spectrum of the analyte molecule and its photoproducts. This should be done especially for molecules containing electrophilic groups such as halogens[36,37] or nitro groups,[38] which are known to decompose easily as a consequence of their interaction with "hot electrons".

Experimental section

Chemicals

^{8Br}A was purchased from Carbosynth Ltd (UK) and A, silver nitrate and sodium citrate were purchased from Sigma Aldrich (Germany). All chemicals were diluted in Millipore water and used without further purifications. Gold nanoparticles with a diameter of 40 nm were purchased from BBI solutions.

Silver nanoparticle preparation

AgNPs were prepared by the well-known procedure of Lee and Meisel.[39] Briefly, 50 ml of 1 mM $AgNO_3$ solution were brought to a rolling boil and 5 ml 38.8 mM trisodiumcitrate were added while the boiling was continued for 1 h under rigorous stirring. The produced AgNPs are 36 ± 10 nm in diameter and show an extinction maximum at 413 nm. The size distribution was determined by atomic force microscopy (AFM) using a Nanosurf Flex AFM equipped with a Tap150-Al-G cantilever in the tapping mode and image processing was performed with Gwyddeon 2.39 software. The UV-Vis-spectra were recorded using a Nanodrop 2000 of Thermo scientific.

Surface enhanced Raman spectroscopy

In order to prepare the samples for the Raman measurements 100 μl of a 50 μM ^{8Br}A solution were incubated for 2 h in 400 μl of the AgNP solution. Subsequently the dispersion was centrifuged and the residue was diluted in Millipore water two times. After a final centrifugation step a 2 μl droplet of the nanoparticle solution was dried on an oxygen plasma cleaned Si wafer. For the measurements in a liquid environment a 4 μl droplet was placed on a Si wafer that was surrounded by a bath of Millipore water to reduce the evaporation of the droplet. The Raman spectra were recorded using a Witec alpha 300 Raman-microscope with a 532 nm and a 785 nm laser and a Horiba Labram Raman-microscope with a 633 nm laser. The laser power was varied in the range from 50 μW to 50 mW and focused with a 10× objective on the sample. Scattering spectra of the sample were obtained using the Witec alpha 300 dark field unit with a 50× HD objective from Zeiss. Data analysis and processing were performed with Origin 9.1 software.

Acknowledgements

This research was supported by the Federal Institute for Materials Research (BAM), a Marie Curie FP7 Integration Grant within the 7th European Union Framework Programme, by the Deutsche Forschungsgemeinschaft (DFG) and the University

of Potsdam. We thank Dr Iwona Dąbkowska, University of Gdańsk, for providing results from *ab initio* calculations.

References

1 M. Moskovits, *J. Raman Spectrosc.*, 2005, **36**, 485–496.
2 J. Prinz, C. Heck, L. Ellerik, V. Merk and I. Bald, *Nanoscale*, 2016, **8**, 5612–5620.
3 G. Baffou and R. Quidant, *Chem. Soc. Rev.*, 2014, **43**, 3898.
4 J. Y. Park, L. R. Baker and G. A. Somorjai, *Chem. Rev.*, 2015, **115**, 2781–2817.
5 P. Christopher, H. Xin, A. Marimuthu and S. Linic, *Nat. Mater.*, 2012, **11**, 1044–1050.
6 S. Mukherjee, F. Libisch, N. Large, O. Neumann, L. V. Brown, J. Cheng, J. B. Lassiter, E. A. Carter, P. Nordlander and N. J. Halas, *Nano Lett.*, 2013, **13**, 240–247.
7 M. J. Kale, T. Avanesian and P. Christopher, *ACS Catal.*, 2014, **4**, 116–128.
8 T. Wadayama and M. Yokawa, *Chem. Phys. Lett.*, 2006, **428**, 348–351.
9 S. M. Kim, S. J. Lee, S. H. Kim, S. Kwon, K. J. Yee, H. Song, G. A. Somorjai and J. Y. Park, *Nano Lett.*, 2013, **13**, 1352–1358.
10 Z. Zhang, T. Deckert-Gaudig and V. Deckert, *Analyst*, 2015, **140**, 4325–4335.
11 W. Xie and S. Schlücker, *Nat. Commun.*, 2015, **6**, 7570.
12 G. Baffou and R. Quidant, *Laser Photonics Rev.*, 2013, **7**, 171–187.
13 A. M. Gobin, M. H. Lee, N. J. Halas, W. D. James, R. A. Drezek and J. L. West, *Nano Lett.*, 2007, **7**, 1929–1934.
14 X. Huang, P. K. Jain, I. H. El-Sayed and M. A. El-Sayed, *Laser. Med. Sci.*, 2008, **23**, 217–228.
15 D. Jaque, L. Martínez Maestro, B. del Rosal, P. Haro-Gonzalez, A. Benayas, J. L. Plaza, E. Martín Rodríguez and J. García Solé, *Nanoscale*, 2014, **6**, 9494.
16 J. A. Webb and R. Bardhan, *Nanoscale*, 2014, **6**, 2502.
17 L. Chomicz, J. Leszczynski and J. Rak, *J. Phys. Chem. B*, 2013, **117**, 8681–8688.
18 M. Wieczór, P. Wityk, J. Czub, L. Chomicz and J. Rak, *Chem. Phys. Lett.*, 2014, **595–596**, 133–137.
19 Y. Park, K. Polska, J. Rak, J. R. Wagner and L. Sanche, *J. Phys. Chem. B*, 2012, **116**, 9676–9682.
20 J. Rackwitz, J. Kopyra, I. Dąbkowska, K. Ebel, M. L. Ranković, A. R. Milosavljević and I. Bald, *Angew. Chem., Int. Ed.*, 2016, **55**, 10248–10252.
21 I. Bald, J. Langer, P. Tegeder and O. Ingólfsson, *Int. J. Mass Spectrom.*, 2008, **277**, 4–25.
22 B. Boudaïffa, *Science*, 2000, **287**, 1658–1660.
23 H. Abdoul-Carime, M. A. Huels, F. Brüning, E. Illenberger and L. Sanche, *J. Chem. Phys.*, 2000, **113**, 2517.
24 R. Schürmann and I. Bald, *J. Phys. Chem. C*, 2016, **120**, 3001–3009.
25 S. Cecchini, S. Girouard, M. A. Huels, L. Sanche and D. J. Hunting, *Radiat. Res.*, 2004, **162**, 604–615.
26 A. Keller, J. Rackwitz, E. Cauët, J. Liévin, T. Körzdörfer, A. Rotaru, K. V. Gothelf, F. Besenbacher and I. Bald, *Sci. Rep.*, 2014, **4**, 7391.
27 K. Watanabe, D. Menzel, N. Nilius and H.-J. Freund, *Chem. Rev.*, 2006, **106**, 4301–4320.
28 C. Boerigter, U. Aslam and S. Linic, *ACS Nano*, 2016, **10**, 6108–6115.
29 M. Pagliai, S. Caporali, M. Muniz-Miranda, G. Pratesi and V. Schettino, *J. Phys. Chem. Lett.*, 2012, **3**, 242–245.
30 R. Kopelman, *Science*, 1988, **241**, 1620–1626.
31 T. L. Thompson and J. T. Yates, *J. Phys. Chem. B*, 2006, **110**, 7431–7435.
32 T. Kim, C.-H. Lee, S.-W. Joo and K. Lee, *J. Colloid Interface Sci.*, 2008, **318**, 238–243.
33 D. A. Weitz and M. Oliveria, *Phys. Rev. Lett.*, 1984, **52**, 1433–1436.
34 Private communication with Dr Iwona Dąbkowska.
35 P. C. do Couto, B. J. Costa Cabral and S. Canuto, *Chem. Phys. Lett.*, 2006, **429**, 129–135.
36 N. Camillone, K. A. Khan, P. J. Lasky, L. Wu, J. E. Moryl and R. M. Osgood, *J. Chem. Phys.*, 1998, **109**, 8045.
37 E. P. Marsh, T. L. Gilton, W. Meier, M. R. Schneider and J. P. Cowin, *Phys. Rev. Lett.*, 1988, **61**, 2725–2725.
38 Z. Zhang, T. Deckert-Gaudig, P. Singh and V. Deckert, *Chem. Commun.*, 2015, **51**, 3069–3072.
39 P. C. Lee and D. Meisel, *J. Phys. Chem.*, 1982, **86**, 3391–3395.

Electronic Supplementary Material (ESI) for Nanoscale.

Electronic Supplementary Information

Real-Time Monitoring of Plasmon Induced Dissociative Electron Transfer to the Potential DNA Radiosensitizer 8-Bromoadenine

R. Schürmann[a,b] and I. Bald[a,b]*

[a]*Institute of Chemistry, Physical Chemistry, University of Potsdam, Karl-Liebknecht-Str. 24-25, 14776 Potsdam, Germany*

**Email: bald@uni-potsdam.de*

[b]*BAM Federal Institute for Materials Research and Testing, Richard-Willstätter-Str. 11, 12489 Berlin, Germany*

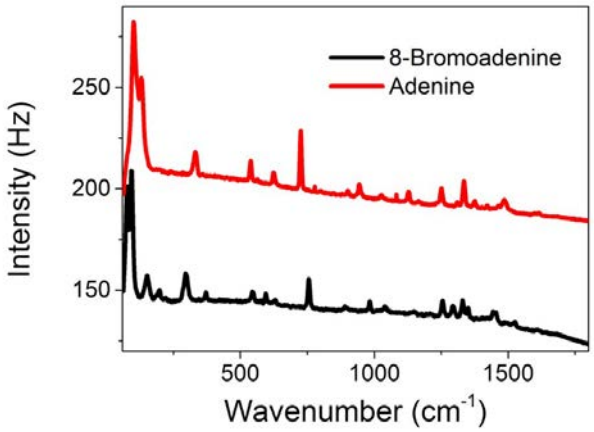

Figure S1: Raman spectra of ^{8Br}A and A powder taken with a 785 nm laser.

NRS 8BrA	SERS ^{8Br}A	Description[1]	NRS Adenine	SERS Adenine	Description [2]
79			102		
93			128		
151			331	337	Δ(C6-C5-N7) - Δ(N1-C6-N6) + Δ(N3-C4-N9)
196			538		Δ(N1-C6-C5) + Δ(C2-N3-C4)
220w			562	565	Γ(N1-C2-N3) + γ(C2-H) - γ(C8-H)
296	299	τ(C4-C5), γ(C8-Br), τ(Pyr ring)	624	628	Δ(C4-C5-N7) - Δ(C4-N9-C8) + Δ (N1-C6-N6)

344	357	Δ(C6-N10), ν(C8-Br), δ(C8-Br), α(Im ring)	725	735	Pyr + Im ring breathing
371			777		ω(NH2)
545	568	δ(Pyr Ring), δ(C8-Br), δ(C6-N10)	900	916	Δ(N1-C2-N3) + Δ(C8-N9-C5)
594		τ(Pyr Ring), τ(Im Ring), γ(C6-N10)	944	968	Δ(N7-C8-N9); γ(N9-H)
628	635	δ(Im Ring), δ(Pyr Ring), ν(C5-C6)	1026	1043	t(NH2); ν(C6-N1)
755	767	Pyr + Im ring breathing	1082	1080	
892		δ(Pyr Ring), ν(C5-N7)	1127	1121	δ(C8-H); ν(C3-N3) + ν(C4-N9) - ν(C5-C6) - ν(C5-N7)
982	984	r(NH2), ν(C6-N1), ν(C2-N1)	1164	1174	δ(C8-H) - δ(N9-H); ν(C8-N9) + (C5-N7) - ν(C4-N9) - ν(C4-N3) - ν(C2-N3)
1040	1032	ν(C8-N9), δ(N9-H), ν(C4-N9)	1250	1267	δ(C8-H) + δ(N9-H); ν(C2-N3) + ν(C8-N7) + ν(C2-N1) - ν(C5-N7) - ν(C4-N9)
1146w	1150	δ(N9-H), ν(C4-N3), δ(Im ring), ν(C4-N9)	1310		δ(C2-H); ν(C2-N3) + ν(C5-N7) - ν(C8-N7) - ν(C4-N9)
1205w			1334	1329	δ(C2-H); ν(C2-N3) + ν (C5-N7) - ν(C8-N7) - ν(C4-N9)
1255	1246	ν(C5-N7), r(NH2), ν(C2-N3), ν(C2-N1)	1374		δ(N9-H); δ(C8-H); ν(C8-N9) + ν(C4-C5) + ν(C2-N3) + ν(C6-N1) - ν(C5-C6) - ν(C2-N1) - ν(C4-N3) - ν(C8-N7)
1294		ν(C2-N3), ν(C5-N7)	1421	1410	ν(C4-N9) + ν(C8-N7) + ν(C6-N1) - ν(C4-C5) - ν(C4-N3) - ν(C8-N9)
1330	1332	δ(C2-H), ν(C6-N10), ν(C8-N9), ν(C2-N1)	1465	1465	δ(N9-H) - δ(C8-H) + δ(C2-H); ν(C8-N9) + ν(C2-N1) + ν(C6-N1) - ν(C2-N3) - ν(C8-N7) - ν(C6-N6)
1447	1432	ν(C8-N7)	1614w	1597	α(NH2); δ(N9-H); ν(C4-C5) + ν(C2-N1) - ν(C5-C6) - ν(C6-N1) - ν(C4-N3) - ν(C2-N3)
1488	1464	δ(C2-H), ν(C6-N1), ν(C6-N10), δ(NH2)			
1520	1552	Δ(NH2), ν(C4-C5), ν(C5-C6)			

Table 1: Assignment NRS bands of A and ^{8Br}A observed in the present experiment and comparison to values reported previously. ω: wagging; δ: in-plane deformation; Δ: in-plane ring deformation of skeletal atoms; γ: out-of-plane deformation; Γ: out-of-plane ring deformation of skeletal atoms; α: scissoring; τ: torsion; t: twisting; ν: stretching; r: rocking; Pyr: pyrimidine; Im: Imidazol. Atoms are labeled according to Fig. 1a.

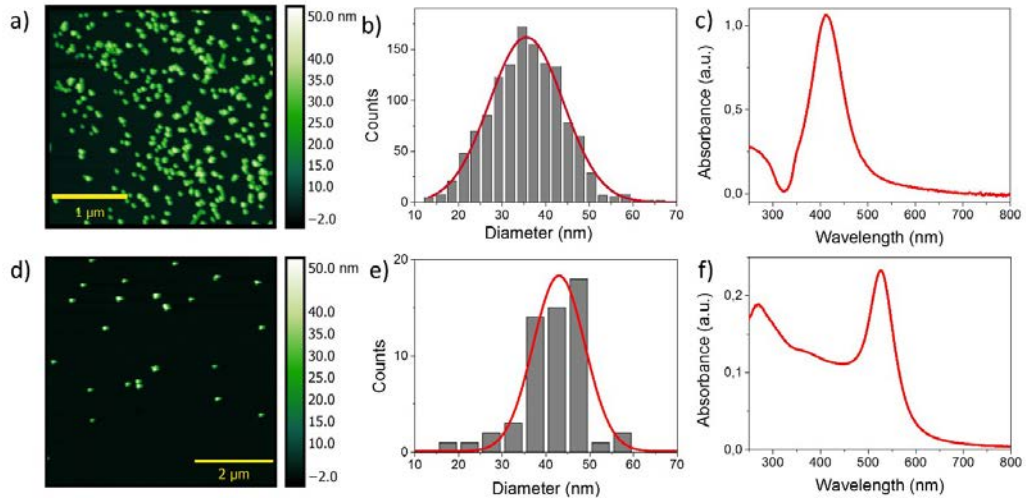

Figure S2: a) AFM image of AgNP, b) Size distribution of AgNP, c) UV-Vis-Absorbtion spectra of AgNP, d) AFM image of AuNP, e) Size distribution of AgNP, f) UV-Vis-Absorbtion spectra of AgNP.

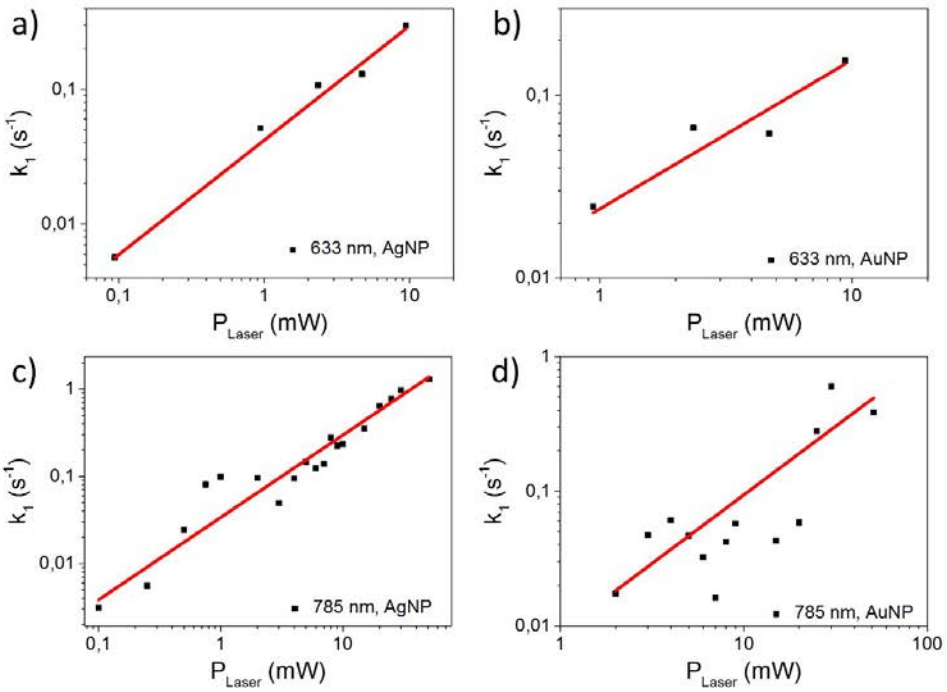

Figure S3: Rate constant k_1 as a function of the incident laser power fitted by a power law function a) AgNP with 633 nm laser, b) AuNP with 633 nm laser, c) AgNP with785 nm laser, d) AuNP with 785 nm laser.

Laser wavelength	AgNP	AuNP
532	0.92 ± 0.09	
633	0.85 ± 0.14	0.82 ± 0.24
785	0.94 ± 0.06	1.02 ± 0.31

Table 2: Power law exponents determined for $k_1 = a \cdot P^b$.

Decrease (cm^{-1})	Increase (cm^{-1})
299	337
575	392
767	628
1387	681
1433	735
1500	968
1525	1043
1620	1080
	1121
	1174
	1223
	1267
	1329
	1410
	1465
	1516
	1538
	1575
	1597

Table 3: Increasing and decreasing Raman bands of ^{8Br}A on AgNP under irradiation with a 532 nm laser.

1 Y.-L. Chen, D.-Y. Wu and Z.-Q. Tian, *J. Phys. Chem. A*, 2016, **120**, 4049–4058.
2 R. P. Lopes, R. Valero, J. Tomkinson, M. P. M. Marques and L. A. E. Batista de Carvalho, *New J. Chem.*, 2013, **37**, 2691.

5 Discussion

Along the track of ionizing radiation LEEs are generated in large quantities and interact with biomolecules like the DNA [193]. In combined chemo-radiation therapy the radiosensitizing action of certain agents can be at least partly assigned to their interaction with these secondary electrons [194]. Typically strong cytotoxic chemotherapeutic agents are applied as radiosensitizers [6]. However, in principle such radiosensitizers do not require further therapeutic action, so that also less toxic compounds could be applied for this purpose. ^{5Br}U was a promising candidate that matches these requirements, but in a clinical phase 3 study no increased survival rate in comparison to the control group was observed [195]. In clinical practice, the number of radiosensitizers is still very limited [196]. Thus, new insights in interaction of potential radiosensitizing molecules with LEEs might help in the development of future therapeutics.
In this section, DEA experiments with the potential radiosensitizer ^{8Br}A in the gas phase are presented. The resonance energies of all observed anions were determined in the region between 0 eV and 9 eV. Furthermore, the energy dependency of the SSB cross section for ^{8Br}A modified and unmodified oligonucleotides was studied with DNA origami nanostructures. All these experiments were performed under UHV conditions, however, there is a strong influence of the aqueous environment on the DEA [19]. Therefore pulsed laser irradiated AuNPs were tested as a nanoscale electron source to study DEA in liquids in a proof of principle experiment for three NBs. Beside the electron induced reactions also a variety of thermal and photo induced reactions can occur in the vicinity of the illuminated AuNPs. In consequence, the influence of thermal decomposition of all four native NBs and their brominated analogues in AuNPs solutions was studied and the effect of the adsorption kinetics was revealed. Pulsed as well as cw laser illuminated nanoparticles are also applied in PTT to kill cancer cells, whereas the focus in this therapy lies on the thermal effects of the system [14]. The role of LEEs and in consequence the application of electrophilic radiosensitizers in PTT were not taken in account so far. Thus, finally the plasmon mediated dissociative electron transfer to ^{8Br}A under low cw laser illumination of noble metal nanoparticles is presented.

5.1 Electron induced reactions of 8-bromoadenine

In order to evaluate the potential of ^{8Br}A as a possible radiosensitizer, the interaction with LEEs was studied for the free molecule in the gas phase. In M1 and M2 DEA to ^{8Br}A was performed for electron energies between 0 eV and 9 eV in a crossed-electron molecular beam setup. In Figure 5.1 a) the recorded negative ion mass spectra at electron energies of 0 eV, 1 eV and 6 eV are shown.

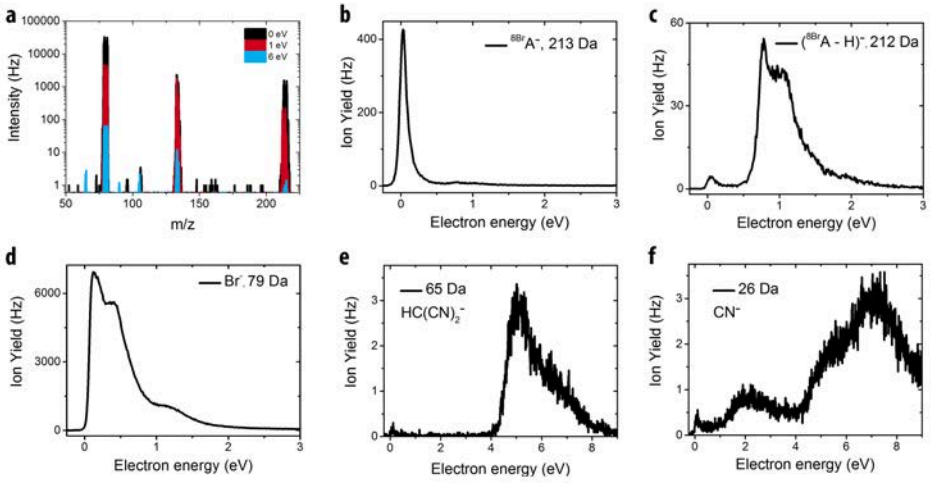

Figure 5.1: a) Negative ion mass spectra of ^{8Br}A for electron energies of 0 eV (black), 1 eV (red) and 6 eV (blue). b)- f) Energy spectra of the anionic fragments with a charge to mass ratio of 213 Da, 212 Da, 79 Da, 65 Da and 26 Da generated by DEA to ^{8Br}A .

At 0 eV the highest total ion yield was measured and the most abundant ion was Br^- with molecular masses of 79 Da and 81 Da. Additionally, also debrominated ^{8Br}A with a mass of 134 Da and the $(^{8Br}A - Br - H)^-$ anion were detected with a high yield. Remarkably the formation of a stable parent anion with molecular masses at 213 Da and 215 Da was observed with high intensity. The signal of all further fragments is more than two orders of magnitude lower. At an electron energy of 1 eV the total yield is decreased and instead of the parent anion new peaks at 212 Da and 214 Da arise, which are assigned to the dehydrogenated ^{8Br}A. Electrons with an energy of 6 eV usually access core excited resonances. At this electron energy a variety of fragments was observed. The formation of most of these anions requires multiple bond cleavages. However, the ion yield dropped by more than two orders of magnitude compared to the electron attachment at lower energies. In figure 5.1 b)- f) energy spectra of some important fragments are shown and the DEA resonances of all fragments are listed in table 5.1. The parent anion presented in figure 5.1 b) is formed in a single resonance at 0 eV. For all non-modified bases such an anion was not observed in the gas phase. Calculations by Iwona Dabkowska presented in M1 demonstrate that the stability of the parent anion can be explained by the formation of a $[Br^- \cdots (^{8Br}A - Br)]$ complex. The energy spectra of the dehydrogentated parent anion is shown in figure 5.1 c). In DEA to A the loss of a single

H-atom is the most abundant dissociation pathway [72]. The resonances for the abstraction of an H-atom from ^{8Br}A are shifted by 0.3 eV to lower energies compared to A [72]. The most abundant fragment is the Br^- - ion. It is formed in three resonances at 0 eV, 0.35 eV and 1.1 eV (see figure 5.1 d)), which are most likely shape- or vibrational Feshbach resonances. However, even far away from these resonances, Br^- is still the most intense fragment. The Br^- ion can be typically formed by the cleavage of the C-Br bond generating an adenyl radical. Such NB radicals are assumed to be an important precursor in the formation of DNA SSBs [97]. Nevertheless, a competitive reaction channel for adenyl radicals in DNA is the formation of 5'desoxy 8,5'cycloadenosine, which does not lead to a SB [102]. In figure 5.1 e) the fragment with a mass of 65 Da is shown, which is formed in a core exited resonance located at 5 eV. Compared to the equivalent anion formed in the DEA to A the signal is shifted by 0.8 eV towards lower energies [72]. The generation of this anion, which is assigned to the debrominated imidazole ring, requires the cleavage of multiple bonds. The fragment with a mass of 26 Da is assigned to CN^- and formed by several resonances located at 2 eV, 5.8 eV and 7.1 eV. CN^- is an important fragmentation product in the DEA to organic molecules and can be formed with high energy selectivity [71]. Compared to the DEA to A the resonances at lower energies are more pronounced [72].

Table 5.1: DEA resonances ^{8Br}A

Molecular mass	Ion						
26 Da	CN^-	0			2	5.8	7.1
65 Da	$C_3N_2H^-$					5	
79 Da	Br^-	0	0.35	1.05			
90 Da	$C_4N_3^-$				2.3	5.2	
92 Da	$C_4N_3H_2^-$					5.1	
105 Da	$C_4N_4H^-$					5.7	
106 Da	$C_4N_4H_2^-$				2.2	5.1	
133 Da	$C_5N_5H_3^-$	0	0.35	1.15			
134 Da	$C_5N_5H_4^-$	0	0.35	1.1			
212 Da	$C_5N_4H_3Br^-$	0.05	0.78	1.02			
213 Da	$C_5N_5H_4Br^-$	0					

In a further experiment presented in M2 the LEEs induced damage to ^{8Br}A containing DNA oligonucleotides was studied in the condensed phase. Thereby, the formation of DNA SBs as a function of the electron dose and energy was examined by using DNA origami structures. As target strands a Bt labeled TT(^{8Br}dATA)$_3$TT sequence and the native TT(ATA)$_3$TT sequence were used. The DNA origami were irradiated with defined doses of LEEs with an energy ranging from 0.5 eV to 9 eV. In order to detect the SB yield SAv was bound to the Bt group of the intact strands and visualized by AFM as shown in figure 5.2 a) and b).

In this way the SB cross section σ_{SB} can be determined from the dose response curves [55]. In figure 5.2 c) σ_{SB} is plotted as a function of the incident electron energy. For all energies the SB cross section is higher for

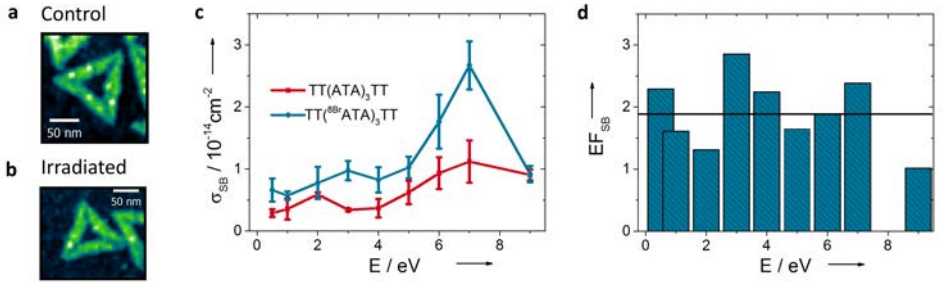

Figure 5.2: a) Non irradiated control sample after the addition of SAv to mark the intact strands. b) Sample irradiated with 7 eV electrons with an electron fluence of $0.53 \cdot 10^{13}\mathrm{cm}^{-2}$. c) Strand break cross section of $^{8\mathrm{Br}}$A modified strand and its unmodified equivalent as a function of the incident electron energy. d) SB enhancement factors as a function of the electron energy calculated from the cross sections presented in c).

the $^{8\mathrm{Br}}$A containing DNA sequence. Both DNA sequences show a maximum of the SB cross section at 7 eV. In this energy region all DNA subunits exhibit several core excited resonances [37]. Especially the cleavage of the C-O and P-O bond in the sugar phosphate backbone need to be mentioned in this context, which is equivalent to a DNA SSB, even though its overall intensity is relatively low [78, 79]. At energies below 2 eV the SB cross section is comparably low, which is unexpected as in this energy region the C-Br cleavage exhibits the strongest resonances. This indicates that the resonances at low energies are suppressed when $^{8\mathrm{Br}}$A is incorporated in the DNA strand or the formation of the adenyl radical does not consequently lead to the formation of a SSB. Alternatively it cannot be excluded that the LEEs partly lose their energy to the surrounding in a two center process before they are captured by the $^{8\mathrm{Br}}$A [197]. In figure 5.2 d) the SB enhancement factor is plotted revealing an average enhancement of 1.9 ± 0.6 due to the sensitization of the target strand with one $^{8\mathrm{Br}}$A molecule. This is one of the highest SB enhancement factors reported so far for halogenated oligonucleotides [61, 13, 198].

5.2 Gold nanoparticles as a source of heat and electrons

The previous experiments were performed under UHV conditions. However, there is strong influence of the aqueous environment on DEA [19, 64, 65]. The main constituent of biological tissue is water, which limits the mean free path of electrons to a nanometer scale. Hence, it would be desirable to perform DEA experiments with a nanoscale electron source in the vicinity of the analyte molecule. A promising candidate for such an electron source are AuNPs irradiated with short laser pulses to generate electrons via thermionic emission. In M3 and M4 the decomposition of NBs induced by AuNPs under illumination with ns laser pulses was studied. In M3 a focused laser beam was used to obtain high laser intensities generating LEEs due to the

high temperatures of the electron gas. The intention of this manuscript was to demonstrate a proof of principle for the possible electron induced decomposition three NBs (U, T and ^{5Br}U) in an aqueous environment and the spectroscopically identification of the reaction products. However, it needs to be taken into account that molecules close to the AuNPs can also be decomposed due to the high temperatures in proximity of the particles. Therefore the thermal decomposition of NBs triggered by laser irradiation of AuNPs was intensively studied in M4. In this study more defined conditions were chosen. The utilization of an unfocused laser beam and a low concentration of AuNPs allows the precise determination of the laser intensity and the irradiated volume. The intensity was set to $7 \cdot 10^{11}$W/cm^2, at which the influence of thermionically emitted electrons can be neglected [145]. Nevertheless, under theses conditions the temperature of the AuNPs can exceed their boiling point (1337 K). Consequently the AuNPs decompose by thermal evaporation into smaller particles. This process was monitored with AFM and UV-Vis absorption spectroscopy. The absorption spectra of the illuminated AuNPs show a decreased and blue shifted SP resonance indicating the AuNPs fragmentation (see figure 5.3 b)). As only a single laser pulse is required to decompose the nanoparticles, the size distribution does not change significantly after the first several hundred pulses. In this way relatively constant conditions can be assumed during the period of the experiment. The NBs strongly absorb UV light due to their $\pi - \pi^*$ transition located between 259 nm and 276 nm depending on the NB. By observation of the corresponding absorption band the integrity of the ring structure can be detected (see figure 5.3 b)).

By plotting the intensity of the $\pi - \pi^*$ transition as a function of the number of pulses N_{Puls} the decomposition kinetics was studied (see figure 5.3 c). The exponential decrease of the band indicates that the reaction follows first order kinetics, so the rate constant could be determined from the exponential fit. In figure 5.3 d) it is shown that the rate constant for the decomposition of ^{8Br}A depends on the repetition rate of the laser. The time between two pulses defines the incubation time of the NB analogues on the AuNPs, making an effect of the adsorption kinetics on the decomposition rate likely. Therefore, the experimentally determined reaction rates where compared with calculated reaction rates. The calculations are based on the assumptions that the adsorption follows Langmuir kinetics and all adsorbed NBs are decomposed during the irradiation leaving behind an adsorbate free surface, as no catalyst poisoning was observed. The differential equation for the concentration of the NBs c_{NB} under these conditions is:

$$\frac{dc_{NB}}{dN_{Puls}} = -k \cdot c_{NB} \tag{5.1}$$

The rate constant k given by:

$$k = \psi \cdot \frac{k_{ad}}{k_{ad} + \psi} \cdot \frac{c_{max} \cdot K_L}{1 + K_L \cdot c^0_{NB}} \tag{5.2}$$

where ψ is the fraction of the solution that is illuminated during one laser pulse, k_{ad} is the adsorption rate with respect to N_{Puls} that depends on the laser repetition rate, c_{max} is the total number of adsorption sites on the AuNPs, K_L is the equilibrium constant and c^0_{NB} is the initial concentration

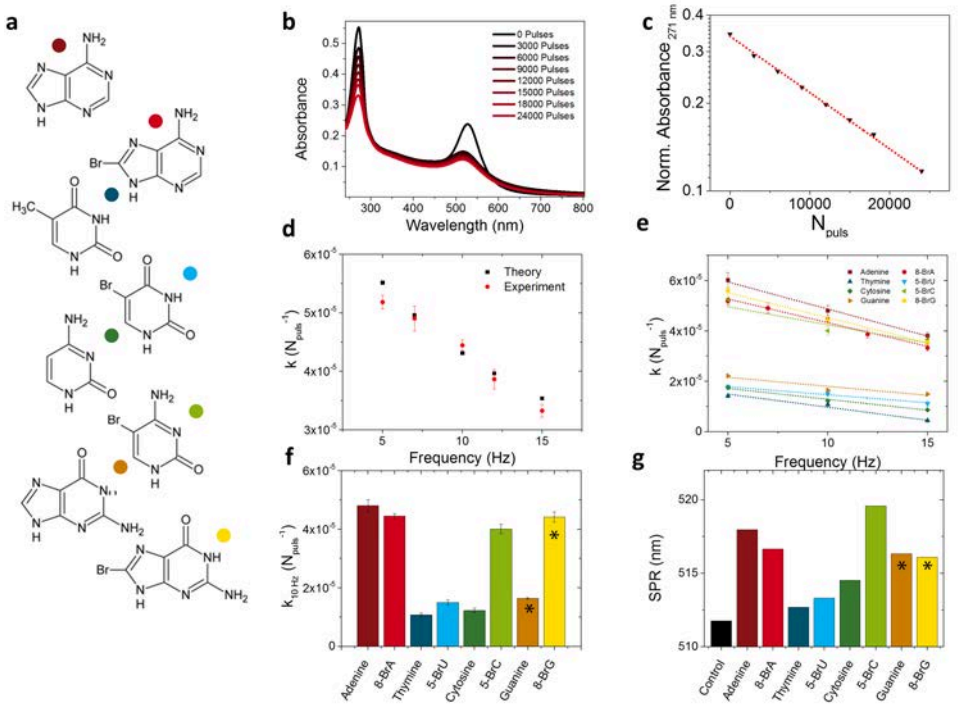

Figure 5.3: a) Molecular structures of A, ^{8Br}A, T, ^{5Br}U, C, ^{5Br}C, G and ^{8Br}G. b) UV-Vis absorption spectra of ^{8Br}A and AuNPs illuminated with ns laser pulses. c) Normalized intensity of the $\pi - \pi^*$ absorption band at 271 nm as a function of the laser pulses plotted with an exponential decay function. d) Experimentally determined and calculated rate constants as a function of the laser repetition rate. e) Rate constants of NB analogues as a function of the laser repetition rate. f) Rate constant k at 10 Hz (same data like in e)). The values for G and ^{8Br}G are marked with a *, since these NBs were dissolved in diluted NaOH instead of pure Millipore water. g) Spectral position of the SPR of AuNPs after irradiation with 6000 laser pulses and the subsequent addition of 20 μM NB analogues.

of the NBs in the solution. A detailed derivation of the reaction rate k is presented in M3. The calculated values for k are in good agreement with the experimentally determined reaction rates (see figure 5.3 e)). It turns out that the adsorption rate k_{ad} is fast, as most likely no time consuming ligand exchange is required [199]. Furthermore, since the diameter of the AuNPs is small (< 10 nm), the surface of the AuNPs mainly consist of non-orientated surface sites that provide fast adsorption rates [200]. A dependence on the laser repetition rate was observed for all four native NBs as well as for their brominated analogues (see 5.3 e)). In figure 5.3 f) the reaction rates at 10 Hz are plotted showing that the highest rates are observed for ^{8Br}A, ^{8Br}G, ^{5Br}C and A. To correlate these findings with the adsorption rate of molecules on the surface of NPs, there is no straight forward method available. In consequence a modified version of the colorimetric method presented by Lu Yu and Na Li was applied that is based on the determination of the SPR shift due to the aggregation of AuNPs [201]. The shift of the SPR is plotted in figure 5.3 g), which correlates fairly well with the decomposition rates.
Even though UV-Vis absorption spectroscopy is a useful tool to obtain an insight to the plasmon mediated decomposition of molecules, the identification of the generated molecular fragments is barely possible by this method. Thus, Raman spectroscopy was used to identify certain reaction products, as the enhanced em-field close to the AuNPs allows to overcome the typically poor scattering cross section of the molecules of interest. Nevertheless, due to the laser irradiation of the AuNPs their size is strongly reduced and consequently their em-enhancement is low. Using higher AuNP-concentrations the SERS spectra of A and ^{8Br}A were determined (see figure 5.4 a). In the spectra of both molecules a new a band at 2140 cm^{-1} arises that can be assigned to the CN stretching vibration of a $C{\equiv\!\equiv}N^-$ ion. This confirms the rupture of the ring structure that was already indicated by UV-Vis spectroscopy. In contrast to the electron induced reactions in the gas phase, a cleavage of the C-Br bond of ^{8Br}A was not observed as no band at approximately 735 cm^{-1} occurs after the irradiation that would originate from the ring breathing mode of the generated A molecule [23].

The addition of a highly concentrated AgNPs solution to the AuNPs containing NBs solution after the irradiation strongly enhances the Raman signal. In this way, fragments that adsorb on the AgNPs can be better identified through the higher signal to noise ratio. In figure 5.4 b) SERS spectra of U, T and ^{5Br}U are presented before and after irradiation with focused laser pulses in a AuNP solution. For U and T a new band at 2140 cm^{-1} was observed as already shown for the A analogues, while the peaks in the fingerprint region do not exhibit major changes. Furthermore, after the irradiation of T a signal at 1900 cm^{-1} arose that can be assigned to a cumulative double bond, which might have its origin in the formation of NCO. Even though NCO^- requires the cleavage of multiple bonds, it can be formed by the DEA to T at 2 eV [202]. The observed new Raman bands increase with ongoing irradiation. The intensity was fitted with a Langmuir adsorption isotherm (see figure 5.4 c)) as it is assumed that due to the surface sensitivity of SERS only the first adsorbed molecular layer significantly contributes to the signal. The potential radiosensitizer ^{5Br}U exhibits a different behavior as signals above 1700 cm^{-1} are comparably low after the irradiation. In

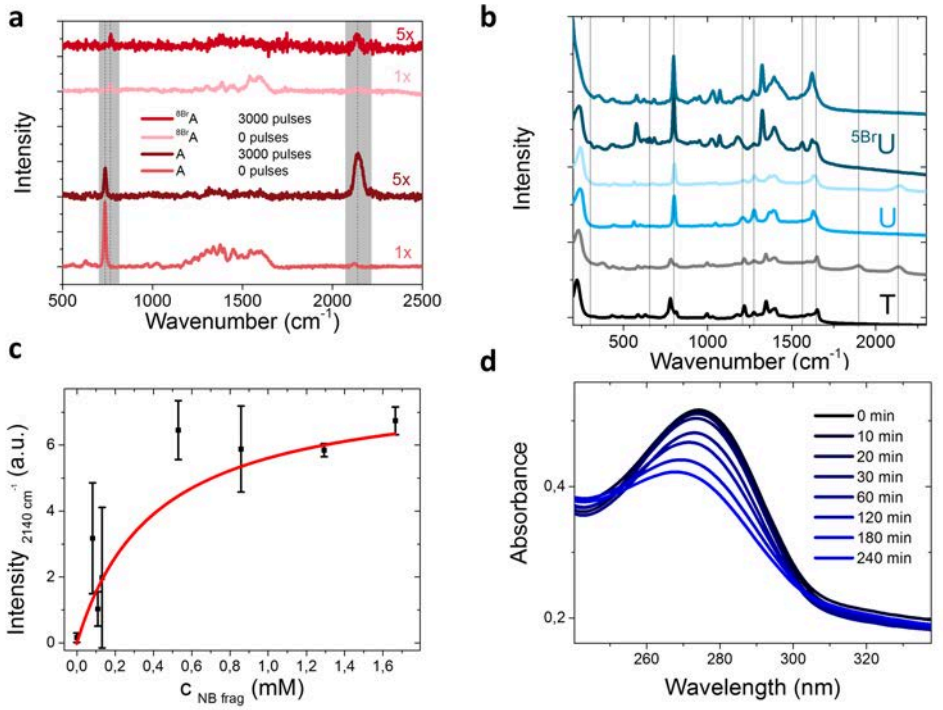

Figure 5.4: a) SERS spectra of ^{8Br}A and A on AuNPs with an initial size of 60 nm before and after the irradiation with 3000 laser pulses (230 mJ/cm^2). b) SERS spectra of T,U and ^{5Br}U on AuNPs before and after the irradiation with 72 000 pulses (4 J/cm^2). In order to enhance the signal AgNPs were added. c) Intensity of the Raman band located at 2140 cm^{-1} plotted as a function of the concentration of the fragmented NBs that was determined from UV-Vis measurements. d) UV-Vis Absorption spectra of a AuNPs containing ^{5Br}U solution under irradiation with intense laser pulses (4 J/cm^2).

contrast, there are significant changes in the fingerprint region of the Raman signal. The signals at 300 cm^{-1} and 560 cm^{-1} vanish, which are assigned to the C-Br bending and stretching vibration, respectively [182]. This indicates a cleavage of the C-Br bond, which is the main dissociation pathway in the DEA to ^{5Br}U [80]. This assumption was strengthened by UV-Vis spectra showing a blue shift of the $\pi - \pi^*$ absorption indicating a transformation from ^{5Br}U to U (see figure 5.4 d)). However, the cleavage of the C-Br bond was also observed under illumination with UV-light [7] and therefore beside DEA also 2 photon processes in the enhanced near-field of the AuNPs might be a reasonable explanation for this observation.

5.3 Hot electron transfer to 8-Bromoadenine

The versatile decomposition pathways make it difficult to identify the proportion of electron induced reactions in the fragmentation of molecules in the vicinity of pulsed laser illuminated AuNPs. Nevertheless, beside thermionic electron emission in intense laser fields also plasmon induced "hot electrons" can be generated in laser illuminated noble metal nanoparticles even un-

der moderate intensities. A transfer of these "hot electrons" to adsorbed molecules on the particle surface can trigger chemical reactions [203]. In manuscript M5 the interaction between ^{8Br}A and continuous wave laser illuminated metal nanoparticles was studied. For this purpose ^{8Br}A was incubated on AgNPs and after washing with H_2O dried on a Si-Wafer. In figure 5.5 a) the Raman spectra of this system are shown. For a short time the Raman spectrum exhibits a vibrational fingerprint that can be assigned to ^{8Br}A .

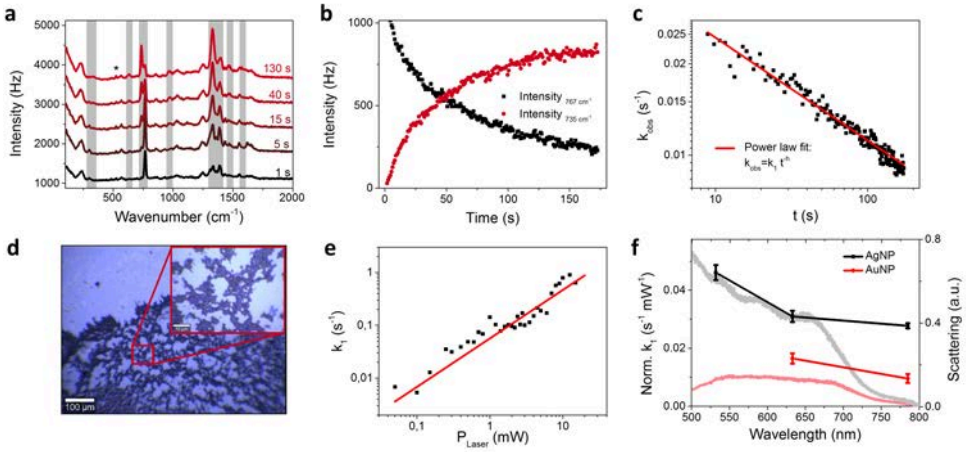

Figure 5.5: a) Raman spectra of ^{8Br}A on AgNPs dried on a Si Wafer illuminated with 250 μW 532 nm laser. The * marks the 520 cm^{-1} line of the Si substrate. b) Intensities of the ring breathing modes of ^{8Br}A at 767 cm^{-1} and A at 735 cm^{-1} as a function of the illumination time (same data like in a)). c) Observed rate constant for the dissociation of ^{8Br}A plotted as a function of the illumination time fitted with the power law function $k_{obs} = t^{-h}$ with $h = 0.33$. d) Light microscopy image of the fractal-like aggregated AgNPs on a Si Wafer. e) Rate constant k_1 for the decay of ^{8Br}A on AgNPs illuminated with a 532 nm laser plotted as a function of the laser intensity and fitted with a power function $I = a^b$ with $b = 0.92 \pm 0.09$. f) Normalized rate constants for the ^{8Br}A decay on AuNPs and AgNPs as a function of the laser wavelength plotted together with typical dark field scattering spectra on the two substrates.

With ongoing illumination the intensity of these bands are decreasing while at the same time new bands are arising that show the fingerprint of A. This process can be explained by plasmonically generated "hot electrons" that are transfered into the LUMO of the adsorbed ^{8Br}A forming a TNI. The TNI subsequently relaxes by the cleavage of the C-Br bond. The intense ring breathing mode of the educts and the products, which are located at 735 cm^{-1} and 767 cm^{-1} respectively, are good markers to track this reaction (See figure 5.5 b)). Figure 5.5 c) shows the observed rate constant of the decomposition of ^{8Br}A as a function of time. With ongoing illumination time the rate constant decreases following a power law. The time dependency of the observed reaction rate k_{obs} can be described by fractal-like kinetics [204],

where the rate constant is given by:

$$k_{obs} = k_1 \cdot t^{-h} \tag{5.3}$$

with k_1 being the reaction rate at $t = 1$ and h is denoting the fractal dimension of the system. The origin of the time dependent reaction rate lies in the heterogeneous spatial distribution of the plasmonic enhancement of the dried AgNPs (see figure 5.5 d)). In the plasmonic hot spots the Raman enhancement as well as the interaction of the molecule with the hot electrons is high. In consequence the molecules that have the largest contribution to the Raman signal decompose more likely than those that experience a minor em-enhancement. Hence, the observed rate constant is decreasing with time. Measurements of the time independent reaction rate k_1 reveal a linear dependence of the reaction rate on the laser intensity over three orders of magnitude indicating a one photon process (see figure 5.5 e)). The linear correlation was observed for illumination at 532 nm, 633 nm and 785 nm as well as on AuNPs. In figure 5.5 f) the rate constants are normalized by the laser intensity and correlated with typical scattering spectra of the Ag and Au substrates. The higher rate constants on Ag compared to Au can be attributed to the higher plasmonic enhancement. However, the normalized rate constants at 785 nm are relatively high, even though the plasmonic enhancement of the substrate is off resonance in this wavelength region. This might be explained by a resonant electron transfer into the LUMO of the adsorbed ^{8Br}A [170]. The AuNPs under NIR laser illumination are of special interest as such systems are applied in PTT. In figure 5.6 a) the Raman spectra of ^{8Br}A on AgNPs in aqueous solution are shown. Also in water the

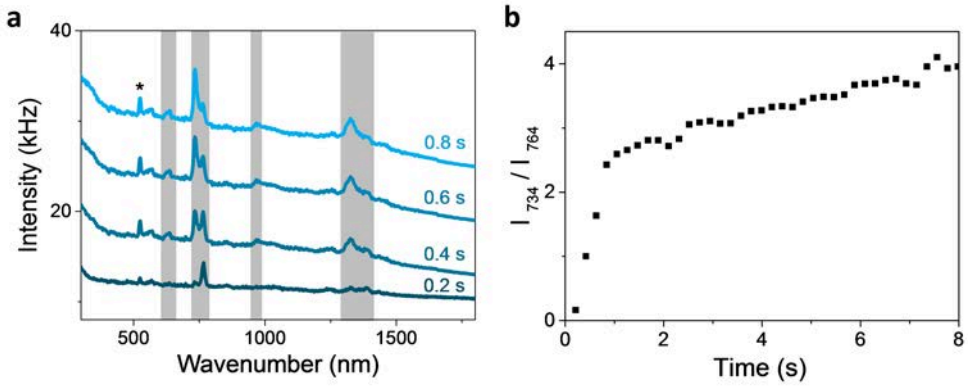

Figure 5.6: a) Raman spectra of ^{8Br}A adsorbed on AgNPs in aqueous solution illuminated with a 785 nm laser with 5.1 mW. The * marks the Si band at 520 cm^{-1}. b) Ratio of the ring breathing modes of ^{8Br}A and A at 734 cm^{-1} and 764 cm^{-1} respectively calculated from the same data set presented in a).

transformation from ^{8Br}A to A was observed. A major fraction of the ^{8Br}A in the focal area was converted within several hundred ms. Even though the reaction rate cannot be quantified due to the diffusion of the AgNPs in the focal area, it seems likely that the speed of reaction is accelerated in an aqueous environment, as the tunneling barrier is lower [205].

6 Summary and Outlook

The interaction of the potential radiosensitizer ^{8Br}A with LEEs was examined in various systems. In the first part of this work it was shown that ^{8Br}A is highly reactive to LEEs in the gas phase. Due to the attachment of electrons with an energy below 2 eV the C-Br bond is cleaved generating Br^- with a high yield in three low energy resonances. In this reaction an adenyl radical is formed that is known to be the precursor for subsequent reactions in the DNA strand including SSBs [102, 97]. Furthermore, in a single resonance close to 0 eV a stable ^{8Br}A parent anion is formed. Such long lived anionic states might increase the transfer of electrons captured by ^{8Br}A to the sugar phosphate backbone and cause a SB in a second step. However, the SB cross sections of ^{8Br}A containing oligonucleotides is relatively low at incident electron energies below 3 eV. The low cross sections at low electron energies could indicate on the one hand that the low lying shape resonances of ^{8Br}A are not present if ^{8Br}A is incorporated in the DNA strand or the electrons partly dissipate their energy to the surrounding before they attach to the NBs. In consequence, the energy of the interacting electrons would be lowered. In order to get more clarity about the influence of the environment on the electron interaction with ^{8Br}A, DEA experiments [65] or electron energy loss spectroscopy measurements [197] of ^{8Br}A located in nanoscale clusters would be beneficial.
The maximum in the SB cross section of the ^{8Br}A-modified DNA sequence, as well as for the non-modified control sequence is located at 7 eV. In this energy regions typically core excited resonances are located. Several DEA-pathways exhibit resonances at this energy in the gas phase that require multiple bond cleavage and lead to the rupture of the ring structure. It is feasible that the electron capture process underlying these resonances, which are responsible for the fragmentation of the ^{8Br}A molecule, might play also an important role as an initial step in the formation of DNA SBs. Even though there are still some open questions regarding the underlying mechanisms of electron induced DNA damage, it has been shown that the incorporation of ^{8Br}A into DNA leads to a significant enhancement ($EF_{SB} = 1.9 \pm 0.6$) in the SSB cross section over the whole energy range between 0.5 eV and 9 eV. Due to the high sensitivity of ^{8Br}A to LEEs, it seems promising to continue the evaluation of the potential of ^{8Br}A as radiosensitizer. In the next step its influence on the DNA DSB cross section

needs to be examined, since DNA SSBs can be easily repaired whereas DSBs are assumed to be a lethal DNA damage. Therefore, DSBs are more relevant with respect to cancer radiation therapy. Furthermore, cell line experiments with cancer cells and healthy cells need to be conducted to determine the action of ^{8Br}A in a biological system.

In the second part of this thesis, laser illumintaed AuNPs were tested as a potential electron source on the nanoscale in order to get a deeper insight in the influence of an aqueous environment on DEA processes. The illumination of AuNPs with focused ns laser pulses revealed reactions to T, U and ^{5Br}U that might be caused by DEA. The generated fragments like U and Br for the decomposition of ^{5Br}U and CN and CNO for the dissociation of T were comparable to those observed for DEA in the gas phase. The fragments were identified by SERS, when a highly concentrated AgNP solution was added to enhance the Raman signal. Even though these proof of principle experiments are promising, in order to use laser illuminated AuNPs as a system to study DEA reactions in water further improvements are required. Therefore, well defined plasmonic structures are necessary that allow a reliable detection of the decomposition products [206]. In addition, the vibrational fingerprints of the expected reaction products need to be systematically recorded. To examine the influence of competing thermal reactions the decomposition of NB analogues was studied in detail for lower laser fluences where an electron emission from the AuNPs is unlikely [145]. It turns out that the thermal decomposition is strongly dependent on the adsorption of the NBs on the AuNPs. In consequence high laser repetition rates might reduce the influence of short range high temperature effects in the decomposition of the NBs. It is expected that the thermionic electron emission from AuNPs depends on the laser intensity [145]. Hence, the influence of the laser fluence should be systematically evaluated, in order to find conditions, where the electron emission is prominent. In this context the use of fs laser pulses should be considered [138, 207]. Yamada et al. performed pump probe laser experiments to quantify the thermionic emission of electrons from laser illuminated AuNPs as hydrated electrons absorb light efficiently at 720 nm [21]. Similar transient absorption measurements should help to improve the irradiation conditions. If the electron induced damage can be distinguished from photo induced and thermal damage, laser irradiated AuNPs can be used to study DEA to DNA strands or other important biomolecules in an aqueous environment.

In the last part the dissociative electron transfer to ^{8Br}A on AgNPs and AuNPs under low intensity cw illumination was monitored by SERS. The fractal-like kinetics of the reaction was determined revealing a strong influence on the plasmonic nanostructures. The observed hot electron transfer opens further questions regarding spectroscopy and catalysis [147]. Under typical SERS conditions the reaction time of ^{8Br}A is shorter than common accumulation times. Hence, it needs to be verified that the measured SERS spectra of electrophilic molecules do not partly or fully show the vibrationally fingerprint of possible photoproducts. As SERS is applied in analytical chemistry [208], such electron induced reactions need to be systematically studied to evaluate their importance.

Beyond that, cw and pulsed laser illuminated AuNPs are applied in cancer PTT but were not combined with electrophilic radiosensitizers so far. Hence, cell experiments with AuNPs and halogenated NBs like ^{8Br}A should be performed in order to evaluate the potential of such a combination.

Bibliography

[1] A. Urruticoechea, R. Alemany, J. Balart, A. Villanueva, F. Vials, and G. Capell, "Recent advances in cancer therapy: an overview," *Current Pharmaceutical Design*, vol. 16, pp. 3–10, Jan. 2010.

[2] W. P. Roos and B. Kaina, "DNA damage-induced cell death by apoptosis," *Trends in Molecular Medicine*, vol. 12, pp. 440–450, Sept. 2006.

[3] P. A. Jeggo and M. Löbrich, "DNA double-strand breaks: their cellular and clinical impact?," *Oncogene*, vol. 26, pp. 7717–7719, Dec. 2007.

[4] L. Sanche, "Biological chemistry: Beyond radical thinking," *Nature*, vol. 461, pp. 358–359, Sept. 2009.

[5] C.-R. Wang, J. Nguyen, and Q.-B. Lu, "Bond Breaks of Nucleotides by Dissociative Electron Transfer of Nonequilibrium Prehydrated Electrons: A New Molecular Mechanism for Reductive DNA Damage," *Journal of the American Chemical Society*, vol. 131, pp. 11320–11322, Aug. 2009.

[6] T. Y. Seiwert, J. K. Salama, and E. E. Vokes, "The concurrent chemoradiation paradigmgeneral principles," *Nature Clinical Practice Oncology*, vol. 4, pp. 86–100, Feb. 2007.

[7] J. Rak, L. Chomicz, J. Wiczk, K. Westphal, M. Zdrowowicz, P. Wityk, M. yndul, S. Makurat, and u. Golon, "Mechanisms of Damage to DNA Labeled with Electrophilic Nucleobases Induced by Ionizing or UV Radiation," *The Journal of Physical Chemistry B*, vol. 119, pp. 8227–8238, July 2015.

[8] I. Bald, J. Langer, P. Tegeder, and O. Inglfsson, "From isolated molecules through clusters and condensates to the building blocks of life," *International Journal of Mass Spectrometry*, vol. 277, pp. 4–25, Nov. 2008.

[9] S. Cecchini, S. Girouard, M. A. Huels, L. Sanche, and D. J. Hunting, "Single-Strand-Specific Radiosensitization of DNA by Bromodeoxyuridine," *Radiation Research*, vol. 162, pp. 604–615, Dec. 2004.

[10] A. Manetto, S. Breeger, C. Chatgilialoglu, and T. Carell, "Complex Sequence Dependence by Excess-Electron Transfer through DNA with Different Strength Electron Acceptors," *Angewandte Chemie International Edition*, vol. 45, pp. 318–321, Jan. 2006.

[11] J. Simons, "How Do Low-Energy (0.1-2 eV) Electrons Cause DNA-Strand Breaks?," *Accounts of Chemical Research*, vol. 39, pp. 772–779, Oct. 2006.

[12] S. Wang, P. Zhao, C. Zhang, and Y. Bu, "The Equally Important Role of Adenine Derivatives to That of Pyrimidine Derivatives in Near-0 eV Electron-Induced DNA Lesions," *ChemPhysChem*, vol. 17, pp. 1669–1677, June 2016.

[13] A. Keller, J. Rackwitz, E. Caut, J. Livin, T. Körzdörfer, A. Rotaru, K. V. Gothelf, F. Besenbacher, and I. Bald, "Sequence dependence of electron-induced DNA strand breakage revealed by DNA nanoarrays," *Scientific Reports*, vol. 4, p. 7391, Dec. 2014.

[14] N. S. Abadeer and C. J. Murphy, "Recent Progress in Cancer Thermal Therapy Using Gold Nanoparticles," *The Journal of Physical Chemistry C*, vol. 120, pp. 4691–4716, Mar. 2016.

[15] R. R. Letfullin, C. Joenathan, T. F. George, and V. P. Zharov, "Laser-induced explosion of gold nanoparticles: potential role for nanophotothermolysis of cancer," *Nanomedicine*, vol. 1, pp. 473–480, Dec. 2006.

[16] G. Baffou and R. Quidant, "Nanoplasmonics for chemistry," *Chemical Society Reviews*, vol. 43, no. 11, p. 3898, 2014.

[17] R. Schürmann, K. Tanzer, I. Dabkowska, S. P. Denifl, and I. Bald, "On the Stability of the Parent Anion of the Potential Radiosensitizer 8-Bromoadenine Formed by Low Energy (< 3 eV) Electron Attachment," *The Journal of Physical Chemistry B*, May 2017.

[18] R. Schürmann, T. Tsering, K. Tanzer, S. Denifl, S. V. K. Kumar, and I. Bald, "Resonant formation of strand breaks in sensitized oligonucleotides induced by low-energy electrons (0.5 - 9 eV)," 2017.

[19] M. McAllister, M. Smyth, B. Gu, G. A. Tribello, and J. Kohanoff, "Understanding the Interaction between Low-Energy Electrons and DNA Nucleotides in Aqueous Solution," *The Journal of Physical Chemistry Letters*, vol. 6, pp. 3091–3097, Aug. 2015.

[20] R. Schürmann and I. Bald, "Decomposition of DNA Nucleobases by Laser Irradiation of Gold Nanoparticles Monitored by Surface-Enhanced Raman Scattering," *The Journal of Physical Chemistry C*, vol. 120, pp. 3001–3009, Feb. 2016.

[21] K. Yamada, K. Miyajima, and F. Mafun, "Thermionic Emission of Electrons from Gold Nanoparticles by Nanosecond Pulse-Laser Excitation of Interband," *The Journal of Physical Chemistry C*, vol. 111, pp. 11246–11251, Aug. 2007.

[22] R. Schürmann and I. Bald, "Effect of adsorption kinetics on dissociation of DNA-nucleobases on gold nanoparticles under pulsed laser illumination," *Phys. Chem. Chem. Phys.*, vol. 19, no. 17, pp. 10796–10803, 2017.

[23] R. Schürmann and I. Bald, "Real-time monitoring of plasmon induced dissociative electron transfer to the potential DNA radiosensitizer 8-bromoadenine," *Nanoscale*, vol. 9, no. 5, pp. 1951–1955, 2017.

[24] B. Alberts, ed., *Molecular biology of the cell*. New York, NY: Garland Science, 4. ed ed., 2002. OCLC: 264948944.

[25] J. D. Watson and F. H. C. Crick, "Molecular Structure of Nucleic Acids: A Structure for Deoxyribose Nucleic Acid," *Nature*, vol. 171, pp. 737–738, Apr. 1953.

[26] P. Yakovchuk, "Base-stacking and base-pairing contributions into thermal stability of the DNA double helix," *Nucleic Acids Research*, vol. 34, pp. 564–574, Jan. 2006.

[27] N. Michelotti, A. Johnson-Buck, A. J. Manzo, and N. G. Walter, "Beyond DNA origami: the unfolding prospects of nucleic acid nanotechnology," *Wiley Interdisciplinary Reviews: Nanomedicine and Nanobiotechnology*, vol. 4, pp. 139–152, Mar. 2012.

[28] C. T. Middleton, K. de La Harpe, C. Su, Y. K. Law, C. E. Crespo-Hernndez, and B. Kohler, "DNA Excited-State Dynamics: From Single Bases to the Double Helix," *Annual Review of Physical Chemistry*, vol. 60, pp. 217–239, May 2009.

[29] V. I. Prokhorenko, A. Picchiotti, M. Pola, A. G. Dijkstra, and R. J. D. Miller, "New Insights into the Photophysics of DNA Nucleobases," *The Journal of Physical Chemistry Letters*, vol. 7, pp. 4445–4450, Nov. 2016.

[30] O. T. Avery, C. M. Macleod, and M. McCarty, "STUDIES ON THE CHEMICAL NATURE OF THE SUBSTANCE INDUCING TRANSFORMATION OF PNEUMOCOCCAL TYPES : INDUCTION OF TRANSFORMATION BY A DESOXYRIBONUCLEIC ACID FRACTION ISOLATED FROM PNEUMOCOCCUS TYPE III," *The Journal of Experimental Medicine*, vol. 79, pp. 137–158, Feb. 1944.

[31] P. W. Laird and R. Jaenisch, "THE ROLE OF DNA METHYLATION IN CANCER GENETICS AND EPIGENETICS," *Annual Review of Genetics*, vol. 30, pp. 441–464, Dec. 1996.

[32] M. Valko, M. Izakovic, M. Mazur, C. J. Rhodes, and J. Telser, "Role of oxygen radicals in DNA damage and cancer incidence," *Molecular and Cellular Biochemistry*, vol. 266, pp. 37–56, Nov. 2004.

[33] P. Peltomaki, "Role of DNA Mismatch Repair Defects in the Pathogenesis of Human Cancer," *Journal of Clinical Oncology*, vol. 21, pp. 1174–1179, Mar. 2003.

[34] J. W. Shay and W. E. Wright, "Role of telomeres and telomerase in cancer," *Seminars in Cancer Biology*, vol. 21, pp. 349–353, Dec. 2011.

[35] N. Kim, M. Piatyszek, K. Prowse, C. Harley, M. West, P. Ho, G. Coviello, W. Wright, S. Weinrich, and J. Shay, "Specific association of human telomerase activity with immortal cells and cancer," *Science*, vol. 266, pp. 2011–2015, Dec. 1994.

[36] L. H. Hurley, "DNA and its associated processes as targets for cancer therapy," *Nature Reviews Cancer*, vol. 2, pp. 188–200, Mar. 2002.

[37] I. Baccarelli, I. Bald, F. A. Gianturco, E. Illenberger, and J. Kopyra, "Electron-induced damage of DNA and its components: Experiments and theoretical models," *Physics Reports*, vol. 508, pp. 1–44, Nov. 2011.

[38] V. Cobut, J. Jay-Gerin, and Y. Frongillo, "Monte Carlo simulation of fast electron and proton tracks in liquid water - I. Physical and physicochemical aspects," *Radiation Physics and Chemistry*, vol. 51, pp. 229–243, Mar. 1998.

[39] S. M. Pimblott and J. A. LaVerne, "Production of low-energy electrons by ionizing radiation," *Radiation Physics and Chemistry*, vol. 76, pp. 1244–1247, Aug. 2007.

[40] F. Uhlig, O. Marsalek, and P. Jungwirth, "Unraveling the Complex Nature of the Hydrated Electron," *The Journal of Physical Chemistry Letters*, vol. 3, pp. 3071–3075, Oct. 2012.

[41] K. R. Siefermann, Y. Liu, E. Lugovoy, O. Link, M. Faubel, U. Buck, B. Winter, and B. Abel, "Binding energies, lifetimes and implications of bulk and interface solvated electrons in water," *Nature Chemistry*, vol. 2, pp. 274–279, Apr. 2010.

[42] S. Ptasiska, S. Denifl, P. Scheier, and T. D. Märk, "Inelastic electron interaction (attachment/ionization) with deoxyribose," *The Journal of Chemical Physics*, vol. 120, pp. 8505–8511, May 2004.

[43] C. J. Tiessen, J. A. Trocchi, J. D. Hein, J. Dech, W. Kedzierski, and J. W. McConkey, "VUV study of electron impact dissociative excitation of thymine," *Journal of Physics B: Atomic, Molecular and Optical Physics*, vol. 49, p. 125204, June 2016.

[44] E. Alizadeh, T. M. Orlando, and L. Sanche, "Biomolecular Damage Induced by Ionizing Radiation: The Direct and Indirect Effects of Low-Energy Electrons on DNA," *Annual Review of Physical Chemistry*, vol. 66, pp. 379–398, Apr. 2015.

[45] B. Boudaiffa, "Resonant Formation of DNA Strand Breaks by Low-Energy (3 to 20 eV) Electrons," *Science*, vol. 287, pp. 1658–1660, Mar. 2000.

[46] X. Luo, Y. Zheng, and L. Sanche, "DNA strand breaks and crosslinks induced by transient anions in the range 2-20 eV," *The Journal of Chemical Physics*, vol. 140, p. 155101, Apr. 2014.

[47] S. V. K. Kumar, T. Pota, D. Peri, A. D. Dongre, and B. J. Rao, "Low energy electron induced damage to plasmid DNA pQE30," *The Journal of Chemical Physics*, vol. 137, no. 4, p. 045101, 2012.

[48] T. M. Orlando, D. Oh, Y. Chen, and A. B. Aleksandrov, "Low-energy electron diffraction and induced damage in hydrated DNA," *The Journal of Chemical Physics*, vol. 128, p. 195102, May 2008.

[49] Q. Bao, Y. Chen, Y. Zheng, and L. Sanche, "Cisplatin Radiosensitization of DNA Irradiated with 220 eV Electrons: Role of Transient Anions," *The Journal of Physical Chemistry C*, vol. 118, pp. 15516–15524, July 2014.

[50] Z. Li, P. Cloutier, L. Sanche, and J. R. Wagner, "Low-Energy Electron-Induced DNA Damage: Effect of Base Sequence in Oligonucleotide Trimers," *Journal of the American Chemical Society*, vol. 132, pp. 5422–5427, Apr. 2010.

[51] Y. Park, A. R. Peoples, G. S. Madugundu, L. Sanche, and J. R. Wagner, "Side-by-Side Comparison of DNA Damage Induced by Low-Energy Electrons and High-Energy Photons with Solid TpTpT Trinucleotide," *The Journal of Physical Chemistry B*, vol. 117, pp. 10122–10131, Sept. 2013.

[52] Y. Park, Z. Li, P. Cloutier, L. Sanche, and J. R. Wagner, "DNA damage induced by low-energy electrons: conversion of thymine to 5,6-dihydrothymine in the oligonucleotide trimer TpTpT," *Radiation Research*, vol. 175, pp. 240–246, Feb. 2011.

[53] Y. Park, K. Polska, J. Rak, J. R. Wagner, and L. Sanche, "Fundamental Mechanisms of DNA Radiosensitization: Damage Induced by Low-Energy Electrons in Brominated Oligonucleotide Trimers," *The Journal of Physical Chemistry B*, vol. 116, pp. 9676–9682, Aug. 2012.

[54] Z. Li, P. Cloutier, L. Sanche, and J. R. Wagner, "Low-Energy Electron-Induced Damage in a Trinucleotide Containing 5-Bromouracil," *The Journal of Physical Chemistry B*, vol. 115, pp. 13668–13673, Nov. 2011.

[55] A. Keller, I. Bald, A. Rotaru, E. Caut, K. V. Gothelf, and F. Besenbacher, "Probing Electron-Induced Bond Cleavage at the Single-Molecule Level Using DNA Origami Templates," *ACS Nano*, vol. 6, pp. 4392–4399, May 2012.

[56] S. Vogel, J. Rackwitz, R. Schürman, J. Prinz, A. R. Milosavljevic, M. Refregiers, A. Giuliani, and I. Bald, "Using DNA Origami Nanostructures To Determine Absolute Cross Sections for UV Photon-Induced DNA Strand Breakage," *The Journal of Physical Chemistry Letters*, vol. 6, pp. 4589–4593, Nov. 2015.

[57] P. W. K. Rothemund, "Folding DNA to create nanoscale shapes and patterns," *Nature*, vol. 440, pp. 297–302, Mar. 2006.

[58] K. Lund, Y. Liu, S. Lindsay, and H. Yan, "Self-Assembling a Molecular Pegboard," *Journal of the American Chemical Society*, vol. 127, pp. 17606–17607, Dec. 2005.

[59] S. H. Park, C. Pistol, S. J. Ahn, J. H. Reif, A. R. Lebeck, C. Dwyer, and T. H. LaBean, "Finite-Size, Fully Addressable DNA Tile Lattices Formed by Hierarchical Assembly Procedures," *Angewandte Chemie International Edition*, vol. 45, pp. 735–739, Jan. 2006.

[60] N. V. Voigt, T. Trring, A. Rotaru, M. F. Jacobsen, J. B. Ravnsbk, R. Subramani, W. Mamdouh, J. Kjems, A. Mokhir, F. Besenbacher, and K. V. Gothelf, "Single-molecule chemical reactions on DNA origami," *Nature Nanotechnology*, vol. 5, pp. 200–203, Mar. 2010.

[61] J. Rackwitz, J. Kopyra, I. Dbkowska, K. Ebel, M. L. Rankovic, A. R. Milosavljevic, and I. Bald, "Sensitizing DNA Towards Low-Energy Electrons with 2-Fluoroadenine," *Angewandte Chemie International Edition*, vol. 55, pp. 10248–10252, Aug. 2016.

[62] J. Nguyen, Y. Ma, T. Luo, R. G. Bristow, D. A. Jaffray, and Q.-B. Lu, "Direct observation of ultrafast-electron-transfer reactions unravels high effectiveness of reductive DNA damage," *Proceedings of the National Academy of Sciences*, vol. 108, pp. 11778–11783, July 2011.

[63] Y. Zheng, P. Cloutier, D. J. Hunting, L. Sanche, and J. R. Wagner, "Chemical Basis of DNA SugarPhosphate Cleavage by Low-Energy Electrons," *Journal of the American Chemical Society*, vol. 127, pp. 16592–16598, Nov. 2005.

[64] J. Koiek, A. Pysanenko, M. Frnk, and J. Fedor, "Microhydration Prevents Fragmentation of Uracil and Thymine by Low-Energy Electrons," *The Journal of Physical Chemistry Letters*, vol. 7, pp. 3401–3405, Sept. 2016.

[65] M. Neustetter, J. Aysina, F. F. daSilva, and S. Denifl, "The Effect of Solvation on Electron Attachment to Pure and Hydrated Pyrimidine Clusters," *Angewandte Chemie International Edition*, vol. 54, pp. 9124–9126, July 2015.

[66] M. B. Hahn, S. Meyer, M.-A. Schröter, H. Seitz, H.-J. Kunte, T. Solomun, and H. Sturm, "Direct electron irradiation of DNA in a fully aqueous environment. Damage determination in combination with Monte Carlo simulations," *Phys. Chem. Chem. Phys.*, 2017.

[67] E. Alizadeh, A. G. Sanz, G. Garca, and L. Sanche, "Radiation Damage to DNA: The Indirect Effect of Low-Energy Electrons," *The Journal of Physical Chemistry Letters*, vol. 4, pp. 820–825, Mar. 2013.

[68] X. Pan, P. Cloutier, D. Hunting, and L. Sanche, "Dissociative Electron Attachment to DNA," *Physical Review Letters*, vol. 90, May 2003.

[69] T. F. O'Malley, "Theory of Dissociative Attachment," *Physical Review*, vol. 150, pp. 14–29, Oct. 1966.

[70] S. Gohlke, *Elektroneninduzierte Dissoziationsprozesse in biologisch relevanten Molekülen.* PhD thesis, Freie Universität Berlin, Berlin, May 2006.

[71] I. Bald, I. Dbkowska, E. Illenberger, and O. Inglfsson, "Energy selective excision of CN following electron attachment to hexafluoroacetone azine ((CF $_3$) $_2$ CNNC(CF $_3$) $_2$)," *Phys. Chem. Chem. Phys.*, vol. 9, no. 23, pp. 2983–2990, 2007.

[72] D. Huber, M. Beikircher, S. Denifl, F. Zappa, S. Matejcik, A. Bacher, V. Grill, T. D. Märk, and P. Scheier, "High resolution dissociative electron attachment to gas phase adenine," *The Journal of Chemical Physics*, vol. 125, no. 8, p. 084304, 2006.

[73] S. Ptasiska, S. Denifl, B. Mrz, M. Probst, V. Grill, E. Illenberger, P. Scheier, and T. D. Märk, "Bond selective dissociative electron attachment to thymine," *The Journal of Chemical Physics*, vol. 123, p. 124302, Sept. 2005.

[74] S. Denifl, S. Ptasiska, M. Probst, J. Hruk, P. Scheier, and T. D. Märk, "Electron Attachment to the Gas-Phase DNA Bases Cytosine and Thymine," *The Journal of Physical Chemistry A*, vol. 108, pp. 6562–6569, Aug. 2004.

[75] S. Denifl, S. Ptasiska, G. Hanel, B. Gstir, M. Probst, P. Scheier, and T. D. Märk, "Electron attachment to gas-phase uracil," *The Journal of Chemical Physics*, vol. 120, pp. 6557–6565, Apr. 2004.

[76] H. Abdoul-Carime, J. Langer, M. A. Huels, and E. Illenberger, "Decomposition of purine nucleobases by very low energy electrons," *The European Physical Journal D*, vol. 35, pp. 399–404, Aug. 2005.

[77] P. D. Burrow, G. A. Gallup, A. M. Scheer, S. Denifl, S. Ptasinska, T. Märk, and P. Scheier, "Vibrational Feshbach resonances in uracil and thymine," *The Journal of Chemical Physics*, vol. 124, p. 124310, Mar. 2006.

[78] I. Baccarelli, F. A. Gianturco, A. Grandi, N. Sanna, R. R. Lucchese, I. Bald, J. Kopyra, and E. Illenberger, "Selective bond breaking in beta -ribose by gas-phase electron attachment around 8 ev," *Journal of the American Chemical Society*, vol. 129, pp. 6269–6277, May 2007.

[79] C. König, J. Kopyra, I. Bald, and E. Illenberger, "Dissociative Electron Attachment to Phosphoric Acid Esters: The Direct Mechanism for Single Strand Breaks in DNA," *Physical Review Letters*, vol. 97, July 2006.

[80] H. Abdoul-Carime, M. A. Huels, F. Brüning, E. Illenberger, and L. Sanche, "Dissociative electron attachment to gas-phase 5-bromouracil," *The Journal of Chemical Physics*, vol. 113, no. 7, p. 2517, 2000.

[81] H. Abdoul-Carime, M. A. Huels, E. Illenberger, and L. Sanche, "Sensitizing DNA to Secondary Electron Damage: Resonant Formation

of Oxidative Radicals from 5-Halouracils," *Journal of the American Chemical Society*, vol. 123, pp. 5354–5355, June 2001.

[82] F. Kossoski and M. T. d. N. Varella, "Negative ion states of 5-bromouracil and 5-iodouracil," *Phys. Chem. Chem. Phys.*, vol. 17, no. 26, pp. 17271–17278, 2015.

[83] F. Kossoski, J. Kopyra, and M. T. d. N. Varella, "Anion states and fragmentation of 2-chloroadenine upon low-energy electron collisions," *Phys. Chem. Chem. Phys.*, vol. 17, no. 43, pp. 28958–28965, 2015.

[84] J. Kopyra, C. Koenig-Lehmann, I. Bald, and E. Illenberger, "A Single Slow Electron Triggers the Loss of Both Chlorine Atoms from the Anticancer Drug Cisplatin: Implications for Chemoradiation Therapy," *Angewandte Chemie International Edition*, vol. 48, pp. 7904–7907, Oct. 2009.

[85] R. Wilken, M. S. Veena, M. B. Wang, and E. S. Srivatsan, "Curcumin: A review of anti-cancer properties and therapeutic activity in head and neck squamous cell carcinoma," *Molecular Cancer*, vol. 10, no. 1, p. 12, 2011.

[86] J. Kopyra, A. Keller, and I. Bald, "On the role of fluoro-substituted nucleosides in DNA radiosensitization for tumor radiation therapy," *RSC Advances*, vol. 4, no. 13, p. 6825, 2014.

[87] C.-R. Wang, A. Hu, and Q.-B. Lu, "Direct observation of the transition state of ultrafast electron transfer reaction of a radiosensitizing drug bromodeoxyuridine," *The Journal of Chemical Physics*, vol. 124, no. 24, p. 241102, 2006.

[88] L. Chomicz, M. Zdrowowicz, F. Kasprzykowski, J. Rak, A. Buonaugurio, Y. Wang, and K. H. Bowen, "How to Find Out Whether a 5-Substituted Uracil Could Be a Potential DNA Radiosensitizer," *The Journal of Physical Chemistry Letters*, vol. 4, pp. 2853–2857, Sept. 2013.

[89] B. Behmand, P. Cloutier, S. Girouard, J. R. Wagner, L. Sanche, and D. J. Hunting, "Hydrated Electrons React with High Specificity with Cisplatin Bound to Single-Stranded DNA," *The Journal of Physical Chemistry B*, vol. 117, pp. 15994–15999, Dec. 2013.

[90] M. Rezaee, E. Alizadeh, P. Cloutier, D. J. Hunting, and L. Sanche, "A Single Subexcitation-Energy Electron Can Induce a Double-Strand Break in DNA Modified by Platinum Chemotherapeutic Drugs," *ChemMedChem*, vol. 9, pp. 1145–1149, June 2014.

[91] J. F. Hainfeld, D. N. Slatkin, and H. M. Smilowitz, "The use of gold nanoparticles to enhance radiotherapy in mice," *Physics in Medicine and Biology*, vol. 49, pp. N309–N315, Sept. 2004.

[92] K. T. Butterworth, S. J. McMahon, F. J. Currell, and K. M. Prise, "Physical basis and biological mechanisms of gold nanoparticle radiosensitization," *Nanoscale*, vol. 4, no. 16, p. 4830, 2012.

[93] S. J. McMahon, W. B. Hyland, M. F. Muir, J. A. Coulter, S. Jain, K. T. Butterworth, G. Schettino, G. R. Dickson, A. R. Hounsell, J. M. OSullivan, K. M. Prise, D. G. Hirst, and F. J. Currell, "Nanodosimetric effects of gold nanoparticles in megavoltage radiation therapy," *Radiotherapy and Oncology*, vol. 100, pp. 412–416, Sept. 2011.

[94] C. Van Bree, N. A. Franken, P. J. Bakker, L. J. Klomp-Tukker, G. W. Barendsen, and J. A. Kipp, "Hyperthermia and incorporation of halogenated pyrimidines: Radiosensitization in cultured rodent and human tumor cells," *International Journal of Radiation Oncology*Biology*Physics*, vol. 39, pp. 489–496, Sept. 1997.

[95] L. Chomicz, J. Rak, and P. Storoniak, "Electron-Induced Elimination of the Bromide Anion from Brominated Nucleobases. A Computational Study," *The Journal of Physical Chemistry B*, vol. 116, pp. 5612–5619, May 2012.

[96] M. Wieczr, P. Wityk, J. Czub, L. Chomicz, and J. Rak, "A first-principles study of electron attachment to the fully hydrated bromonucleobases," *Chemical Physics Letters*, vol. 595-596, pp. 133–137, Mar. 2014.

[97] L. Chomicz, J. Leszczynski, and J. Rak, "Electron-Induced Degradation of 8-Bromo-2-deoxyadenosine 3,5-Diphosphate, a DNA Radiosensitizing Nucleotide," *The Journal of Physical Chemistry B*, vol. 117, pp. 8681–8688, July 2013.

[98] K. Westphal, J. Wiczk, J. Miloch, G. Kciuk, K. Bobrowski, and J. Rak, "Irreversible electron attachment a key to DNA damage by solvated electrons in aqueous solution," *Org. Biomol. Chem.*, vol. 13, no. 41, pp. 10362–10369, 2015.

[99] M. Zdrowowicz, L. Chomicz, J. Miloch, J. Wiczk, J. Rak, G. Kciuk, and K. Bobrowski, "Reactivity Pattern of Bromonucleosides Induced by 2-Hydroxypropyl Radicals: Photochemical, Radiation Chemical, and Computational Studies," *The Journal of Physical Chemistry B*, vol. 119, pp. 6545–6554, June 2015.

[100] M. Russo, L. B. Jimenez, Q. G. Mulazzani, M. D'Angelantonio, M. Guerra, M. A. Miranda, and C. Chatgilialoglu, "Chemical Radiation Studies of 8-Bromo-2-deoxyinosine and 8-Bromoinosine in Aqueous Solutions," *Chemistry - A European Journal*, vol. 12, pp. 7684–7693, Oct. 2006.

[101] L. B. Jimenez, S. Encinas, M. A. Miranda, M. L. Navacchia, and C. Chatgilialoglu, "The photochemistry of 8-bromo-2-deoxyadenosine. A direct entry to cyclopurine lesions," *Photochem. Photobiol. Sci.*, vol. 3, no. 11-12, pp. 1042–1046, 2004.

[102] C. Chatgilialoglu, M. Guerra, and Q. G. Mulazzani, "Model Studies of DNA C5 Radicals. Selective Generation and Reactivity of 2-Deoxyadenosin-5-yl Radical," *Journal of the American Chemical Society*, vol. 125, pp. 3839–3848, Apr. 2003.

[103] M. Auffan, J. Rose, J.-Y. Bottero, G. V. Lowry, J.-P. Jolivet, and M. R. Wiesner, "Towards a definition of inorganic nanoparticles from an environmental, health and safety perspective," *Nature Nanotechnology*, vol. 4, pp. 634–641, Nov. 2009.

[104] S. A. Maier, *Plasmonics: fundamentals and applications*. New York: Springer, 2007.

[105] K. Haume, S. Rosa, S. Grellet, M. A. miaek, K. T. Butterworth, A. V. Solovyov, K. M. Prise, J. Golding, and N. J. Mason, "Gold nanoparticles for cancer radiotherapy: a review," *Cancer Nanotechnology*, vol. 7, Dec. 2016.

[106] J. F. Hainfeld, D. N. Slatkin, T. M. Focella, and H. M. Smilowitz, "Gold nanoparticles: a new X-ray contrast agent," *The British Journal of Radiology*, vol. 79, pp. 248–253, Mar. 2006.

[107] J. W. Krumpfer, T. Schuster, M. Klapper, and K. Müllen, "Make it nano-Keep it nano," *Nano Today*, vol. 8, pp. 417–438, Aug. 2013.

[108] J. Song, J. Zhou, and H. Duan, "Self-Assembled Plasmonic Vesicles of SERS-Encoded Amphiphilic Gold Nanoparticles for Cancer Cell Targeting and Traceable Intracellular Drug Delivery," *Journal of the American Chemical Society*, vol. 134, pp. 13458–13469, Aug. 2012.

[109] D. Jaque, L. Martnez Maestro, B. del Rosal, P. Haro-Gonzalez, A. Benayas, J. L. Plaza, E. Martn Rodrguez, and J. Garca Sol, "Nanoparticles for photothermal therapies," *Nanoscale*, vol. 6, p. 9494, Apr. 2014.

[110] X. Huang, P. K. Jain, I. H. El-Sayed, and M. A. El-Sayed, "Plasmonic photothermal therapy (PPTT) using gold nanoparticles," *Lasers in Medical Science*, vol. 23, pp. 217–228, July 2008.

[111] A. M. Gobin, M. H. Lee, N. J. Halas, W. D. James, R. A. Drezek, and J. L. West, "Near-Infrared Resonant Nanoshells for Combined Optical Imaging and Photothermal Cancer Therapy," *Nano Letters*, vol. 7, pp. 1929–1934, July 2007.

[112] X. Huang, B. Kang, W. Qian, M. A. Mackey, P. C. Chen, A. K. Oyelere, I. H. El-Sayed, and M. A. El-Sayed, "Comparative study of photothermolysis of cancer cells with nuclear-targeted or cytoplasm-targeted gold nanospheres: continuous wave or pulsed lasers," *Journal of Biomedical Optics*, vol. 15, no. 5, p. 058002, 2010.

[113] K. K. Maiti, U. Dinish, A. Samanta, M. Vendrell, K.-S. Soh, S.-J. Park, M. Olivo, and Y.-T. Chang, "Multiplex targeted in vivo cancer detection using sensitive near-infrared SERS nanotags," *Nano Today*, vol. 7, pp. 85–93, Apr. 2012.

[114] E. Ozbay, "Plasmonics: Merging Photonics and Electronics at Nanoscale Dimensions," *Science*, vol. 311, pp. 189–193, Jan. 2006.

[115] M. A. Garcia, "Surface plasmons in metallic nanoparticles: fundamentals and applications," *Journal of Physics D: Applied Physics*, vol. 44, p. 283001, July 2011.

[116] C. Noguez, "Surface Plasmons on Metal Nanoparticles: The Influence of Shape and Physical Environment," *The Journal of Physical Chemistry C*, vol. 111, pp. 3806–3819, Mar. 2007.

[117] M. J. Kale, T. Avanesian, and P. Christopher, "Direct Photocatalysis by Plasmonic Nanostructures," *ACS Catalysis*, vol. 4, pp. 116–128, Jan. 2014.

[118] P. K. Jain, K. S. Lee, I. H. El-Sayed, and M. A. El-Sayed, "Calculated Absorption and Scattering Properties of Gold Nanoparticles of Different Size, Shape, and Composition: Applications in Biological Imaging and Biomedicine," *The Journal of Physical Chemistry B*, vol. 110, pp. 7238–7248, Apr. 2006.

[119] G. Mie, "Beiträge zur Optik trüber Medien, speziell kolloidaler Metallösungen," *Annalen der Physik*, vol. 330, no. 3, pp. 377–445, 1908.

[120] S. Link and M. A. El-Sayed, "Shape and size dependence of radiative, non-radiative and photothermal properties of gold nanocrystals," *International Reviews in Physical Chemistry*, vol. 19, pp. 409–453, July 2000.

[121] S. K. Ghosh and T. Pal, "Interparticle Coupling Effect on the Surface Plasmon Resonance of Gold Nanoparticles: From Theory to Applications," *Chemical Reviews*, vol. 107, pp. 4797–4862, Nov. 2007.

[122] G. C. Schatz and R. P. Van Duyne, "Electromagnetic Mechanism of Surface-Enhanced Spectroscopy," in *Handbook of Vibrational Spectroscopy* (J. M. Chalmers and P. R. Griffiths, eds.), Chichester, UK: John Wiley & Sons, Ltd, Aug. 2006. DOI: 10.1002/0470027320.s0601.

[123] P. K. Jain, X. Huang, I. H. El-Sayed, and M. A. El-Sayed, "Review of Some Interesting Surface Plasmon Resonance-enhanced Properties of Noble Metal Nanoparticles and Their Applications to Biosystems," *Plasmonics*, vol. 2, pp. 107–118, Sept. 2007.

[124] U. Kreibig and M. Vollmer, *Optical Properties of Metal Clusters*, vol. 25 of *Springer Series in Materials Science*. Berlin, Heidelberg: Springer Berlin Heidelberg, 1995.

[125] S. L. Westcott, S. J. Oldenburg, T. Lee, and N. J. Halas, "Construction of simple gold nanoparticle aggregates with controlled plasmonplasmon interactions," *Chemical Physics Letters*, vol. 300, pp. 651–655, Feb. 1999.

[126] C. Noguez, "Optical properties of isolated and supported metal nanoparticles," *Optical Materials*, vol. 27, pp. 1204–1211, Apr. 2005.

[127] G. Baffou and R. Quidant, "Thermo-plasmonics: using metallic nanostructures as nano-sources of heat: Thermoplasmonics," *Laser & Photonics Reviews*, vol. 7, pp. 171–187, Mar. 2013.

[128] G. Baffou, R. Quidant, and C. Girard, "Heat generation in plasmonic nanostructures: Influence of morphology," *Applied Physics Letters*, vol. 94, p. 153109, Apr. 2009.

[129] G. Baffou, R. Quidant, and F. J. Garca de Abajo, "Nanoscale Control of Optical Heating in Complex Plasmonic Systems," *ACS Nano*, vol. 4, pp. 709–716, Feb. 2010.

[130] H. H. Richardson, M. T. Carlson, P. J. Tandler, P. Hernandez, and A. O. Govorov, "Experimental and Theoretical Studies of Light-to-Heat Conversion and Collective Heating Effects in Metal Nanoparticle Solutions," *Nano Letters*, vol. 9, pp. 1139–1146, Mar. 2009.

[131] A. O. Govorov, W. Zhang, T. Skeini, H. Richardson, J. Lee, and N. A. Kotov, "Gold nanoparticle ensembles as heaters and actuators: melting and collective plasmon resonances," *Nanoscale Research Letters*, vol. 1, pp. 84–90, Nov. 2006.

[132] A. O. Govorov and H. H. Richardson, "Generating heat with metal nanoparticles," *Nano Today*, vol. 2, pp. 30–38, Feb. 2007.

[133] R. R. Letfullin, T. F. George, G. C. Duree, and B. M. Bollinger, "Ultrashort Laser Pulse Heating of Nanoparticles: Comparison of Theoretical Approaches," *Advances in Optical Technologies*, vol. 2008, pp. 1–8, 2008.

[134] G. Gonzlez-Rubio, A. Guerrero-Martnez, and L. M. Liz-Marzn, "Reshaping, Fragmentation, and Assembly of Gold Nanoparticles Assisted by Pulse Lasers," *Accounts of Chemical Research*, vol. 49, pp. 678–686, Apr. 2016.

[135] V. K. Pustovalov, "Light-to-heat conversion and heating of single nanoparticles, their assemblies, and the surrounding medium under laser pulses," *RSC Adv.*, vol. 6, no. 84, pp. 81266–81289, 2016.

[136] M. Strasser, K. Setoura, U. Langbein, and S. Hashimoto, "Computational Modeling of Pulsed Laser-Induced Heating and Evaporation of Gold Nanoparticles," *The Journal of Physical Chemistry C*, vol. 118, pp. 25748–25755, Nov. 2014.

[137] D. Werner, S. Hashimoto, and T. Uwada, "Remarkable Photothermal Effect of Interband Excitation on Nanosecond Laser-Induced Reshaping and Size Reduction of Pseudospherical Gold Nanoparticles in Aqueous Solution," *Langmuir*, vol. 26, pp. 9956–9963, June 2010.

[138] S. Hashimoto, D. Werner, and T. Uwada, "Studies on the interaction of pulsed lasers with plasmonic gold nanoparticles toward light manipulation, heat management, and nanofabrication," *Journal of Photochemistry and Photobiology C: Photochemistry Reviews*, vol. 13, pp. 28–54, Mar. 2012.

[139] R. E. Cavicchi, D. C. Meier, C. Presser, V. M. Prabhu, and S. Guha, "Single Laser Pulse Effects on Suspended-Au-Nanoparticle Size Distributions and Morphology," *The Journal of Physical Chemistry C*, vol. 117, pp. 10866–10875, May 2013.

[140] N. Matsuo, H. Muto, K. Miyajima, and F. Mafun, "Single laser pulse induced aggregation of gold nanoparticles," *Physical Chemistry Chemical Physics*, vol. 9, no. 45, p. 6027, 2007.

[141] A. Poletti, G. Fracasso, G. Conti, R. Pilot, and V. Amendola, "Laser generated gold nanocorals with broadband plasmon absorption for photothermal applications," *Nanoscale*, vol. 7, no. 32, pp. 13702–13714, 2015.

[142] T. Katayama, K. Setoura, D. Werner, H. Miyasaka, and S. Hashimoto, "Picosecond-to-Nanosecond Dynamics of Plasmonic Nanobubbles from PumpProbe Spectral Measurements of Aqueous Colloidal Gold Nanoparticles," *Langmuir*, vol. 30, pp. 9504–9513, Aug. 2014.

[143] K. Metwally, S. Mensah, and G. Baffou, "Fluence Threshold for Photothermal Bubble Generation Using Plasmonic Nanoparticles," *The Journal of Physical Chemistry C*, vol. 119, pp. 28586–28596, Dec. 2015.

[144] H. Muto, K. Miyajima, and F. Mafun, "Mechanism of Laser-Induced Size Reduction of Gold Nanoparticles As Studied by Single and Double Laser Pulse Excitation," *The Journal of Physical Chemistry C*, vol. 112, pp. 5810–5815, Apr. 2008.

[145] A. Pyatenko, M. Yamaguchi, and M. Suzuki, "Mechanisms of Size Reduction of Colloidal Silver and Gold Nanoparticles Irradiated by Nd:YAG Laser," *The Journal of Physical Chemistry C*, vol. 113, pp. 9078–9085, May 2009.

[146] Y. Takeda, T. Kondow, and F. Mafun, "Selective decomposition of nucleic acids by laser irradiation on probe-tethered gold nanoparticles in solution," *Phys. Chem. Chem. Phys.*, vol. 13, no. 2, pp. 586–592, 2011.

[147] X. Zhang, Y. L. Chen, R.-S. Liu, and D. P. Tsai, "Plasmonic photocatalysis," *Reports on Progress in Physics*, vol. 76, p. 046401, Apr. 2013.

[148] Y. Kim, D. Dumett Torres, and P. K. Jain, "Activation Energies of Plasmonic Catalysts," *Nano Letters*, vol. 16, pp. 3399–3407, May 2016.

[149] J. Y. Park, S. M. Kim, H. Lee, and I. I. Nedrygailov, "Hot-Electron-Mediated Surface Chemistry: Toward Electronic Control of Catalytic Activity," *Accounts of Chemical Research*, vol. 48, pp. 2475–2483, Aug. 2015.

[150] Z. Zhang, T. Deckert-Gaudig, P. Singh, and V. Deckert, "Single molecule level plasmonic catalysis a dilution study of p-nitrothiophenol on gold dimers," *Chem. Commun.*, vol. 51, no. 15, pp. 3069–3072, 2015.

[151] P. Christopher, H. Xin, A. Marimuthu, and S. Linic, "Singular characteristics and unique chemical bond activation mechanisms of photocatalytic reactions on plasmonic nanostructures," *Nature Materials*, Oct. 2012.

[152] S. Mukherjee, F. Libisch, N. Large, O. Neumann, L. V. Brown, J. Cheng, J. B. Lassiter, E. A. Carter, P. Nordlander, and N. J. Halas, "Hot Electrons Do the Impossible: Plasmon-Induced Dissociation of H $_2$ on Au," *Nano Letters*, vol. 13, pp. 240–247, Jan. 2013.

[153] K. Watanabe, D. Menzel, N. Nilius, and H.-J. Freund, "Photochemistry on Metal Nanoparticles," *Chemical Reviews*, vol. 106, pp. 4301–4320, Oct. 2006.

[154] B. Persson, "Polarizability of small spherical metal particles: influence of the matrix environment," *Surface Science*, vol. 281, pp. 153–162, Jan. 1993.

[155] W. Xie and S. Schlücker, "Hot electron-induced reduction of small molecules on photorecycling metal surfaces," *Nature Communications*, vol. 6, p. 7570, July 2015.

[156] Z. Zhang, T. Deckert-Gaudig, and V. Deckert, "Label-free monitoring of plasmonic catalysis on the nanoscale," *The Analyst*, vol. 140, no. 13, pp. 4325–4335, 2015.

[157] A. Campion and P. Kambhampati, "Surface-enhanced Raman scattering," *Chemical Society Reviews*, vol. 27, no. 4, p. 241, 1998.

[158] M. Moskovits, "Surface-enhanced spectroscopy," *Reviews of Modern Physics*, vol. 57, pp. 783–826, July 1985.

[159] S. Schlücker, "Surface-Enhanced Raman Spectroscopy: Concepts and Chemical Applications," *Angewandte Chemie International Edition*, vol. 53, pp. 4756–4795, May 2014.

[160] K. Kneipp, Y. Wang, H. Kneipp, L. T. Perelman, I. Itzkan, R. R. Dasari, and M. S. Feld, "Single Molecule Detection Using Surface-Enhanced Raman Scattering (SERS)," *Physical Review Letters*, vol. 78, pp. 1667–1670, Mar. 1997.

[161] S. Nie, "Probing Single Molecules and Single Nanoparticles by Surface-Enhanced Raman Scattering," *Science*, vol. 275, pp. 1102–1106, Feb. 1997.

[162] D. J. Gardiner and H. J. Bowley, eds., *Practical Raman spectroscopy*. Berlin: Springer, 1989. OCLC: 246612753.

[163] E. Smith and G. Dent, *Modern Raman Spectroscopy - A Practical Approach: Smith/Modern Raman Spectroscopy - A Practical Approach*. Chichester, UK: John Wiley & Sons, Ltd, Dec. 2004. DOI: 10.1002/0470011831.

[164] E. C. Le Ru and P. G. Etchegoin, *Principles of surface-enhanced Raman spectroscopy: and related plasmonic effects*. Amsterdam: Elsevier, 1. ed ed., 2009. OCLC: 229031783.

[165] J. Gersten and A. Nitzan, "Electromagnetic theory of enhanced Raman scattering by molecules adsorbed on rough surfaces," *The Journal of Chemical Physics*, vol. 73, pp. 3023–3037, Oct. 1980.

[166] K. A. Willets and R. P. Van Duyne, "Localized Surface Plasmon Resonance Spectroscopy and Sensing," *Annual Review of Physical Chemistry*, vol. 58, pp. 267–297, May 2007.

[167] L. Seballos, T. Y. Olson, and J. Z. Zhang, "Effects of chromophore orientation and molecule conformation on surface-enhanced Raman scattering studied with alkanoic acids and colloidal silver nanoparticles," *The Journal of Chemical Physics*, vol. 125, p. 234706, Dec. 2006.

[168] J. Prinz, C. Heck, L. Ellerik, V. Merk, and I. Bald, "DNA origami based AuAg-coreshell nanoparticle dimers with single-molecule SERS sensitivity," *Nanoscale*, vol. 8, no. 10, pp. 5612–5620, 2016.

[169] M. Moskovits, "Surface-enhanced Raman spectroscopy: a brief retrospective," *Journal of Raman Spectroscopy*, vol. 36, pp. 485–496, June 2005.

[170] C. Boerigter, U. Aslam, and S. Linic, "Mechanism of Charge Transfer from Plasmonic Nanostructures to Chemically Attached Materials," *ACS Nano*, vol. 10, pp. 6108–6115, June 2016.

[171] M. Pagliai, S. Caporali, M. Muniz-Miranda, G. Pratesi, and V. Schettino, "SERS, XPS, and DFT Study of Adenine Adsorption on Silver and Gold Surfaces," *The Journal of Physical Chemistry Letters*, vol. 3, pp. 242–245, Jan. 2012.

[172] B. Giese and D. McNaughton, "Surface-Enhanced Raman Spectroscopic and Density Functional Theory Study of Adenine Adsorption to Silver Surfaces," *The Journal of Physical Chemistry B*, vol. 106, pp. 101–112, Jan. 2002.

[173] J. Liu, "Adsorption of DNA onto gold nanoparticles and graphene oxide: surface science and applications," *Physical Chemistry Chemical Physics*, vol. 14, no. 30, p. 10485, 2012.

[174] A. Sarmah and R. K. Roy, "Interaction between Small Gold Clusters and Nucleobases: A Density Functional Reactivity Theory Based Study," *The Journal of Physical Chemistry C*, vol. 119, pp. 17940–17953, Aug. 2015.

[175] B. Giese and D. McNaughton, "Surface-Enhanced Raman Spectroscopic Study of Uracil. The Influence of the Surface Substrate, Surface Potential, and pH," *The Journal of Physical Chemistry B*, vol. 106, pp. 1461–1470, Feb. 2002.

[176] C. Otto, T. J. J. van den Tweel, F. F. M. de Mul, and J. Greve, "Surface-enhanced Raman spectroscopy of DNA bases," *Journal of Raman Spectroscopy*, vol. 17, pp. 289–298, June 1986.

[177] F. Latorre, S. Kupfer, T. Bocklitz, D. Kinzel, S. Trautmann, S. Gräfe, and V. Deckert, "Spatial resolution of tip-enhanced Raman spectroscopy – DFT assessment of the chemical effect," *Nanoscale*, vol. 8, no. 19, pp. 10229–10239, 2016.

[178] L. M. Freeman, L. Pang, and Y. Fainman, "Maximizing the Electromagnetic and Chemical Resonances of Surface-Enhanced Raman Scattering for Nucleic Acids," *ACS Nano*, vol. 8, pp. 8383–8391, Aug. 2014.

[179] K. Kneipp, H. Kneipp, V. B. Kartha, R. Manoharan, G. Deinum, I. Itzkan, R. R. Dasari, and M. S. Feld, "Detection and identification of a single DNA base molecule using surface-enhanced Raman scattering (SERS)," *Physical Review E*, vol. 57, pp. R6281–R6284, June 1998.

[180] B. Giese and D. McNaughton, "Interaction of anticancer drug cisplatin with guanine: Density functional theory and surface-enhanced Raman spectroscopy study," *Biopolymers*, vol. 72, no. 6, pp. 472–489, 2003.

[181] Y.-L. Chen, D.-Y. Wu, and Z.-Q. Tian, "Theoretical Investigation on the Substituent Effect of Halogen Atoms at the C $_8$ Position of Adenine: Relative Stability, Vibrational Frequencies, and Raman Spectra of Tautomers," *The Journal of Physical Chemistry A*, vol. 120, pp. 4049–4058, June 2016.

[182] V. K. Rastogi, M. A. Palafox, L. Mittal, N. Peica, W. Kiefer, K. Lang, and S. P. Ojha, "FTIR and FT-Raman spectra and density functional computations of the vibrational spectra, molecular geometry and atomic charges of the biomolecule: 5-bromouracil," *Journal of Raman Spectroscopy*, vol. 38, pp. 1227–1241, Oct. 2007.

[183] P. C. Lee and D. Meisel, "Adsorption and surface-enhanced Raman of dyes on silver and gold sols," *The Journal of Physical Chemistry*, vol. 86, pp. 3391–3395, Aug. 1982.

[184] S. R. Panikkanvalappil, M. A. Mackey, and M. A. El-Sayed, "Probing the Unique Dehydration-Induced Structural Modifications in Cancer Cell DNA Using Surface Enhanced Raman Spectroscopy," *Journal of the American Chemical Society*, vol. 135, pp. 4815–4821, Mar. 2013.

[185] S. R. Panikkanvalappil, M. A. Mahmoud, M. A. Mackey, and M. A. El-Sayed, "Surface-Enhanced Raman Spectroscopy for Real-Time Monitoring of Reactive Oxygen Species-Induced DNA Damage and Its Prevention by Platinum Nanoparticles," *ACS Nano*, vol. 7, pp. 7524–7533, Sept. 2013.

[186] W. GmbH, "WITec alpha300 Series Raman AFM SNOM High-Resolution Optical and Scanning Probe Microscopy Systems."

[187] G. Fasman, *Handbook of biochemistry and molecular biology. Sect. B Vol. 2: Nucleic acids [Nomenclature, nucleic acids, enzymes involved with nucleic acid function, genetics and biology].* 3. ed ed., 1975. OCLC: 60429870.

[188] J. W. Park, K. C. Cundy, and B. N. Ames, "Detection of DNA adducts by high-performance liquid chromatography with electrochemical detection," *Carcinogenesis*, vol. 10, pp. 827–832, May 1989.

[189] D. B. Dunn and J. D. Smith, "Effects of 5-halogenated uracils on the growth of Escherichia coli and their incorporation into deoxyribonucleic acids," *The Biochemical Journal*, vol. 67, pp. 494–506, Nov. 1957.

[190] S. V. K. Kumar, S. T. Tare, Y. V. Upalekar, and T. Tsering, "Dose controlled low energy electron irradiator for biomolecular films," *Review of Scientific Instruments*, vol. 87, p. 034302, Mar. 2016.

[191] G. Binnig, C. F. Quate, and C. Gerber, "Atomic Force Microscope," *Physical Review Letters*, vol. 56, pp. 930–933, Mar. 1986.

[192] Y. Martin, C. C. Williams, and H. K. Wickramasinghe, "Atomic force microscopeforce mapping and profiling on a sub 100 scale," *Journal of Applied Physics*, vol. 61, pp. 4723–4729, May 1987.

[193] L. Sanche, "Interaction of low energy electrons with DNA: Applications to cancer radiation therapy," *Radiation Physics and Chemistry*, vol. 128, pp. 36–43, Nov. 2016.

[194] Y. Zheng, D. J. Hunting, P. Ayotte, and L. Sanche, "Role of Secondary Low-Energy Electrons in the Concomitant Chemoradiation Therapy of Cancer," *Physical Review Letters*, vol. 100, May 2008.

[195] M. D. Prados, C. Scott, H. Sandler, J. C. Buckner, T. Phillips, C. Schultz, R. Urtasun, R. Davis, P. Gutin, T. L. Cascino, H. S. Greenberg, and W. J. Curran Jr, "A phase 3 randomized study of radiotherapy plus procarbazine, CCNU, and vincristine (PCV) with or without BUdR for the treatment of anaplastic astrocytoma: a preliminary report of RTOG 9404," *International Journal of Radiation Oncology*Biology*Physics*, vol. 45, pp. 1109–1115, Dec. 1999.

[196] H. Choy, ed., *Chemoradiation in cancer therapy*. Cancer drug discovery and development, Totowa, N.J: Humana Press, 2003.

[197] J. Lengyel, J. Koiek, M. Frnk, and J. Fedor, "Self-Scavenging of Electrons in Fe(CO) $_5$ Aggregates Deposited on Argon Nanoparticles," *The Journal of Physical Chemistry C*, vol. 120, pp. 7397–7402, Apr. 2016.

[198] J. Rackwitz, M. L. Rankovic, A. R. Milosavljevic, and I. Bald, "A novel setup for the determination of absolute cross sections for low-energy electron induced strand breaks in oligonucleotides The effect of the radiosensitizer 5-fluorouracil*," *The European Physical Journal D*, vol. 71, Feb. 2017.

[199] J.-W. Park and J. S. Shumaker-Parry, "Strong Resistance of Citrate Anions on Metal Nanoparticles to Desorption under Thiol Functionalization," *ACS Nano*, vol. 9, pp. 1665–1682, Feb. 2015.

[200] R. Dinkel, B. Braunschweig, and W. Peukert, "Fast and Slow Ligand Exchange at the Surface of Colloidal Gold Nanoparticles," *The Journal of Physical Chemistry C*, vol. 120, pp. 1673–1682, Jan. 2016.

[201] L. Yu and N. Li, "Binding Strength of Nucleobases and Nucleosides on Silver Nanoparticles Probed by a Colorimetric Method," *Langmuir*, vol. 32, pp. 5510–5518, June 2016.

[202] F. F. da Silva, C. Matias, D. Almeida, G. Garca, O. Inglfsson, H. D. Flosadttir, B. marsson, S. Ptasinska, B. Puschnigg, P. Scheier, P. Limo-Vieira, and S. Denifl, "NCO, a Key Fragment Upon Dissociative Electron Attachment and Electron Transfer to Pyrimidine Bases: Site Selectivity for a Slow Decay Process," *Journal of The American Society for Mass Spectrometry*, vol. 24, pp. 1787–1797, Nov. 2013.

[203] M. L. Brongersma, N. J. Halas, and P. Nordlander, "Plasmon-induced hot carrier science and technology," *Nature Nanotechnology*, vol. 10, pp. 25–34, Jan. 2015.

[204] R. Kopelman, "Fractal Reaction Kinetics," *Science*, vol. 241, pp. 1620–1626, Sept. 1988.

[205] P. C. do Couto, B. J. Costa Cabral, and S. Canuto, "Electron binding energies of water clusters: Implications for the electronic properties of liquid water," *Chemical Physics Letters*, vol. 429, pp. 129–135, Sept. 2006.

[206] A. Sanchez-Iglesias, P. Aldeanueva-Potel, W. Ni, J. Perez-Juste, I. Pastoriza-Santos, R. A. Alvarez-Puebla, B. N. Mbenkum, and L. M. Liz-Marzan, "Chemical seeded growth of Ag nanoparticle arrays and their application as reproducible SERS substrates," *Nano Today*, vol. 5, pp. 21–27, Feb. 2010.

[207] J. Wirth, F. Garwe, R. Meyer, A. Cseki, O. Stranik, and W. Fritzsche, "Plasmonically Enhanced Electron Escape from Gold Nanoparticles and Their Polarization-Dependent Excitation Transfer along DNA Nanowires," *Nano Letters*, vol. 14, pp. 3809–3816, July 2014.

[208] M. Fan, G. F. Andrade, and A. G. Brolo, "A review on the fabrication of substrates for surface enhanced Raman spectroscopy and their applications in analytical chemistry," *Analytica Chimica Acta*, vol. 693, pp. 7–25, May 2011.

Declaration of Authorship

I hereby confirm that I have authored this PhD thesis independently and without use of others than the indicated sources. All passages which are literally or in general matter taken out of publications or other sources are marked as such.

Potsdam, June 2017

Robin Mathis Schürmann